

# High Resolution Measurements with Silicon Drift Detectors for Compton Camera Applications

DISSERTATION

zur Erlangung des Grades eines Doktors  
der Naturwissenschaften

vorgelegt von

Dipl.-Phys. Tuba Çonka Nurdan  
geb. am 18. Mai 1975 in Ankara, Türkei

eingereicht beim Fachbereich Physik  
der Universität Siegen  
Siegen 2004

Gutachter der Dissertation: Prof. Dr. A.H. Walenta  
Prof. Dr. N.A. Pavel

Datum der Disputation: 24.01.2005

Prüfer: Prof. Dr. H.D. Dahmen  
Prof. Dr. N.A. Pavel  
Prof. Dr. A.H. Walenta

Internetpublikation der Universitätsbibliothek Siegen: **urn:nbn:de:hbz:467-892**

To my parents Türel and İsmail Çonka  
and  
my husband Kıvanç Nurdan



# Zusammenfassung

Vorrangiges Ziel nuklear-medizinischer Untersuchungen ist die genaue und schnelle Ortsbestimmung der Radionuklidverteilung in radioaktiv markierten Gewebe oder Organen. Gegenüber den heutigen PET und SPECT-Techniken kann der Einsatz einer Compton-Kamera grundsätzlich die Ortsauflösung und die Effizienz verbessern. Weil es notwendig ist, ein ganzes Streuungereignis in der Compton-Kamera zu rekonstruieren, ist die Detektortechnologie sehr anspruchsvoll. Brauchbare Detektoren sind in der Vergangenheit nicht verfügbar gewesen. Deshalb, ein neuer Detektortyp, die Siliziumdriftdetektor (SDD), entwickelt für Experimente in der Röntgen-Astrophysik, zeigt erfolversprechende Eigenschaften. Der Test eines solchen Systems ist das Hauptziel dieser Doktorarbeit.

Die Optimierung eines Compton-Kamera-Systems bezüglich der Effizienz und der Ortsauflösung stellt ein komplexes Multiparameterproblem dar, welches von verschiedenartigen Detektoreigenschaften abhängt. Um die optimalen Detektorparameter zu bestimmen, wird deren Einfluss auf die Leistungsfähigkeit des Compton-Kamera-Systems in dieser Arbeit anhand von analytischen Systemmodellen und Monte-Carlo-Simulationen untersucht.

Ein Comptonkamerateaufbau wurde mit einem 19-kanäligen SDD mit direkt implementierten JFETs als Streudetektor und einer Anger-Kamera ohne Bleikollimator als Absorptionsdetektor realisiert. Das äquivalente Ladungsrauschen der SDD Kanäle wurde bei 10 °C und einer Pulsformzeitkonstante von 100 ns zu 30 - 40 Elektronen rms gemessen. Ein neues Konzept wurde für die schnelle Detektorauslese, welche für diese Anwendung wichtig ist, entwickelt. Das System ist so ausgelegt, dass die Messungen in jeder Detektororientierung und unter beliebigen kinematischen Bedingungen durchgeführt werden können.

Compton-Kamera-Koinzidenzen bei hoher Statistik wurden durch Bestrahlen der SDD-Zellen mit einer fein-kollimierten 1 Ci  $^{137}\text{Cs}$  aufgenommen. Mit diesem System gemessene Zeit-, Energie- und Winkelverteilungen von Koinzidenzen werden in dieser Arbeit vorgestellt. Es wird gezeigt, dass es mit dem Streudetektor, welcher eine hervorragende Energieauflösung aufweist, möglich ist, mit der Ortsbestimmung in zwei Detektoren die Quellenverteilung genau zu rekonstruieren.

## Abstract

The accurate and rapid location of the radionuclide distribution in radioactively labeled tissue or organs is the goal of nuclear medicine. The Compton camera, in principle, can improve the spatial resolution and efficiency with respect to today's PET and SPECT techniques. Since it is necessary to reconstruct a full scattering event in the Compton camera, the detector technology is very demanding. Useful detectors have not been available in the past. However, a new detector type, the Silicon Drift Detector (SDD), developed for experiments in x-ray astrophysics show promising features. The test of such a system is the main objective of this thesis.

The optimization of a Compton camera system in terms of efficiency and resolution is a complex multiparameter problem which depends on various detector properties. The influence of these parameters on the performance of the Compton camera system is investigated in this work using the analytical system models and Monte Carlo simulations in order to find optimum detector parameters.

Compton camera test setup has been constructed using a 19 channel SDD with on-chip JFET as the scatter detector and an Anger camera without a lead collimator as the absorption detector. The equivalent noise charge of the SDD channels at 10 °C with a shaping time of 100 ns was measured to be between 30-40 electrons rms. New readout scheme has been implemented for the fast readout of the detector which is crucial for this application. The system is designed such that the measurements can be done in all detector orientations and kinematical conditions.

Compton camera coincidence events with high statistics have been acquired by irradiating the SDD cells with a finely-collimated 1 Ci  $^{137}\text{Cs}$  source. Time, energy and angular distributions of coincidence events measured with this detector system are presented in this work. It is shown that with the scatter detector having an excellent energy resolution, it is possible to reconstruct the source distribution accurately using the locations of the interactions measured in two detectors.



# Contents

<b>1. Introduction</b>	1
1.1 Literature Review of Compton Camera Systems	2
1.1.1 Applications in Astrophysics: Compton Telescopes	2
1.1.2 Compton Camera for Industrial Applications	5
1.1.3 Compton Camera in Nuclear Medicine	6
1.2 Objectives of this Work	8
1.3 Overview of Dissertation	9
<b>2. Theoretical Considerations for the Compton Camera System Design</b>	11
2.1 Principles of Compton Camera Imaging	11
2.2 Interaction of Photons	12
2.2.1 Photon Interactions in the Scatter Detector	13
2.2.2 Photon Interactions in the Absorption Detector	17
2.3 Interactions of Electrons	19
2.3.1 Energy Loss of Electrons in the Scatter Detector	20
2.3.2 Range of Electrons	21
2.3.3 Angular Distribution of Recoil Electrons	24
<b>3. Impact of the Detector Parameters on the Compton Camera Performance</b>	27
3.1 Doppler Broadening	28
3.1.1 Doppler Broadened Angular Uncertainty	30
3.2 Energy Resolution of the Electron Detector	32
3.2.1 Angular Uncertainty due to Energy Resolution	33
3.3 Geometric Factors in Angular Uncertainty	34
3.3.1 Effect of the Detector Orientation	36
3.3.2 Optimization of the Thickness of the Electron Detector	37
3.4 Overall Angular Uncertainty	40
<b>4. Description and Characterization of the Compton Camera System</b>	43
4.1 Choice of the Radioisotope for Compton Camera Imaging	43
4.2 Scatter Detector: Silicon Drift Detector	46
4.2.1 Principle of Operation	47
4.2.2 SDD with on-chip Electronics	48
4.2.3 19-channel Silicon Drift Detector	52
4.3 Absorption Detector: Anger Camera	56
4.4 The Compton Camera Setup	58
<b>5. Front-End Electronics and Data Acquisition System</b>	61
5.1 Front-End Electronics of the Silicon Drift Detector	61
5.1.1 The First Stage of the SDD Front-End Electronics	61
5.1.2 Preamplifier	63
5.1.3 Shaper	66
5.2 Data Acquisition System	68
5.3 Spectroscopic Measurements with a Single Cell SDD	69

<b>6. Measurements and Results</b>	71
6.1 Spectroscopic Performance of the Scatter Detector	71
6.2 Measurements with the Absorption Detector	75
6.2.1 Timing Characteristics of the Anger Camera	77
6.3 First Coincidence Signals	78
6.4 Coincidences with a Finely Collimated Beam	80
6.5 High-Statistics Coincidence Measurements	85
<b>7. Conclusions and Future Work</b>	91
7.1 Conclusions	91
7.2 Future Work	93
<b>A. Appendices for Chapter 2</b>	97
A.1 Derivation of the Compton Equation	97
A.2 Probability of Single Compton Scattering	98
A.3 Angular and Energy Distribution of Recoil Electrons	99
<b>B. Appendices for Chapter 3</b>	101
B.1 Angular Uncertainty due to Geometric Factors	101
B.1.1 The Contribution of the Scatter Detector	101
B.1.2 Spatial Resolution and the Depth of Interaction in the Scatter Detector	101
B.1.3 The Contribution of the Absorption Detector	103
<b>C. Appendices for Chapter 4</b>	107
C.1 Decay Scheme for $^{137}\text{Cs}$	107
C.2 Layout of the Single Cell SDD	108
C.3 19-cell Silicon drift detector	109
C.3.1 Bonding Layout of the 19-cell SDD	109
C.3.2 Aluminum Nitride Carrier Ceramic	110
C.3.3 Bias Board with the First Stage Readout Electronics	111
C.3.4 Rubber Inter-connectors	114
C.3.5 Detector Housing	115
C.3.6 Detector Window	115
C.4 Power Supply for the SDD	116
<b>D. Appendices for Chapter 5</b>	123
D.1 Choice of the Transistors for the First Stage of the SDD Front-End Electronics	123
D.2 Calculation of the Equivalent Noise Charge	123
D.3 SPICE Simulations for the Preamplifier and Shaper	125
D.4 Preamplifier-Shaper Carrier PCB	125
<b>References</b>	129

# 1. Introduction

The rapid and accurate location of radionuclide tracer distributions in tissue or organs is the goal of nuclear medicine. The importance relies on the fact that the radioactive tracers are coupled to pharmaceuticals and hence their distribution mirrors the path of the latter. The energy and the direction of the photon emitted from the patient's body have to be measured as accurately as possible. Most planar and single photon emission computed tomography (SPECT) imaging in nuclear medicine is performed by an Anger camera [Ang58] equipped with a parallel hole collimator to determine the direction of the photon. The collimator restricts the number of radionuclides that can be used in medical applications. The energy of the photon has to be at most few hundred keV, otherwise it penetrates through the collimator in all directions and the secondaries produce high background. However, high energetical photons could produce better visualization of the deep-situated lesions and higher resolution images due to the decrease in the average number of Compton scattering events inside the patient's body. Collimators not only restrict the number of available radionuclides but also impose an inverse relation between the spatial resolution, the detection sensitivity and the uniformity. Besides, a mechanical collimator provides only linear sampling of the object at a fixed angular view. Therefore, in order to obtain the necessary samples for imaging it is necessary to rotate the camera around the object or introduce a motion between the object and the camera. All these limitations due to a mechanical collimator can be overcome by an electronic collimation technique of a "Compton Camera".

A Compton camera consists of two detector components (Fig. 1.1), the electron detector (scatter detector), where a fraction of the photons emitted from the object undergoes Compton scattering and a second detector (absorption detector) where the scattered photon is detected. The energy of the recoil electron in the first detector is measured allowing together with the location of the scattered photon in the second detector to reconstruct the position and direction of the incoming gamma ray, which is the reason for the name "Compton Camera". In other words, the scatter detector acts as an electronic collimator, replacing the mechanical collimator of the gamma camera. Position and energy measurements in both detectors are used for reconstructing the location of the origin of the radiation in the object. Because of

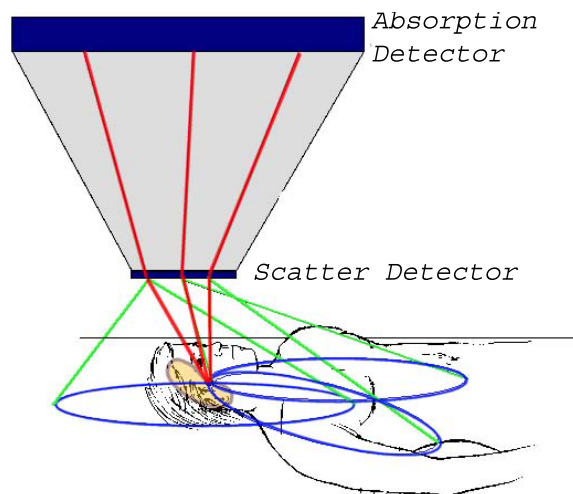


**Fig. 1.1:** Principle of Compton camera imaging

the kinematics of the Compton process the gamma emitting source is found to be located on a cone around the backprojection direction of the scattered photon, where the opening angle of the cone is the Compton scattering angle  $\theta$ . By recording many such events, the radionuclide distribution can be determined with a precision which, in principle, should only be limited by statistics and by intrinsic physical processes.

Compton camera is a desirable detector not only in nuclear medicine but also in gamma-ray astronomy and nuclear waste or industrial imaging due to its advantages mentioned above. However, building an instrument with high angular resolution and a reasonable field of view in the energy range of interest in these fields present serious design challenges. The primary problem results from the fact that gamma-rays are not appreciably refracted by matter and therefore can not be focused in the usual optical sense. Two techniques have been developed that provide good imaging capability. The first of these, coded-aperture-mask imaging, consists of a position-sensitive detector which is exposed to the instrument's field of view through openings in an otherwise opaque mask (like Anger Camera's collimator). This method performs reasonably good only up to 500 keV and with a small efficiency due to the mask. The second technique is the Compton camera imaging which performs best in the region 500 keV to 2 MeV. It can also be designed to perform with reasonable efficiencies in the region as low as 100 keV up to 10 MeV.

## 1.1 Literature Review of Compton Camera Systems

The Compton coincidence technique was first used in 1950 by Hofstadter and McIntyre [Hof50] for accurate energy determination of gamma-rays. They had two NaI crystals to measure the recoil electron energy at the first and the backscattered photon energy at the second scintillator. Since the introduction of this coincidence technique, Compton camera imaging was introduced mainly in three fields of application, namely astrophysics, industrial and nuclear medicine and actually has already been used in astrophysics and industrial applications. Compton Camera technology for astrophysics is well advanced, since the scope of the detection is easier and more clearly to be defined. Also it is easier to reconstruct a point-like source or object of known and simple structure than complicated and a priori unknown source distributions. Many detector developments for Compton camera in astrophysics are tested and experience has been gained with different types of detectors from which the work on Compton camera for nuclear medicine has partially profited. For this reason, it is interesting to follow briefly the development of Compton camera imaging in this field and to correlate that to the developments for nuclear medicine applications. The examples of Compton cameras for industrial applications are also given in another subsection to complete the overview of existing Compton camera systems.

### 1.1.1 Applications in Astrophysics: Compton Telescopes

The most important parameters of any astronomical telescope is its angular resolution and its sensitivity. Point sources are of considerable interest in gamma-ray astronomy. In order to detect the point sources, an instrument with directional information is needed. It is required to resolve the point source in two dimensions, therefore the depth of information is not necessary but a very high directional resolution is a key point. Spectral accuracy is needed both for resolving different sources and for the measurement of polarization, thus a telescope should have a good energy resolution. Instrument should be sensitive enough to detect weak galactic sources but sensitivity is not as crucial as in the case of medical applications due to the fact that the observation time of galactic source can be increased whereas this time is restricted for patients. The imaging system should also have background rejection capabilities. Beside cosmic and solar gamma-rays there exist a huge background of atmospheric and locally produced  $\gamma$ -rays and time coincidence and efficient veto counters are needed to reject the unwanted background events.

Photons with energies less than 0.5 MeV could be detected by the photoelectric process and the information about their arrival direction could be obtained by using collimators. Above 50 MeV, detectors measuring pair production with good angular resolution were used successfully. The collimation technique did not work properly in the MeV energy range because of the high penetration power of gamma rays at these energies. The intermediate energy interval from 0.5 to 30 MeV is one of the most interesting interval in the whole spectrum. In this interval many interesting events such as the nuclear reactions on the sun and the stars, the acceleration mechanisms on the sun and stars, the abundances of the elements can be studied. The existing detectors had either no or very poor directional information and the massive

collimators produced high background rate. In the energy range between few hundred keV and about 30 MeV the cross section is dominated by the Compton effect. Compton telescopes making use of this process are well suited for the MeV range.

The first double-scatter Compton telescope was built in 1961 by Peterson and Howard using NaI crystals [Pet61]. This instrument was flown on Orbiting Solar Observatory (OSO-1) but was not successful due to its low efficiency ( $< 1\%$ ) combined with a high background rate. Schönfelder et al. [Sch73] proposed more improved telescope in 1973. Their test setup consisted of two large plastic scintillator detectors 1.2 m apart. The first scintillator was a single piece viewed by a photomultiplier tube (PMT) and the second detector had nine large scintillator blocks each of which was viewed by one PMT. A gamma ray emitted from  $^{60}\text{Co}$  or  $^{24}\text{Na}$  sources first Compton scattered in the upper scintillator and the scattered gamma ray interacted in the lower scintillator where the sequence was confirmed by time-of-flight measurements. There was also another scintillator under the upper one which was used as an anticoincidence detector to reject the electrons and the charged particles leaving the upper scintillator. With the time-of-flight measurements a better background rejection capability than for the instrument of Peterson and Howard was achieved. Hence, time-of-flight systems proved to be essential for Compton telescopes. The prototype telescope had an half opening angle of  $15^\circ$  (hwhm), an energy resolution of 20% (hwhm) and an absolute detection efficiency of 0.5% with a low background rate. This telescope was designed to investigate the diffuse cosmic and atmospheric  $\gamma$ -ray component. The energy and angular resolution of the telescope needed to be improved to study possible structures in the diffuse  $\gamma$ -ray spectrum. The next telescope was a modified and improved version of the first one and it was called “COMPTEL” (The Imaging COMPton TELEscope) [Sch84]. It was designed in such a way to have sufficient sensitivity to detect discrete cosmic  $\gamma$ -ray sources. COMPTEL consisted of a liquid scintillator as the first detector and a NaI as the second detector (Fig. 1.2). The first detector had seven cells each of which had a diameter of 24 cm and a depth of 8.5 cm. Each cell was read-out by eight PMTs of 5 cm diameter. The second detector had 14 NaI scintillators each 28 cm in diameter by 7.5 cm in depth and was viewed by seven PMTs of 7.5 cm diameter. Both detectors were surrounded by veto domes to provide a charged particle shield. With the measurement of event locations and energies in both detectors, the arrival direction of gamma-ray could be found to lie on the surface of a cone of half angle  $\theta$ . 6% energy resolution and  $1.3^\circ$  angular resolution were achieved at 2.75 MeV. COMPTEL was chosen to be one of the four instruments selected for flight on the Gamma Ray Observatory (GRO) mission of NASA in 1991. Shortly after GRO was launched COMPTEL observed a direct MeV image of a cosmic gamma-ray burst for the first time [Win92]. COMPTEL was the first Compton telescope and the first satellite telescope to explore 1-30 MeV gamma-ray region. Its wide range of operation modes made it possible to achieve important discoveries in the gamma-ray astronomy, about solar neutrons and the map of galactic plane [Sch95]. Similar Compton telescope developments were performed at the University of California, Riverside [Her75] and at the University of New Hampshire [Loc81], both with segmented liquid scintillators.

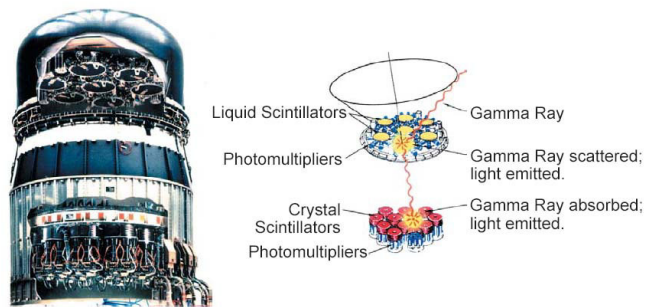


Fig. 1.2: Photomontage and schematic view of COMPTEL [Sch03]

The use of scintillator blocks restricted the angular accuracies and resolutions of gamma-ray telescopes. In late 80's a group from the University of California and the University of Texas at Dallas proposed a Compton telescope that uses scintillating fibers and position sensitive PMTs (PSMPTs) [Ata89]. The

telescope consisted of Compton-pair production converter made of scintillating plastic fibers coupled to PSPMTs, gas drift time projection chamber (TPC) and a calorimeter composed of a combination of scintillating glass fibers, lead and plastic scintillating fiber planes. 3-dimensional tracking information of Compton electrons and pair production tracks could be obtained with the help of good conversion point resolution of scintillating plastic fibers. In the next prototype system, TPC was not used to make the system free from flammable gas or cryogenics. This system consisting of a scintillating fiber converter and a calorimeter both composed of a bundle of scintillating fibers viewed with PSPMTs had an excellent time resolution better than 2 ns, but the angular resolution of 17.5 mrad (rms) observed for 1.2 MeV photons was limited due to systematic effects. Later it could be improved to achieve a resolution of 4 mrad [Ant90].

Liquid Xenon Time Projection Chamber (LXeTPC) was proposed to be used for the construction of a Compton telescope consisting of a single 3D position sensitive detector in 1989 [Apr89]. Like with scintillating fibers, 3-dimensional track imaging was also possible with LXeTPC. The aim of the LXeGRIT project was to increase the efficiency which was relatively low ( $\approx 1\%$ ) with the previous Compton telescopes due to the restriction on the event topology to two interactions recorded in two separate detectors. The prototype LXeTPC was designed to detect both the ionization and the scintillation signals. The scintillation light of Xe was used to provide an event trigger and PMTs were coupled to a quartz window of the detector. Two orthogonal planes of parallel wires with a pitch of 3 mm were placed for x-y coordinate measurement near the anode. The absolute drift time measurement with the help of the trigger signal from the scintillation provides a depth of interaction resolution of 300  $\mu\text{m}$  [Apr02]. In order to minimize the signal loss due to electron trapping by impurities at long drift distances, an intense work on the purification of LXe was performed and an energy resolution of  $8.8\% \times (1 \text{ MeV}/E)^{1/2}$  was achieved. Using the reconstruction algorithm developed to determine the sequence of interactions, multiple Compton interactions could be successfully ordered with a 60% efficiency for 1.8 MeV photons.

The Tracking and Imaging Gamma-Ray Experiment (TIGRE), first named as a Silicon Compton Recoil Telescope (SCRT) [O'N92], was the first project to propose tracking the recoil electrons and electron-positron pairs in multilayers of silicon scatterer instead of using time-of-flight method and it had also a gamma-ray polarimetry feature. With the time-of-flight method the inter-detector distance had to be large which limited the field of view. The electron tracking method not only improves the field of view but also the accuracy with which the gamma-ray's origin is determined. The prototype instrument prepared for a balloon flight has an active tracking converter of 16 layers of double-sided silicon (Si) strip detector each having a volume of  $10 \times 10 \times 0.03 \text{ cm}^3$  with 128 orthogonal strips on each side and a calorimeter consisting of 5 arrays of  $256 \times 1 \times 3.5 \text{ cm}^3$  CsI(Tl) crystals coupled to photodiode detectors. The tracker has an energy resolution of 4.6 keV FWHM at 122 keV and the calorimeter 5% FWHM at 662 keV [Bha04]. 92% of the electron track directions could be correctly identified with a test setup consisting of 4 layers of  $4 \times 4 \text{ cm}$  300  $\mu\text{m}$  thick double-sided Si strip detectors and a single Ge detector [O'N03].

Germanium detector as a scatter detector is a good choice for astrophysics where the gamma energy is rather high; often well above 1 MeV. The Doppler broadening due to the precollision momentum of the Compton electron is negligible in this energy range whereas in nuclear medicine where the gamma energy is at most an MeV, Ge is not the most ideal scatter detector due to its high atomic number (3.1). The first measurements with a small Ge Compton telescope was performed at Oak Ridge National Laboratory [Pie89]. A single Ge detector was used as the scattering element and a four detector array was used as the collector-plane detector. It was concluded that a planar scatter detector would improve the data quality, the number of detector elements in both scatterer and absorber needs to be increased and the timing between two planes has to be improved.

The Compton telescope development at the Naval Research Laboratory (NRL) started with the Advanced Telescope for High Energy Nuclear Astrophysics (ATHENA) in the early 1990's. The aim of this project was to achieve significant improvements in sensitivity, energy and angular resolutions compared to those achieved by COMPTEL and INTEGRAL. This goal could be reached by using Germanium detectors instead of scintillators used in COMPTEL. The configuration combined a high resolution Compton telescope with a coded aperture imaging system for the detection of both hard X-ray and a higher energetic gamma rays. The upper detector consisted of 2 layers of  $400 \times 5 \times 5 \times 1 \text{ cm}^3$  Germanium (Ge) strip detectors and the lower detector had 5 layers of them. The detector had 2 mm position resolution in two

coordinates and 2.5 keV energy resolution at 1 MeV. A 1 mm thick coded mask was mounted 2 m above the upper detector and a coarse collimator just above the upper detector were mounted [Joh95]. The High-Resolution Compton Telescope (HRCT) investigated the depth-of-interaction resolution with the Ge strip detectors by the readout of both sides of the detector [Kro00] and the resolution of less than 500  $\mu\text{m}$  was achieved [Wul02]. In 1999 a new concept of 3-Compton technique was proposed by Kurfess et al. [Kur00], which would increase the few percent efficiency of Compton telescopes up to 50%. In 1987, Kamae et al. [Kam87] were the first to propose this idea with an instrument consisting of multiple layers of Si detectors and a scintillator detector surrounding them. In 1990, Dogan et al. [Dog90] realized that the position and energy of gamma ray could be determined without stopping it completely. Therefore, high resolution detectors can be used in stack and Si would be the best candidate due to its high resolution capability at room temperature. Many test detector systems were constructed at NRL to check the performance and the detector development group has concentrated on high resolution, large area, thick Si and Ge strip detectors with three dimensional readout capability. Double-sided Si strip detectors from SINTEF, Si(Li) detectors from LBNL [Tin03] and from Jülich [Pro03] are investigated further. Similar work is ongoing at Nuclear Compton Telescope (NCT) project where multi layers of 15 mm thick large area 3-D positioning cross strip Ge detectors are used to build the telescope [Bog04].

As the satellite mission of COMPTEL finished in 2000, the Max-Planck-Institut für extraterrestrische Physik started to build its successor: the Medium Energy Gamma Astronomy (MEGA) camera [Sho00]. The aim was to improve the sensitivity of COMPTEL by a factor of 10 using modern detector technology and to be able to perform polarization studies. A prototype detector consisting of a tracker which contains 11 layers of 3x3 arrays of 500  $\mu\text{m}$  thick double-sided Si strip detector, each 6x6  $\text{cm}^2$  in size, fitted with 128 orthogonal p and n strips on opposite sides with 470  $\mu\text{m}$  pitch and a calorimeter which consists of 20 modules, each with an array of 10x12 CsI(Tl) scintillator bars of cross-sections 5x5  $\text{mm}^2$  readout with monolithic arrays of Si PIN-diodes has been constructed. The thickness of CsI was chosen to be 8 cm on the bottom, 2 cm on the upper side and 4 cm on the lower side walls considering decreasing photon energy with increasing scattering angle. An energy resolution of 15-20 keV (FWHM) and a position resolution of 290  $\mu\text{m}$  for the tracker, 40-100 keV energy resolution in the range of 0.511-1.274 MeV and 2 cm depth of interaction resolution with the double-sided readout of 8 cm deep CsI for the calorimeter have been achieved [And03]. The final telescope will have 6x6 arrays of Si detector in each layer and the CsI will be 8 cm deep on the bottom and 4 cm on the side walls. A balloon flight is planned for the prototype detector in 2004 [Kan04]. Recently the tracking of recoil electron in a Xe-filled micro-well detector [Blo04] and the readout of CsI crystals by Si drift detectors for MEGA experiment [Mar04] were proposed.

### 1.1.2 Compton Camera for Industrial Applications

The other field, where Compton cameras are already in use and demanded as gamma-ray imagers is that of industrial applications like in environmental remediation, in survey of nuclear industrial sites and in nuclear treaty verifications. The instrument should have a high energy resolution in order to image multiple radionuclides in such complex radiation environments. The imager should have a high efficiency to be able to identify the hidden radioactive substance quickly. Position resolution of the imaging system should be good enough such that its contribution to the angular uncertainty should not be dominating factor over other effects. In these fields of application, the localization of the radioactivity is the main issue but the sources of radioactivity do not have such a complex fine structure as in the case of nuclear medicine applications. Therefore the image quality is not as vital as in the field of nuclear medicine.

Industrial gamma-ray fields differ from those imaged in nuclear medicine or astronomy in a way that they are spatially extended multi-energy gamma-ray fields. For instance, during the survey of the nuclear power plant steam generator  $^{137}\text{Cs}$  indicates a leaking fuel assembly,  $^{60}\text{Co}$  shows the location of rust in the system, in the presence of  $^{24}\text{Na}$  in the cooling water. The Ring Compton scatter Camera (RCC) was the first camera to perform the task of imaging these fields [Mar94]. The RCC consisted of a 4x4 planar 6 mm thick HPGe elements each having a size of 5 mm and 16 circular cylinder NaI(Tl) crystals with a diameter of 19.1 mm and a length of 50.8 mm. It was demonstrated that this camera holds promise for nuclear industrial applications because such multi-energy gamma-ray fields are common in nuclear power plants and radioactive waste facilities. Some members of the group developing RCC later started

to work on a Compton camera based on 3D position sensitive CZT (CCC) detector arrays [Du01] which was shown to be more portable and superior to silicon and HPGe in terms of efficiency and resolution.

The characterization of mixed waste containers requires a determination of the activity level, form and composition of the radioactive wastes in order to determine the methods of disposal. These requirements forced the researchers to improve the energy resolution in order to be able to image multiple radionuclides in a complex field. King et al. performed experiments with HPGe detectors and the results demonstrated the point source resolution of 0.5 to 1 cm at a source-camera distance ranging from 0.25 to 1 m [Kin94].

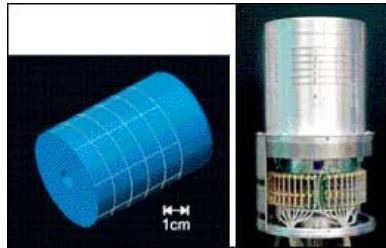


**Fig. 1.3:** Full volume Compton camera currently being tested for imaging measurements at LLNL [Vet]

Multiple Compton method [Dog90] inspired the development of compact and portable industrial Compton cameras. The simulations showed that an angular resolution of  $2^\circ$ - $7^\circ$  and an efficiency of 2.5-22% over the energy range of 150-1000 keV could be achieved with 20 layers of 1 mm thick Si surrounded by a 21 cm high CsI side counter [Dog94]. Lawrence Livermore National Laboratory (LLNL) group proposed a new approach of using a single coaxial HPGe detector (Fig. 1.3). In this way, good energy resolution of Ge would improve the background rejection compared to CZT or scintillator and compared to a system requiring two detectors in coincidence, a higher efficiency can be obtained with a single large volume detector [Sch01]. Preliminary studies and measurement with a GRETA prototype detector showed a factor of about 10 improvement in efficiency compared to a detector system consisting of two Ge detectors. This efficiency can be improved further because only 2-site events with full energy deposition with an energy threshold of 3.5 keV were considered in the first measurements.

### 1.1.3 Compton Camera in Nuclear Medicine

Unlike industrial and astronomical applications, mostly single photon emitters or for some specific applications radionuclides with well separated multiple lines are used in nuclear medicine. Therefore, spectroscopic performance is not the vital issue in medical imaging but a much better energy resolution is required in the first detector. In nuclear medicine, one deals with the distributed sources of lower energies (100-600 keV). The main challenge lies on the fact that high position resolution, highest possible sensitivity and powerful reconstruction techniques are required to image rather complex structures in 3-dimensions in a limited data acquisition time and with limited number of emitted gamma from the source to reduce the applied dose for the patient. All these requirements make the application of Compton camera imaging technique in nuclear medicine very challenging and this work is concentrated on this field of application of a Compton camera.

Compton imaging technique in nuclear medicine was first proposed by Todd, Nightingale and Everett in 1974 [Tod74]. They proposed a camera consisting of a lattice of Si Schottky barrier arrays of 0.5 mm cubic elements.

Three dimensional silicon tracker which would satisfy the position and energy resolution demands of the design of Everett and his colleagues was very difficult to fabricate at that time. After a detailed study of theoretical design considerations [Sin83] and image reconstruction methods, Singh and Doria designed the germanium-scintillation camera (GSC). The first GSC test setup consisted of a two modules of a  $5 \times 5 \times 6 \text{ mm}^3$  Ge detector and a gamma camera having a NaI crystal which is 22 cm in diameter, placed 5 cm from the first detector. A point spread function (PSF) of 1 cm was obtained with a  $^{99m}\text{Tc}$  point source placed 4.6 cm away from the Ge detector [Sin84]. With the next setup which consisted of  $4 \times 4$  Ge detector and an Anger camera having a NaI crystal which is 25 cm in diameter and 1/2 inch thick, readout via 19 PMTs, it was shown that the PSF improved considerably at higher energies (662 keV of  $^{137}\text{Cs}$ ) [Sin86].

Due to the cryogenical cooling, Ge detector was expensive, required special handling and maintenance and imposed some constraints on the system geometry and configuration. To overcome these practical disadvantages, Singh investigated  $\text{Cd}_{1-x}\text{Zn}_x\text{Te}$  (CZT) detector as the first detector [Sin95]. Experimental results showed that Ge was more efficient than CZT by a factor of 2.5 and the resolution was also factor 2 better for a photon energy of 140 keV. However, at 662 keV the detection efficiency of Ge and CZT were comparable and the resolution of CZT could also be as good as the resolution of Ge with improvements in the charge transport properties of CZT.

In 1981 Walenta and Brill proposed to build a high pressure multiwire plane gas detector as the scatter detector in order to be able to track recoil electrons more accurately [Wal81]. Time expansion chamber as a scatter detector and a Ge detector as an absorption detector have been used [San88]. A detailed study of the recoil electron's track and multiple scattering of electrons is given in the PhD thesis of Gebser [Geb90].

The project at the Royal Marsden Hospital concentrated on the Si microstrip or two dimensional position sensitive Si drift detector in coincidence with a NaI(Tl) gamma camera [Sol88] for medical imaging in the energy range of 0.1-1 MeV. It was shown that the number of noisy events would be less with stacked silicon detectors than with a Ge detector.

For the detection of multi-vertex events, a high pressure self-triggered scintillation drift chamber with a large field of view was proposed. Xe was used in a 30 cm diameter 4 cm deep chamber which was viewed by an array of 19 PMTs [Bol97]. Energy resolution of 2.2% FWHM at 122 keV, 2D position resolution of 3.7 mm FWHM, a depth resolution of 0.6 mm FWHM, a system resolution of 25 mm at 10 cm source distance were achieved and 1,2,3,4 or more vertex events could be reconstructed. The detector can be operated in a 2D mode as an alternative to an Anger camera or in a 3D mode triggered by a scintillation signal for Compton camera applications. The main problems associated with the first design were the low Compton efficiency of Xe, large Doppler broadening due to its high atomic number and the loss of light on the way from the light-generating region to the PMTs. The next design was made by using an optical readout based on scintillating fibers which surround the electrodes in the chamber. A cylindrical Compton camera consisting of a multilayer electroluminescence camera (MELC) filled with high pressure Ar or Ne as a scatter detector and another MELC filled with high pressure Xe as an absorption detector were proposed [Bol98].

The main problem of the first prototype built by Singh was that the second detector had a high single rates which overloaded the readout electronics, the signal-to-noise ratio in the Ge detector was low at low energies and at high energies NaI detector had low photopeak-to-total ratio. The Michigan group extended the work of Singh by using Si pad detectors in place of Ge, employing a ring geometry for the second detector and conducting extensive Monte Carlo and lower bound studies including Doppler broadening effect to determine the performance expectations [LeB98]. A ring geometry was first proposed by Martin et al. [Mar93] to improve the resolution and the count rates in the second detector. The first prototype (C-SPRINT) consisted of a  $3\times 3\times 1\text{ cm}^3$  Si pad detector module pixellated into a 22 by 22 array of  $1.2\times 1.2\text{ mm}^2$  elements with a 1 keV FWHM energy resolution and an existing SPECT imaging system (SPRINT) which was made up of eleven modules arranged in a 50 cm diameter and 10 cm long cylinder. Each module is composed of 44 3 mm wide, half inch thick, and 15 cm long NaI(Tl) bars viewed by 20 38 mm PMTs arranged in a close-packed hexagonal array. The time resolution was measured to be 41 ns FWHM by using the backplane pulse from the  $n^+$  side of Si detector for first detector timing and the dead time for the coincidence readout was 1-3 ms. The second generation Si detectors were readout with VA32C/TA32 chip that provided triggering from the front side of the pixels and by producing less noisy trigger signals it improved the time resolution by a factor of three. The resolution of 15 mm FWHM was measured with a  $^{99m}\text{Tc}$  source and the comparisons with Anger camera showed that at this energy the Anger camera had far superior imaging capability than the C-SPRINT which was most likely due to the shortcomings in the reconstruction algorithm [LeB99b]. Theoretical studies showed that C-SPRINT needed 45 times the count rate of the mechanically system to achieve the same performance at 140 keV, whereas with  $^{113m}\text{In}$  this factor was reduced to 5. It was further shown that by improving the existing geometry and by using a larger volume of silicon detector, the gain of 5 in noise equivalent sensitivity is achievable at 391.7 keV with the Compton camera relative to an Anger Camera [LeB99c]. The recent work in the frame of an international CIMA (Compton Imaging for Medical Applications) collaboration is recently focused on applications such as prostate imaging probe, very high resolution small animal

PET [Stu03] and scintimammography [Zha04] which uses a stack of thick silicon pad/strip detectors in coincidence with a NaI scintillator detector.

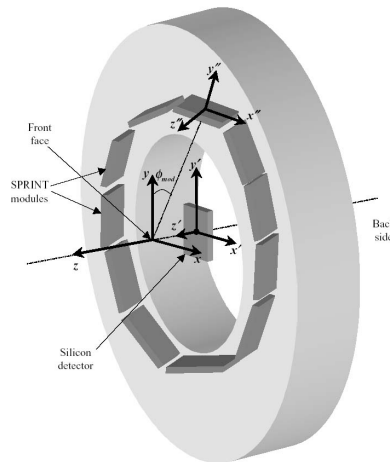


**Fig. 1.4:** Illustration of C-SPRINT System [LeB99a]

A small laboratory prototype for positron emitter imaging was proposed and designed at the University College London in cooperation with the Imperial College [Sca00]. The prototype consisted of two layers of  $6 \times 6 \text{ cm}^2$  area,  $500 \mu\text{m}$  thick double-sided silicon strip detectors, each having 128 channels/side as the scattering medium and a small 1 cm thick Ge detector of 3.6 cm diameter as the absorption detector. It was shown that having a stack of silicon detectors would improve the gain by few orders of magnitude compared to a mechanically collimated system. The current system of this group consists of a large scattering detector and a smaller absorption detector, both of which are pixellated HPGe detectors [Roy04]. The scattering detector is a Ge ring with an outer diameter of 10 cm, an inner diameter of 6 cm and a thickness of 4 mm. 8 blocks of total  $152 \text{ } 4 \times 4 \text{ mm}^2$  pixels are distributed around the ring. The second detector consists of  $5 \times 5$  block of 1 cm thick  $4 \times 4 \text{ mm}^2$  pixels and its diameter is 2.8 cm. The reason for making the inner part of the first detector inactive was to increase the depth resolution and hence to have a stereoscopic view of the source.

NRL group proposed to use radio-nuclides that emit a three-gamma cascade (like  $^{94}\text{Tc}$ ) and positron-decay isotopes that are accompanied by a coincident gamma ray (such as  $^{14}\text{O}$ ) [Kur02]. In this way, the location for each decay can be determined uniquely which leads to an improved imaging with reduced dose. An ideal detector to achieve this goal consists of many layers of 3D position sensitive Si or Ge detectors which cover a large solid angle that should be greater than  $3\pi$  steradian.

The prototype Compton camera systems, which have significantly pushed the development of Compton camera imaging in medicine, are summarized in Tab. 1.1.

## 1.2 Objectives of this Work

As can be seen in the literature review, the Compton camera concept is not a new but almost a 30 years old concept. It has been successfully applied in gamma-ray astronomy and industrial imaging. Its use in nuclear medicine has been demonstrated by many prototype or test systems but a clinically available Compton camera system has not been constructed yet. The medical imaging application of the Compton camera poses different challenges than those faced by other applications. Significant improvements in detector performances and efficiency of the system have to be achieved in order to compete with modern versions of the Anger camera and in some areas with PET systems.

A Compton camera system has been designed and constructed to study the influence of the detector parameters on the camera performance and the feasibility of the Compton camera imaging. The main emphasis of building such a system is to get an information on position resolution, vertex detection principle with an ultimate goal of high resolution detector design for small animal imaging. Silicon drift

Time	Group	Proposed Detector System	Achievement	Problem
1983-1995	Singh et al.	HPGe or CZT scatterer NaI absorber	$\approx 6.7$ mm, FWHM resolution for point source @ $E_\gamma=662$ keV at 5 cm distance	- high singles at NaI - low signal-to-noise ratio @ Ge at low E - low photopeak efficiency @ NaI at high E
1998-1999	LeBlanc et al.	Si pad detector array NaI ring detector array	13.6 mm, FWHM @ $E_\gamma=140.5$ keV at 10 cm distance	- energy resolution in Si should be improved - 3-9 ms dead time in Si - low photopeak-to-total ratio in NaI

**Tab. 1.1:** Summary of significant Compton camera developments for applications in nuclear medicine

detector with on-chip electronics [HLL] has been selected as the scatter detector due to its excellent energy resolution. An Anger camera without its lead collimator [Int] is used as an absorption detector in order to have a large field of view of the scattered radiation. It is the first system employing a silicon drift detector with on-chip electronics for Compton camera applications and radiating this detector with high energetic gamma rays. The system is not quite optimized in terms of detector parameters but it was aimed to build and test the system quickly to experimentally confirm system models. A custom designed readout electronics has been developed and a special effort was given to the fast readout of the silicon detector to improve the timing characteristics for the coincidence. Extensive Monte Carlo simulations and analytical calculations have been developed and conducted and the results are compared with measurements. Measurements were performed using finely-collimated  $^{137}\text{Cs}$  source with an energy of 661.7 keV. It could be shown for the first time that such a detector arrangement allows a reconstructed angular resolution of the order of 1 degree which makes it suitable for medical applications with high resolution imaging.

### 1.3 Overview of Dissertation

This dissertation is organized into seven chapters. The first chapter presents an extensive survey of the history of Compton camera development for gamma-ray astronomy, industrial applications and medical imaging and discusses the objectives and contributions of this work.

In Chapter Two, theoretical considerations for the Compton camera system design are introduced. First of all, the principle of Compton camera imaging and based on this principle the required type of photon interactions in detectors are discussed. Detailed study of photon and electron interactions in the scatter and absorption detectors are presented. Using the photon interaction cross section tables and the results of the Monte Carlo simulations, suitable detector materials are investigated.

In Chapter Three, influence of the various detector parameters on the performance of the Compton camera system is discussed. Among these parameters, energy resolution of the scatter detector, Doppler broadening due to the pre-collisional momentum of the recoil electron and the geometric factors such as pixel size, depth of interaction resolution, positioning are included. The models for the theoretical angular uncertainty of the designed system are presented. Analytical and Monte Carlo tools were used to model the angular resolution. The system modeling was utilized both as a guide for designing the system and as a comparison factor against the experimental results.

Chapter Four describes the experimental setup constructed for the Compton camera imaging. The principle of operation and performance of individual detectors as well as the mechanical setup and the system geometry are presented.

Chapter Five presents the custom-designed front-end electronics of the scatter detector and the data acquisition system of the whole system. Both measured and simulated performance of the readout electronics and the spectroscopic measurements performed with a single cell silicon drift detector are provided.

Calibration procedure for scatter and absorption detectors, results of the coincidence measurements and imaging results for a point source are presented in Chapter Six. Measured recoil electron and scattered photon energies as a function of the scattering angle are included. The angular resolution determined from the final reconstructed image is compared with the theoretical expectation for the angular resolution.

Chapter Seven presents conclusions and some ideas for the further work.

## 2. Theoretical Considerations for the Compton Camera System Design

The interaction of the radiation with the detector material determines the design and properties of the detector system. In this chapter the theory and principles of the Compton camera imaging with the review of interactions playing an important role in the system are presented.

### 2.1 Principles of Compton Camera Imaging

For the reconstruction of the image of a gamma-ray emitting object, one has to have a directional information of the gamma quanta incident on the detector. For Positron Emission Tomography (PET) this directional information is mainly obtained from the time coincidence detection of the two back-to-back gamma quanta emitted via positron annihilation. In addition mechanical collimators refine this information and suppress random coincident events. In the case of Single Photon Emission Computed Tomography (SPECT) technique a mechanical collimator made of a material with high nuclear charge  $Z$  is used. This principle which is used in the so called Anger Camera, is explained for a parallel hole collimator in Fig. 2.1. The holes are arranged such that the gamma-rays directed along the long-axis of each hole are transmitted and the rest is absorbed by the wall between the holes (septa).

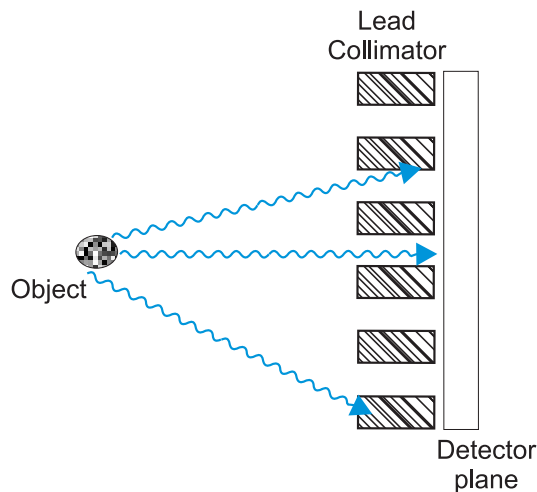


**Fig. 2.1:** Parallel-hole collimator technique allowing only photons normal to the surface of the collimator reach the detector

Pin-hole collimators and diverging/converging collimators are other examples of various collimator types. Lead and tungsten are the most popular materials used for collimators due to their high absorption capability. Such a mechanical collimation, except coded aperture, imposes a limit on the sensitivity which is inversely proportional to the spatial resolution [Web88]. A way to overcome this problem is to use the technique of electronic collimation. With this method, it is possible to increase the efficiency, to improve the sensitivity and resolution and to allow higher energy photons to be imaged as discussed in the previous chapter.

For a Compton camera system (Fig. 2.2) the mechanical collimator of a SPECT system is replaced by an active detector, where the fraction of the photons emitted from the target are Compton scattered and the position of the interaction and the energy of the recoil electron  $E_e$  are measured. The scattered photons leaving the first detector and absorbed in the second detector are used to measure the deposited energy and position of interaction in the absorption detector. The time coincident events in two detectors are processed for the reconstruction of the actual source location. The energy deposited in the first detector gives an estimate of the scattering angle ( $\theta$ ) of the incoming photon from Compton kinematics. The sum of the energies gives the energy of the incoming photon in the case of a full energy deposition in both detectors. When each event is backscattered, the incident photon vector is found to be located on a conical shell with an angular thickness  $\Delta\theta$  which will be discussed in the next chapter. The scatter detector takes the role of an electronic collimator. Therefore, Compton camera has also been named as an electronically collimated gamma camera.

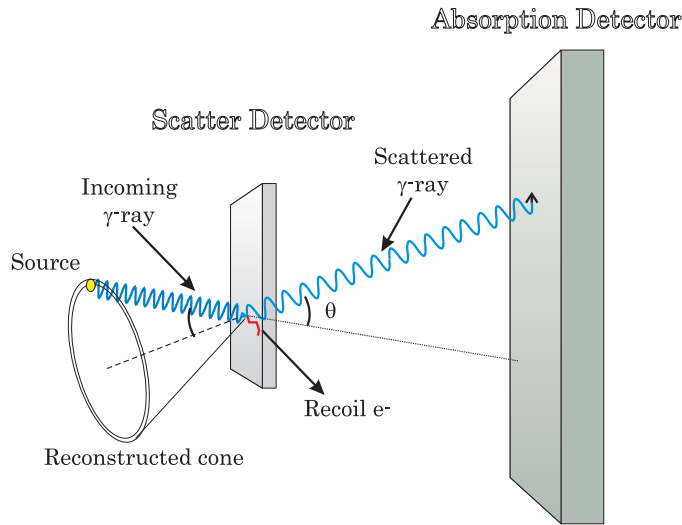


**Fig. 2.2:** Compton camera operating principle

New ideas such as making use of multiple interactions in a stack of detectors or in a single thick detector were proposed later on, but the original principle of the Compton camera, which is also the method used in this work, requires that an incoming photon Compton scatters in the scatter detector and the scattered photon undergoes a photoelectric absorption in the absorption detector. The probability of these interactions depends on the detector material and the energy of the incoming radiation. Therefore, the choice of detector materials and the type of radionuclide plays an important role in the performance of the system.

## 2.2 Interaction of Photons

To estimate the efficiency of the Compton camera system, it is necessary to understand photon interactions in matter. Photon interactions are covered in several books such as [Eva82; Mar69] and therefore, it is not intended to give a full treatment of these interactions in this section, the main focus will rather be given on the investigation of appropriate detector materials which have high efficiency for certain types of photon interactions in the energy range of interest.

A collimated beam of monoenergetic photons shows a truly exponential attenuation in matter because photons are absorbed or scattered in a single event. In other words, photons that penetrate the matter have had no interaction, while those undergoing an interaction have been eliminated from the beam. The total number of photons which do not suffer an interaction in matter is:

$$I(x) = I_0 \exp(-\mu x) \quad (2.1)$$

where  $I_0$  is the incident beam intensity,  $x$  is the thickness of the target and  $\mu$  is the attenuation coefficient. Attenuation coefficient is the probability that the photon interacts with the material it is traversing per unit length it travels. Photons may have interaction with atomic electrons, with nucleons, with the electric field surrounding nuclei or electrons which result in the complete absorption or elastic scattering or inelastic scattering of the electromagnetic radiation. The main interactions of photons in matter are *photoelectric effect*, *Compton scattering* and *pair production*. In the photoelectric absorption process a photon with an energy of  $h\nu$  impinges on an atom transferring its entire energy to an electron (mostly K-shell electron) which is ejected from the atom with an energy of  $E_e = h\nu - E_b$  where  $E_b$  is the binding energy of the electron. The scattering of gamma-rays from atomic nuclei is elastic (coherent scattering: *Thomson* if scattered by the nucleus, *Rayleigh* if scattered by atomic electrons) but their scattering from atomic electrons is inelastic which is called Compton scattering [Com23]. In Compton scattering photon gives off part of its energy to an electron (recoil electron) and it is deflected through angle  $\theta$  with respect to its original direction. Pair production occurs when the gamma-ray energy exceeds twice the rest-mass energy of an electron ( $2 \times 511$  keV). In this interaction, the photon is completely absorbed and electron-positron pair is created. This process mainly occurs in the nuclear field but also to some degree in the field of an electron. The most probable of these interactions versus atomic number of the absorber and the photon energy is shown in Fig. 2.3.

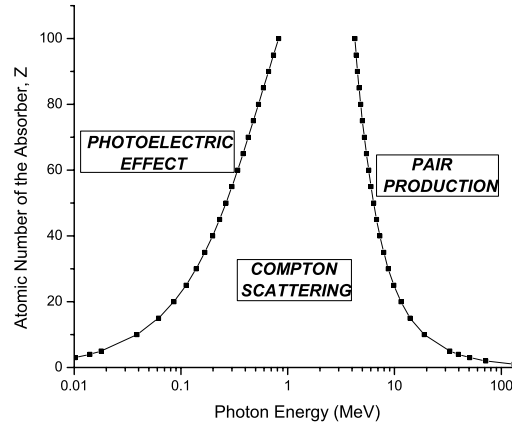


**Fig. 2.3:** The dominant photon interaction as a function of photon energy for different absorbers

This plot clearly shows that Compton scattering is the predominant interaction mechanism in the nuclear medicine energy range ( $E_\gamma \geq 70$  keV) for  $Z \leq 20$ . The attenuation coefficient for different photon interactions in silicon and NaI(Tl) as a function of the photon energy is given in Fig. 2.4. Si and NaI are chosen for this example to study the interaction cross sections for low- $Z$  and high- $Z$  materials because these are the detector materials used in this work.

At low energies, below 57 keV in silicon and 265 keV in NaI, photoelectric effect is the dominant process. At higher energies Compton scattering is dominant up to 15 MeV in silicon and 7 MeV in NaI where pair production in nuclear field becomes more probable interaction.

### 2.2.1 Photon Interactions in the Scatter Detector

The sensitivity of the camera system increases when the following conditions are fulfilled in the first detector:

- Incoming  $\gamma$ -ray Compton scatters in the scatter detector
- Recoil electron is absorbed in this detector
- Scattered photon leaves the first detector without undergoing further interactions

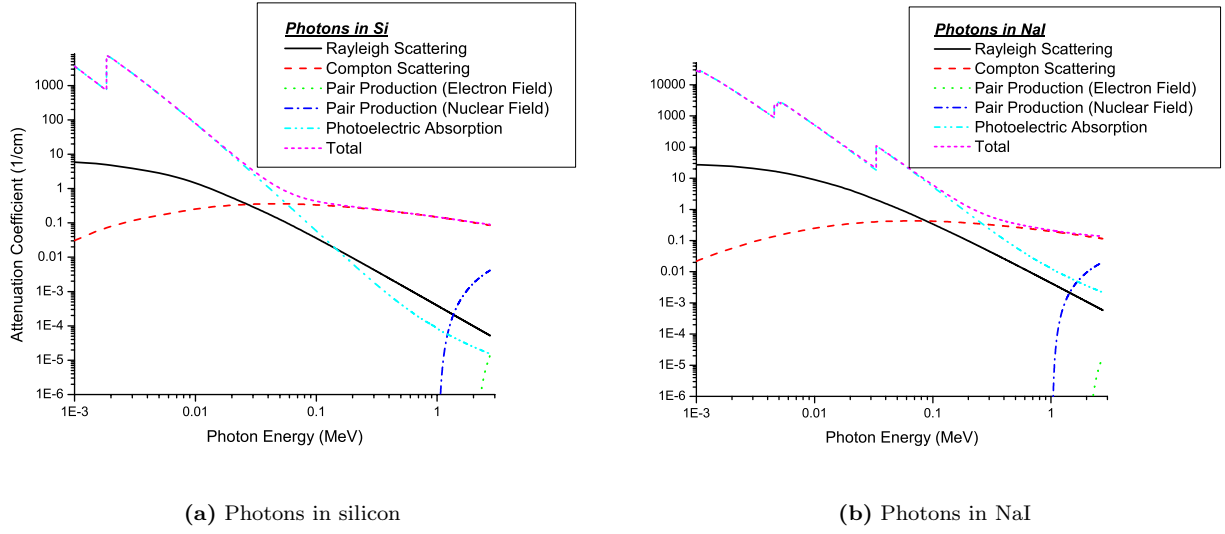


**Fig. 2.4:** Attenuation coefficient as a function of the photon energy in silicon ( $Z=14$ ) and NaI ( $Z_{eff}=45.8$ ). The data was obtained from XCOM: Photon Cross Sections Database [XCO]. Mass attenuation coefficient given in XCOM is converted into linear attenuation coefficient which is just the mass attenuation coefficient times the density of the material.

The probability of a single Compton scatter followed by an escape of the scattered photon from the scatter detector depends upon the Compton to total cross section for the first detector. The angular distribution function per unit steradian of solid angle  $\Omega$  can be calculated using the *Klein-Nishina formula* [Kle29]:

$$\frac{d\sigma}{d\Omega} = \frac{r_0^2}{2} \frac{1 + \cos^2 \theta}{(1 + \varepsilon(1 - \cos \theta))^2} \left( 1 + \varepsilon^2 \frac{(1 - \cos \theta)^2}{(1 + \cos^2 \theta)(1 + \varepsilon(1 - \cos \theta))} \right) \text{ unpolarized radiation} \quad (2.2a)$$

$$\frac{d\sigma}{d\Omega} = r_0^2 \frac{\sin^2 \vartheta}{(1 + \varepsilon(1 - \cos \theta))^2} \left( 1 + \varepsilon^2 \frac{(1 - \cos \theta)^2}{2 \sin^2 \vartheta (1 + \varepsilon(1 - \cos \theta))} \right) \text{ polarized radiation} \quad (2.2b)$$

where  $r_0$  is the classical electron radius which is defined as  $r_0 = e^2/m_e c^2$ ,  $\varepsilon = E_\gamma/m_e c^2$  and  $\vartheta$  is the angle between the electric vector of the incident photon and the direction of the scattered photon. The probability of Compton scattering of the incident photon from an electron increases linearly with the atomic number due to the fact that more electrons are available as scattering targets in a high- $Z$  material. It increases gradually as the photon energy increases up to about 1 MeV and then it falls off at higher energies (Fig. 2.4). The differential cross section as a function of scattering angle for unpolarized radiation is shown in Fig. 2.5 for different radionuclides. There is a tremendous increase in the fraction of the forward-scattered photons, as the photon energy increases.

The total collision cross section is obtained by integrating over all scattering angles,

$$\sigma = \int \sigma(\theta) 2\pi \sin(\theta) d\theta \quad (2.3)$$

the result being

$$\sigma = 2\pi r_0^2 \left\{ \frac{1 + \varepsilon}{\varepsilon^2} \left[ \frac{2(1 + \varepsilon)}{1 + 2\varepsilon} - \frac{1}{\varepsilon} \ln(1 + 2\varepsilon) \right] + \frac{1}{2\varepsilon} \ln(1 + 2\varepsilon) - \frac{1 + 3\varepsilon}{(1 + 2\varepsilon)^2} \right\} \text{ cm}^2/\text{electron} \quad (2.4)$$

For an absorber having  $N$  atoms/cm<sup>3</sup> and  $Z$  electrons/atom, the attenuation coefficient ( $\mu$ ) for Compton scattering is  $\sigma NZ$  (cm<sup>-1</sup>). Fig. 2.6 shows the mass attenuation coefficient, Compton to total in-

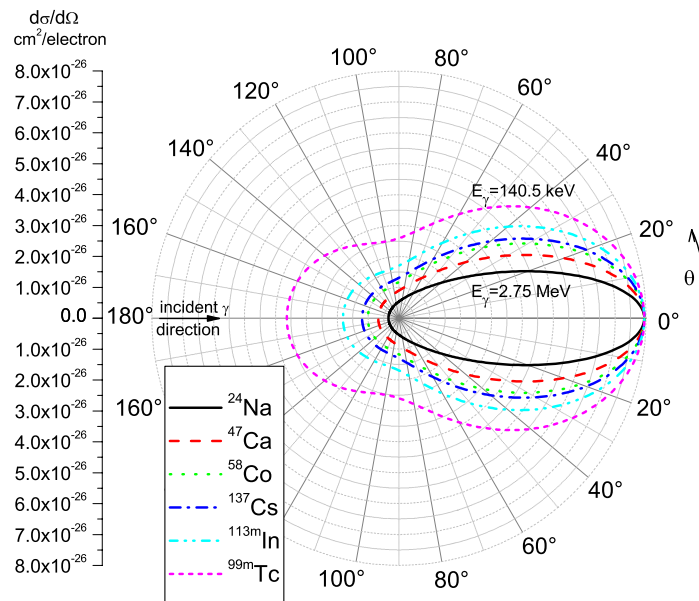
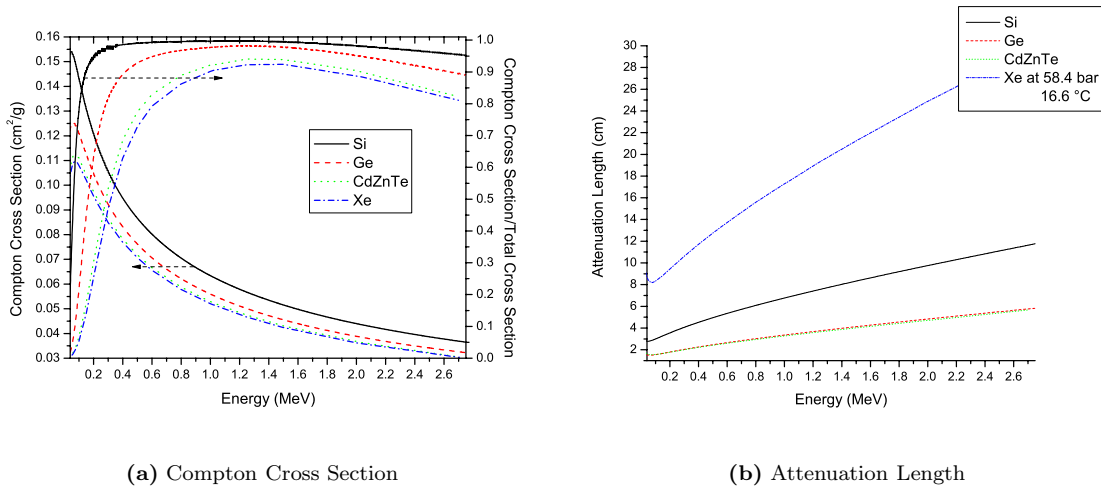


**Fig. 2.5:** Polar representation of the angular dependence of the differential cross section for Compton scattering of unpolarized radiation for  $^{99m}\text{Tc}$ ,  $^{113m}\text{In}$ ,  $^{137}\text{Cs}$ ,  $^{58}\text{Co}$ ,  $^{47}\text{Ca}$  and  $^{24}\text{Na}$  with photon energies of 140.5 keV, 391.7 keV, 661.7 keV, 810.8 keV, 1.3 MeV and 2.75 MeV, respectively.



(a) Compton Cross Section

(b) Attenuation Length

**Fig. 2.6:** Energy dependence of Compton cross section and attenuation length for proposed scatter detector materials ( $d_{Si}=2.33 \text{ g/cm}^3$ ,  $d_{Ge}=5.323 \text{ g/cm}^3$ ,  $d_{Cd_{0.9}Zn_{0.1}Te}=5.78 \text{ g/cm}^3$  and at  $P=58.4 \text{ bar}$ ,  $T=16.6 \text{ }^\circ\text{C}$   $d_{Xe}=1.11 \text{ g/cm}^3$ )

teraction ratio and attenuation length for Compton scattering as a function of  $E_\gamma$  for different detector materials.

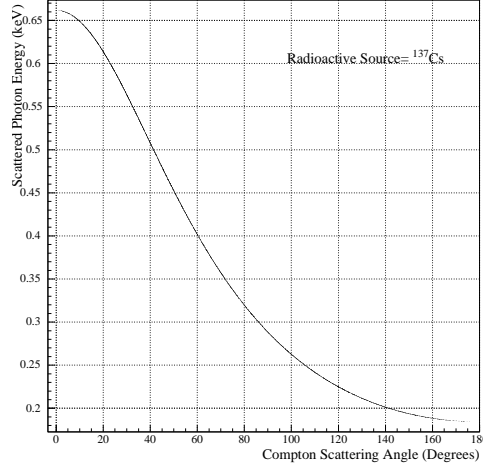


**Fig. 2.7:** The energy distribution of scattered photons as a function of  $\theta$  for  $E_\gamma=661.7$  keV

Silicon has the highest mass attenuation coefficient among the four detector materials but due to its low density almost twice the volume of silicon compared to germanium is necessary to have the same probability of a Compton scattering. The sensitivity of the system does not only depend on the Compton scattering but also on the Compton to total interaction ratio for the scatter detector (Fig. 2.6(a)). Silicon seems to be the best candidate considering the probability for a photon interaction to be Compton scattering. For  $^{113m}\text{In}$  if an incoming photon has an interaction in Si then 98.5% of these interactions are Compton scattering whereas in Ge this probability drops to 89%.

Another important point to increase the efficiency for the scatter detector is to have the scattered photon leave the detector without further interactions. Therefore, the interaction probability for the scattered photon should be minimized by choosing the appropriate detector material and by optimizing the thickness of the detector (discussed in more detail in 3.3.2). The probability of single Compton scattering ( $P_{SC}$ ) depends on energies of the incoming and scattered photon, as well as the thickness of the detector. The energy of the scattered photon ( $\gamma'$ ) can be calculated by using the *Compton shift* equation (Appendix A.1):

$$\frac{1}{h\nu'} - \frac{1}{h\nu} = \frac{1}{m_e c^2} (1 - \cos \theta) \quad (2.5)$$

where  $h\nu$  and  $h\nu'$  are the energies of the incoming photon and the scattered photon, respectively,  $m_e c^2$  is the rest mass of the electron (0.511 MeV). The scattered photon energy as a function of Compton scattering angle for  $^{137}\text{Cs}$  is shown in Fig. 2.7. The probability of a Compton scattering followed by the escape of the scattered photon can be expressed as follows (Appendix A.2):

$$P_{SC} = \frac{1}{\chi_C} e^{-d/\chi'_0} \frac{\chi_0 \chi'_0}{\chi_0 - \chi'_0} \left[ e^{\frac{\chi_0 - \chi'_0}{\chi_0 \chi'_0} d} - 1 \right] \quad (2.6)$$

where  $\chi_C$  is the Compton scattering attenuation length for  $\gamma$ ,  $\chi_0$  is the total attenuation length for  $\gamma$ ,  $\chi'_0$  is the total attenuation length for  $\gamma'$  calculated for  $\bar{E}_{\gamma'}$  and  $d$  is the thickness of the detector. At 391.7 keV photon energy the single Compton probability in 1 mm thick Si would be 2% and as the energy increases this probability would decrease due to higher penetration of photons. The thickness of the detector is an important parameter and its effect on the single Compton efficiency will be discussed in the next chapter. The effect of the photon energy can be calculated from the formula given above and more accurate estimate can be made by Monte Carlo simulations. Monte Carlo simulation package developed for this project has been used to study the fraction of photons undergoing a single Compton scattering in the scatter detector. The fraction of such events is given in Fig. 2.8 for all interactions and also for all hits at the 1 mm thick scatter detector as a function of the energy of the incoming photon.

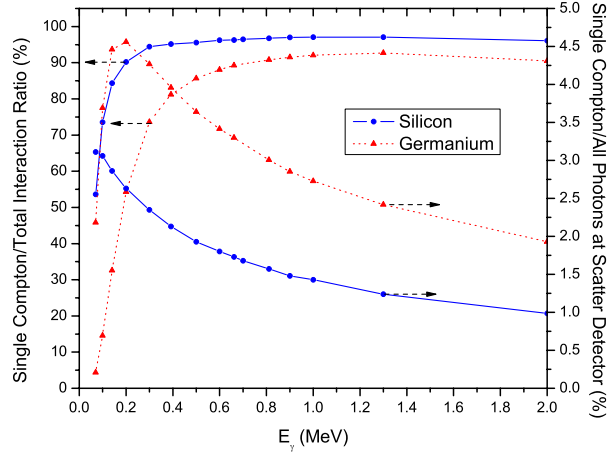


**Fig. 2.8:** The probability of a single Compton scattering for all interactions and all photons reaching the 1 mm thick scatter detector

When all the photons hitting the scatter detector are considered, in the whole energy range studied germanium is more efficient than silicon for Compton events followed by the escape of the scattered photon but Si is more efficient than Ge for single Compton to total interaction ratio. The geometrical acceptance of the scatter detector can be improved by making it larger, therefore single Compton to total hits was considered rather than single Compton to total number of photons emitted by the source. The simulation package developed for this work is written in C++ language, CLHEP [CLH] library is used for coordinate transformations and XCOM data is read from data files for different detector materials in 1 keV steps and interpolated to obtain the coefficients for all energy values. Particles are taken as rays and the intersection of rays with detector planes is used to check the current medium of the particle. The attenuation length is determined by using the XCOM data and Monte Carlo methods. For more detailed simulations where the background events are also present, GEANT (Detector Description and Simulation Tool) [GEA94] is used in combination with GLECS (GEANT Low-Energy Compton Scattering) [Kip02].

### 2.2.2 Photon Interactions in the Absorption Detector

The scattered photons after leaving the first detector should:

- fall into the solid angle subtended by the absorption detector
- undergo a photoelectric absorption depositing all their energy

in order to increase the detection sensitivity. The first requirement can be fulfilled with a large enough detector volume and with an appropriate orientation of the second detector (more detail on this is given in Chapter 3) such that it covers the angular region where most of the scattered photons are located. The interaction cross section for photoelectric effect is more complicated than the one for Compton scattering due to its strong dependence on  $E$  and  $Z$  and therefore there exists no single expression for the calculation of the photoelectric cross section for the whole range of  $E_\gamma$  and  $Z$ . The cross section in the energy region which is at some distance from the K-edge is given by nonrelativistic Born approximation [Mar69]:

$$\sigma_{pe}^K = \left(\frac{32}{\varepsilon^7}\right)^{1/2} \alpha^4 Z^5 \sigma_{Th} \text{ cm}^2/\text{atom} \quad (2.7)$$

where  $\varepsilon$  is the reduced photon energy,  $\alpha$  is the fine structure constant and  $\sigma_{Th}$  is the Thomson cross section for elastic scattering of photons which is given as  $\sigma_{Th} = \frac{8}{3}\pi r_e^2$ . It is assumed that only K-shell

electrons contribute to the cross section, that is why the superscript K is used in  $\sigma_{pe}^K$ . In the region of K-edge where the  $E_\gamma$  is comparable with the K-electron binding energy, electron wave functions are used to introduce a multiplicative correction function of the form  $f[\nu_K/(\nu_K - \nu)]^{1/2}$ . For gamma energies much larger than the electron rest-mass, the cross section takes the following form:

$$\sigma_{pe}^K = \frac{1.5}{\varepsilon} \alpha^4 Z^5 \sigma_{Th} \quad (2.8)$$

Besides energy of the photon, the cross section depends also on the atomic number and this dependence can be approximated by  $\sigma_{pe}^K \propto Z^n$  where n varies between 4 and 5 depending on the energy range. Therefore, the absorption detector should be made from a high-Z material to increase the photoelectric absorption efficiency. Scintillators such as NaI(Tl), CsI, LSO(Ce) ( $\text{Lu}_2\text{SiO}_5$ ) as well as semiconductors like Ge and CZT are some examples of absorption detector materials which have already been proposed for Compton camera applications. The cross section and attenuation length for photoelectric absorption, its fraction in the total interaction cross section and the total attenuation length calculated using XCOM is shown in Fig. 2.9.

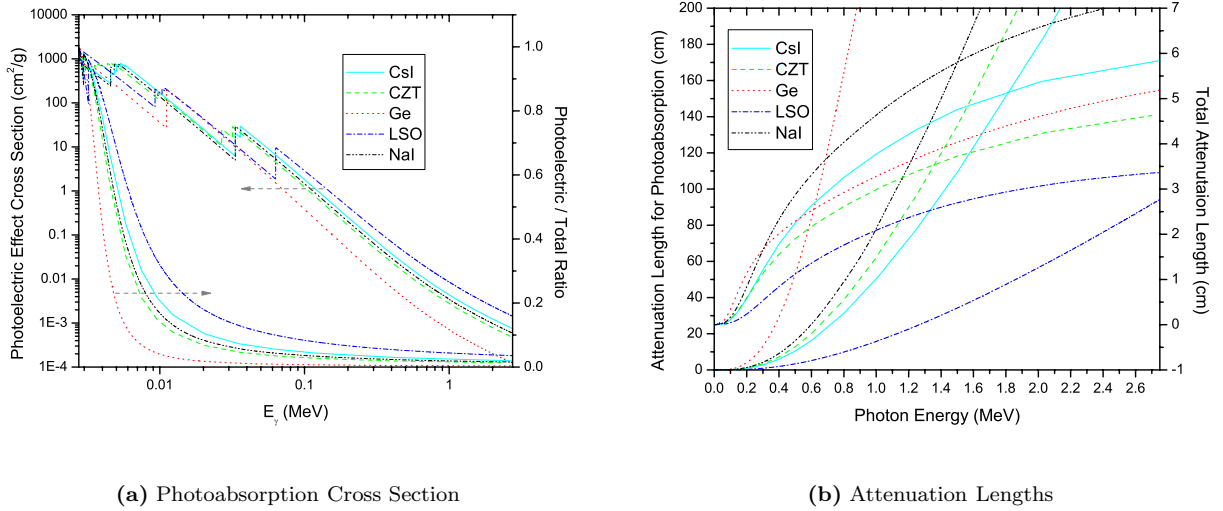


**Fig. 2.9:** Energy dependence of photoelectric effect cross section and attenuation length for some proposed absorption detector materials ( $d_{CsI}=4.53 \text{ g/cm}^3$ ,  $d_{Cd_{0.9}Zn_{0.1}Te}=5.78 \text{ g/cm}^3$ ,  $d_{Ge}=5.323 \text{ g/cm}^3$ ,  $d_{LSO}=7.42 \text{ g/cm}^3$  and  $d_{NaI}=3.67 \text{ g/cm}^3$ )

The photoelectric cross section as a function of photon energy does not differ much for these detector materials and LSO has the highest photoelectric to total ratio among all. The difference in their densities show itself in the attenuation length curves where LSO has the shortest attenuation length. NaI(Tl) is not quite efficient in stopping the scattered photons but it is superior to LSO(Ce) and CsI(Tl) in terms of light yield which is 75% and 45% compared to NaI(Tl), respectively. Compton camera system is based on a coincidence measurements and the timing characteristics of the detectors are very important for the system performance. LSO(Ce) has the fastest response among scintillators considered for this application so far. Ge has the cooling constraint and CZT is acquired in small quantities which are more expensive than most of the scintillators. Therefore, scintillators are more suitable for Compton camera applications as absorption detector material. Some scintillators and their important properties are listed in Tab. 2.1. In terms of energy resolution and fast response LSO(Ce) seems to be the best candidate for the absorption detector scintillator but the price of LSO is still high (10 mm thick LSO crystal having a diameter of 70 mm costs around 3000 USD) which may be a problem when large solid angle coverage is to be realized.

Monte Carlo simulations were performed to study the efficiency for photoelectric absorption in LSO and NaI. Scatter and absorption detectors were placed in parallel and the interactions of photons arriving

Crystal	NaI (Tl)	CsI	CsI (Tl)	CeF <sub>3</sub>	BaF <sub>2</sub>	BGO	PbWO <sub>4</sub>	LSO (Ce)	GSO (Ce)
Density (g/cm <sup>3</sup> )	3.67	4.51	4.51	6.16	4.89	7.13	8.3	7.4	6.71
Radiation Length (cm)	2.59	1.85	1.85	1.68	2.06	1.12	0.9	1.14	1.37
Molière Radius (cm)	4.8	3.5	3.5	2.63	3.4	2.3	2.0	2.3	2.37
Interaction Length (cm)	41.4	37.0	37.0	26.2	29.9	21.8	18	21	22
Refractive Index	1.85	1.95	1.79	1.68	1.50	2.15	2.2	1.82	1.85
Hygroscopicity	Yes	Slight	Slight	Slight	No	No	No	No	No
Luminescence (nm)	410	420	560	340	300	480	560	420	440
(at peak) (fast)		310		300	220		420		
Decay Time (ns)	230	35	1300	25	630	300	50	40	60
(fast)		6		8	0.9		10		
Light Yield (%)	100	5.6	45	8	21	9	0.1	75	30
		2.3			2.7		0.6		

**Tab. 2.1:** Properties of some common inorganic scintillators

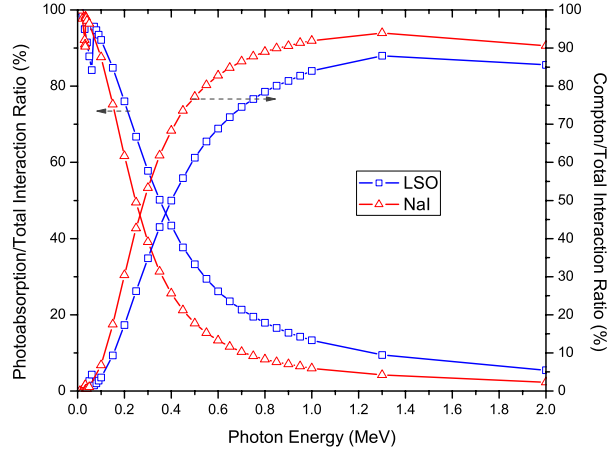


**Fig. 2.10:** The percentage of photoelectric and Compton events in 1.5 cm thick NaI and LSO as a function of the energy of the incoming photon

in the second detector were studied. XCOM data was used to calculate the attenuation length for different photon interactions. Finally, the percentage of all events that are photoelectric absorption and Compton scattering was plotted in Fig. 2.10 as a function of the energy of the incoming photon.

The photoabsorption efficiency drops as the energy increases for both materials but it falls off more quickly for NaI and the fraction of Compton scattered events in NaI is higher than in LSO. In fact, for the energy range of interest it is almost 50% probability for having the scattered photons fully absorbed in the absorption detector. The high rate of Compton events decreases the efficiency of the camera system and causes background events in which the energy is only partially deposited. This problem can be solved if events other than photoabsorption are also considered for the event reconstruction.

## 2.3 Interactions of Electrons

The study of electron interactions is vital for Compton camera imaging for several reasons. First of all, the sensitivity of the system depends on the capture of the recoil electron because the electrons escaping

from the first detector deliver only a partial energy information. The tracking of the electron's path improves the determination of the interaction location in the first detector. In this way, the source is found to be located on the arc of an event circle, rather than anywhere on the event circle, and this improves the system performance.

There exist three main interaction mechanisms [Mar69] by which electrons lose their kinetic energy as they pass through a matter:

- *Inelastic collisions with atomic electrons:* Møller scattering
- *Elastic scattering on atoms:* Coulomb scattering
- *Inelastic nuclear scattering with emission of bremsstrahlung*

Energy loss due to ionization and excitation is defined as collisional loss and the energy loss by emission of bremsstrahlung or electromagnetic radiation is called a radiative loss. The total energy loss of electrons consisting of collisional and radiative parts can be expressed as:

$$\left(\frac{dE}{dx}\right)_{total} = \left(\frac{dE}{dx}\right)_{coll.} + \left(\frac{dE}{dx}\right)_{rad.} \quad (2.9)$$

and the approximate ratio of radiative and collisional losses is given by [Eva82]:

$$\frac{(dE/dx)_{rad.}}{(dE/dx)_{coll.}} \simeq \frac{ZE_e/MeV}{1400m_e c^2} \quad (2.10)$$

For the energy range of interest, where the energy of electron is at most an MeV, collisional energy loss is the dominant mechanism whereas loss of energy by emission of radiation becomes dominant above few 10's of MeV or in absorbers of high atomic number.

### 2.3.1 Energy Loss of Electrons in the Scatter Detector

Collisional energy loss of electrons in the scatter detector is predominant both due to the energy range of electrons in this detector and the necessity of having a low-Z detector material as a scatter detector. The collisional energy loss of charged particles in matter is calculated by Bethe-Bloch formula but for electrons this formula needs some modifications. First of all, the deflection of the incoming electron has to be taken into account because in the standard formula it was assumed that the incoming charged particle remains undeflected which is mostly the case for heavy charged particles but not for light electrons. Another reason for a modification is that the electron collides with an electron, therefore the colliding particles are identical which is not the case for heavier charged particles like muons being scattered by atomic electrons. With these considerations Bethe-Bloch formula for an electron takes the following form [Gru96]:

$$-\left(\frac{dE}{dx}\right)_{coll.} = 4\pi N_a r_0^2 m_e c^2 \rho \frac{Z}{A} \frac{1}{\beta^2} \left[ \ln \frac{\gamma m_e c^2 \beta \sqrt{\gamma - 1}}{\sqrt{2} I} + \frac{1}{2}(1 - \beta^2) - \frac{2\gamma - 1}{2\gamma^2} \ln 2 + \frac{1}{16} \left(\frac{\gamma - 1}{\gamma}\right)^2 \right] \quad (2.11)$$

where  $N_a$  is Avogadro's number,  $\rho$  is the density of absorbing material and

$$\begin{aligned} \beta &= \frac{v}{c} = \sqrt{1 - \frac{1}{\left(\frac{E_e}{m_e c^2} + 1\right)^2}} \\ \gamma &= \frac{E_e + m_e c^2}{m_e c^2} = (1 - \beta^2)^{-1/2} \quad (\text{Lorentz factor}) \\ I &= Z \left(12 + \frac{7}{Z}\right) \text{ eV} \quad Z < 13 \quad (\text{mean ionization potential [Leo94]}) \\ &= Z(9.76 + 58.8Z^{-1.19}) \text{ eV} \quad Z \geq 13 \end{aligned}$$

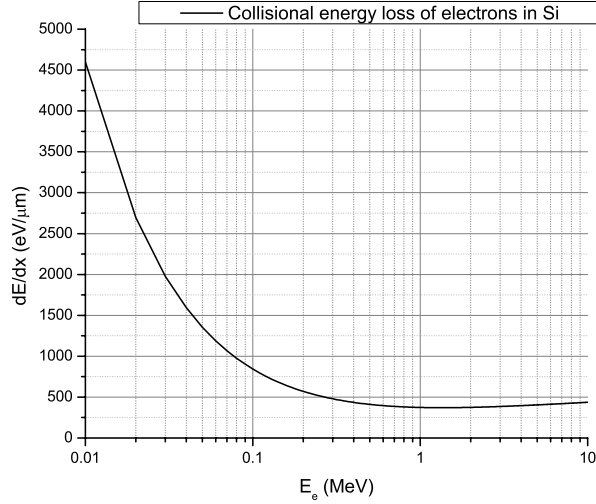


**Fig. 2.11:** Energy loss of electrons in silicon as a function of their energy. Only collisional losses are considered and radiative losses are not included.

The collisional energy loss as a function of electron energy is shown in Fig. 2.11 for silicon. Energy loss of electrons decreases as the energy increases and it is minimum at 1.3 MeV of electron energy where the particles are known as *minimum ionizing*. Above this energy logarithmic dependence becomes more important in (2.11) and  $dE/dx$  increases with increasing  $E_e$ .

The second mechanism by which electron loses its energy in an absorber is an energy loss by radiation: Bremsstrahlung which becomes important at high energies. The emission of electromagnetic radiation accompanies an acceleration or deceleration of a charged particle. The acceleration of a charged particle with mass  $m$  and charge  $ze$  in the Coulomb field of an atom  $Ze$  is proportional to  $zZe^2/m$ . The intensity of radiation is related to the acceleration quadratically and therefore is proportional to  $(zZe^2/m)^2$ . The probability of a radiative interaction is inversely proportional to the mass of a charged particle and for this reason it is observed with much higher probability for electrons than for higher charged particles. The energy loss due to radiation is given by Bethe-Heitler equation [Mus95]

$$-\left(\frac{dE}{dx}\right)_{rad.} = \frac{\rho N_a}{A} E_e Z^2 f(\ln E_e) \sim E_e Z^2 \ln(E_e) \quad (2.12)$$

where  $f(\ln E_e)$  is a linear function of  $\ln E_e$ . At 500 keV of electron energy, the energy loss of electrons due to bremsstrahlung is about 1% of the total energy loss in silicon and for a heavier material this percentage increases only to 3.5% in NaI(Tl). The critical energy at which collisional losses equals radiation losses is 51.1 MeV for silicon which is out of energy range considered in this work.

### 2.3.2 Range of Electrons

In addition to inelastic collisions, electrons also suffer several elastic Coulomb collisions in the matter. In these collisions an electron loses small fraction of its energy and it is deflected from its path. These scatterings are classified as single scattering, plural scattering in case of up to 20 scatterings and multiple scattering for scatterings which occur more than 20 times. As a result, the path length of an electron differs from its penetration length in matter. Fig. 2.12 shows GEANT simulation of some Compton events in 300  $\mu\text{m}$  Si where various electron paths can be observed.

In addition to these small angle scatterings, electrons may also be deflected in large angles by scattering from nuclei. Electron's backscattering cross section is proportional to  $Z^2/\beta^4$ , therefore it becomes more probable for high- $Z$  absorbers and low  $E_e$ .

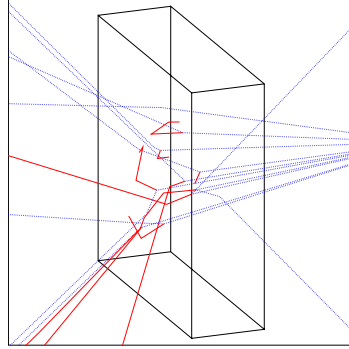


**Fig. 2.12:** Interactions of 662 keV photons in 300  $\mu\text{m}$  thick silicon simulated with GEANT and GLECS where photons are blue and electrons are red. Examples of single scattering, plural scattering and backscattering can be seen.

The distribution of range (R) and path length (S) in oxygen for electrons with an energy of 19.6 keV was experimentally determined by Williams [Wil31]. Williams used his cloud chamber for the measurement of S and the range data was taken by using thin foils. In the foil method the number of electrons passing through foils of different thicknesses are recorded. Thus, in the foil method, the range measured for an electron can only be approximately equal to the true path length if the electron does not suffer any scattering or straggling. The result of the experiment comparing the fraction of electrons transmitted through a target of thickness  $x$  for two different measurements as a function of the target thickness is shown in Fig. 2.13.

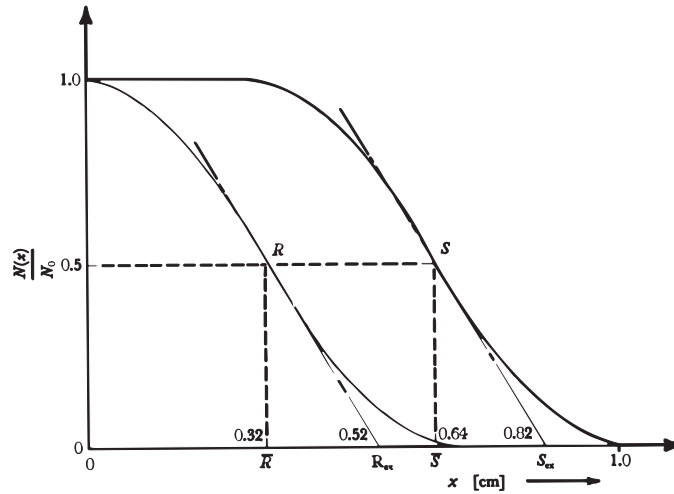


**Fig. 2.13:** The distribution of S and R for 19.6 keV electrons in an oxygen gas at STP (from [Mar69])

The mean path length is 24% greater than the extrapolated range and it was measured to be 48% greater in Argon. This difference is entirely due to scattering and straggling of electrons and the two different methods can produce similar results only when none of these effects take place. The broad distribution of path lengths is due to straggling, or in other words due to the statistical fluctuations in the distribution of energy loss. It is important to note that the mean range is only half of the mean path length for this data.

The theoretical calculations of energy losses discussed in section 2.3.1 concern the mean energy losses. Thus, the integral of the total energy loss corresponds to a mean path length of an electron:

$$\bar{s} = \int \left( \frac{dE}{dx} \right)_{total}^{-1} ds \quad (2.13)$$

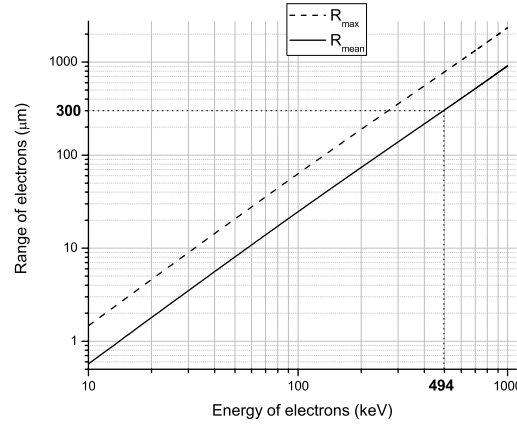


**Fig. 2.14:** Kanaya-Okayama range of electrons in silicon including both maximum and mean penetration lengths

Several theoretical studies were performed for the calculation of the range of an electron since early 1900 and among these, Kanaya and Okayama's study is one of the most popular one. Kanaya and Okayama [Kan72] developed a modified model for electron diffusion following Lindhard's theory in amorphous solid targets. According to their model, which takes elastic and inelastic scattering events into account, the maximum range of electrons can be defined as:

$$R_{max} = \frac{2.76 \cdot 10^{-11} A E_e^{5/3} \left(1 + \frac{E_e}{2m_e c^2}\right)^{5/3}}{Z^{8/9} \rho \left(1 + \frac{E_e}{m_e c^2}\right)^{4/3}} \quad (2.14)$$

This result was shown to agree with experimental data in the energy range of 10-1000 keV. Following (2.14) the energy of electrons at depth was found to be equal to  $E = (1 - y)^{3/5} E_e$  where  $y$  is the reduced depth and defined as the ratio of the diffusion depth to a maximum range. Kanaya et al. also defined the fractional electron transmission so that the fraction of transmitted electrons can be calculated as a function of depth:

$$\eta_T = \exp\left(-\frac{\gamma y}{1 - y}\right) \quad (2.15)$$

where effects of diffusion loss due to multiple collisions for returning electrons and energy attenuation due to electronic collisions are included in the  $\gamma$  term which was defined to be  $\gamma = 0.187 Z^{2/3}$ . By using the fractional electron transmission equation the diffusion depth, where the fraction of transmitted electrons is 1/2, in other words the mean range, can be found:

$$R_{mean} = \frac{\ln 2}{\ln 2 + 0.187 Z^{2/3}} R_{max} \quad (2.16)$$

The maximum and the mean range of electrons in silicon are calculated from equations (2.14) and (2.16) and plotted as a function of the electron energy in Fig. 2.14.

The recent studies show that Monte Carlo method is more powerful and reliable procedure to study the penetration of high energetic electrons in matter. Geant simulations were done to compare the range-energy relation with the theoretical result. Geant simulates the energy loss and scattering of electrons at each step of the particle. The distance that an electron moves until it stops is then calculated using equation (2.13). Fig. 2.15 shows the range as a function of kinetic energy for recoil electrons that are absorbed in a 300  $\mu\text{m}$  thick silicon detector shown in Fig. 2.12. The distribution of energy loss for these electrons is also shown in this figure.

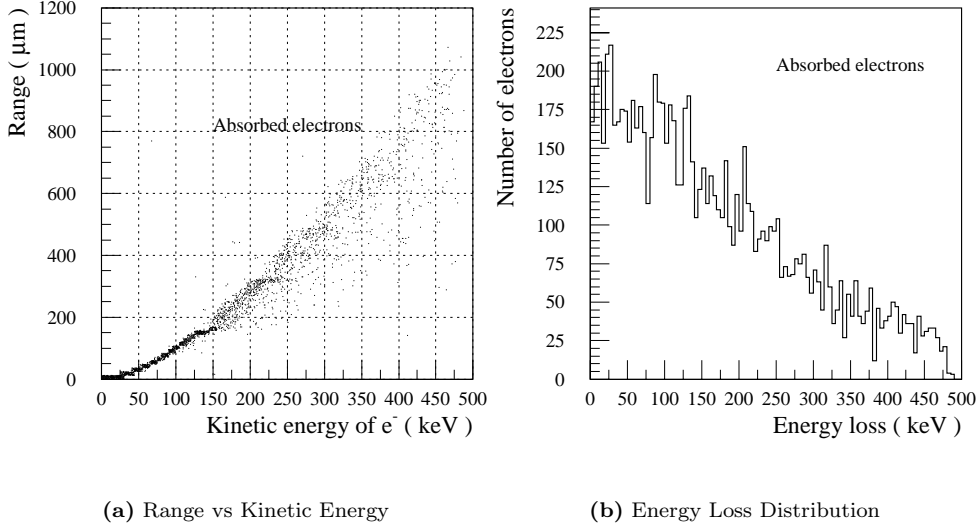


**Fig. 2.15:** Electron range in 300  $\mu\text{m}$  Si as a function of electron's kinetic energy and the distribution of energy loss in this detector for electrons that do not escape Si, simulated with GEANT.

### 2.3.3 Angular Distribution of Recoil Electrons

The directional distribution of electrons in the scatter detector is of considerable importance for the Compton camera system. The scattering angles of a photon and an electron are related to each other through the formula

$$\cot \phi = (1 + \epsilon) \tan \frac{\theta}{2} \quad (2.17)$$

which shows that the scattering angle of the electron can not exceed  $90^\circ$ . The relation between the scattering angles of the recoil electron and scattered photon and their relation with the energy of the recoil electron are plotted in Fig. 2.16 for  $E_\gamma = 662 \text{ keV}$ .

Due to the dependence of  $\phi$  on  $\theta$ , the directional distribution of recoil electrons also depend on the directional distribution of scattered photons. The number of recoil electrons per angle of projection  $\phi$  is given by (Appendix A.3) :

$$\frac{d\sigma}{d\phi} = \frac{d\sigma}{d\Omega} \frac{\sin \theta}{\sin \phi} \frac{d\theta}{d\phi} 2\pi \sin \phi \quad (2.18)$$

where  $d\sigma/d\Omega$  (differential collision cross section) is given in equation (2.2a). It can be seen in Fig. 2.17(a) that the distribution has a strong dependence on the energy of the initial photon and as the energy of the incoming beam increases the maximum of the  $d\sigma/d\phi$  distribution shifts to a smaller scattering angle for the recoil electron. The number-energy spectrum of Compton electrons is also interesting to see the energy distribution of the electrons produced by Compton scattering (Fig. A.15). This can easily be computed using equation (2.18) (Appendix A.3) which then gives the following result:

$$\frac{d\sigma}{dE_e} = \frac{d\sigma}{d\Omega} 2\pi \sin \theta \frac{(1 + \epsilon(1 - \cos \theta))^2}{\epsilon \sin \theta e_\gamma} \quad (2.19)$$

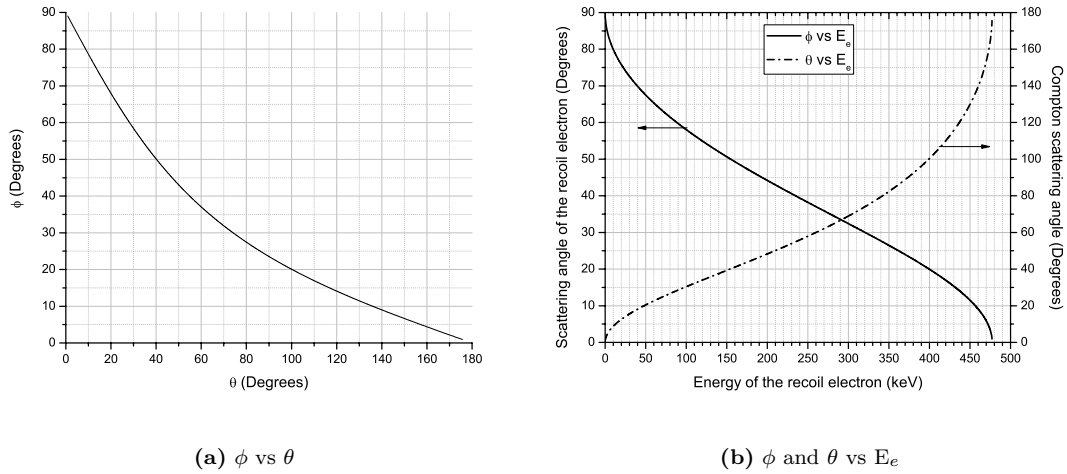


**Fig. 2.16:** The variation of the scattering angle of the recoil electron as a function of the scattering angle of the Compton photon and their dependence on the energy of the recoil electron for the incoming photon energy of 662 keV

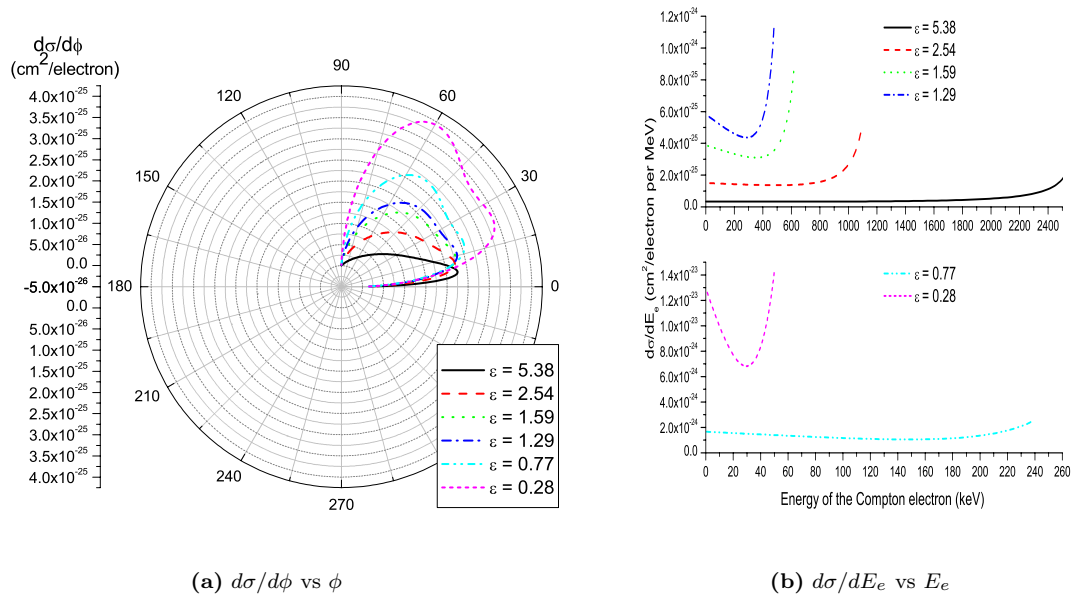


**Fig. 2.17:** Angular and energy distribution of Compton electrons for various energies of the incoming photon



### 3. Impact of the Detector Parameters on the Compton Camera Performance

The optimization of a Compton camera system in terms of efficiency and resolution is a complex multi-parameter problem. There exist several detector parameters that influence the performance of the Compton camera system [ÇN02; ÇN01]. Fig. 3.1 shows the principle of Compton camera imaging with some important detector parameters and notations, which are going to be used in the following sections.

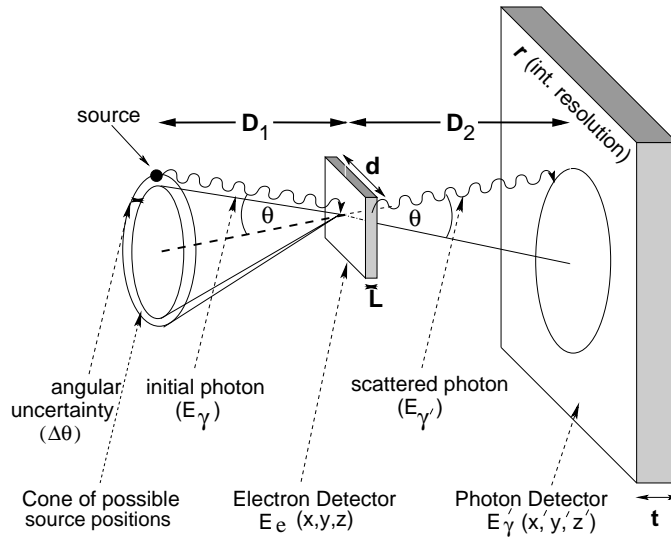


**Fig. 3.1:** The principle of Compton camera imaging and main detector parameters of the system

Coincidence events are recorded between the two detectors from radiation which Compton scatters from the first detector onto the second detector, both detectors being position and energy sensitive. Photons scattered at a certain angle from the scatter (electron) detector produces elliptical profiles on the absorption (photon) detector. Backprojection of each point of an ellipse produces a conical surface passing through the object to be imaged. Projection of a cone onto a plane produces an ellipse and the overall width of this ellipse depends both on the uncertainty in the scattered photon direction and the uncertainty of calculating the Compton scattering angle. The azimuthal uncertainty of an ellipse is due to the lack of information in the direction of the recoil electron. The whole circle of possible object location reduces to a segment if the recoil electron is tracked in the electron detector.

The imaging performance of the Compton camera system increases with the accuracy of determining the cone associated with each coincident event. This accuracy itself depends upon the overall angular uncertainty  $(\Delta\theta)$ . There are three factors contributing to  $\Delta\theta$ :

- Physics factor: Doppler broadening  $(\Delta\theta_D)$
- Electronic noise and statistical factor: Energy resolution of the electron detector  $(\Delta\theta_E)$
- Geometric factors: pixel size and thickness of both detectors, source-detector and inter-detector distances  $(\Delta\theta_g)$

### 3.1 Doppler Broadening

The derivation of the Compton equation (2.5) given in Appendix A.1 assumes that the gamma-ray interacts with a free electron whose initial momentum is zero. This approximation is good enough for high energetic photons ( $E_\gamma \geq 1$  MeV) interacting in a low-Z material. However, the recoil electron is neither at rest nor free, but it is bound to its atomic nucleus with non-zero orbital momentum. With the initial momentum of the recoil electron taken into account equation (2.5) takes the following form [Rib75]:

$$E_{\gamma'}^{Doppler} = \frac{E_\gamma}{1 + \varepsilon(1 - \cos\theta)} \left( 1 - \frac{p_z |\mathbf{p}_\gamma - \mathbf{p}_{\gamma'}|}{m_e E_\gamma} \right) \quad (3.1)$$

where  $p_z$  is the projection of the electron's pre-collision momentum on the scattering vector  $\mathbf{p}_{\gamma'} - \mathbf{p}_\gamma$ . For  $p_z$  being equal to zero, equation (3.1) reduces to equation (2.5).

The distribution of the electron's pre-collision momentum is different for each material and it also varies with the physical state of the material, therefore the scattered photon energy has no unique value for given  $E_\gamma$  and  $\theta$ . The electron momentum direction is randomly distributed with respect to the incident photon direction. As a result, the energy distribution of the scattered photon broadens around  $E_{\gamma'}$ , the value of the scattered photon energy if the electron is at rest. This effect is called *Doppler broadening* and it was first interpreted by DuMond in 1929 [DuM29]. This broadened distribution is called *Compton profile* which is denoted as  $J_i(p_z)$  where the subscript  $i$  corresponds to the shell number. The Compton profile depends mainly on the following factors:

- Atomic number of the material: higher  $Z \Rightarrow$  Doppler broadening  $\nearrow$
- Electron's atomic shell state: inner shell  $\Rightarrow$  larger  $p_z \Rightarrow$  Doppler broadening  $\nearrow$
- Energy of the incoming photon: high  $E_\gamma \Rightarrow$  Doppler broadening  $\searrow$  ( $\propto 1/E_\gamma$ )
- Compton scattering angle: larger  $\theta \Rightarrow$  Doppler broadening  $\nearrow$

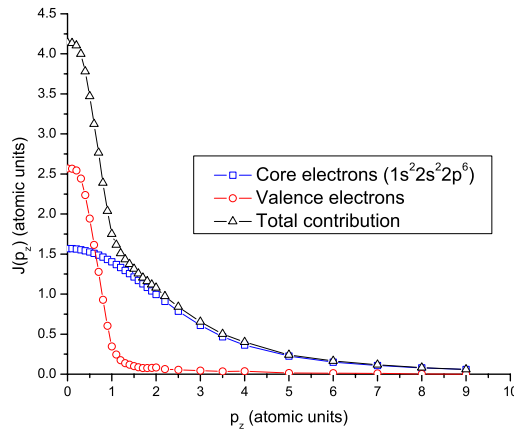
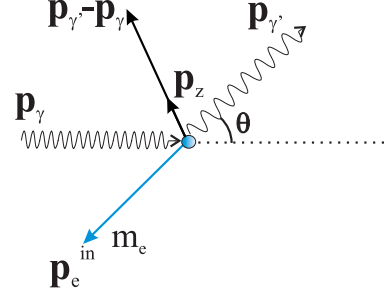


**Fig. 3.2:** Core, valence and total Compton profiles for crystalline silicon from Reed's data ([Ree72])

Besides broadening of the scattered photon energy distribution, the binding effect also appears as a reduction in the Compton scattering cross section and a reduction in the forward scattering of the photon.

The differential cross section per unit solid angle can be written in terms of Klein-Nishina differential cross section as [Rib82]:

$$\left(\frac{d\sigma}{d\Omega}\right)_{bc} = \frac{d\sigma}{d\Omega} S(E_\gamma, \theta, Z) \quad (3.2)$$

where  $S(E_\gamma, \theta, Z)$  is the incoherent scattering function in the impulse approximation which is defined in terms of Compton profile as:

$$S(E_\gamma, \theta, Z) = \sum_i \int_{-\infty}^{p_{i,max}} dp_z J_i(p_z) \quad (3.3)$$

where  $J_i(p_z)$  is the contribution from each orbital whose sum over all shells give the total Compton profile and  $p_{i,max}$  is the highest value of  $p_z$  for which an electron in the  $i^{th}$  shell can be excited. The incoherent scattering function converges to the number of electrons in each sub-shell when  $p_{i,max}$  goes to infinity. Extensive table for values of Compton profiles for  $1 < Z < 102$  can be found in [Big75].

Compton profiles for a certain material show differences between its atomic or molecular state and its solid state due to atomic binding effects in the lattice. For this reason, experimental Compton profile data of Reed and Eisenberger [Ree72] is used to study the Doppler broadening in a crystalline silicon. For the measurement of Compton profiles, they used a  $^{123m}\text{Te}$  source which emits photons of 159 keV energy. The source was placed in a lead block which has an opening such that emitted photons hit directly the sample but not the detector. The sample was made thick enough to obtain a reasonable count rate together with high signal-to-noise ratio and thin enough to minimize the probability of multiple scattering events which decrease the accuracy of the Compton profile measurement. Five different high purity silicon crystals were used: slices of 25.4 mm diameter which are 1.68, 3.76, 9.53 mm thick and 25.4 mm long cylinders with diameters of 11.43 mm and 25.4 mm. The sample was placed in a vacuum chamber which had a 254  $\mu\text{m}$  thick Be radiation window through which both the incoming and scattered radiation were transmitted. The scattered radiation was collimated so that only a certain angular region of scattered radiation was detected in the 5 mm thick Ge(Li) detector. The intensity of the scattered beam was used to calculate

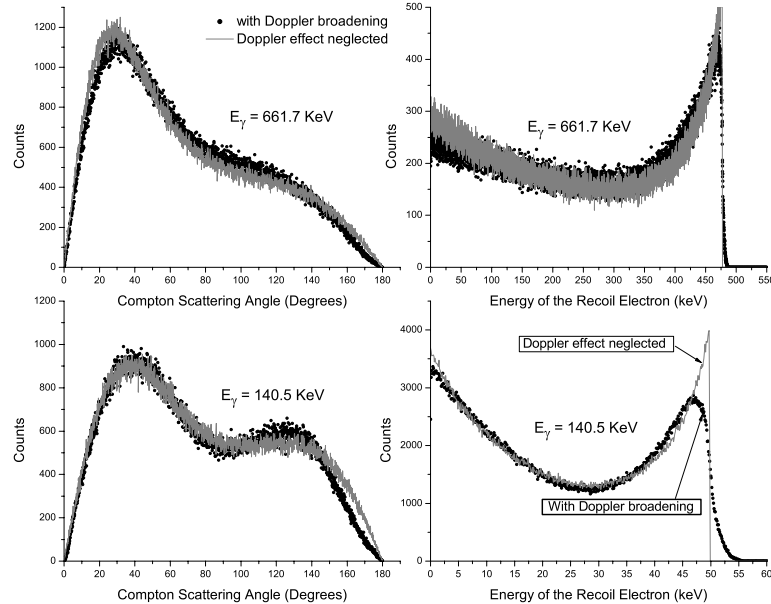


**Fig. 3.3:** Angular distribution of the scattered photon and the energy distribution of the recoil electron for bound and unbound electrons in silicon. Compton profile data for crystalline silicon given in [Ree72] is used for the MC simulation.

Compton profiles with the method described in [Eis72]. Two sets of values for  $J(q)$  are provided; one is for core electrons and the other for valence electrons (Fig. 3.2).  $J(q)$  for core electrons were calculated from atomic wave functions and for valence electrons these were subtracted from the measured  $J(q)$  values. For Monte Carlo (MC) simulations, the Compton profile data is given in an array and the electron momentum was picked randomly from a momentum distribution. The Doppler broadened scattered photon energy is sampled according to the distribution of the bound electron momentum [Hol00]. To perform this task, the photon is transformed into electron's rest frame where Klein-Nishina calculations are performed and finally both particles are transformed back to the lab frame.

Fig. 3.3 shows the distributions of the Compton scattering and the energy of the recoil electron for bound and unbound electrons in silicon. The energy of the incoming photon was taken to be 140.5 and 661.7 keV and it is clear that at low energies the distributions change considerably when the precollision momentum of the electron is taken into account. The angular distribution shows that in the bound case small and large scatter angles are slightly suppressed. The energy distribution of the recoil electron at the Compton edge becomes more broadened than it is when the electron is considered to be at rest. Compared with free electrons at rest, electrons bound to a nucleus with non-zero momentum change the distributions as follow:

- The probability of Compton scattering at low energies becomes slightly higher than predicted by the Klein-Nishina equation (Eq. 2.2a)
- Small and large scatter angles are slightly suppressed for low energies of the incoming photon
- Energy distributions of the recoil electron and the scattered photon change

### 3.1.1 Doppler Broadened Angular Uncertainty

The angular uncertainty due to Doppler broadening can be determined by measuring the broadening of the distribution of the Compton scattering angle for fixed scattering angles. For instance, if  $45^\circ$  of scattering angle is taken, an angular distribution peaking at  $45^\circ$  is obtained, which is broadened due to Doppler effect. This broadened angular distribution is called a Doppler profile.

Doppler profile of silicon for different photon energies and the comparison of the profile for Si and Ge are shown in Fig. 3.4. Both figures 3.4(a) and 3.4(b) are produced for a constant scattering angle

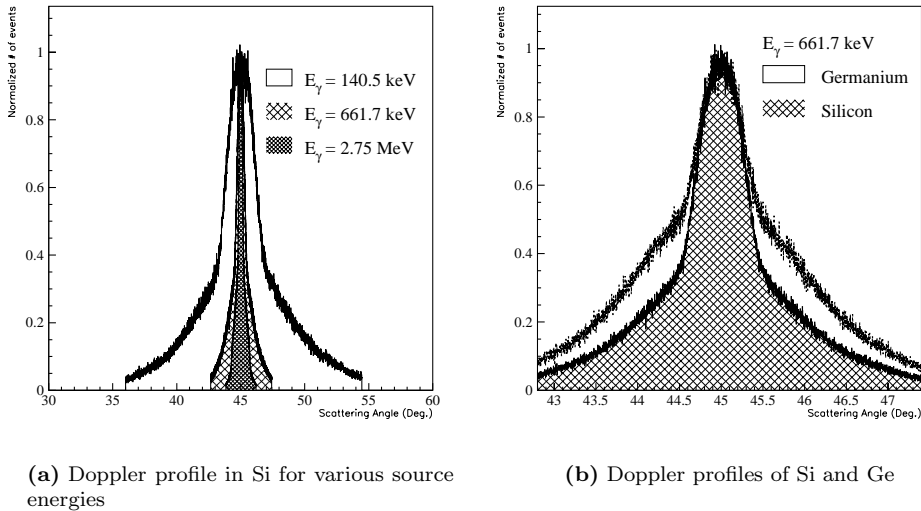


**Fig. 3.4:** Doppler profile for a fixed energy of the recoil electron corresponding to  $45^\circ$  scattering angle for various energies of the incoming photon in Si and for  $^{137}\text{Cs}$  source in Si and Ge

of  $45^\circ$ , therefore the energy of the recoil electron is taken to be fixed. Fig. 3.4(a) shows that the effect of the precollision electron momentum becomes more important for lower energies. This makes higher energetic radionuclides more favorable for Compton camera applications in nuclear medicine. Having high energetic photons would reduce the achievable resolution limit to lower values. Fig. 3.4(b) is another supporting result for choosing silicon as the scatter detector. The deterioration in angular resolution is more pronounced for detector materials with higher atomic number because of the dependence of the Doppler effect on the shell structure of the atoms. Among various scatter detector materials proposed for Compton camera applications, silicon has the best performance in terms of the Doppler-limited angular resolution limit and it is followed by Ge, Xe and CdTe. Recent study on the Doppler limit for various materials showed that the best angular resolution can be reached with alkaline and alkaline earth metals, the worst with materials having filled p and d orbitals and overall silicon would be the best semiconductor [Zog03].

The angular uncertainty due to Doppler broadening is determined using the FWHM of the Doppler profile. Doppler profiles for all scattering angles are obtained and their FWHM values are calculated. The distributions in Fig. 3.4 have long tails compared to Gaussian distributions. In fact, Doppler profile is a combination of multiple Gaussian distributions which originate from contributions of different shells of the atom. The contribution of outer shells produces sharper distribution due to the fact that electrons in these shells are less energetic, which causes the deviation from free and unbound electron case to be small. The electrons from inner shells are responsible for the long tail of the distribution (Fig. 3.2). After having trials with different functions, combination of three Gaussian functions were found to be good enough to fit the curve. The angular uncertainty (FWHM) for crystalline silicon as a function of Compton scattering angle is plotted in Fig. 3.5 for different photon energies. This result shows that the angular resolution strongly depends on the Compton angle such that it becomes worse for larger angles. This is an important result that should be considered when designing the camera system. It shows that it is better for the second detector to cover the region into which higher energetic photons scatter or in other words it should cover the forward scattering region. Forward region is not only favourable for angular uncertainty due to Doppler broadening but also for the higher cross section of Compton scattering (Fig. 2.5) and the lower range of electrons (Fig. 2.15) in this region.

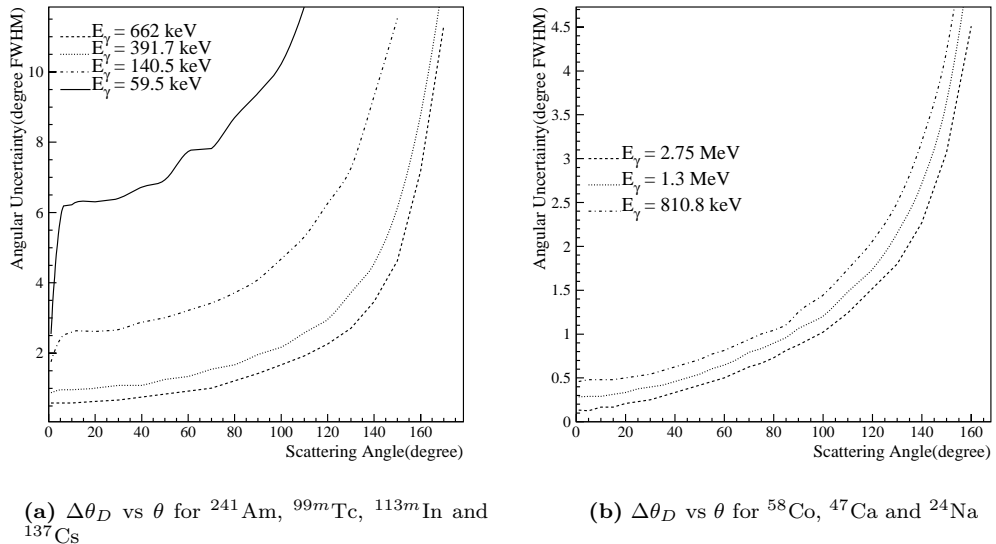


**Fig. 3.5:** Angular uncertainty due to Doppler broadening for different initial photon energies in Si

## 3.2 Energy Resolution of the Electron Detector

The accuracy with which the energy of the recoil electron in the scatter detector is determined influences the overall angular uncertainty. Random noise within the detector and readout electronics, statistical fluctuations in the number of charge carriers are the main factors causing imperfect energy resolution, assuming there are no deviations in the operating conditions of the detector. The statistical fluctuations impose the lower limit in the achievable energy resolution due to the fact that there is no way to improve it, whereas other sources of the noise can be improved.

In a semiconductor detector, incoming ionizing radiation gives up its energy through ionization and lattice vibrations. If all the energy was spent for ionization with a fixed energy transfer, there would be no fluctuations in the number of electron-hole pairs or if the mechanisms that result in the formation of a charge carrier were totally uncorrelated, the total number of charge carriers would be described by Poisson statistics. However, none of these situations describes the reality and Fano [Fan47] was the first to introduce the modification to the Poisson case to define the observed statistical fluctuations in the number of charge carriers where he defines the *Fano factor* as  $F = \langle (N - \langle N \rangle)^2 \rangle / \langle N \rangle$ . The number of charge carriers is typically a large number, therefore the response function of a detector has a Gaussian shape and the full width at half maximum (FWHM) of a Gaussian distribution is used to define the detector resolution. The standard deviation of the peak in the pulse height spectrum is proportional to  $\sqrt{FN}$ . As a result, the contribution of the statistical noise to the energy resolution can be expressed with the following equation:

$$\Delta E_{FWHM}^{statistical} = 2.35w\sqrt{F\frac{E}{w}} \text{ eV} \quad (3.4)$$

where  $w$  is the energy required to create an electron-ion pair in a semiconductor detector and the equation is multiplied by this factor to convert it to energy units.

Another factor determining the energy resolution is the random noise within the detector and readout electronics which is expressed in terms of equivalent noise charge (ENC). ENC is the signal which produces output amplitude that is equivalent to the rms noise and its contribution to the energy resolution is simply expressed as:

$$\Delta E_{FWHM}^{noise} = 2.35wENC \text{ eV} \quad (3.5)$$

where ENC is in units of electron charges.

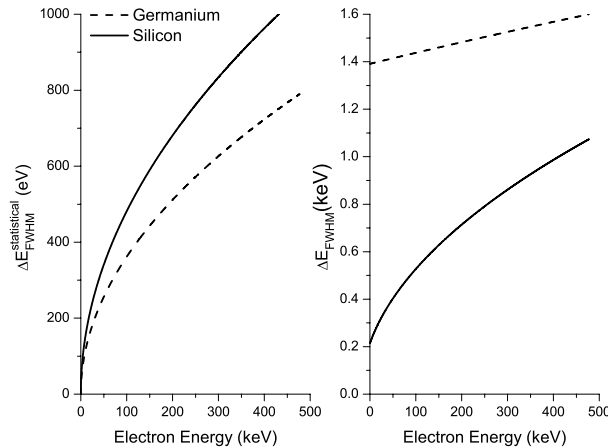


**Fig. 3.6:** Energy resolution due to statistical noise and the total energy resolution as a function of the electron energy where ENC for Si is taken as 25 electrons and for Ge 200 electrons. The Fano factor for Si and Ge are 0.115 and 0.08, the pair creation energies are 3.65 eV and 2.96 eV, respectively.

Assuming that the individual sources of fluctuation in the energy distribution are independent and each one is symmetric [Kno99], the overall energy resolution is the quadrature sum of the individual

contributions:

$$\Delta E_{FWHM} = 2.35w\sqrt{ENC^2 + \frac{FE}{w}} \text{ eV} \quad (3.6)$$

The total energy resolution and the Fano limit alone are shown in Fig. 3.6 for both Si and Ge. In terms of the statistical factor, Ge performs better than Si due to its lower pair creation energy and Fano factor. When the electronics noise for existing detectors is considered, the typical ENC value for Ge is around 200 electrons which is also the case for silicon detectors but silicon drift detectors with on-chip readout electronics outperform these with an ENC of about 25 electrons rms at room temperature. Due to the fact that the scatter detector used in this work is of this type of a silicon detector, the ENC for silicon was taken to be 25 electrons rms and the one for Ge 200 electrons rms. With these ENC figures, the overall energy resolution of the silicon drift detector is better than a Ge detector as shown on the right plot of Fig. 3.6.

### 3.2.1 Angular Uncertainty due to Energy Resolution

The energy resolution of the electron detector transforms into an uncertainty in the Compton scatter angle. The angular uncertainty can be approximated by applying an error propagation on the Compton equation as derived in equation (A.18) and rearranging the terms gives the following relation:

$$\Delta\theta_E = \frac{(1 + \varepsilon(1 - \cos\theta))^2}{\varepsilon \sin\theta E_\gamma} \Delta E_{FWHM} \quad (3.7)$$

or in terms of energies only, the angular resolution can be expressed as:

$$\Delta\theta_E = \frac{E_\gamma}{E_{\gamma'} \sqrt{2E_e \varepsilon E_{\gamma'} - E_e^2}} \Delta E_{FWHM} \quad (3.8)$$

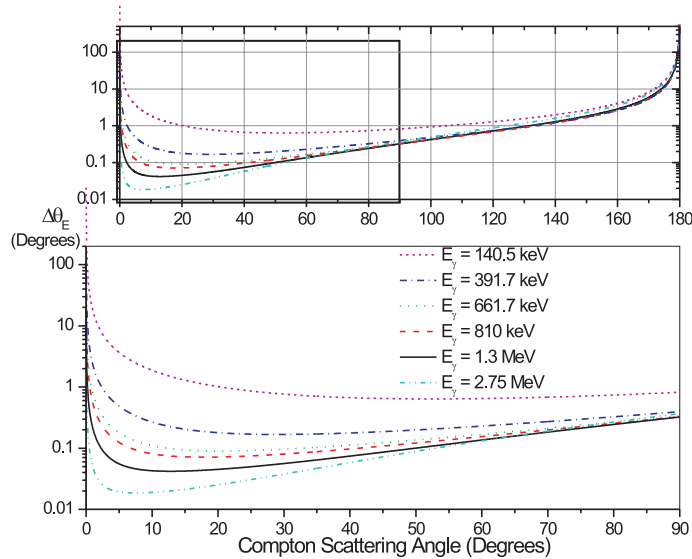


**Fig. 3.7:** Angular uncertainty due to the resolution of the scatter detector for different energies of the incoming photon in a silicon detector with an ENC of 25 electrons rms

The angular uncertainty due to the energy resolution of the first detector is plotted in Fig. 3.7 for various energies of the incoming photon. The detector is a silicon detector with an equivalent noise charge of 25 electrons rms. Like the Doppler broadening, the behaviour of the energy resolution also favours

the forward scattering region to minimize the angular uncertainty. Angular resolution becomes better at high energies and the advantage of having higher energetic source increases in the forward scattering region.

### 3.3 Geometric Factors in Angular Uncertainty

Geometric uncertainties in the measurements of the interaction positions in two detectors result in additional uncertainty in the determination of the Compton scatter angle. There are several factors affecting the angular uncertainty, these are:

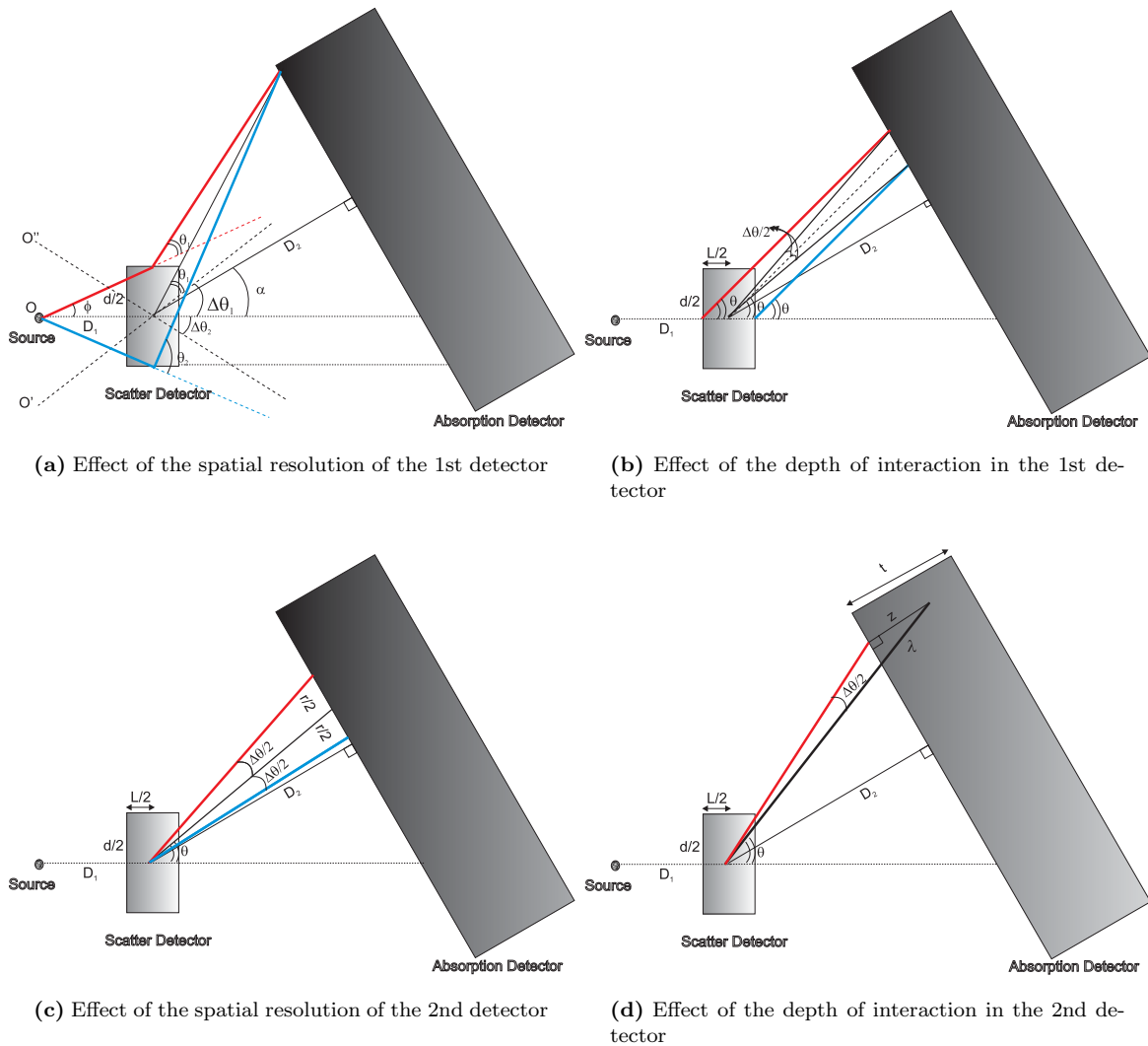


**Fig. 3.8:** Geometric factors influencing the accurate determination of the Compton scattering angle  $\theta$

- $D_1$ : The distance between the object to be imaged and the scatter detector's center
- $D_2$ : Inter-detector distance
- $d$ : pixel size of the scatter detector

- L: depth of interaction resolution of the scatter detector
- r: spatial resolution of the absorption detector
- t: depth of interaction resolution of the absorption detector
- The orientation of the absorption detector

Geometric factors can be studied in two groups: the contribution of the scatter detector and the contribution of the absorption detector. Within these groups the study can be further categorized into two groups by investigating effects of the pixel size and the depth of interaction in each detector individually. Models developed for determining these effects quantitatively are demonstrated in Fig. 3.8. The method is based on the geometric and trigonometric relationships which are provided in more detail in Appendix B.1. Position resolution and penetration in each detector can be analyzed individually or combined. The components of the scatter detector were analyzed with a combined model and those of the absorption detector were studied individually. There is no special reason for choosing this way and in fact both detectors were studied in two different ways and their difference was found to be negligible. The contributions of the pixel size and the depth of interaction in the electron and photon detectors can be analytically estimated as:

$$\Delta\theta_s = \arctan \left\{ \left[ 1 - \frac{1}{2D_2} \sqrt{d^2 + L^2} \cos(180 - \xi - \alpha) \right] \tan(\theta - \alpha + \phi_1) + \frac{1}{2D_2} \sqrt{d^2 + L^2} \sin(180 - \xi - \alpha) \right\} \\ - \arctan \left\{ \left[ 1 + \frac{1}{2D_2} \sqrt{d^2 + L^2} \cos(180 - \xi - \alpha) \right] \tan(\theta - \phi_2 - \alpha) - \frac{1}{2D_2} \sqrt{d^2 + L^2} \sin(180 - \xi - \alpha) \right\} \quad (3.9)$$

$$\Delta\theta_{a_{pixel\ width}} = 2(\theta - \alpha) - 2 \arctan \left[ \tan(\theta - \alpha) - \frac{r}{2D_2} \right] \quad (3.10)$$

$$\Delta\theta_{a_{depth\ of\ int.}} = 2(\alpha - \theta) + 2 \arctan \left[ \frac{z}{2D_2} \tan(\theta - \alpha) + \tan(\theta - \alpha) \right] \quad (3.11)$$

where the angles  $\phi_1 = \frac{d/2}{D_1+L/2}$ ,  $\phi_2 = \frac{d/2}{D_1-L/2}$  and  $\xi = \arctan(d/L)$  are shown in Fig. B.1 and  $\alpha$  is the angle between the normal of the first detector and the normal of the second detector, as shown in Fig. 3.8(a). The overall geometrical uncertainty is calculated by combining the contribution of each resolution element:

$$\Delta\theta_g = \sqrt{\Delta\theta_s^2 + \Delta\theta_{a_{pixel\ width}}^2 + \Delta\theta_{a_{depth\ of\ int.}}^2} \quad (3.12)$$

The variation of the angular uncertainty due to geometric factors is plotted in Fig. 3.9 as a function of the scattering angle for a detector system where the normal vectors of two detectors make an angle of  $45^\circ$  between each other. For each curve only one of the parameters was modified to see the effect of each factor individually. The spatial and depth of interaction resolution values for the reference system were chosen according to our Compton camera system. Fig. 3.9(a) shows that the angular uncertainty is most sensitive to the variation of the spatial resolution of the scatter detector. A factor of 2 improvement in the spatial resolution of this detector results in an angular resolution which is 1.8 times better at its minimum. The second most effective factor is the depth of interaction in the absorption detector. Better depth of interaction resolution does not affect the angular uncertainty curve at its minimum but it lowers the uncertainty around this point, causing a lower angular uncertainty in average. It is notable that almost all the curves in Fig. 3.9(a) have their minima around  $45^\circ$  which is due to the orientation of the detectors. The normal of the scatter detector makes an angle of  $45^\circ$  with the normal of the second detector, namely  $\alpha$  of Fig. 3.8(a) is equal to  $45^\circ$ . For this reason, the depth of interaction resolution has a least effect for a scattered photon penetrating into the second detector orthogonally. To estimate the angular uncertainty due to the depth of interaction, the point where the photon stops in the absorption detector is projected onto the detector surface where the signal is readout (B.1.3.2). The difference between this point and the reconstructed point coincides when the photon moves in parallel to the normal of the detector and this difference becomes larger at other scattering angles. As a result, the angular uncertainty due to

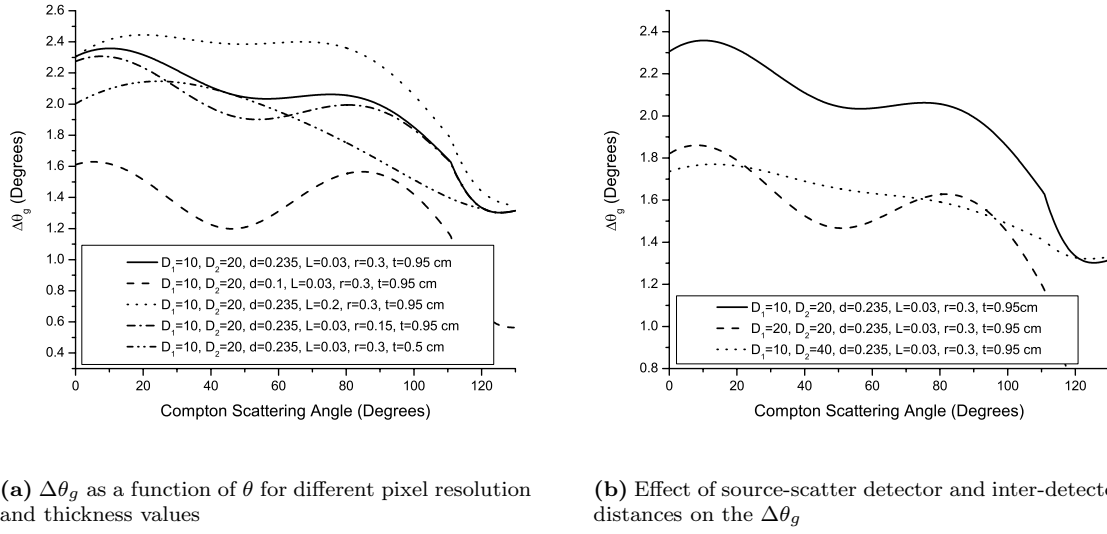
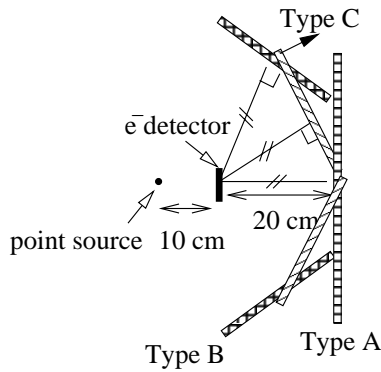


**Fig. 3.9:** Influence of detector parameters on the angular uncertainty as a function of the scattering angle for  $\alpha=45^\circ$  and  $E_\gamma=661.7$  keV

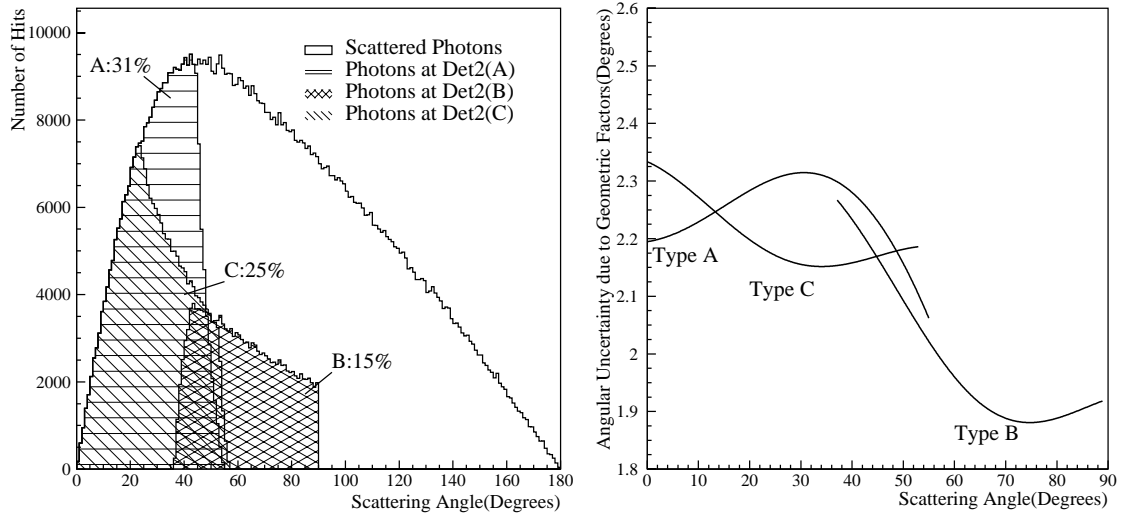
geometric factors shows a minimum whose location depends on the orientation of the detectors. The distance between the object and the first detector and the inter-detector distance also enter the formulae of geometric uncertainty. Their effect on the angular uncertainty is shown in Fig. 3.9(b) in comparison with the reference system. The angular resolution improves with increasing  $D_1$  and  $D_2$ . However, finally the angular uncertainty is translated into the position uncertainty with which the location of the source is determined and the position uncertainty is proportional to  $D_1$ . Therefore, the location of the source can be determined with a better precision when the scatter detector is placed close to the source.

### 3.3.1 Effect of the Detector Orientation



The orientation of the detectors plays an important role in terms of the efficiency and the variation of the angular uncertainty due to the geometry as a function of the scattering angle. As discussed in the previous section, the scattering angle at which the angular uncertainty is minimized is different for different orientations. The cross section for Compton scattering in the first detector is a function of the scattering angle as shown in Fig. 2.5. Therefore, the number of photons hitting the absorption detector also changes with the orientation of this detector.

Three different orientations for the absorption detector are considered to study the influence of the orientation in the efficiency and the behaviour of the angular uncertainty. These different orientations were chosen based on the existing Anger camera systems. Type A describes a planar  $\gamma$  detector of diameter 40 cm, placed 20 cm from the electron detector. Type B and C both consist of two  $20 \times 20$  cm<sup>2</sup> detectors, which are symmetrically placed with respect to the normal vector of the electron detector at a distance of 20 cm. The first detector is placed 10 cm away from the on-axis point source. First the angular coverage of all three types of detectors was studied. Fig. 3.10(a) shows the fraction of the scattered photons that hit the gamma detector after leaving the silicon detector of 1.75 cm diameter for incoming photons of 661.7 keV energy. The main concern with Type A and Type C is the fact that



(a) Scattered photon efficiency of the photon detector for A, B and C type of configurations of the photon detector for  $E_\gamma=661.7$  keV

(b)  $\Delta\theta_g$  vs  $\theta$  for A,B and C type of configurations of the photon detector

**Fig. 3.10:** Angular coverage of the scattered photons for different orientations of the photon detector and the angular uncertainty due to geometry for these orientations

they cover an angular region where also the photons that do not interact in the silicon detector fall into. This causes much higher rate in the second detector due to such direct hits and a resulting higher false coincidence rate. Type B has the advantage of covering the angular range with high scattering rate, but not the angular range, where most of the unscattered photons from the object are expected. In this configuration, the false coincidence rate can be considerably reduced.

The angular uncertainty due to geometric factors as a function of the scattering angle shows a different behaviour for each type of configurations of the photon detector due to the fact that the angle between the normal vectors of the two detectors varies for each configuration. This is demonstrated in Fig. 3.10(b) where the angular uncertainty due to the geometry is plotted as a function of the Compton scattering angle for A,B and C type of configurations. The minimum angular uncertainty is achieved at different scattering angle for each configuration. The angular uncertainty for configuration B is lower than for A due to the fact that the thickness of the first detector is much smaller than the spatial resolution for the system considered and this results in a lower uncertainty for larger  $\alpha$ . Besides, the scattered photons entering perpendicular to the surface of the second detector are less energetic for the configuration B compared to the configuration A, therefore the contribution of the depth of interaction is smaller which results in a smaller uncertainty. For the orientation of the photon detector, one needs to find an optimum configuration by considering a large angular coverage of the scattered photons where the geometric contribution to the angular uncertainty is low. A planar gamma camera with a motor system that makes it adjustable to any of these configurations was chosen for this work in order to be able to optimize the system in terms of this geometric factor.

### 3.3.2 Optimization of the Thickness of the Electron Detector

The thickness of the electron detector is a critical parameter since a thin detector is favorable for single Compton events but at the same time it should be thick enough to capture the recoil electrons. The probability for full  $e^-$  containment increases with the thickness, which is essential for the precise mea-

surement of the energy of the recoil electron. Monte Carlo simulations were performed to examine the effect of the thickness on the reconstruction efficiency. The following parameters have an impact on the efficiency [Dog94]:

- $f_{SC}$  : the fraction of single Compton events followed by the escape of the scattered photon
- $P_{EC}$  : the probability of the recoil electron being captured in the scatter detector

The product of these two factors corresponds to a single Compton scattering with full containment of the recoil electron. For various detector thicknesses, the fraction of single Compton events, the fraction of those events in which the recoil electron is absorbed and the product  $f_{SC}P_{EC}$  were recorded. All possible photon interactions including the elastic scattering are taken into account and the cross sections for these events are obtained from the XCOM database. Fig. 3.11 shows that the fraction of the single Compton events decreases with the increasing thickness and the probability for the capture of the recoil electron increases with the thickness, as expected. The product of these two factors shows a shallow maximum around 4.5 mm of silicon detector thickness for  $E_\gamma = 661.7$  keV. This result suggests the optimum thickness of the electron detector in terms of single Compton events followed by the capture of the recoil electron to be approximately around 4.5 mm for silicon. The source is a point-like source which emits photons that are not only normally incident to the electron detector but are incident to the detector in all directions. When the same simulation is performed for normally incident photons, the peak position remains unchanged.

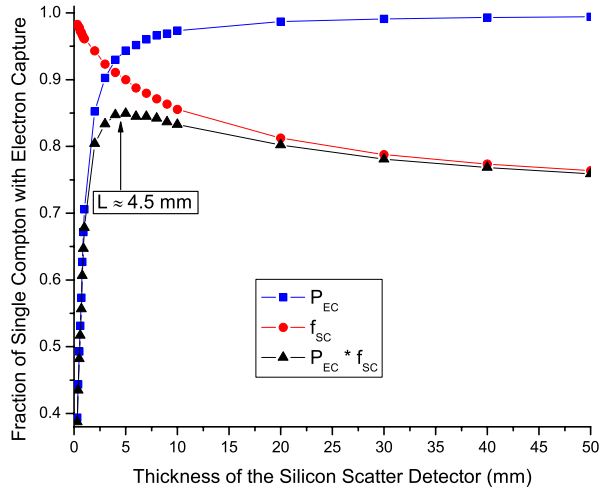


**Fig. 3.11:** Results from Monte Carlo simulations showing the fraction of single Compton events followed by an escape of the scattered photon,  $f_{SC}$ , the fraction of these events in which the recoil electron is captured in silicon,  $P_{EC}$  and their product for 661.7 keV photons hitting the electron detector in all directions

The simulation result shown in Fig. 3.11 only considers the efficiency in the scatter detector; namely the fraction of events which are single Compton scattering followed by the full containment of the recoil electron. For the overall system efficiency, the absorption detector's contribution should also be taken into consideration. The simulation was performed for 1M events emitted from the  $^{137}\text{Cs}$  source which is collimated such that all the photons hit the scatter detector. The scatter detector is a silicon detector with a size of 1.75 cm. 1.5 cm thick 19.5 cm large NaI(Tl) absorption detector is placed 20 cm away from the first detector and its normal vector is taken to be parallel to the normal vector of the scatter detector, in other words the two detectors are parallel planar detectors. The fraction of the single Compton events with full electron capture in the first detector followed by the photoelectric absorption of the scattered photon in the second detector was calculated. In addition, for the same events in the scatter detector, all

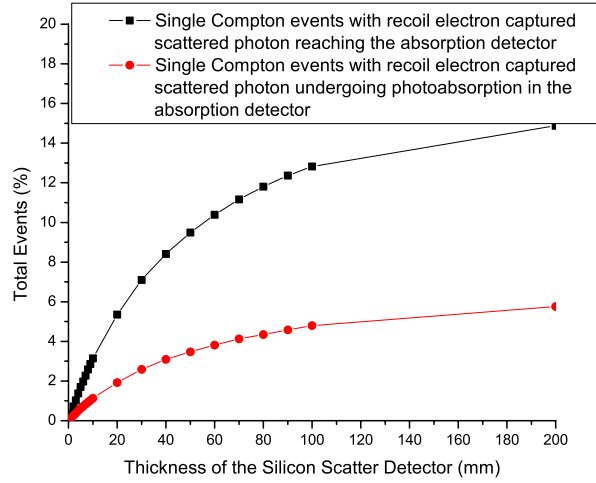


**Fig. 3.12:** Results from Monte Carlo simulations showing the fraction of single Compton events with full containment of the electron energy in Si followed by: *i*) the scattered detector reaching the absorption detector, *ii*) a photoabsorption of the scattered photon in the absorption detector for 662 keV gamma rays and 1.5 cm thick 19.5 cm large NaI(Tl) absorption detector placed 20 cm away from the silicon detector which is 1.75 cm in size

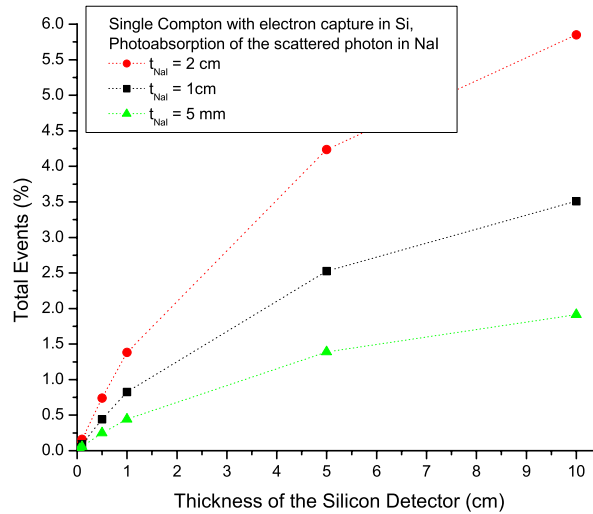


**Fig. 3.13:** The fraction of single Compton events with full containment of the electron energy in Si followed by a photoabsorption of the scattered photon in the absorption detector for 662 keV gamma rays as a function of the thickness of the 1.75 cm large Si detector for different thicknesses of the NaI detector which has a diameter of 19.5 cm

scattered photons hitting the absorption detector were also considered. The result is shown in Fig. 3.12 for various thickness values of the silicon detector. The efficiency in both plots increases with increasing thickness of the scatter detector and reaches a value where the saturation occurs due to the fact that above certain thickness almost all the incoming photons undergo an interaction in the silicon detector which results in the saturation of the fraction of single Compton events followed by the electron capture.

This plot suggests that the first detector should be at least few cm thick to have a reasonable efficiency. The difference between the previous result of 4.5 mm optimum thickness is due to the fact that in this configuration only a certain range of scattering angles is covered by the second detector, however, in Fig. 3.11 the whole range of scattering angles is considered which would be the case with a second detector of  $4\pi$  coverage. With such an absorption detector covering the whole range of scattering, the efficiency would increase by a factor of 7 compared to the planar absorption detector considered in Fig. 3.12.

On the other hand, the absorption detector can also be made thicker to increase this efficiency as shown in Fig. 3.13. However, increasing the thickness of the absorption detector would impose a larger contribution to the angular uncertainty unless a detector with good depth of resolution capability is considered. Therefore, one needs to find a compromise considering opposing trends and constraints in designing the Compton camera system.

### 3.4 Overall Angular Uncertainty

Individual contributions to the angular uncertainty should be combined to estimate the total angular uncertainty. If all the components were Gaussian in nature, then the total angular uncertainty could be written as follows:

$$\Delta\theta_{total1} = \sqrt{\Delta\theta_D^2 + \Delta\theta_E^2 + \Delta\theta_g^2} \quad (3.13)$$

but as discussed in 3.1, Doppler profiles are not Gaussian in nature. To overcome this problem, Doppler broadening and the energy resolution can be summed and quadratically added to the geometric factor as follows:

$$\Delta\theta_{total2} = \sqrt{(\Delta\theta_D + \Delta\theta_E)^2 + \Delta\theta_g^2} \quad (3.14)$$

A better estimate of the total angular spread can be obtained by averaging the two results as shown in [LeB99a]:

$$\Delta\theta = \frac{1}{2}(\Delta\theta_{total1} + \Delta\theta_{total2}) \quad (3.15)$$

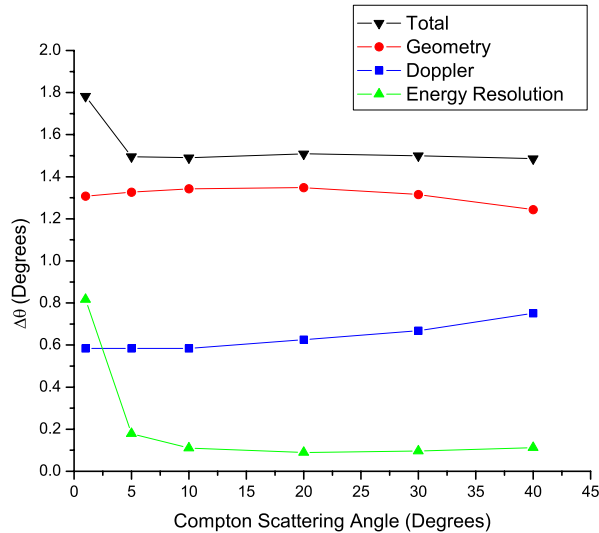


**Fig. 3.14:** Total angular uncertainty estimated for a system shown in Fig. 7.1(a) having a Si scatter detector with  $200 \mu\text{m}$  position and  $300 \mu\text{m}$  depth of interaction resolutions and 25 electrons rms ENC placed 2 cm away from the  $^{137}\text{Cs}$  source and 5 cm away from the Si(Li) detector which has a position resolution of 1 mm and a depth information for parallax suppression 1 mm as well.

The total angular uncertainty estimated for the planned future system defined in 7.2 is plotted as a function of the scattering angle in Fig. 3.14 where the central modules of the two detectors are considered. The scatter detector is a controlled drift detector [Cas04a] with an ENC of 25 electrons rms and the energy of the incoming photon is 661.7 keV. The absorption detector is a newly developed thick Si(Li) detector [Pro04] with a double-sided strip readout. For this system, the geometric uncertainty is more dominant factor than other factors in this angular range.

The spatial spread in the measurement of the source location can be written as:

$$\Delta x = D_1 \tan(\Delta\theta) \quad (3.16)$$

which is about 540  $\mu\text{m}$  in average in the forward scattering region for the system considered in Fig. 3.14. There are several parameters which can be improved to get much better result. The Doppler broadening imposes a lower limit in the achievable resolution. 25 electrons rms energy resolution of the silicon drift detector is an excellent performance compared to other available detectors. Therefore, the geometric factors can be improved further in a way that better spatial resolution and depth of interaction resolution in both detectors are achieved. Other parameters such as the distance between the source and the first detector and the inter-detector distance are parameters which can be relatively easily modified.



## 4. Description and Characterization of the Compton Camera System

A Compton camera system was designed and constructed to study the imaging performance of such a system. The system consists of a radioactive source, a scatter detector and a planar absorption detector. Custom designed frontend electronics for the first detector and a custom designed data acquisition system for both detectors were used to readout the data. The conceptual design of the system is shown in Fig. 4.1. Photons emitted from a collimated  $^{137}\text{Cs}$  source irradiate the scatter detector. A silicon drift detector

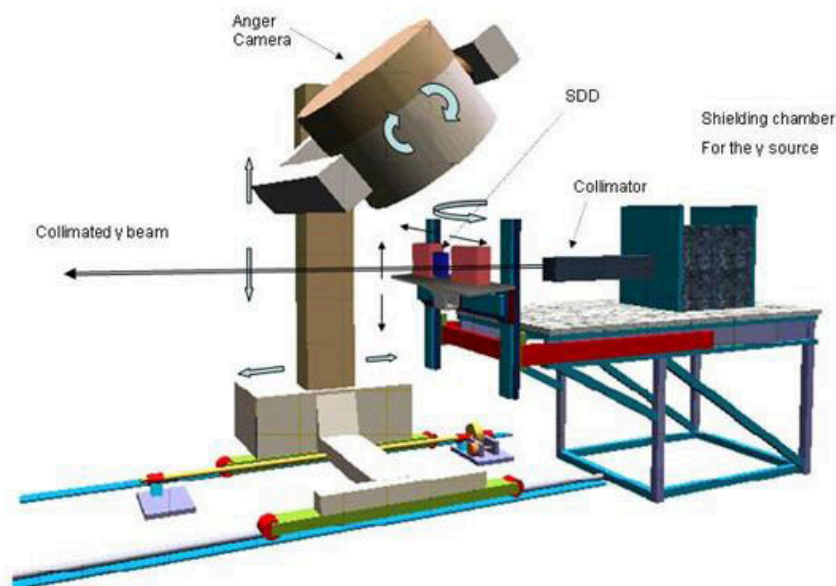


**Fig. 4.1:** Conceptual design of the Compton camera test setup

with on-chip electronics was chosen as a scatter detector due to its excellent energy resolution. An Anger camera without its collimator is used as an absorption detector considering its large angular coverage and relatively quick availability. In this chapter, it is aimed to introduce each of these components with necessary technical details.

### 4.1 Choice of the Radioisotope for Compton Camera Imaging

Nuclear medicine uses radiation to provide diagnostic information about the functioning of person's specific organs, or to treat them. In nuclear diagnostic examinations, patients are injected with a small dose of a radiopharmaceutical, which concentrates in certain tissues or organs after being distributed

by the blood. There are certain characteristics of radionuclides that make them appropriate for nuclear medicine imaging, such as:

- a suitable physical half-life: short half-life decreases the absorbed dose
- decay via photon emission: preferably no beta emission to minimize the dose
- photon energy high enough to penetrate the body

The most common radionuclide of diagnostic imaging is  $^{99m}\text{Tc}$  which is used in more than 90% of nuclear medicine studies. It has a physical half-life of 6.02 hours and emits 140.5 keV gamma rays. Main application fields of this radioisotope include brain, heart, liver (gastroenterology), lungs, bones, thyroid, and kidney imaging, regional cerebral blood flow, equine nuclear imaging, antibodies, red blood cells, replacement for  $^{201}\text{Tl}$ . Other radioisotopes in common use in nuclear medicine and their main application fields [NMR] include (energy and half-life data obtained from [LBL]):

$\implies$   $^{123}\text{I}$ :  $E_\gamma = 158.97$  (83 %) and  $528.96$  (1.39 %) keV,  $t_{1/2} = 13.27$  h.

Brain, thyroid, kidney, and myocardial imaging, cerebral blood flow (ideal for imaging), neurological disease (Alzheimer's).

$\implies$   $^{111}\text{In}$ :  $E_\gamma = 171.28$  (90 %) and  $245.39$  (94 %) keV,  $t_{1/2} = 2.81$  d.

Detection of heart transplant rejection, imaging of abdominal infections, antibody labeling cellular immunology, used with  $^{67}\text{Ga}$  for soft tissue infection detection and osteomyelitis detection, concentrates in liver, kidneys, high specific activity, white blood cell imaging, cellular dosimetry, myocardial scans, treatment of leukemia, imaging tumors.

$\implies$   $^{67}\text{Ga}$ :  $E_\gamma = 93.31$  (39.2 %),  $184.58$  (21.2 %),  $300.22$  (16.8 %),  $393.53$  (4.68 %) keV,  $t_{1/2} = 3.26$  d.

Imaging of abdominal infections, detect Hodgkins/non-Hodgkins lymphoma, used with  $^{111}\text{In}$  for soft tissue infections and osteomyelitis detection, evaluate sarcoidosis and other granulomatous diseases, particularly in lungs and mediastinum.

$\implies$   $^{201}\text{Tl}$ :  $E_\gamma = 135.34$  (2.56 %),  $167.43$  (10 %) keV and a characteristic X-ray at  $\approx 80$  keV,  $t_{1/2} = 3.04$  d.

Clinical cardiology, heart imaging, less desirable nuclear characteristics than  $^{99m}\text{Tc}$  for planar and SPECT imaging, myocardial perfusion, cellular dosimetry.

The energies of useful radionuclides for SPECT applications are restricted to at most a few hundred keV due to the fact that higher energies penetrate the collimator septa of the Anger camera which has a limited thickness. However, for Compton camera applications higher energetic radionuclides are not only usable but also required for improving the position resolution. Some high energy gamma emitting radionuclides of biological interest proposed for Compton camera applications are listed in Tab. 4.1. Among these radionuclides  $^{137m}\text{Ba}$  and  $^{113m}\text{In}$  are distinct in a sense that they do not emit any beta particles.  $^{113m}\text{In}$  was already used mainly in the period from 1966 to 1977 for many different purposes such as placenta scanning, lung perfusion scintigraphy, imaging of liver, bone, heart, thyroid, brain, kidney [Con01].

For the laboratory tests of the system, a radioisotope having a long half-life is needed so that during many years of research there is enough radioactivity available which is crucial for collecting enough Compton coincidence statistics and for keeping the costs as low as possible. In fact, this was proved to be useful by using the same  $^{137}\text{Cs}$  source that was bought in 1983 for the previous Compton camera project in our detector group.  $^{137}\text{Cs}$  source emits gamma-rays of 661.7 keV energy (Appendix C.1) which is suitably high to explore the advantageous of the Compton camera imaging. At this energy 99.4 % of the gamma interactions occurring in silicon are Compton scattering (Fig. 2.6) and the mean angular uncertainty due to Doppler broadening in the forward scattering region is only  $0.83^\circ$  (Fig. 3.5). Therefore, with a good choice of detectors it is in principle possible to achieve an angular resolution below  $1^\circ$  and a reasonable efficiency at this energy.

Element	Gamma-ray Energy (MeV)	Abundance (%)	Half-life
<sup>28</sup> Mg	0.0306	95	20.91 h
	0.4006	36.6	
	0.9417	38.3	
	1.3423	52.6	
<sup>43</sup> K	0.3728	87	22.3 h
	0.3969	11.85	
	0.5934	11.26	
	0.6175	79.2	
<sup>113m</sup> In	0.3917	64.2	1.66 h
<sup>85</sup> Sr	0.5140	96	64.84 d
<sup>74</sup> As	0.5958	59.3	17.77 d
	0.6348	15.4	
<sup>137m</sup> Ba	0.6617	90.11	2.55 m
<sup>52</sup> Mn	0.7442	90.0	5.59 d
	0.9355	94.5	
	1.4341	100	
<sup>58</sup> Co	0.8108	99	70.86 d
<sup>59</sup> Fe	1.0992	56.5	44.50 d
	1.2916	43.2	
<sup>65</sup> Zn	1.1155	50.60	244.26 d
<sup>47</sup> Ca	1.2971	71	4.54 d
<sup>24</sup> Na	1.3686	100	14.96 h
	2.7540	99.94	
<sup>42</sup> K	1.5247	18	12.36 h

Tab. 4.1: High energy gamma emitting radionuclides of biological interest [Bri04]

The <sup>137</sup>Cs source in the form of a 7.1 mm high ceramic cylinder of 5.5 mm diameter is placed in a stainless steel capsule. Its activity was 48.1 GBq (1.3 Ci) in 1983, its current activity can be estimated as follows:

$$A = A_0 e^{-\lambda t} = 48.1 e^{-(0.693 \cdot 21/30.07)} = 29.6 \text{ GBq (0.8 Ci)} \quad (4.1)$$

where A is the current activity, A<sub>0</sub> is the initial activity, t is the time interval since the source strength was calibrated, λ is the decay constant which is equal to ln 2/t<sub>1/2</sub> and t<sub>1/2</sub> = 30.07 years for this source.

The number of photons emitted by the source per second can be found using:

$$N = A \cdot BR \cdot BF \quad (4.2)$$

where BR is the branching ratio for the emission of the energy of interest, which is equal to 0.944 for 661.7 keV energy, BF is the branching fraction for the considered mode of decay and it is 0.9011 for this decay mode. 1 Ci of activity corresponds to  $3.7 \cdot 10^{10}$  disintegrations per second and substituting these values in the equation gives  $2.5 \cdot 10^{10}$  photons of 661.7 keV per second. In order to shield this radiation and to obtain a beam which is azimuthally symmetric, the <sup>137</sup>Cs source is placed in a lead setup (Fig. 4.2) that was built during the previous Compton camera project [Geb90]. In order to reduce the background radiation caused by photons scattered from the wall, a beam catcher made of 40 cm thick beton having a lead cylinder with a hole in the center (to reduce the scattering) was placed such that the direct beam enters this hole before reaching the wall. With all these radiation protection precautions, the radiation in the laboratory was measured not to exceed the natural background radiation.

To determine the beam intensity after the collimation, the angular deviation of the beam profile should be measured. NaI(Tl) detector which is placed 2.1 m away from the beam with a 1 mm wide slit collimator in front was used for this measurement. The beam profile obtained by moving the slit collimator resulted in a Gaussian distribution with a standard deviation of 0.18° (Fig. 4.3). The measurement was repeated for different configurations such as 400 μm wide slit collimator scanning the detector, a lead block scanning

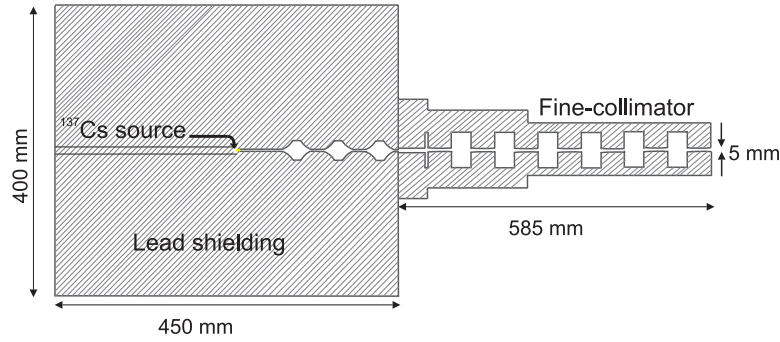


Fig. 4.2: Lead setup used to shield and collimate the  $^{137}\text{Cs}$  source

the detector, a lead block moving in front of the beam and also by performing the measurements with a silicon drift detector. All these measurements resulted in an angular deviation of the beam which agree with the  $\sigma$  value of approximately  $0.18^\circ$ . The intensity of the beam after the collimation can now be calculated using the following relation [Geb90]:

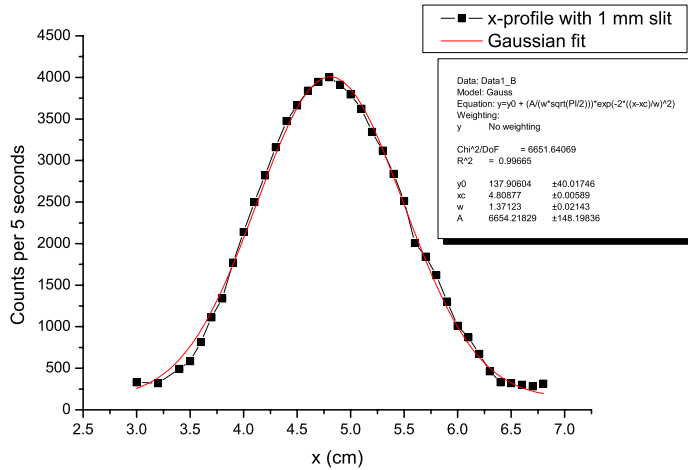


Fig. 4.3: Beam profile measured using a NaI detector which was 2.1 m away from the beam with a 1 mm wide slit collimator moving in front of it

$$I = N \frac{2\pi\sigma^2}{4\pi} \quad (4.3)$$

which results in approximately 120000 counts per second from the collimated beam.

## 4.2 Scatter Detector: Silicon Drift Detector

A monolithic array of 19 channel Silicon Drift Detectors (SDDs) with integrated electronics has been chosen as the scatter detector of the Compton camera system. Before the characterization of this detector, it is useful to explore the SDD with a special attention on this type of SDD which has its first stage amplification implemented directly on the detector chip.

### 4.2.1 Principle of Operation

Semiconductor drift detector was invented by Emilio Gatti and Pavel Rehak in 1983 [Gat84b]. Their invention resulted from the application of the new charge transport scheme where the electric field responsible for the charge transport was independent of the depletion field in a fully depleted semiconductor detector [Gat84a]. A full depletion of a thin, large silicon wafer was achieved through a small  $n^+$  contact at the

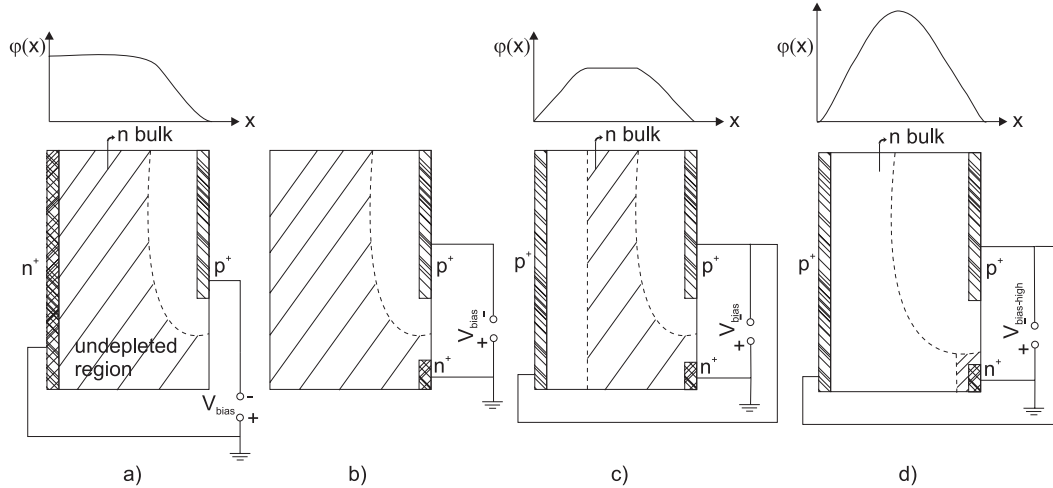


**Fig. 4.4:** a) partially depleted diode, b) diode with a side depletion, c) partially depleted double diode, d) fully depleted double diode [Lut99]

edge of the wafer which is positively biased with respect to the  $p^+$  contacts covering both surfaces of the wafer. In a conventional diode the ohmic  $n^+$  and  $p^+$  contacts had been realized to extend over the full area of each side of the wafer as shown in Fig. 4.4a). In fact, the ohmic  $n^+$  contact can be placed anywhere on the undepleted bulk of the wafer (Fig. 4.4b)). If one considers a double diode as shown in Fig. 4.4c), at small voltages applied to the electrodes two space-charge regions with an undepleted bulk in the middle occurs. At higher voltages (Fig. 4.4d)), depleted regions extend further such that the conductive undepleted region separating them almost disappears, it only covers the region around the  $n^+$  electrode. This is electrostatically equivalent to having a single diode which is twice as thick with  $p^+n$  junctions at two sides of the wafer and an  $n^+$  electrode at the edge. The retraction of the conductive channel at the depletion voltage results in an abrupt drop of the capacitance. The potential distribution changes with increasing the bias voltage such that a potential valley is formed. The potential energy has a parabolic shape; with an electron potential minimum in the middle of the wafer. The width of the depletion region can be approximated for the acceptor concentration being much larger than the donor concentration ( $N_A \gg N_D$ ) as follows:

$$w_d = \sqrt{\frac{2\epsilon_0\epsilon V_{bias}}{qN_D}} \quad (4.4)$$

where  $\epsilon_0 = 8.85 \cdot 10^{-14}$  F/cm is the free-space permittivity,  $\epsilon$  is the dielectric constant which is equal to 11.9 for silicon,  $V_{bias}$  is the bias voltage and  $N_D$  is typically around  $10^{12}$  cm $^{-3}$ . Therefore, to fully deplete a 300  $\mu$ m thick wafer, the bias voltage should be around -70 V. With the sideward depletion, the depletion is performed from both sides and the bias voltage required to deplete the whole wafer is four times lower than the voltage needed to deplete it from one side only as in the simple diode.

Silicon drift detector was constructed based on the principle of sideward depletion, with an additional electric field component applied parallel to the surface of the wafer that forces the electrons to drift in the valley towards the  $n^+$  electrode (anode), while the holes drift towards the  $p^+$  electrodes, as shown in Fig. 4.5. This is achieved by implantation of a strip array of  $p^+n$  junction on both surfaces with an additional potential gradient which is adjusted such that the anode has the highest positive potential, therefore collecting all the electrons accumulated in the local minimum of the potential valley.

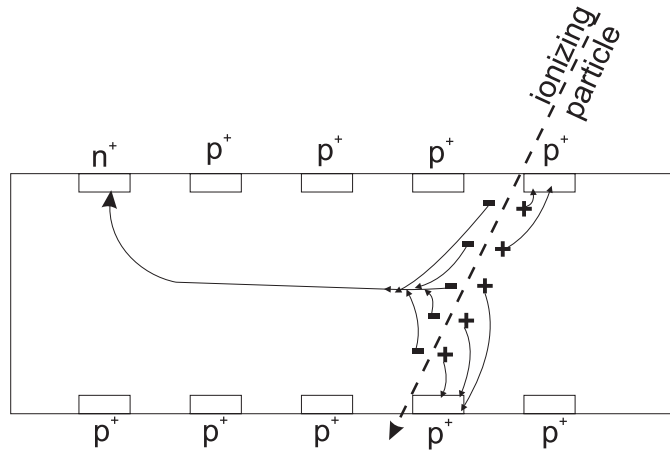


**Fig. 4.5:** Side view of the silicon drift chamber. Both surfaces are covered by a strip array of  $p^+$  junction electrodes, which provides the depletion and the lateral drift field. The  $p^+$  electrodes are biased such that the potential minimum for the electrons is located in the middle of the wafer. A voltage gradient between the strips creates an additional field which is parallel to the surface of the wafer. Electrons created by the passage of a charged particle drift to the  $n^+$  readout anode, while holes move to the  $p^+$  electrodes.

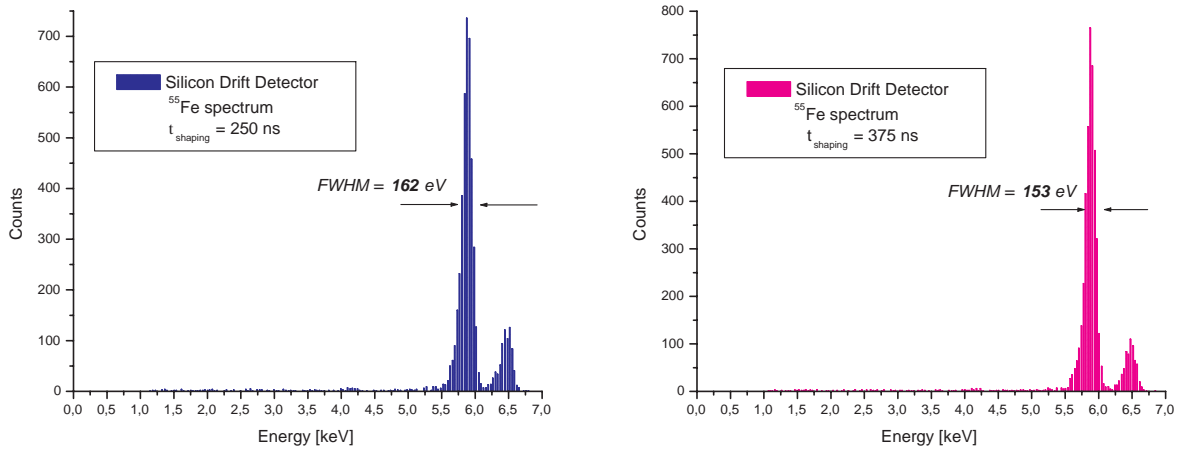
The signal at the anode of the silicon drift detector is induced only when electrons approach close to the anode. As in the gas drift chamber, the drift time of electrons within the wafer determined from the time delay between the passage of a fast particle and the signal appearance at the anode can be used for position measurements. It is also possible to achieve two-dimensional position measurements by dividing the anode into small pads. In this way, the same position resolution as a very fine microstrip silicon detector is achieved but with much less readout channels.

To achieve a good energy resolution, it is necessary to reduce the leakage current and the capacitance of a detector. By the introduction of improved technologies such as planar process using high purity silicon wafers [Kem80], the leakage current could be decreased considerably and the typical value with the current technology is around  $1 \text{ nA/cm}^2$ . The capacitance of the silicon detector depends on the device architecture and in conventional diodes it is strongly dependent on the sensitive area such that to decrease the capacitance either the sensitive area should be made small or the thickness of it should be increased. However, the readout capacitance of the silicon drift detector is decoupled from the sensitive area. Therefore with the invention of the silicon drift detector, significant reduction in the detector capacitance could be observed compared to other existing detectors [Kem87].

#### 4.2.2 SDD with on-chip Electronics

To take the full advantage of the low readout capacitance, new type of silicon drift detector with integrated on-chip first stage amplification was designed [Lec96]. In the standard silicon diode the  $n^+$  readout electrode is connected to the front-end electronics via bond wires. In this way, it is difficult to obtain a match between the anode capacitance and the input capacitance of the preamplification. Besides, the connection between the anode and the preamplifier adds a considerable stray capacitance to the system. This problem could be overcome by integrating the first transistor of the preamplifier directly on the detector chip in a source follower configuration. With this configuration, it is not only possible to reach high energy resolution (Fig. 4.6) as a result of the negligible stray capacitance but also to process the signals at a shorter time because of the reduced rise time of the signals. The section of a cylindrical silicon drift detector with integrated n-channel junction field effect transistor (JFET) is shown in Fig. 4.7.

The n-type high resistivity ( $\sim 2 \text{ k}\Omega \text{ cm}$ ) silicon wafer is fully depleted by  $p^+$  electrodes and  $p^+$  back contact reverse biased with respect to the n substrate. The radiation enters from the non-structured homogeneous  $p^+$  junction on the back side which is obtained by making a shallow Boron implantation of



(a)  $^{55}\text{Fe}$  spectrum obtained with a shaping time of 250 ns

(b)  $^{55}\text{Fe}$  spectrum obtained with a shaping time of 375 ns

**Fig. 4.6:**  $^{55}\text{Fe}$  spectrum obtained with a commercial single cell SDD at different shaping times. The detector chip is cooled down to about  $-10\text{ }^\circ\text{C}$  and the detector is in a TO8 package mounted on a bias and readout board produced by KETEK. Amptek A250 preamplifier is utilized on the readout board whose output is connected to an external NIM shaper (TC244). The data acquisition was performed with a TDS220 digital oscilloscope's GPIB interface.

10 to 50 nm depth. The  $\text{p}^+$  rings on the other side are the field electrodes which are biased with increasing negative voltage from the inner ring to the outermost one. The biasing of the field electrodes is established through integrated voltage divider which is formed by p-channel enhancement mode MOSFETs [Lec93]. The integrated voltage driver in fact consists of MOS diodes covering the gaps between the  $\text{p}^+$  rings with the aluminum connected to the next ring. With this configuration, each of them can be considered as an enhancement mode MOSFET whose gate is shorted with its drain. Enhancement mode MOSFET acts as a switch such that at zero gate voltage there exist no charge carriers and increasing the voltage causes the flow of charge carriers from source to drain. In this way, only the first and the last of the 18 rings need to be biased to apply the voltage to all the rings. When the potential difference between the first and the last ring exceeds the threshold voltage of the MOS diodes times the number of diodes, all the

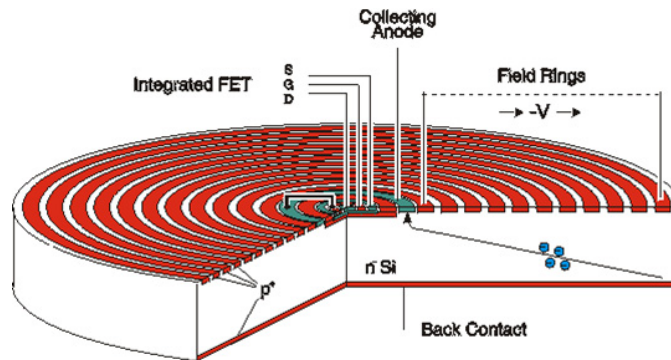


**Fig. 4.7:** Sectional view of the cylindrical silicon drift detector with on-chip transistor

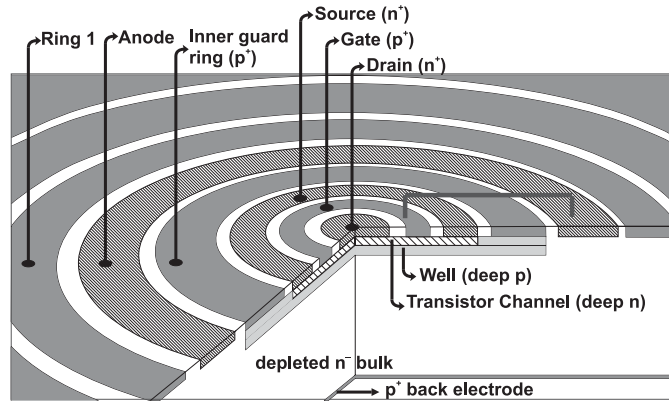


**Fig. 4.8:** Central region of the SDD where the integrated single-sided n-channel JFET and the anode are located. The deep p implantation, biased through the inner guard ring, separates the transistor region from the detector bulk. Scarce hatching refers to lightly doped n regions, while more dense hatching is used for heavily doped n regions. Similarly heavily p doped regions are shown as dark gray and the lightly p doped regions are filled with light gray.

transistors are switched on. With the flow of holes from the inner to the outer rings, the bias voltage of each ring is supplied in a controllable manner. The field electrodes are biased such that the inner ring has the least negative potential ( $V_{R1} \approx -5$  V) and the outermost ring has the most negative potential ( $V_{R18} \approx -90$  V) whose magnitudes are subject to variations from one chip to another. The anode is an  $n^+$  implantation in the form of a ring located at the center. The potential energy for electrons fall from the edge of the backside to the anode. Therefore, electrons created in the detector volume drift to the anode with a drift velocity of 1 to 10  $\mu\text{m}/\text{ns}$  while holes drift to the  $p^+$  regions.

The integrated transistor shown in more detail in Fig. 4.8 is a non-conventional single sided n-channel JFET. The transistor channel is made by a deep phosphorus implantation and a circular deep p implantation biased through an inner guard ring (IGR) separates the transistor from the bulk. The  $p^+$  gate of the JFET is directly coupled to the anode by an aluminum strip. The signal and leakage electrons arriving at the anode lower the anode potential. As a result the gate potential is also lowered and this change is followed by the source. The drain of the JFET is kept at a constant positive potential ( $V_D \approx 10$  V), therefore lowered anode potential causes an increased drain-gate voltage difference. The negative voltage appearing at the  $p^+$  gate reversely biases the junction, thus depleting the transistor channel which results in a current drop through the transistor which can be measured. As more electrons arrive at the anode, the gate becomes more reverse biased compared to the channel. At some point, the gate discharges by a breakdown of the gate-channel junction. With this process, the reset mechanism of the detector is established automatically without any need for an external reset.

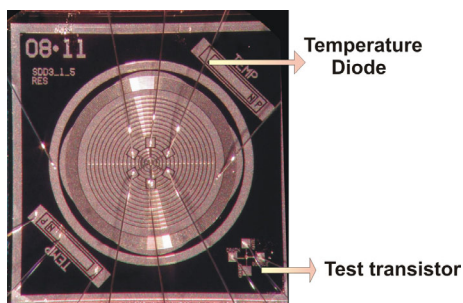


**Fig. 4.9:** 1 cell cylindrical SDD

It is necessary to know the characteristics of this on-chip JFET, not only for the proper operation of the detector but also for electrical simulations of it. However, to measure the transistor characteristics, it is not possible to use the on-chip transistor since there is no access to the gate of this transistor due to its direct coupling to the anode. Cylindrical single cell silicon drift detectors (Appendix C.2) produced by the Max-Planck-Institute Semiconductor Laboratory (MPG HLL) include a JFET located at the corner of the detector chip which has the same characteristics as the one integrated on the detector area as shown in Fig. 4.9. This test transistor is bonded to the support ceramic for the measurement of the transistor characteristics. The inner guard ring of the transistor was biased by -15 V in

order to obtain the same operating conditions as the integrated JFET. The drain-source current as a

function of drain-source voltage for constant gate-source voltages is shown in Fig. 4.10(a).

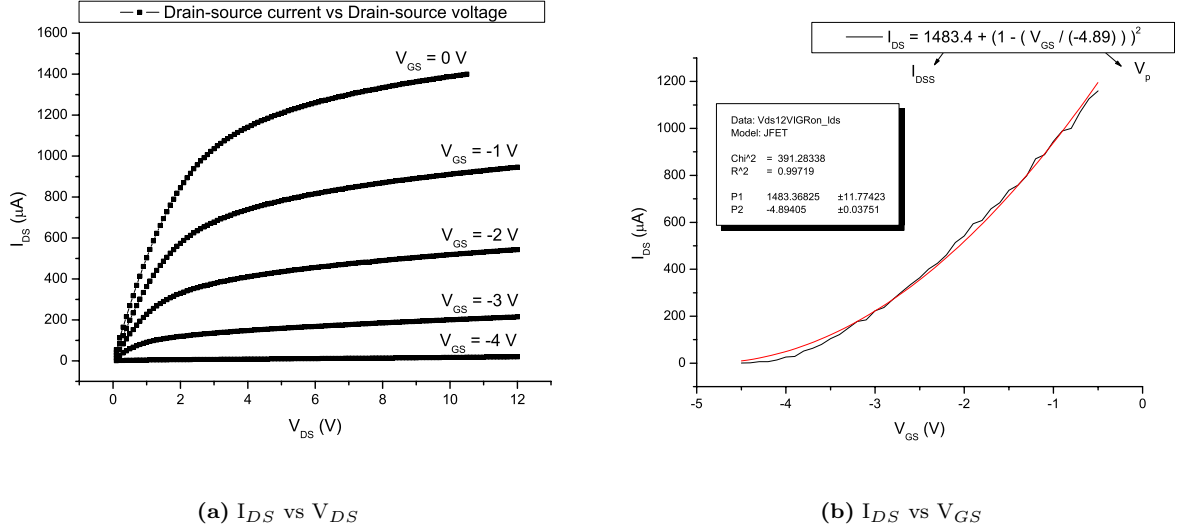


**Fig. 4.10:** Characteristic curves for the on-chip JFET at room temperature: (a) Drain-source current as a function of the drain-source voltage for constant values of the gate-source voltage, (b) Experimental data and the fit of the drain-source current versus gate-source voltage for  $V_{DS} = +12$  V using the approximation (4.6)

From the slopes of the linear and saturated regions of Fig. 4.10(a), the drain-source resistance is found to be  $2.3$  k $\Omega$  in the linear region and  $33$  k $\Omega$  in the saturated region. The drain-source current in the linear and the saturated region can be calculated theoretically using the following equations:

$$I_{DS} = I_{DSS} \left[ -2 \left( 1 - \frac{V_{GS}}{V_P} \right) \frac{V_{DS}}{V_P} - \left( \frac{V_{DS}}{V_P} \right)^2 \right] \quad (\text{ohmic region}) \quad (4.5)$$

$$= I_{DSS} \left( 1 - \frac{V_{GS}}{V_P} \right)^2 \quad (\text{saturation region}) \quad (4.6)$$

where  $I_{DSS}$  is the drain saturation current,  $V_P$  is the pinch-off voltage, i.e., the gate-to-drain voltage at which the channel becomes first pinched. At a fixed drain-source voltage of  $12$  V, the drain-source current is measured for various gate-source voltages and the resulting curve is fit using the equation for the saturation region. These fit parameters are then used for determining the variation of the transconductance as a function of the drain-source current. The transconductance of a JFET is defined as:

$$g_m = \left. \frac{\partial I_{DS}}{\partial V_{GS}} \right|_{V_{DS}} = -\frac{2I_{DSS}}{V_P} \left( 1 - \frac{V_{GS}}{V_P} \right) \quad (4.7)$$

and is plotted in Fig. 4.11 as a function of the drain-source current. During the operation of the SDD the source of the JFET is connected to a constant current source which delivers around  $300$   $\mu\text{A}$  current and this corresponds to approximately  $300$   $\mu\text{Siemens}$  of transconductance. These characteristic curves for the JFET are specific to the SDD that we have. The saturation current and pinch-off voltage are larger than typical values [Fio98]. It was reported that there may be fluctuations from one chip to another, depending on the production.

Fig. 4.9 also shows the temperature diodes located at the upper left and the lower right of the detector chip. With the temperature diode, it is possible to monitor the temperature directly on the detector chip which is necessary for the accurate determination of the operating conditions. The detector bulk leakage current doubles in silicon for about every  $7$   $^\circ\text{C}$  increase in temperature and these figures

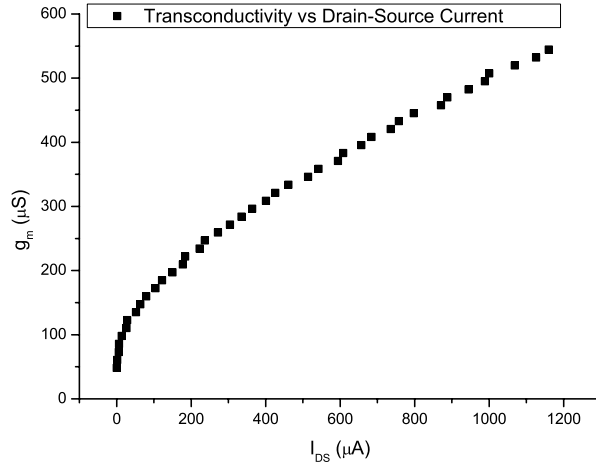


**Fig. 4.11:** The variation of the transconductance of the on-chip JFET with changing drain-source current

show the importance of the exact chip temperature measurement. This measurement is performed by reading the voltage difference of the p and n sides of the diode upon the flow of about  $1 \mu A$  current. The voltage values recorded at few different temperatures can then be used for the calibration of the diode.

### 4.2.3 19-channel Silicon Drift Detector

Silicon drift detectors with on-chip electronics exist in a large variety of topologies and applications. While the cylindrical single cell detector found applications in high-resolution high-count-rate X-ray spectroscopy [Str98], portable EDXRF (Energy Dispersive X-ray Fluorescence) spectroscopy [Fio99a], as scintillation photodetector for gamma-ray spectroscopy [Fio97], the demand for larger area silicon detectors in various applications forced the development of multi-anode SDDs. Monolithic arrays of hexagonal 6, 7, 12, 19, 39 and 61 SDDs have been produced for application fields like gamma-ray spectroscopy [Fio99b] and holography [Han00]. Depending on the experimental requirements, the multicells are arranged in a linear fashion, as a closed ring or like a honeycomb. With this work, a new application field was introduced by using this type of detector in Compton camera imaging.

19-channel SDD consists of a monolithic array of 19 SDDs arranged in an honeycomb structure as shown in Fig. 4.12. The hexagonal geometry of the individual cells minimizes the dead area between them. The area of each unit is  $5 \text{ mm}^2$ , corresponding to a total active area of  $95 \text{ mm}^2$  for the whole detector. The distance between the center of two contiguous cells is about 2.8 mm in the horizontal and 2.4 mm in the vertical directions. Each SDD channel has its own on-chip JFET, therefore there exist 19 signal lines to be readout. A single cell SDD requires several voltages for the operation as shown in Fig. C.2. A multichannel SDD was designed by MPI HLL such that the bonding pads for these voltages of each channel are bonded to common voltage bond rings located in the outer region of the chip. In this way, only the outer voltage rings are supplied with voltages which are then distributed to all channels.

The same type of detector used for scintillator readout [Fio02b] was mounted on two ceramics: one for inner 7 rings and the other for the outer 12 rings. The ceramic for the inner rings overlaps with the detector area which makes this design unsuitable for this work. A new bonding layout designed in the frame of this work was first tested successfully [Hon00] on a dummy silicon chip on which the bonding pads and rings were printed (Appendix C.3.1). There are, however, some constraints in mounting the 19-cell detector which is to be used as a scatter detector of a Compton camera system. In order to avoid scattering through support ceramic, which may contribute to background by being detected at the second detector, the ceramic to which the detector is mounted is designed to surround the chip as shown in Fig. 4.12. In this way, there is no material through which the beam passes before and after hitting

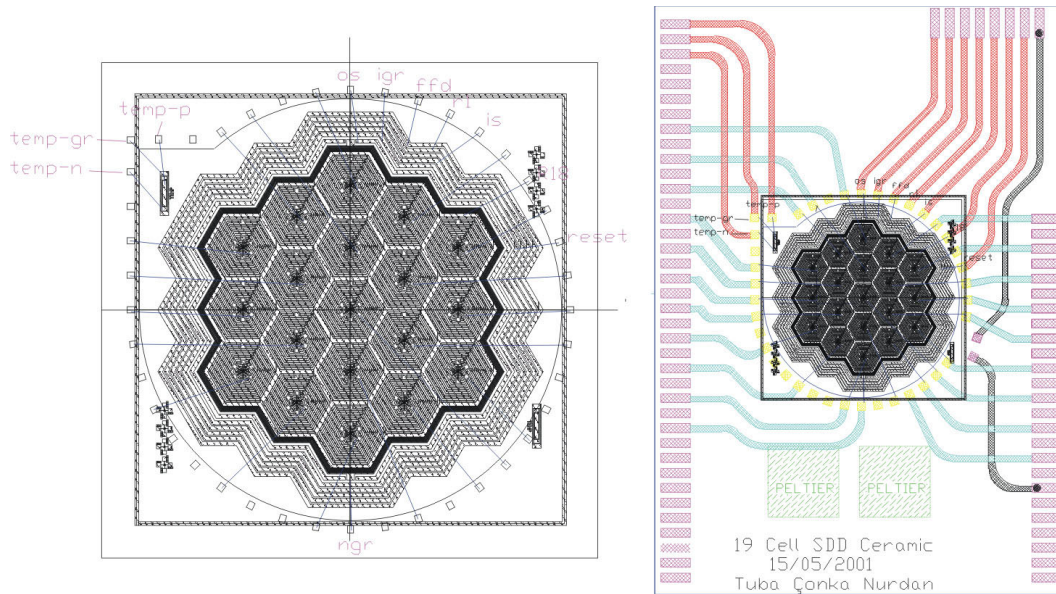


**Fig. 4.12:** The layout of the 19-cell SDD bonded on the support ceramic

the detector chip, except the thin radiation window.

In order to be able to cool the detector chip and to maintain stable temperature during the detector operation, thermoelectric cooler (peltier device) is used. Peltier is a small semiconductor device formed by two metallized ceramic plates and an array of Bismuth Telluride couples (n- and p-type) sandwiched between them. When a DC current is applied heat is moved from one side of the device to the other side, where it must be removed with a heatsink. Although peltiers are not the most efficient devices for cooling, this disadvantage is more than offset by the advantages of no moving parts, no Freon refrigerant, no noise, no vibration, very small size, long life, capability of precision temperature control. Two 8.2x8.2 mm large 2.7 mm high Melcor (Type FC 0.6-31-0.6L / Model: 46290) [AMS] peltiers electrically connected in series are glued with a thermally conductive epoxy to the support ceramic. One large peltier element could also be used instead of two small peltiers in series but this type of peltier was available at KETEK GmbH [KET] where the detector was mounted. The maximum current for these peltiers is about 1.2 A, corresponding to a maximum voltage of 3.75 V and the recommended operating current is around 800 mA. The terminals of the peltiers are connected to the PID (Proportional Integral Derivative) temperature controller unit [Lai04] which control the supply current with the feedback received from the on-chip temperature diode. According to the selected temperature value, the temperature controller unit regulates the current flowing to the peltier elements in such a way as to keep the temperature constant during the measurement, i.e. increases the current when this value is exceeded and decreases it when the temperature is lower than this value.

To fully benefit the cooling performance of the peltier elements, Aluminum Nitride (AlN) was chosen as the ceramic material for detector mounting due to its high thermal conductivity. Aluminum oxide (Alumina) ( $\text{Al}_2\text{O}_3$ ) which is a common material used in detector mounting has a thermal conductivity of 10-35  $\text{W}/\text{m}^\circ\text{K}$  whereas AlN has a thermal conductivity of 170-190  $\text{W}/\text{m}^\circ\text{K}$  and a thermal expansion coefficient that matches to silicon better than other high thermal conductive ceramics like SiC and BeO. The data sheet for the Carborundum Hi-Therm Aluminum Nitride from Saint-Gobain Industrial Ceramics [BSR] used as a support ceramic is given in Appendix C.3.2 together with typical property values of other ceramics for comparison. Detailed simulations and measurements on the thermal performance of the detector carrier ceramic can be found at the master thesis of K. Laihem [Lai04]. The printing of the signal and voltage lines on the AlN was performed with the thick-film hybrid technology at the hybrid laboratory of the detector physics and electronics group. The conducting paths are printed using a gold paste which also wire bonds extremely well with Al wires and for crossovers, the conductor levels in

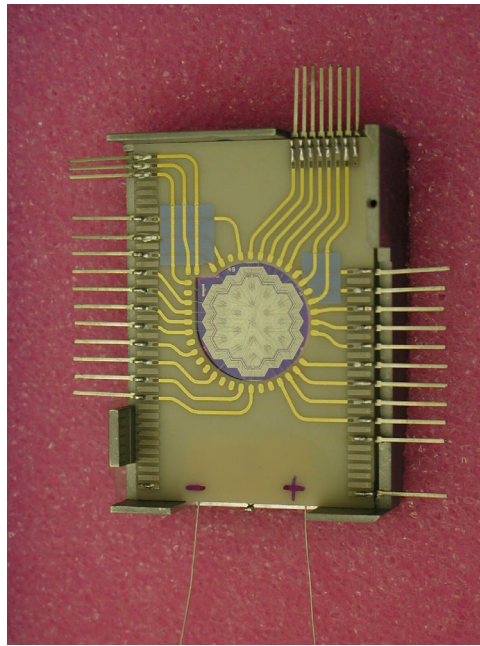


**Fig. 4.13:** 19 cell SDD mounted to the support ceramic where the ceramic substrate is AlN, the conducting paths are printed using Au paste, the pads for soldering are from AgPd and the blue layer is the dielectric material isolating conducting layers from each other.

screen-printed patterns are isolated from each other using the dielectric paste. Unfortunately the paste used for Alumina can not be used for AlN, for this reason special AlN paste designed for applications on AlN substrates was bought [ESL](gold:8835-1B, dielectric:4907). The AlN support ceramic with the 19 cell SDD mounted is shown in Fig. 4.13. The wires seen at the bottom belong to the peltier elements which are glued to the back side of the ceramic. The pins located at the upper right side correspond to the power lines, whereas the signal lines are distributed on the right and the left side of the ceramic. The bonding pad of the back electrode is at the back side of the ceramic and it is carried to the front side via through contact. The information on the dimensions and the pin layout of the ceramic is given in Appendix C.3.2.

The detector ceramic is then connected to the bias PCB (Printed Circuit Board) board which includes the power filter circuit and the first stage of the front-end electronics as shown in its schematics in Appendix C.3.3. While connecting the pins of the ceramic to this PCB, several factors such as additional capacitance this connection contributes to the system and the flexibility in decoupling the ceramic from the PCB should be taken into consideration. When the PCB needs to be modified or replaced by another one, it is important to be able to remove the ceramic easily. Soldering is not a good choice not only for the reason that it is not flexible in this manner, but also soldering the pins to the PCB is not advised in the presence of the detector. Even if the detector is covered for protecting its surface, the glue used in glueing the detector chip to the ceramic may dissolve above 55 °C. Zero-force connector is a flexible solution in terms of the practical way of inserting and removing the connections. However, they are usually quite thick which is not suitable for making the detector housing compact and they add at least few pF's to the total capacitance. Besides, the distance between its pins is 2.54 mm which suits the signal connection but not the power lines which are 1.27 mm apart from each other. Special rubber inter-connectors used for LCD's is a better choice considering all the constraints. GB type conducting rubbers produced by the firm ShinEtsu Polymer [MHW] were chosen for this application. This type of connector has one row of gold-plated brass wires in silicon rubber (Appendix C.3.4) to connect two parallel boards, both having one row of contact pads with a minimum pitch of 0.2 mm. Distance between the parallel boards should be 1 mm minimum and the inter-connector has to be compressed (5-15 %) between the contact surfaces. In this case, the pins of the ceramic acts as one of these boards and the PCB is the second one. Each

gold-plated wire has a diameter of  $30\ \mu\text{m}$  and the pitch is around  $100\ \mu\text{m}$ . Each pin-to-PCB connection is achieved by approximately 10 of these wires which secure the connection. The compression of the rubber is performed using a plexiglass holder placed above the pins.

Several requirements needed to be fulfilled in designing the housing of the scatter detector. First of all, it should be designed such that the material on the path of the incoming and scattered radiation should be minimized. Another requirement concerns effective removal of the heat from the warm side of the peltiers. For this reason, the part of the metal housing was designed to have a contact with the warm side of the peltiers. Since the heat conduction with air ( $k_{air} = 0.025596\ \text{W/m.K}$  at  $20\ ^\circ\text{C}$ ) is not quite sufficient to cool the detector down to negative temperature values, the housing was designed to have a water ( $k_{water} = 0.60475\ \text{W/m.K}$ ) flow inside the metal as shown in Appendix C.3.5. A bucket of water and a cooling kit consisting of a water pump and a radiator are used to obtain the continuous flow of water. In addition to above design considerations, the detector housing should also be gas-tight to be able to flush dry nitrogen (Stickstoff 6.0 with  $>99,9999\ \text{Vol. \%}$  purity from Messer Griesheim [Mes]) regularly. This is necessary to keep the detector in a moisture-free environment to avoid its degradation and also to avoid condensation which may appear when the detector is cooled below the dew point which is about  $18\ ^\circ\text{C}$  at room temperature for 60% humidity. The detector housing designed upon the consideration of all these concerns is shown in Fig. 4.14.

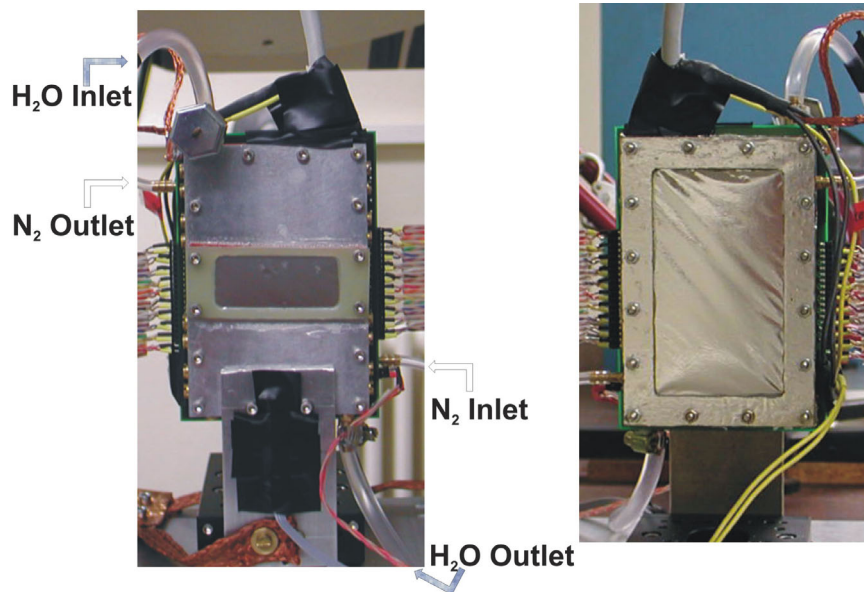


**Fig. 4.14:** The front and the back side of the Al housing for the scatter detector. The bias board is sandwiched between two parts of the Al housing which have O-rings in the inner part. The detailed AutoCAD drawing is given in Appendix C.3.5.

Usually thin Be window is preferred for these detectors to enable soft X-ray detection. However, for such a large area of the detector box, it would be very expensive to get a Be window and anyway the energy range of interest is much higher than soft X-rays.  $8\ \mu\text{m}$  thick pin-hole free Al foil [Goo] is used as a radiation window for both sides of the detector box. X-ray transmission behaviours of  $8\ \mu\text{m}$  thick Be and Al are shown in Appendix C.3.6 for an energy range of  $100\ \text{eV} - 30\ \text{keV}$ .

Last but not the least point concerns the supply of the power for the detector. Several bias voltages needed for the operation of the SDD are supplied from a custom-designed power supply unit whose technical details are given in Appendix C.4. Special sequence has been implemented in switching the detector power on and off [Fio02a] mainly in order to protect the on-chip JFET. The generally accepted rule is to turn on the low voltages first and then the high voltages of the last ring and the back electrode. The reverse order should be followed while turning the power supplies off.

### 4.3 Absorption Detector: Anger Camera

The absorption detector chosen for this Compton camera system is a refurbished Anger camera without a collimator. This choice was made considering the need for a large detector system which can be made available for the Compton camera measurements in a short time and at a reasonable cost.

The camera is a conventional Anger camera consisting of a NaI(Tl) crystal readout by an array of photomultiplier tubes (PMTs). It employs a 15-inch diameter by 3/8-inch thick NaI(Tl) crystal viewed by 37 3-inch diameter PMTs, arranged in hexagonal arrays with the tubes at the points of a hexagon and the first tube at the center. Pulse signals from the PMTs are fed through summing matrix circuits to four output signals called  $x^+$ ,  $x^-$ ,  $y^+$  and  $y^-$  as shown in Fig. 4.15.

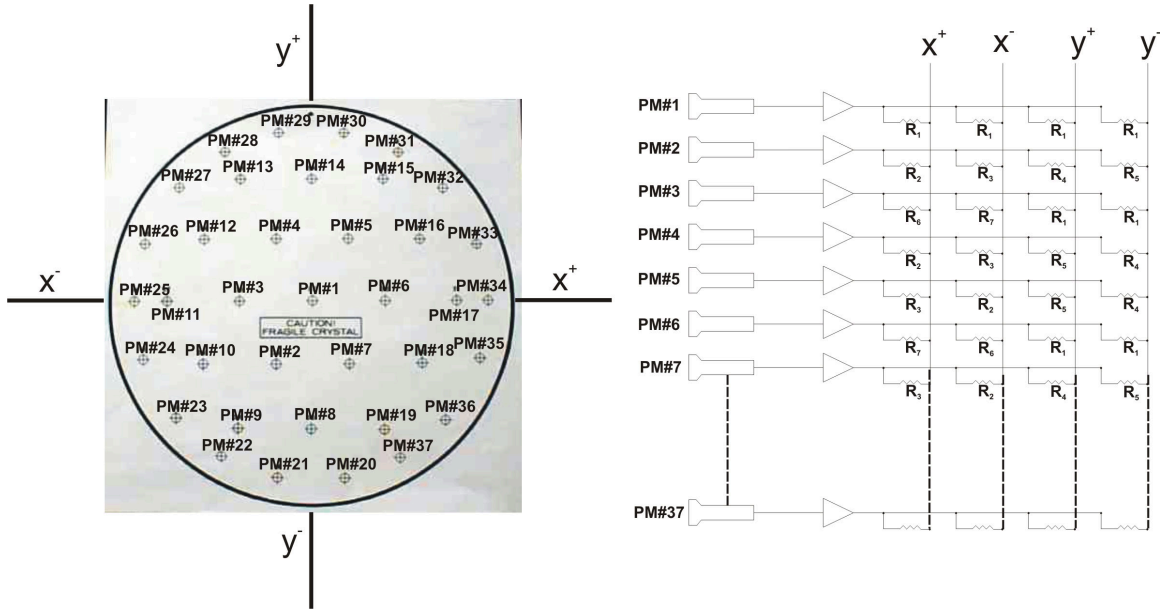


**Fig. 4.15:** The positions of the PMTs and the resistive matrix circuits for the calculation of  $x^+$ ,  $x^-$ ,  $y^+$  and  $y^-$  signals, which in turn are used to generate  $x$ - and  $y$ - position signals.

The summing matrix circuits combine the signals from the individual PMTs in such a way that the relative amplitudes of the  $x^+$  and  $x^-$  signals and of the  $y^+$  and  $y^-$  signals are proportional to the location of the scintillation event with respect to the center. For this calculation, the center of gravity or in other words Anger logic is utilized; which defines for instance  $x^+$  as follows:

$$x^+ = \frac{\sum P_i r_i}{\sum P_i} \quad (4.8)$$

where  $P_i$  is the PMT pulse and  $r_i$  is a positional weight which is determined by the value of the resistor connected to  $x^+$  output. The same formula applies for other coordinates but with different positional weights due to different values of the resistors connected to the corresponding outputs. For example, the resistance connected to  $x^+$  terminal of the 6th PMT ( $R_7$ ) is smaller than the resistance at the  $x^-$  terminal ( $R_8$ ) so that this PMT transfers most of its signal to the positive  $x$  coordinate. Its  $y$  coordinate should have an equal weight in the positive and negative directions, therefore the same resistor is used for these terminals. Similarly, the 1st PMT sends equal signals to the four leads since it is at the center of the array.

The analog processing of the PMT signals of the Anger camera used in this project is shown in detail in Fig. 4.16. Each signal is amplified at the variable gain amplifier and is transmitted to the decoder where the  $x^+$ ,  $x^-$ ,  $y^+$ ,  $y^-$  and the sum ( $z_{ratio}$ ) signals are created. The four terminals are processed further in differential amplifiers to obtain  $x$ - and  $y$ - position signals. These signals are however energy dependent and should be divided by the total signal:

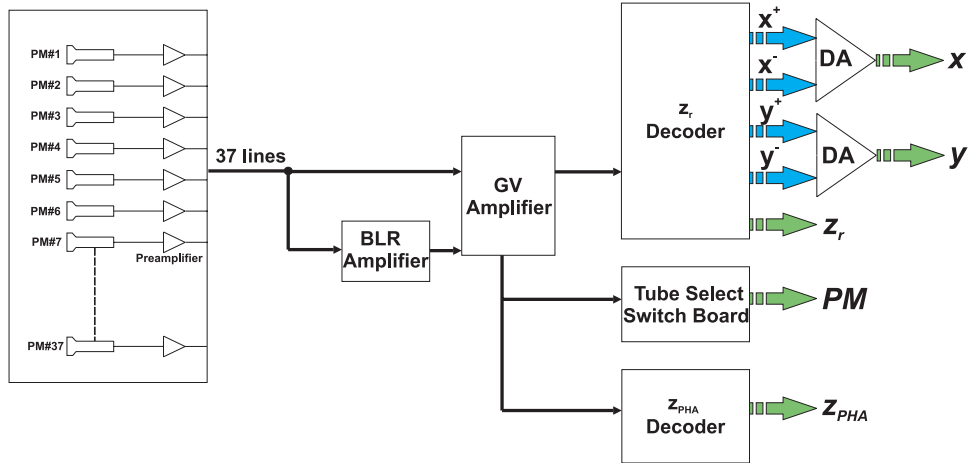


**Fig. 4.16:** Block diagram showing the main analog processing units for the Anger camera position and energy signals

$$x = k(x^+ - x^-)/z \quad (4.9)$$

$$y = k(y^+ - y^-)/z \quad (4.10)$$



**Fig. 4.17:** Anger camera used as an absorption detector for the Compton camera system

The calculation of the energy independent position values is performed by the data acquisition software by dividing the  $x$ - and  $y$ - position signals with  $z_r$  which is obtained by the summation of the four coordinate signals at the summing amplifier. The constant  $k$  is determined by analyzing the homogeneity of the count distribution of the totally irradiated camera in the 2D plot. The second  $z$  signal ( $z_{PHA}$ ) is obtained from signals which are amplified in the base-line restorer and variable gain amplifiers whose output is fed to the pulse-height analyzer. The energy spectrum of the photons arriving in the absorption detector is obtained using the  $z_{PHA}$  signal. The pulse-height analyzer is needed for adjusting the energy

window such that the background can be eliminated. In standard SPECT applications of the Anger camera, the energy window is also adjusted for the selection of the photopeak region. The PM signal is the calibration signal for single PMTs which is selected on the tube select switch board. As a result, there exist five outputs coming from the camera head, namely  $x$ ,  $y$ ,  $z_r$ ,  $z_{PHA}$  and the PM signals.

The camera used as the absorption detector is shown in Fig. 4.17. The camera has an embedded motor system which enables a vertical translation and two-axes rotational motion of the camera head. There is an ongoing project for automizing this motor system using a micro-controller based motor control system. In this way the orientation of the absorption detector becomes computer-controllable and measurements at different angular regions can be performed with a single detector.

The reported position resolution of this Anger camera is 3-4 mm FWHM. A simulation code has been developed for estimating the position resolution of the system which could eventually be developed further for the position calibration of the detector. The processes starting from the scintillation to the collection of charges at the anode of the PMT are implemented using statistical estimates. According to these estimates the conversion efficiency of the initial photon energy into scintillation photons is 13%, 30% of the scintillation light is lost at the crystal and the crystal-PMT interface, only 20% of the scintillation photons reaching the photocathode eject photoelectrons from which 75% arrive at the dynode. The gain factor of the PMT is taken to be  $10^6$  and using the number of electrons per scintillation process the current signal is calculated. To estimate the position uncertainty a well collimated beam of photons is sent to a point on the crystal. The location of the scintillation calculated with the center of gravity method is a broadened distribution as shown in Fig. 4.18. The incoming photon energy is taken to be 500 keV and the resulting position uncertainties are few mm FWHM, as reported.

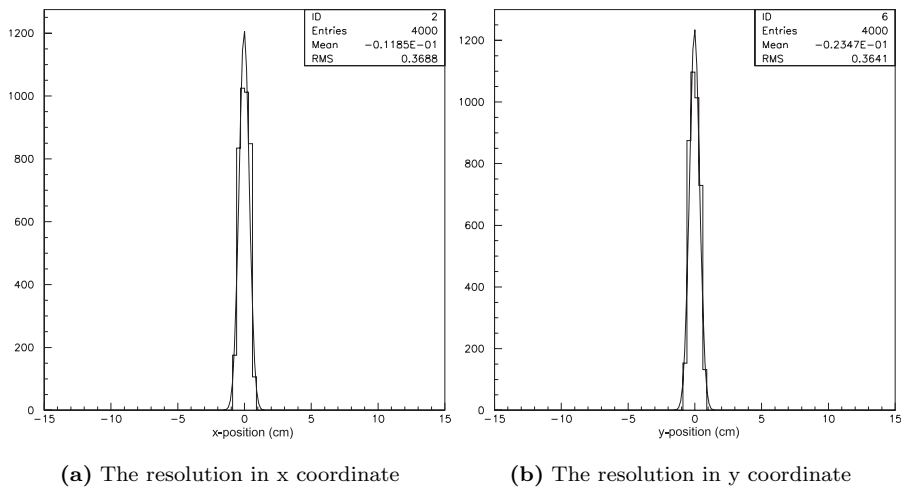
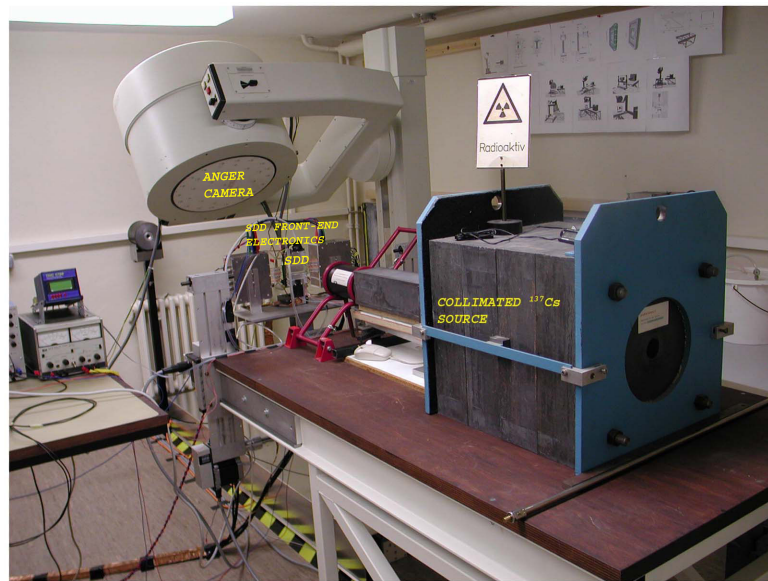


Fig. 4.18: Simulated position resolution performance of the Anger camera

## 4.4 The Compton Camera Setup

The Compton camera system consisting of a 19 cell SDD as a scatter detector and an Anger camera as an absorption detector is shown in Fig. 4.19. The silicon detector and its front-end electronics boxes are mounted on a motor system which moves in horizontal, vertical and rotational directions. In this way, Compton electrons in all directions and kinematics can be studied. The detector housing is placed on an additional moving stage which enables up to 2 cm change in the source-SDD distance ( $D_1$ ) with a micron precision. The distance from the location of the source in the collimator to the surface of the silicon detector is around 115 cm. In addition to the embedded motor system of the Anger camera, another degree of freedom to its motion has been added by placing the camera on a moving stage. This system provides a translational motion to the Anger camera as a whole. In this way, not only the inter-detector



**Fig. 4.19:** Compton camera system with a 19-cell SDD scatterer and an Anger camera absorber

distance ( $D_2$ ) can be varied in a larger scale but also both forward and back scattering regions can be studied.



## 5. Front-End Electronics and Data Acquisition System

This chapter mostly concerns the front-end electronics for the silicon drift detector and the data acquisition system for both detectors. The analog readout electronics of the Anger camera is embedded on the camera head, therefore only the digital part of the camera readout will be mentioned.

### 5.1 Front-End Electronics of the Silicon Drift Detector

#### 5.1.1 The First Stage of the SDD Front-End Electronics

The first stage of the front-end electronics concerns the stage between the detector and the preamplifier. In the standard readout architecture, integrated JFET acting as a source follower is coupled to a charge sensitive preamplifier through a capacitance. The source load of the source follower is a current supply degenerated by a resistance. The output impedance of this load is high enough in order to have a voltage gain of one for the source follower. The transconductance ( $g_m$ ) of the n-channel on-chip JFET is about  $300 \mu\text{S}$  as shown in Section 4.2.2 and the time constant  $\tau = C_{total}/g_m$  produces a rise time of  $2.2\tau$  which is of the order of 300 ns. This rise time introduces a lower limit to the usable shaping time for this signal. However, for Compton camera applications it is important to have fast trigger signals from the

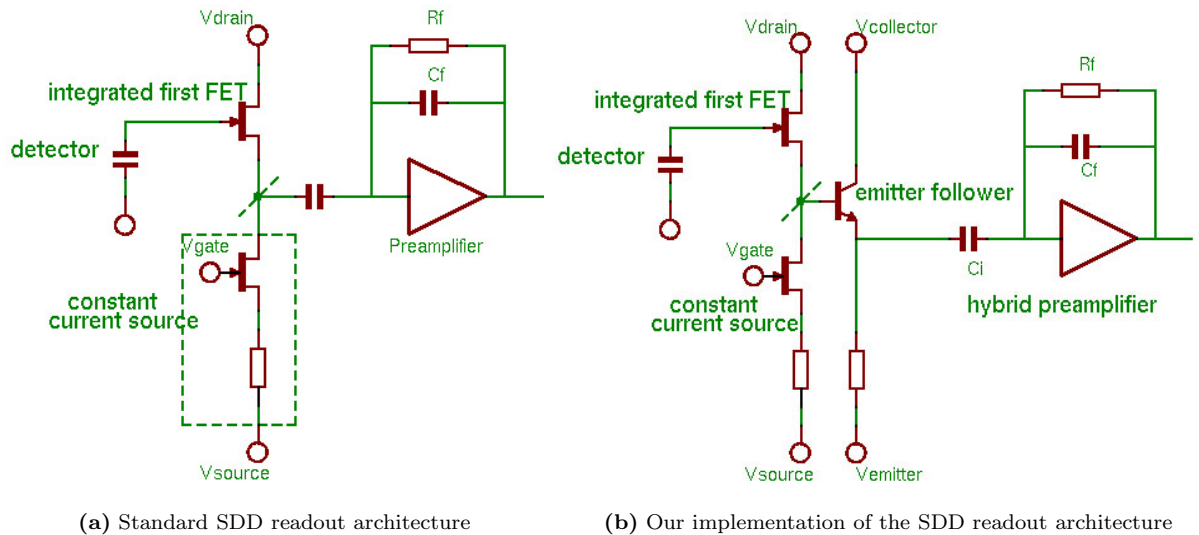
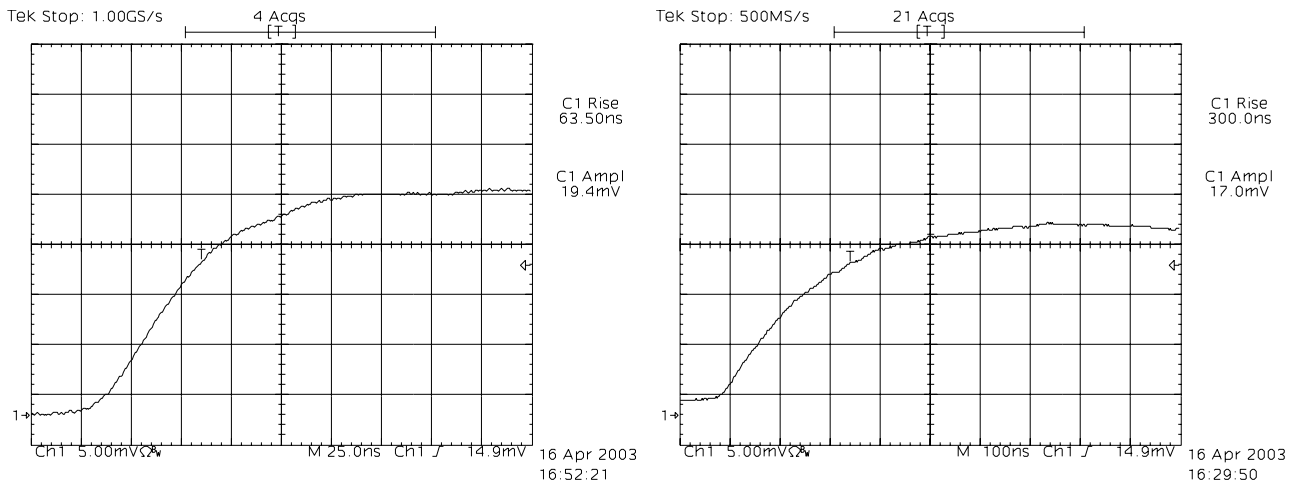


**Fig. 5.1:** The standard readout architecture for the SDD and a new readout architecture developed for the fast readout of the SDD

first detector which can be achieved with fast shaping of the signals. One way to obtain a fast trigger signal would be to readout the back electrode where the holes arrive. The mobility for the holes is lower than the electron mobility but the hole signal is generated faster due to the fact that they do not need

to drift to the middle of the wafer like electrons. This way of fast readout has already been achieved with a Controlled Drift Detector (CDD) [Cas04b] and is under research for the SDD. To achieve the fast readout for the SDD, new readout architecture implemented within the frame of this work is shown in Fig. 5.1(b).

The new readout architecture has an additional emitter follower stage following the source follower stage of the on-chip JFET. Emitter followers and source followers were successfully used as low noise preamplifiers for proportional counters in the past [Far83]. Having the first transistor followed by a second transistor in an emitter follower configuration has certain advantages. First of all, the signal after the emitter follower stage becomes more immune to pick-up noise. The front-end electronics can be placed far away from the detector, provided that the emitter-follower is as near as possible to the detector. Furthermore, due to a lower stray capacitance, the rise time of the signals decreases considerably, which makes the use of a short shaping time ( $< 100$  ns) possible. Bipolar junction, junction field effect and ultra-fast SiGET low-noise transistors had been tested both for this application and for the constant current source. Finally, the driver transistor for this stage was chosen to be a bipolar junction transistor (BJT). The selection of this type of transistor is based on the dynamic range, noise contribution and input capacitance requirements which were checked both with the measurements and the PSPICE [PSP03] electronic circuit simulations. As shown in Appendix D.1 SiGET transistors have much better performance in terms of speed but due to the very narrow operating range for the voltage across their collector-emitter junctions, it was not quite convenient to use them for this first version. Finally, it was decided to use a JFET (2N4416) and a BJT (BFT25) for the constant current source and the emitter follower circuits, respectively. Fig. 5.2 shows the SDD signals at the preamplifier output with and without the emitter follower stage when the detector is irradiated with a  $^{55}\text{Fe}$  source.



(a) Preamplifier output with the emitter-follower stage (25 ns/div)

(b) Preamplifier output without the emitter-follower stage (100 ns/div)

**Fig. 5.2:** The preamplifier output with and without the emitter follower stage when the SDD is irradiated with a  $^{55}\text{Fe}$  source. About a factor of 5 improvement can be observed with the emitter follower. The signal amplitude is lower in the absence of the emitter follower stage due to the increased capacitance leading to the attenuation of the signal.

The rise time of the preamplifier signal reduces almost by a factor of 5 in the presence of the emitter follower stage. The difference between the two signals appears not only in the time scale but also in the voltage scale. Lower signal amplitude without the emitter follower is due to the higher capacitance which causes the attenuation of the signal. It was also observed that the noise contribution of the emitter follower circuit is negligible. Spectroscopic measurements were performed with a single cell SDD whose output is connected to the hybrid preamplifier followed by a NIM shaper module (Tennelec TC244). The

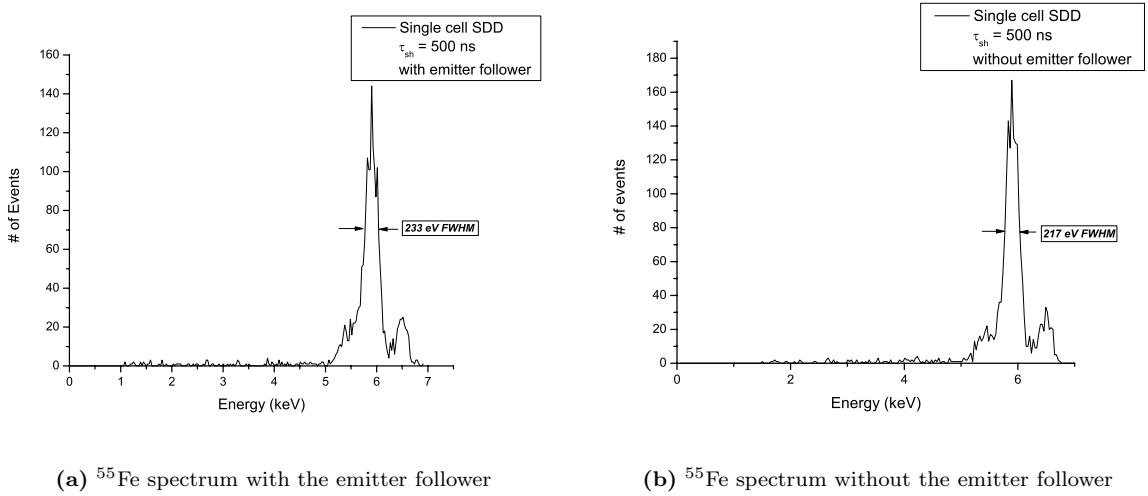


**Fig. 5.3:**  $^{55}\text{Fe}$  spectrum measured with a single cell SDD with and without the emitter follower stage at room temperature. The difference in ENC is only about 2 electrons rms.

spectra obtained with and without the emitter follower stage are shown in Fig. 5.3. The emitter follower circuit together with the constant current source are implemented on a small PCB which is placed between the detector and the preamplifier. In order to keep the measurement conditions unchanged, a PCB of the same size but only with the constant current source is used at the same location for the measurements without the emitter follower stage. The difference between the FWHM energy resolution at Mn  $K_\alpha$  peak corresponds to 2 electrons rms. However, with the emitter follower stage, the preamplifier can be placed further away and under this condition this difference in the resolution almost disappears.

### 5.1.2 Preamplifier

The most common readout architecture of the SDD with on-chip electronics includes a low-noise charge sensitive preamplifier (A250 [AMP]) which is configured as a voltage preamplifier for the SDD readout. Having 19 of this hybrid preamplifier would exceed the budget constraints. Instead a custom designed low-noise voltage preamplifier was chosen to be implemented on a multi-channel board at our hybrid laboratory. This preamplifier is a modified version of a preamplifier which was used for one of the first prototypes of the SDD [Ch.96]. The block diagram of the preamplifier with the first stage of the front-end electronics and the detector part is shown in Fig. 5.5. The voltage preamplifier consists of an injection capacitance  $C_i$  followed by a charge sensitive preamplifier whose gain is approximately the ratio between the injection capacitor and the feedback capacitor. The value of the  $C_i$  is important since on one hand this capacitance should be high enough to induce a reasonable amount of charge to the shaper, on the other hand, it should be low enough not to cause any rise-time limitations. Considering all these constraints together with the influence of  $C_i$  on the noise performance, the final version of the preamplifier had been designed [Fio02a] to have a 22 pF of  $C_i$  and 1 pF of the feedback capacitor which is parallel to the 100 M $\Omega$  feedback resistor. These values of the  $R_f$  and  $C_f$  results in a decay time constant of  $R_f C_f = 100 \mu\text{s}$  for the output of the voltage step. A step

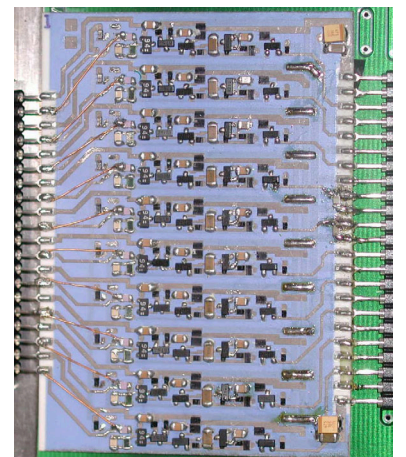


**Fig. 5.4:** 10-channel hybrid preamplifier

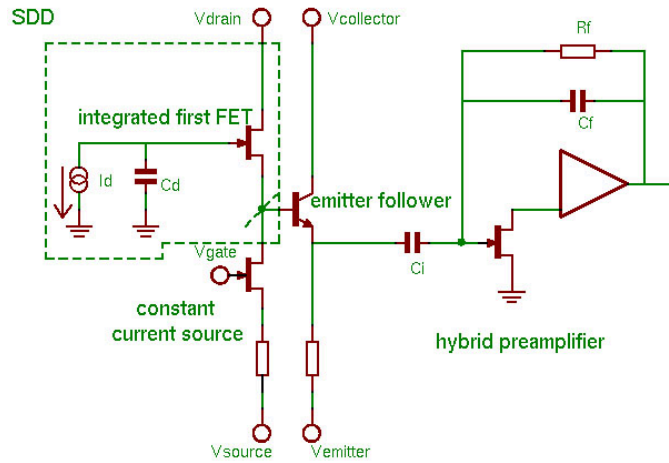


Fig. 5.5: Schematics of the detector coupled to an emitter follower stage followed by a preamplifier

voltage applied to the input of the preamplifier results in an output signal of 8 ns rise time as shown in Fig. D.3.

Considering the number of channels needed for the readout of the SDD, the layout of the preamplifier board with ten channels have been designed and produced in our hybrid laboratory. The 10-channel board shown in Fig. 5.4 is implemented on a hybrid board by using a thick film and SMD technologies. The power consumption of each preamplifier channel is around 130 mW according to PSPICE simulations. Both the input and the output stages of the preamplifier are single-ended. Considering the fact that the shaper is placed very close to the preamplifier, there was no need for a differential drive.

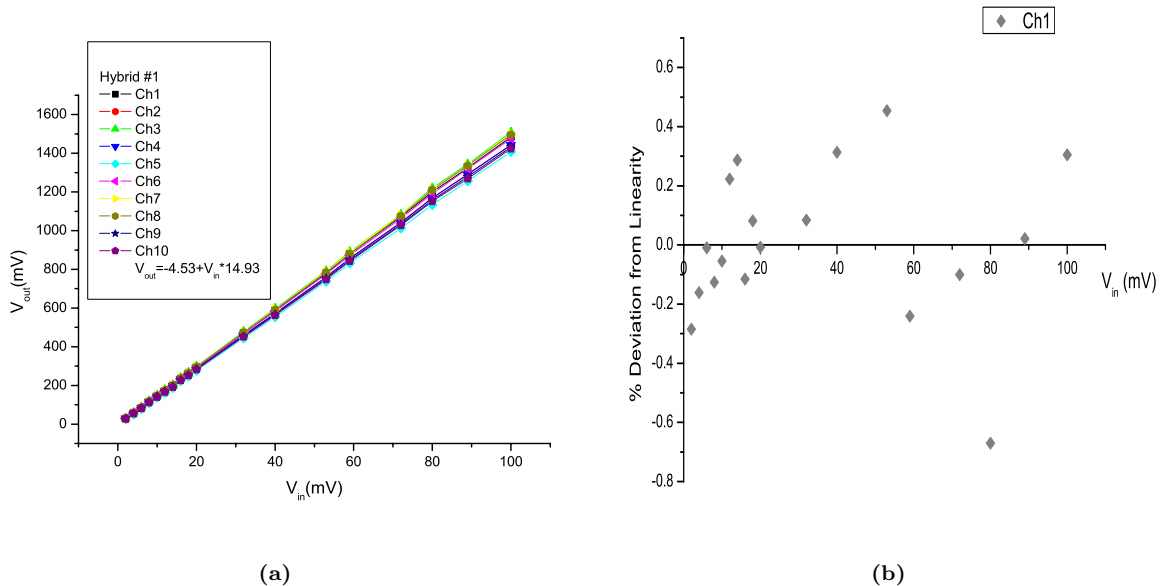
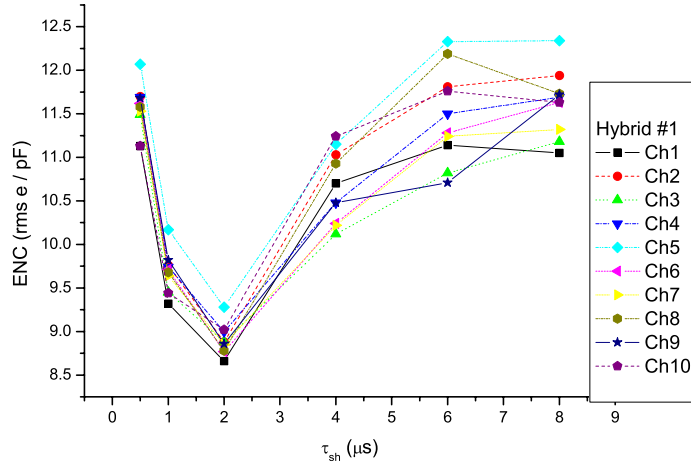


Fig. 5.6: (a) Linearity for all the channels, (b) Percent deviation from linearity for the first preamplifier channel

In order to test the linearity of the preamplifier, the response of the preamplifier to a step voltage has

been measured for different amplitudes of the input signal. The amplitude of the output signal measured for different input voltages is shown in Fig. 5.6(a) for all the channels. The linear fit shows that the average voltage gain of the preamplifier is approximately 15 which differs from the estimated value of 22 due to additional input capacitance added to the injection capacitance in series. The percent deviation from linearity shown in Fig. 5.6(b) is below 0.8%.



**Fig. 5.7:** ENC contribution of the preamplifier measured for all channels

Noise measurements have been performed in order to estimate the noise contribution of the preamplifier to the whole detector and the readout system. For performing these measurements the preamplifier output is connected to a spectroscopy amplifier (Model 1413). The equivalent noise charge (ENC) calculated for an input capacitance of 1 pF (Appendix D.2) is shown in Fig. 5.7. A charge input was generated using a voltage step fed into a 1 pF test capacitor connected to the preamplifier input. The peak noise voltage of the preamplifier/shaper system was measured with an analog oscilloscope at a very low trigger rate ( $\leq 100$  Hz) and this level corresponds to four to five standard deviations. The measured values obtained with this method were also confirmed with a digital oscilloscope's (LeCroy 9362) standard deviation measurement.

The minimum noise is obtained at a shaping time of 2  $\mu\text{s}$  and the ENC increases for shaping times that are higher and lower than this value. For the Compton camera application, the shaping time should be much shorter than  $\mu\text{s}$  range which is not quite favorable for the noise performance of the preamplifier but the difference is only 2 electrons rms per pF of input capacitance which is not very critical for this application and with the SDD which has a typical capacitance of the order of few hundred fFs. The ENC values are given in  $e^-$  rms/pF units which translate into 2-4 electrons rms for 300 fF of detector capacitance. Therefore, the noise contribution of this low noise preamplifier to the whole detector and the readout system is only few electrons rms. Similar noise figures were also observed with the PSPICE simulations (the method explained in Appendix D.2) performed before the production of the preamplifiers. The simulated ENC value of 4 electrons rms/pF is obtained with an ideal shaper of 1  $\mu\text{s}$  shaping time connected to the output of the preamplifier.

With the help of the measurements performed for the characterization of the on-chip JFET (Fig. 4.10), it was possible to produce the SPICE model for the SDD in order to simulate the detector and the readout electronics. The energy of the recoil electrons captured in the SDD can reach few hundred keV for incoming photon energy of 662 keV as shown in Fig. 2.16, therefore it is important to have a preamplifier with a high dynamic range. The simulations showed that the preamplifier response does not saturate up to around 400 keV of deposited energy.

### 5.1.3 Shaper

An in house developed hybrid shaper has been chosen for the filtering and further amplification of the SDD signals. The shaper is a simple CR-RC shaper with an adjustable pole-zero cancellation and gain. Ten of the already existing two channel hybrid shapers are used for the 19 channel detector.

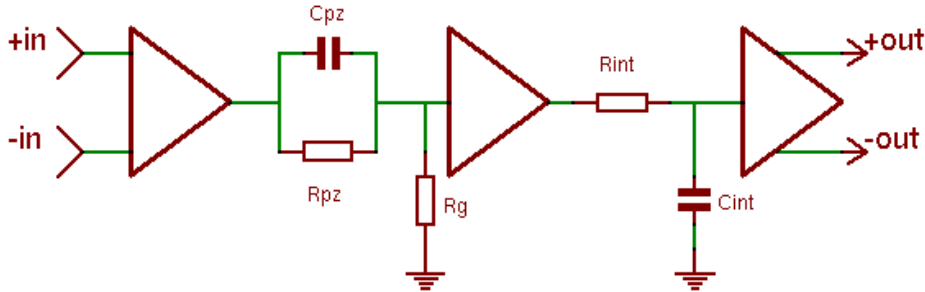


**Fig. 5.8:** Block diagram of the semi-Gaussian shaper. For the integrator, gain and pole-zero adjustment parts the scripts int, g and pz are used for the corresponding components.

The block diagram of the shaper is shown in Fig. 5.8 while the full schematics is given in Appendix D.3. The first stage is a differential amplifier with a variable gain, adapted to a unipolar signal coming

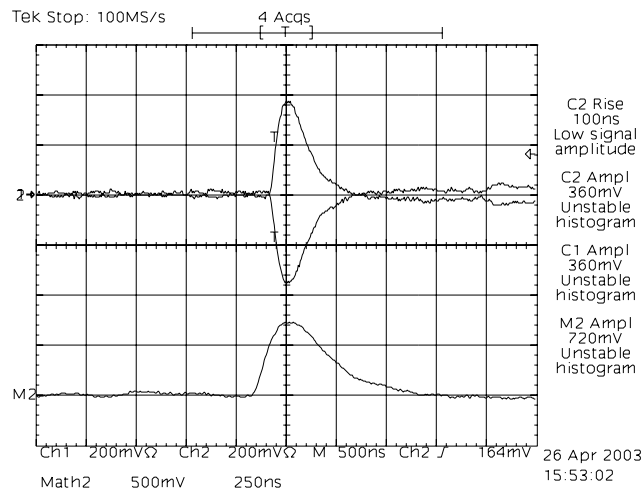


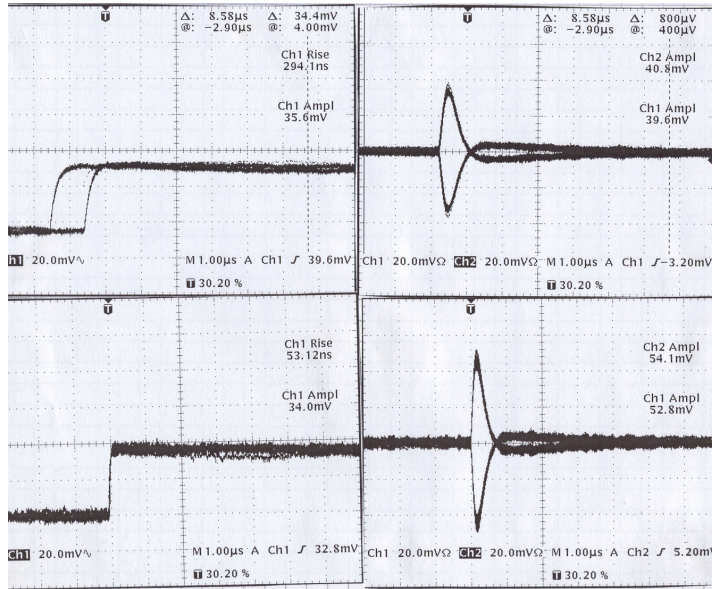
**Fig. 5.9:** Shaper output obtained with a single cell SDD irradiated with a  $^{55}\text{Fe}$  source. The upper waveforms are the symmetrical differential outputs. Below is the resulting waveform when the difference of the positive and the negative outputs is taken.

from the preamplifier. It is followed by a pole-zero filter and an integrator realized by passive components. The last stage was designed such that a load of  $50\ \Omega$  on each output results in a symmetric signal as shown in Fig. 5.9. The input voltage range of the ADC's used in the data acquisition system is 2 V peak-to-peak. For this reason, the amplification factor of the shaper is adjusted to its minimum value in order to cover maximum possible range of the energy of the recoil electrons absorbed in the SDD. Though the energy resolution measured with a single cell SDD dropped with a factor of 1.25 from the maximum gain (280 eV FWHM at Mn  $K_{\alpha}$  line of the  $^{55}\text{Fe}$ ) of the shaper to the minimum gain (348 eV FWHM), the energy resolution is still very good, besides it is more important to cover the full range of the recoil electron energy for the performance of the Compton camera.

Certain aspects were taken into account while choosing the appropriate shaping time. The rise time of the preamplified signal is about 60 ns as shown in Fig. 5.2. To avoid a ballistic deficit, a shaping time which is not much shorter than the rise time of the input signal should be chosen. As shown in

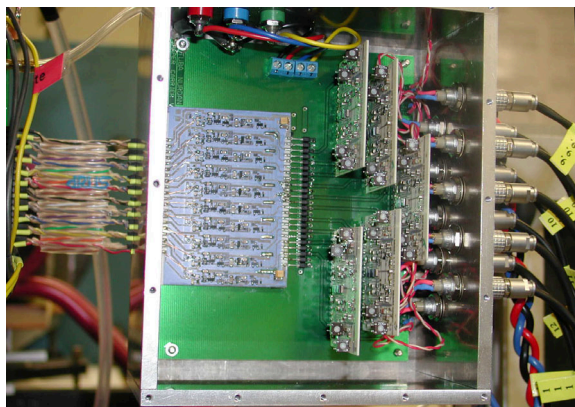
the previous chapter, the minimum value for the preamplifier noise is obtained at a shaping time of  $2 \mu\text{s}$  which is quite long for this application. Two different versions of this shaper with different shaping times were used during the measurements. For measurements requiring very fast shaping, a rise time of  $50 \text{ ns}$  has been used and for most of the coincidence measurements  $100 \text{ ns}$  of rise time has been sufficient.

Fig. 5.10 shows the preamplifier and shaper output signals without and with the emitter follower stage. In addition to the increased rise time an attenuated signal is observed in the absence of the emitter follower stage.



**Fig. 5.10:** Preamplifier and shaper signals when the single cell SDD is irradiated by  $^{55}\text{Fe}$  source. The upper waveforms are obtained without, the lower waveforms with the emitter follower stage

A PCB has been designed to carry one 10-channel preamplifier board and 5 of the 2-channel shaper boards on a single board. In this way, two of these boards in metal boxes for electromagnetic shielding could be placed on the right and on the left side of the detector for the readout of the 19 SDD channels. The board with preamplifier and shapers is shown in Fig. 5.11 while its schematics and the layout are given in Appendix D.4.



**Fig. 5.11:** Carrier PCB designed for the 10-channel preamplifier board and five of 2-channel shaper boards connected to 10 SDD channels on one side and to the data acquisition system on the other side.

## 5.2 Data Acquisition System

A custom-designed FPGA (Field Programmable Gate Array) based data acquisition (DAQ) system developed for the Compton camera system has been used [Nur05; Nur03b; Nur03a]. The block diagram of the system is shown in Fig. 5.12.

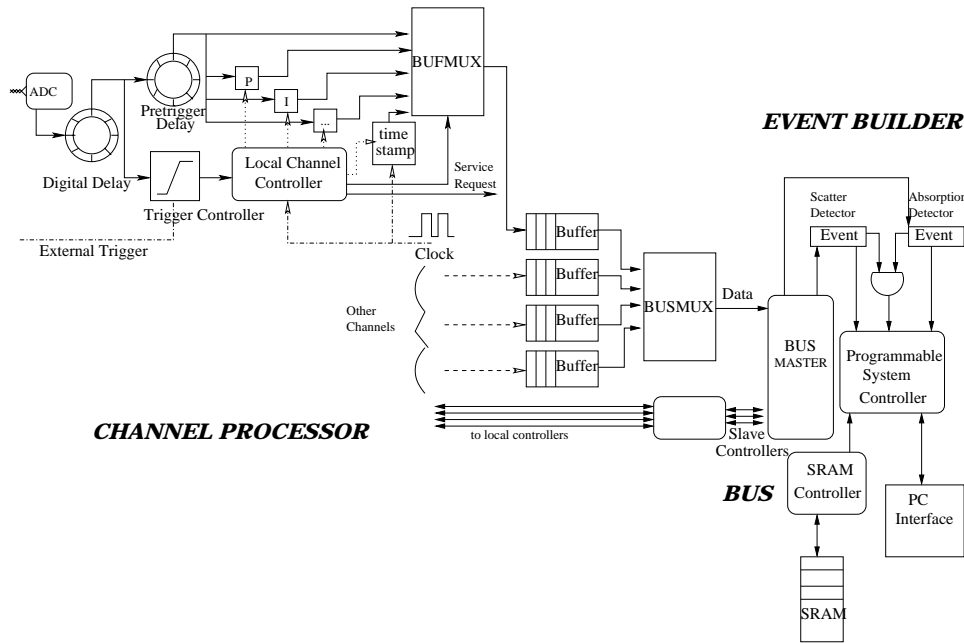


Fig. 5.12: Block diagram of the Data Acquisition System.

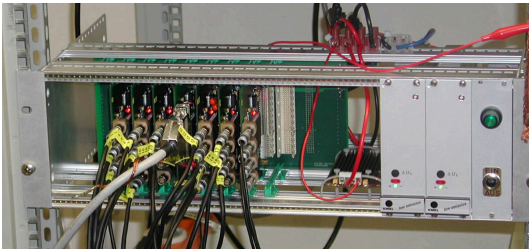


Fig. 5.13: The Data Acquisition System

The DAQ system shown in Fig. 5.13 consists of channel processor modules, an event builder module and a bus system which transfers the data between the channel processors and the event builder. Each channel processor module has four input channels and a single XILINX FPGA for processing all of the four channels. FPGA is a programmable logic device which consists of logic elements like gates or lookup table RAMs, flip-flops and programmable interconnect wiring. In addition to being programmable, FPGAs are also reprogrammable, since their logic functions and interconnect are defined by RAM cells. In this way the same hardware design could be

used both for the scatter and the absorption detectors. This flexibility of FPGAs and other good features such as short development times, low production costs make them ideal for this custom designed data acquisition system. Six of channel processor modules are used for the readout of 19 SDD cells and 4 outputs of x, y, z and corrected energy signals of the Anger camera. The bus can be populated with up to 8 channel processor modules and 1 event builder module. The event builder module is the master of the whole system which also utilizes an FPGA for performing the necessary tasks.

The shaper outputs of both detectors are connected to the channel processor which has both analog and digital sections. The analog part receives the analog signals, sends them to an ADC where they are digitized with a 66 MHz clock frequency and 12-bit resolution. System performance tests show that the effective resolution of the ADCs is around 10.5-11 bits. The digital signal is then transferred to the FPGA where the operations like time-stamping, integration, the storage of the raw data and peak-finding are performed. Each of the four channels has a dedicated buffer in the FPGA which has a depth of 255 words. This corresponds to the storage of up to 255 events in the buffer, depending on the number of

selected operations. In the standard configuration, time-stamping (3 words) and peak finding (1 word) operations are used, therefore the event capacity is around 64. In order to minimize the effect of the baseline on the signal, baseline subtraction is performed during the peak-finding operation.

As the event capacity is reached at the buffer, the slave bus controller signals the bus master in the event builder module which activates the data transfer unit. This unit transfers the burst data to the static RAM located on the event builder module with a rate of 100 MBps. The static ram has a storage capacity of up to 1 MWord which corresponds to 250 kevents in the standard configuration. A processor implemented in the FPGA provides the filtering for the coincident events. In this processor, the time-stamps of the events from the Anger camera and the SDD are checked and according to the given time window, the good events are selected and the rest is purged. The data is then transferred to the data acquisition computer via parallel port connection where the further analysis of the coincidence events are performed.

### 5.3 Spectroscopic Measurements with a Single Cell SDD

The performance tests of the readout electronics were performed further with a single cell SDD whose leakage current was reported to be around 100 pA [ÇN04b]. The spectroscopic measurements were performed by using the analog and digital readout electronics described in the previous sections. The differential shaper output is connected to one channel of the channel processor module. Instead of using the whole data acquisition system with the bus, a parallel port interface card developed for testing the modules is used for this 1-cell detector. The channel processor module is connected to this interface board and the digitized signals are transferred to a PC via parallel port connection.

The first measurements were performed using a  $^{55}\text{Fe}$  source which is commonly used to check the resolution of the detector. The spectrum measured at room temperature is shown in Fig. 5.14(a) where both  $\text{Mn K}_\alpha$  and  $\text{K}_\beta$  peaks can be seen clearly. The ENC is about 33 electrons rms which includes the noise contributions from the detector and the readout electronics. Fig. 5.14(b) shows the variation of the ENC as a function of the shaping time. The FWHM energy resolution at  $\text{Mn K}_\alpha$  is about 240 eV at a shaping time of 500 ns and increases with longer and shorter shaping times.

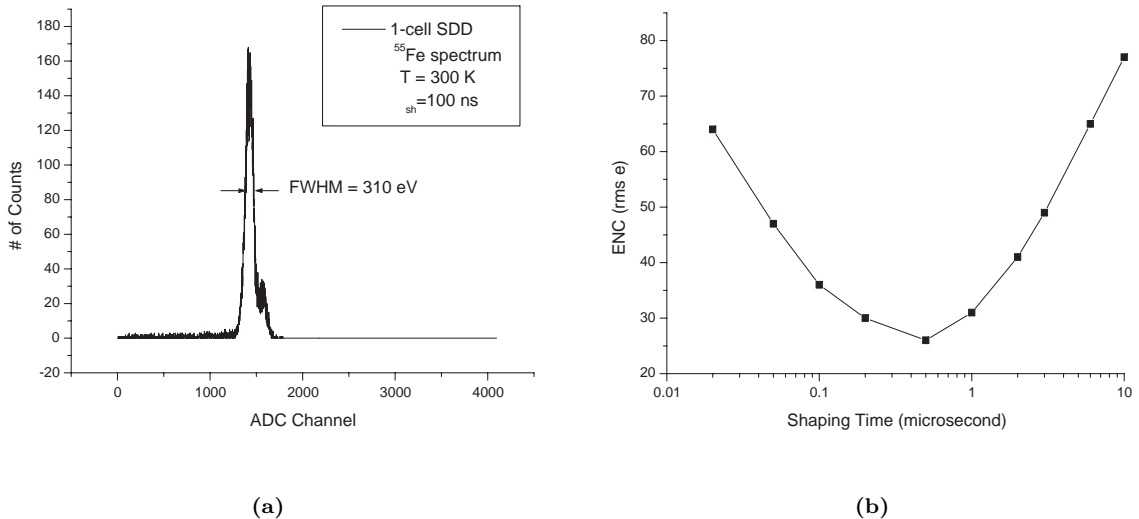


**Fig. 5.14:** (a)  $^{55}\text{Fe}$  spectrum (b) Energy resolution as a function of the shaping time

With the Compton camera, it is aimed to use high energetic radionuclides which emit photons of at least few hundred keV energy.  $^{55}\text{Fe}$  is the standard source used to demonstrate the energy resolution of

this detector but it is also interesting to observe the detector response at higher energies. The spectra obtained with  $^{109}\text{Cd}$  and  $^{133}\text{Ba}$  sources are shown in Fig. 5.15. The counts are multiplied by a factor of 10 for the energy region above 35 keV in order to see the peaks more clearly.

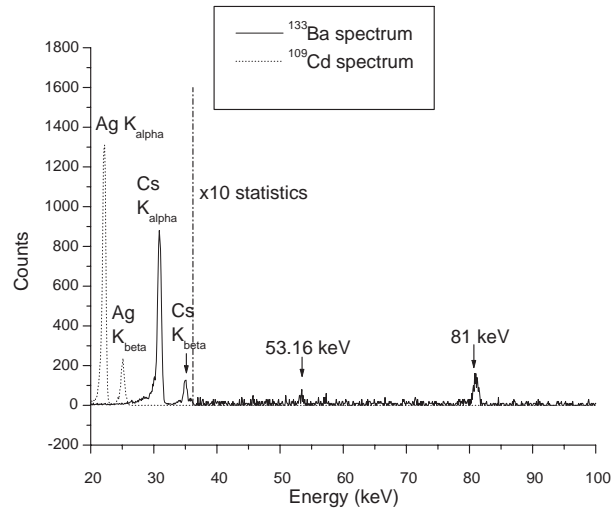


**Fig. 5.15:**  $^{109}\text{Cd}$  and  $^{133}\text{Ba}$  spectra obtained with the single cell SDD which is read-out by the front-end electronics and the data acquisition system described in this chapter.

## 6. Measurements and Results

### 6.1 Spectroscopic Performance of the Scatter Detector

The first measurements with the 19-cell SDD have been performed at room temperature and with the detector and preamplifier boards placed in a test box as shown in Fig. 6.1.

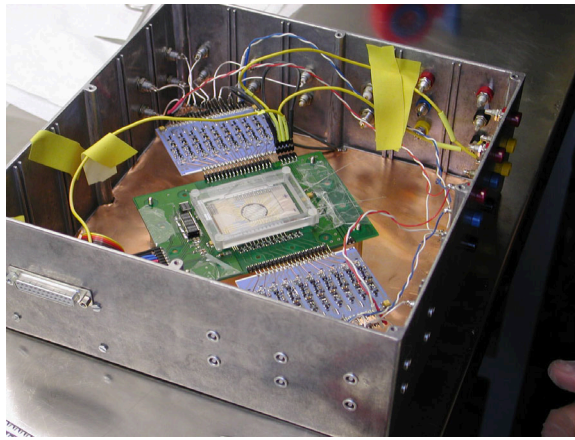


**Fig. 6.1:** Test box for the 19 cell SDD

The output of the preamplifier is connected to the hybrid shaper having a rise time of 100 ns. The shaped signal is then digitized at the channel processor board that is connected to the parallel-port interface board. The temperature diode was not readout in the test box, therefore the exact temperature at the detector chip was unknown but the room temperature in the laboratory was around 20 °C. Spectroscopic measurements were performed with an uncollimated tablet-shaped  $^{55}\text{Fe}$  source that irradiates all the channels of the detector. The resulting energy spectra of 2000 events for 17 SDD cells are shown in Fig. 6.2. Channels 6 and 16 require different biasing conditions than the other cells such that their gain are quite low at the operating voltages of the others. The voltages for the drift field, the reset diode and the back electrode are adjusted to find the optimum operating conditions for all the channels. Unfortunately, these two channels need much higher back voltage for a decent signal which is higher than the optimum for other channels. Therefore channels 6 and 16 are not included in this analysis and at further measurements.

The energy resolution fluctuates between 359 eV to 555 eV FWHM at Mn  $K_{\alpha}$  line of the  $^{55}\text{Fe}$  source. In fact, the fluctuation is less than these extreme values show because the energy resolution is above 430 eV FWHM only for two detector channels. The worst energy resolution is obtained with the 10th channel which performs better at higher depletion voltage than other channels and unfortunately at higher depletion voltages the energy resolution of other channels need to be sacrificed as shown in Fig. 6.3. With this channel included, the average energy resolution is around 407 eV FWHM which corresponds to 45 electrons rms of ENC. After the characterization of the detector in the test box, the SDD is mounted in its housing. Peltier terminals are connected to the temperature controller unit which receives the feedback from the on-chip temperature diode. In addition to this, the temperature controller gets the room temperature information from an external temperature diode which is thermally coupled to the Al housing. With all the necessary electrical and mechanical connections completed for cooling

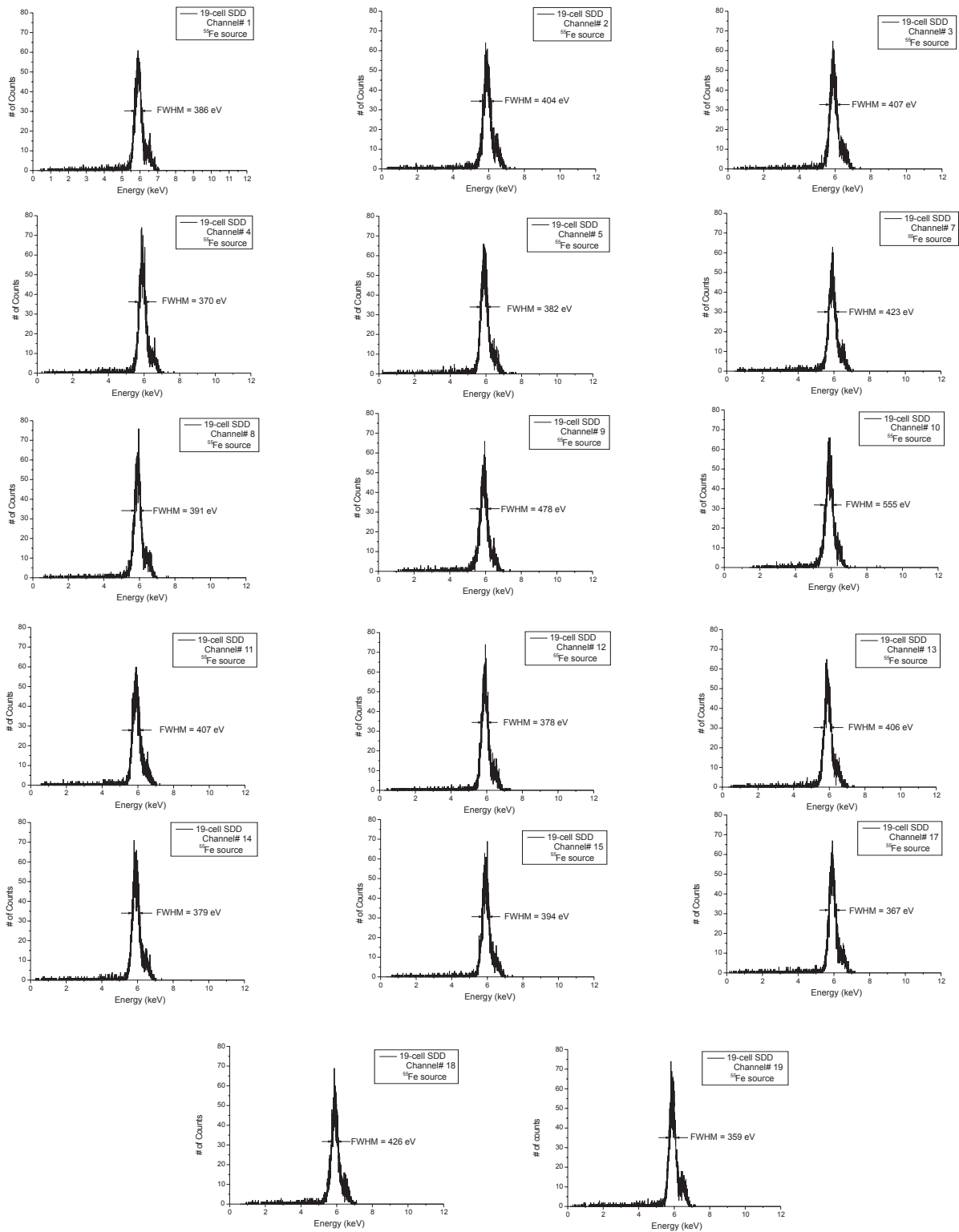
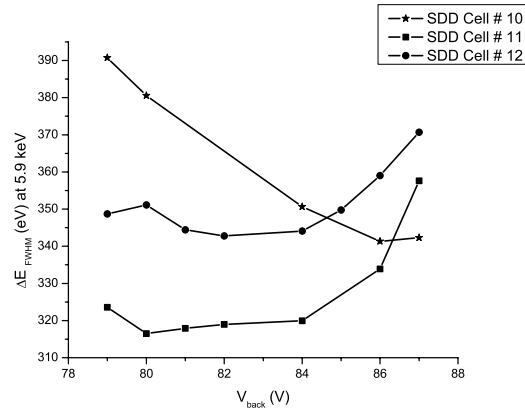
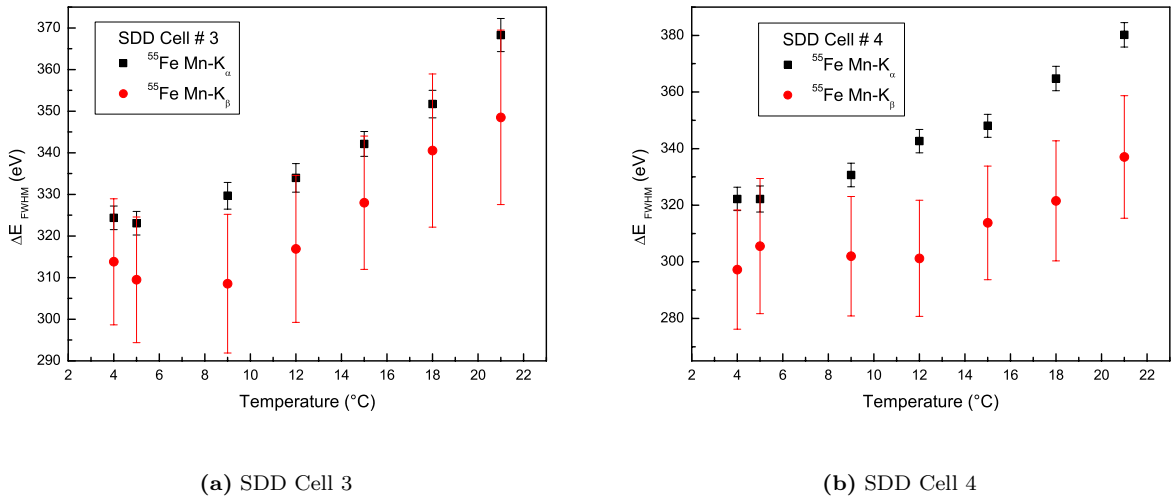


Fig. 6.2:  $^{55}\text{Fe}$  energy spectra measured with SDD channels at room temperature



**Fig. 6.3:** Energy resolution at the Mn- $K_\alpha$  line of  $^{55}\text{Fe}$  as a function of the voltage at the back electrode for few channels. 10th channel performs better at higher depletion voltages where other channels perform worse.

the detector, the spectroscopic measurements could be performed at a fixed known temperature. The effect of temperature on the energy resolution of the detector has been analyzed in detail at the thesis of K. Laihem [Lai04]. The FWHM energy resolution measured at the Mn- $K_\alpha$  and Mn- $K_\beta$  lines of  $^{55}\text{Fe}$  at different chip temperature values is shown in Fig. 6.4 for two SDD channels. The energy resolution



**Fig. 6.4:** The variation of the FWHM energy resolution at Mn- $K_\alpha$  and Mn- $K_\beta$  lines as a function of the detector temperature measured directly on the chip.

improves considerably when the detector is cooled from 22 °C down to 10 °C. Cooling the detector chip below 5 °C does not cause a considerable change in the energy resolution due to the fact that at lower temperatures the resolution is limited by the  $1/f$  noise, which is supposed to be temperature independent. For this reason, further measurements have been performed at 10 °C of chip temperature. The mean energy resolution for all the SDD channels at this temperature corresponds to an ENC of about 40 electrons rms.

The data received from the data acquisition system includes the ADC channel number and peak value

of the signal for each event. The peak data is then histogrammed where the ADC channel number of the peak center corresponds to the energy of the gamma. For the calibration of the SDD channels,  $^{55}\text{Fe}$  and  $^{109}\text{Cd}$  sources are used as shown in Fig. 6.5(a). The photopeaks in the energy spectrum are well described with a Gaussian function whose width is related to the energy resolution. The known photopeak energy versus the channel number of the center of the photopeak obtained from the Gaussian fit is plotted as shown in Fig. 6.5(b). Finally the linear relation between the channel number and the energy is extracted from the linear fit of this calibration curve. The same procedure is applied for all the SDD channels.

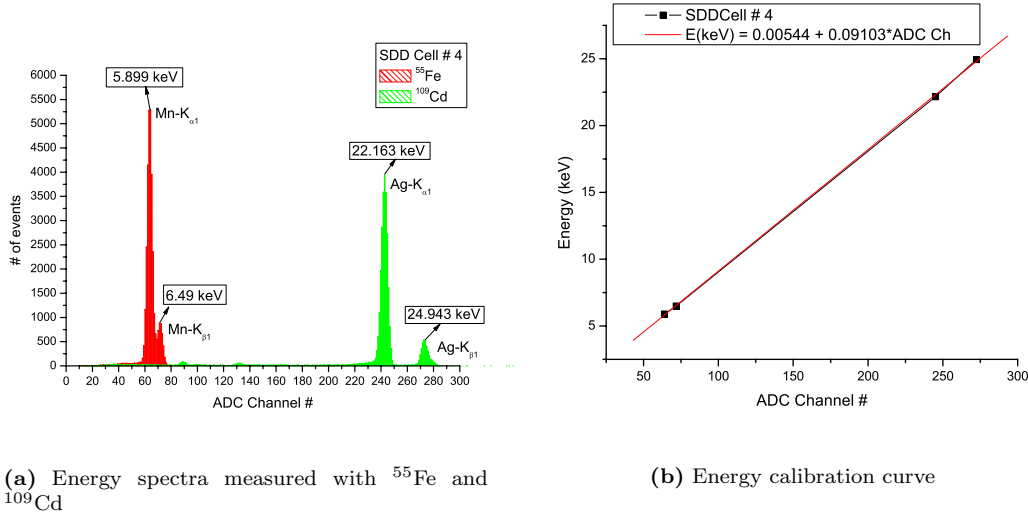


**Fig. 6.5:** Energy calibration procedure where first the histogram of the peak data is plotted, then the calibration curve is used to derive the relation between the ADC channel number and the energy.

Spectroscopic measurements were also performed using a NIM shaper (Tennelec TC244) to check the energy resolution at longer shaping times. The spectra obtained with a shaping time of 250 ns and 375 ns are shown in Fig. 6.6. The resolution degrades at shaping times that are longer than 250 ns which shows that the optimum shaping time is around this value.

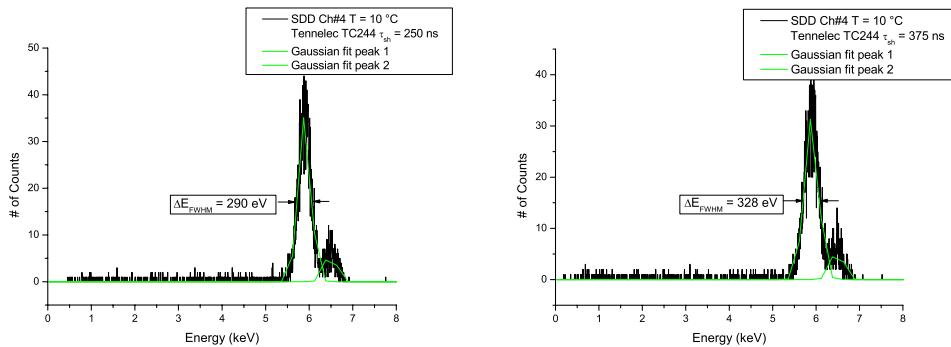


**Fig. 6.6:**  $^{55}\text{Fe}$  energy spectra measured with a Tennelec TC244 shaper at shaping times of 250 ns and 375 ns.

## 6.2 Measurements with the Absorption Detector

Anger camera has two different  $z$  sum signals one of which ( $z_R$ ) is used for the division of the coordinate signals in order to get an energy-independent coordinate information and the other sum signal ( $z_{PHA}$ ) is used for energy measurements. The  $^{137}\text{Cs}$  spectra obtained with the two sum signals are shown in Fig. 6.7 where the extra amplification of the  $z_R$  signal can easily be observed.

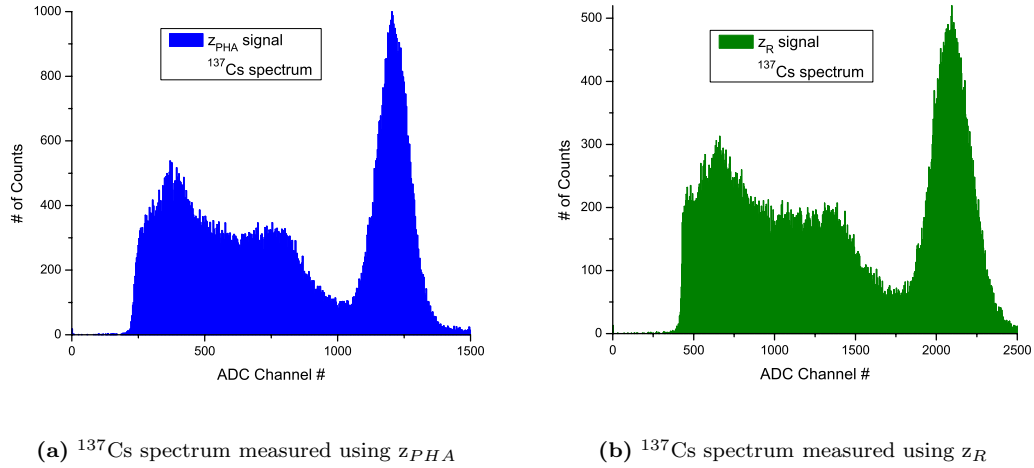


**Fig. 6.7:**  $^{137}\text{Cs}$  energy spectra measured with the two different  $z$  sum signals of the Anger camera. The only difference between the two is the higher amplification factor of the  $z_R$  which is used to obtain energy independent coordinate information.

The spectroscopic measurements were first performed by placing the source at each test point which corresponds to the center of photomultiplier tubes to check the uniformity of their response. The spectra obtained at the center, at the edge and at the regions in between are shown in Fig. 6.8. The photopeak efficiency decreases when moving from the center to the edge resulting in a degraded energy resolution by a factor of 1.5 %.

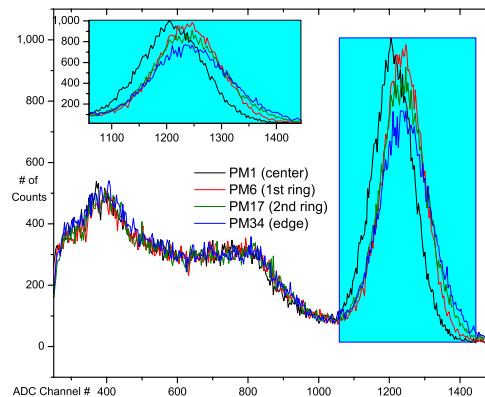


**Fig. 6.8:** Pulse height spectra measured at the center of PMTs located at the centre, at the first ring around the center, at the second ring around the center and at the edge. The attenuation in the pulse-height is observed when moving towards the edge where the energy resolution is 1.5 % worse than at the center.

The energy calibration measurements of the absorption detector is performed with  $^{137}\text{Cs}$  and  $^{133}\text{Ba}$  sources. The calibrated  $^{137}\text{Cs}$  spectrum in detail and the spectra from both sources are shown in Fig. 6.9. The energy resolution of NaI(Tl) is not good enough to discriminate different peaks of  $^{133}\text{Ba}$  source

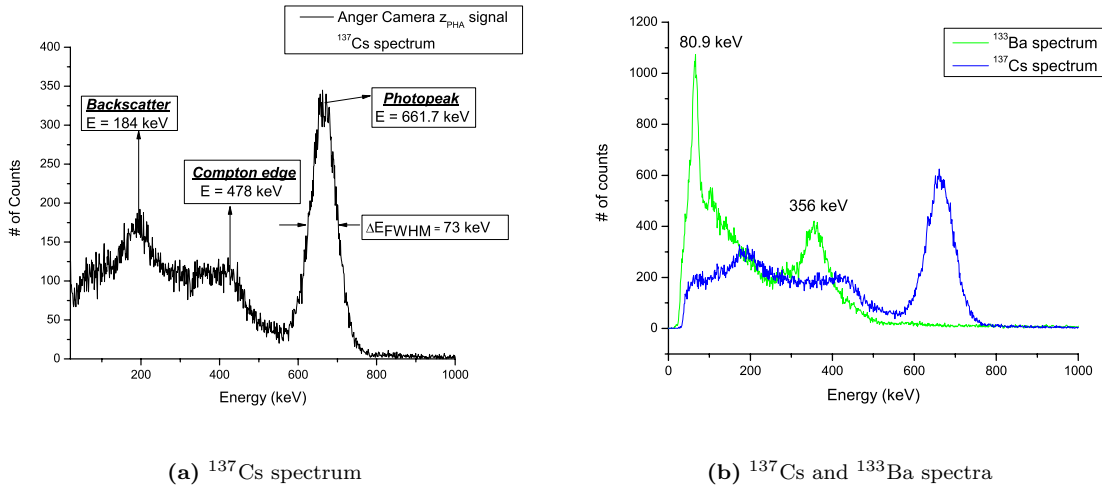


**Fig. 6.9:** Calibrated pulse height spectra measured with  $^{137}\text{Cs}$  and  $^{133}\text{Ba}$  sources

around 300 keV (276.4 keV (7.16 %), 302.9 keV (18.33 %), 356 keV (62.05 %) and 383.9 keV (8.94 %)), therefore a broad peak around the main line is observed. The mean energy resolution determined from the spectrum of the detector with the whole detection area illuminated by the source is around 11 % FWHM.

The x and y coordinate signals are first divided by the sum signal  $z_R$  and multiplied with a constant which needs to be determined. This constant has two components one of which is the scaling factor and

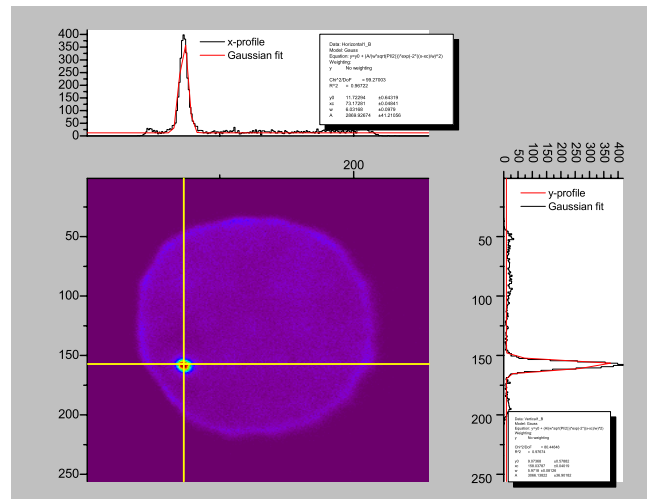


**Fig. 6.10:** x and y coordinate distributions obtained with a collimated source directed on a point on the camera.

the other is an empirical factor. The scaling factor is calculated theoretically considering the reported intrinsic resolution of the camera as follows: The diameter of the detector is 420 mm and the given

intrinsic resolution is 3 mm. Under these conditions, the minimum number of bits needed to resolve one pixel is 8 which gives a scaling factor of 256. The second factor is determined empirically by adjusting the center of the coordinate system to be located at (128,128) such that a symmetrical distribution is obtained around the center. The coordinate calibration of the Anger camera is performed with a collimated  $^{57}\text{Co}$  source which emits mainly photons of 122 keV energy. The surface of the detector is scanned in x and y directions and the mean of the resulting x and y distributions are compared with the known locations of the beam. A correction software was developed using the results of these measurements and more details will be available in the master thesis of J. Lu [Lu05]. An example of the coordinate distributions for one location of the source is shown in Fig. 6.10. The FWHM of x- and y- distributions correspond to a position resolution of about 10 mm without any extra correction algorithm applied on the data.

### 6.2.1 Timing Characteristics of the Anger Camera

In order to determine the time resolution of the Anger camera signal, the experimental setup shown in Fig. 6.11 was constructed. The setup is similar to the Compton camera system where the SDD is replaced

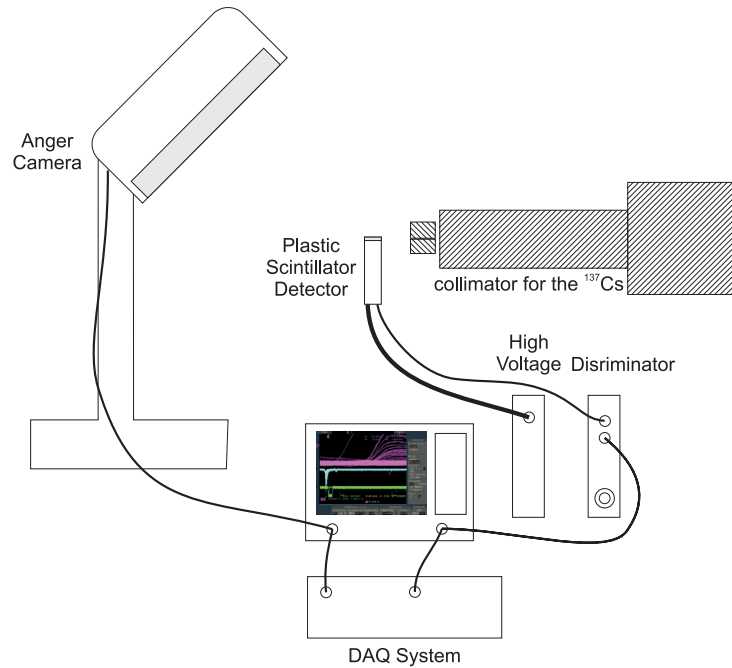


**Fig. 6.11:** Experimental setup arranged for the measurement of the timing characteristics of the Anger camera signal.

with a plastic scintillator detector for more accurate timing measurements. The plastic scintillator is a 5 mm thick cylinder with a diameter of 19 mm. The detector is placed such that the propagation length of the beam is along the diameter of the scintillator. Both the fast time signal of the Anger camera provided for fast triggering purposes and the energy signal were used for the coincidence measurements with the plastic scintillator. The time stamps of two detector signals were collected in continuous mode without enabling the coincidence logic. Fig. 6.12 shows the time coincidence curve obtained by subtracting these time stamps both with the time and the energy signals of the Anger camera. The time signal of the Anger camera is delayed by 200 ns with respect to the signal of the plastic scintillator. The energy signal of the camera has 60 ns longer delay than the time signal with respect to the fast plastic scintillator response. The FWHM of both distributions is approximately 45 ns which corresponds to the time resolution of the Anger camera.

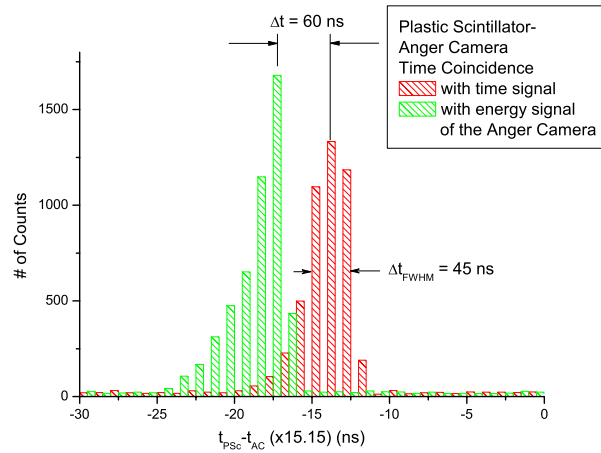


**Fig. 6.12:** Time coincidence curve for the events occurring in the plastic scintillator and in the Anger camera. The curve is a histogram of time stamps differences of the two detector signals. The measurements were performed with the time signal and also with the energy signal of the Anger camera.

### 6.3 First Coincidence Signals

The first coincidence signals [ÇN03; ÇN04a] were examined by direct observation on the oscilloscope. First of all, the signal produced by low energetic photons interacting in the scatter detector is measured. A faster shaper with a rise time of 50 ns has been used for these measurements. The shaper output when the SDD is irradiated with a  $^{55}\text{Fe}$  is shown in Fig. 6.13. With the photons of 6 keV energy, the signal

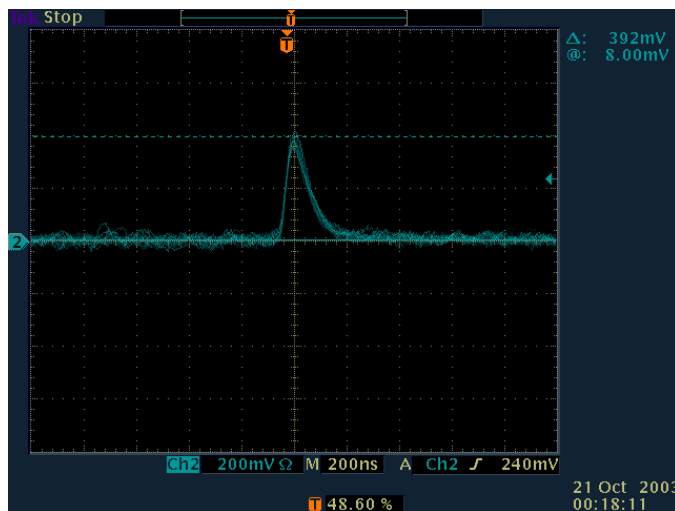
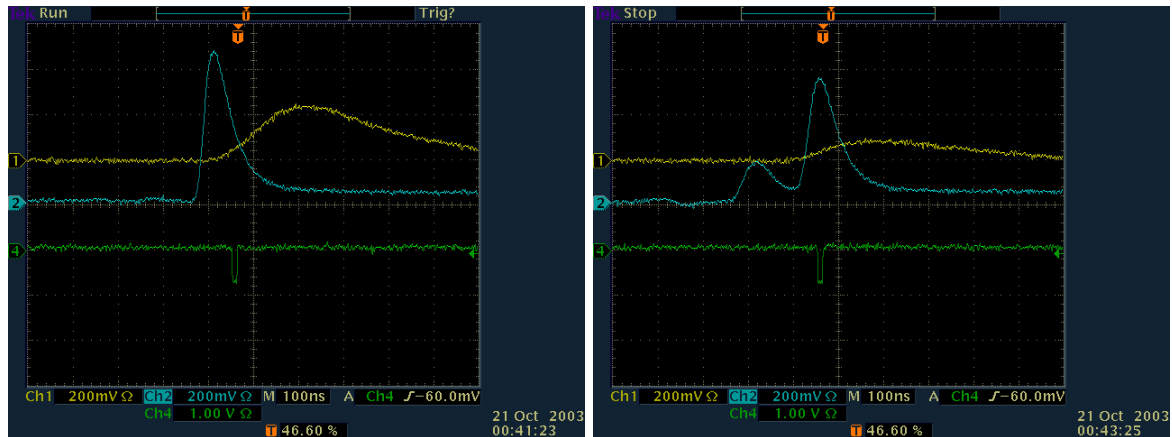


**Fig. 6.13:** Shaper output obtained with the SDD irradiated with 5-6 keV photons emitted from a  $^{55}\text{Fe}$  source.

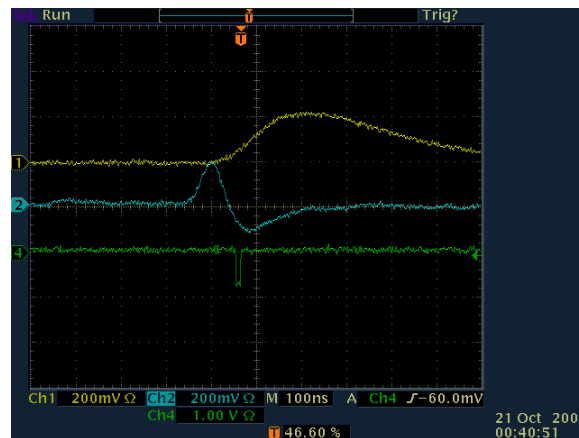
looks fine in terms of pole-zero cancellation, etc. There is a single pulse which varies in amplitude slightly due to 5.9 and 6.4 keV photons emitted.

After observing the SDD signals with X-rays, the detector is irradiated with gamma-rays emitted from a  $^{137}\text{Cs}$  source. The signals from the scatter detector and the absorption detector are connected to the coincidence unit whose gate signal is used as a trigger source for the detector signals. Fig. 6.14 shows the coincidence signals where various signal shapes of the SDD are observed, unlike the previous measurement



(a)

(b)



(c)

**Fig. 6.14:** Various shaper outputs obtained with  $^{137}\text{Cs}$  source. In each figure: middle signal: SDD signal, upper signal: Anger camera signal, lower signal: Coincidence gate

with an X-ray. The signal form shown in Fig. 6.14(a) occurs often when the energy deposited in the SDD is quite high. The signal with a double peak shown in Fig. 6.14(b) seems to be produced as a result of double Compton events occurring in the silicon. The statistical analysis of the SDD signals need to be performed to see the frequency of occurrence for such different signal forms. For this purpose, 2000 SDD signals were collected with a finely collimated beam ( $500\ \mu\text{m}$ ) directed on the center of an SDD cell and another set of 2000 signals was collected with the beam directed at the edge of the cell. With the SDD cell irradiated in the middle, it takes about 37 minutes to collect 2000 events, whereas when it is irradiated at the edge, the acquisition time extends up to 140 minutes. Out of 2000 signals only 4 in the central region and 1 in the edge region were observed to have double peak which agrees with a small probability of having double Compton scattering for  $661.7\ \text{keV}$  energetic photons in  $300\ \mu\text{m}$  thick silicon. The bipolar signal shown in Fig. 6.14(c) probably occurs when some of the electrons move toward the drain of the on chip JFET instead of moving toward the anode. The electron cloud diffuses more when the interaction occurs at the edge of the cell where the electric field is weaker. Out of 2000 SDD signals measured with a  $^{137}\text{Cs}$  source, 139 bipolar signals are observed with the beam directed to the center, but at the edge the number of bipolar signals increased to 403. The negative tail can be explained as follows: when the electrons reach the anode region, some of them could go to the transistor channel which is at

more positive potential than the anode. In this case, they move away from the anode and this produces the negative tail of the signal. This type of signals were observed to occur more frequently when the Compton scattering happens in a region where the electric field is weaker and also when the energy of the incoming beam is high. Only 1 out of 10000 signals measured with  $^{55}\text{Fe}$  source and 12 out of 1000 signals measured with  $^{109}\text{Cd}$  have bipolar shapes, whereas the fraction of bipolar events with a  $^{137}\text{Cs}$  source is much higher. When the energy is higher, more charge is created, the first part of the charge cloud reaches the anode and this makes the anode more negative compared to the drain which causes the remaining part of the cloud to tend to be attracted by the transistor channel.

The detailed pulse-shape analysis of such different signal forms may deliver useful information on the direction of the recoil electron which should be considered for the future project.

## 6.4 Coincidences with a Finely Collimated Beam

The next step was to examine the possibility of discriminating an event that occurs around the anode region of the SDD cell from an event occurring at the edge of the detector cell. For this measurement, fast shaping is a crucial requirement and a shaper with a rise time of 50 ns has been utilized. The beam should also be adjusted such that the collimation is fine enough to be able to scan different regions of the single cell. An additional lead block having a hole of  $400\ \mu\text{m}$  diameter is placed in front of the main collimator for fine collimation. The beam profile is measured at the location of the SDD where the beam

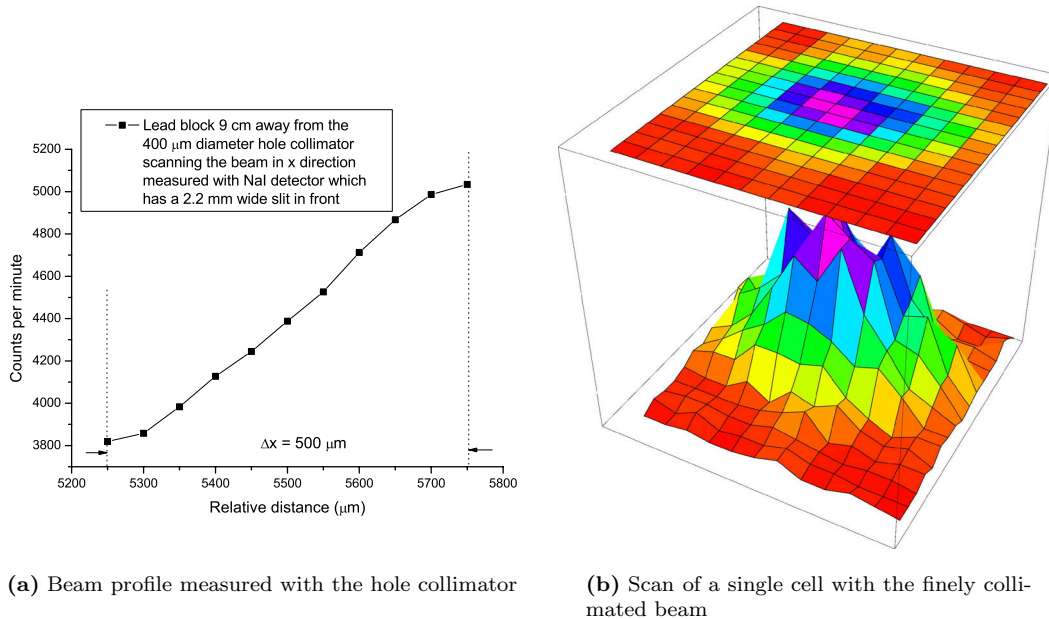


**Fig. 6.15:** Beam profile measured with the hole collimator placed in front of the main collimator shown in Fig. 4.2 and the count distribution obtained by scanning the single cell of the SDD in  $400\ \mu\text{m}$  steps with the finely collimated beam.

spread is only  $500\ \mu\text{m}$  as shown in Fig. 6.15(a). The x-y scan of one of the SDD cells with this finely collimated photon beam of  $661.7\ \text{keV}$  energy is shown in Fig. 6.15(b). The number of events was recorded for each position only for one minute and the hexagonal form of a cell is still clearly visible despite the low statistics. The accuracy of the collimation is also proven with this result.

The setup is arranged as shown in Fig. 6.16 for coincidence measurements to study the scattering events at different regions of the scatter detector [CN04c]. Considering the size of the beam spread, this study would at best be performed at the center and at the edge of the cell. The difference between the time stamps of the SDD and Anger camera events has been analyzed as a function of the drift field in

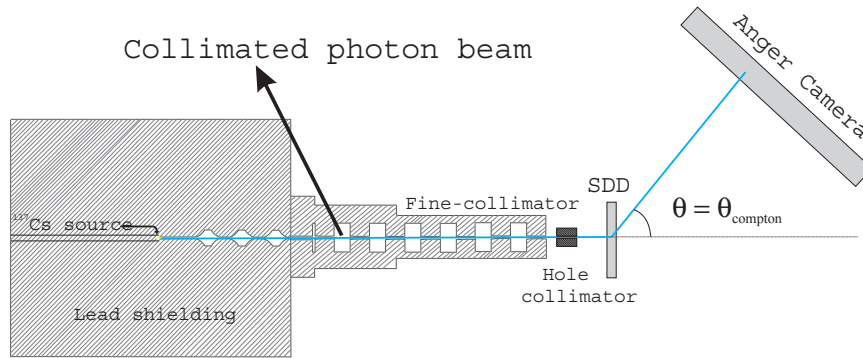


**Fig. 6.16:** Compton coincidence setup with a finely collimated photon beam.

the silicon detector. The results are shown both for the SDD cell irradiated at the center (6.17(a)) and at the edge (6.17(b)) in Fig. 6.17. At usual operating conditions of the scatter detector, the time stamp

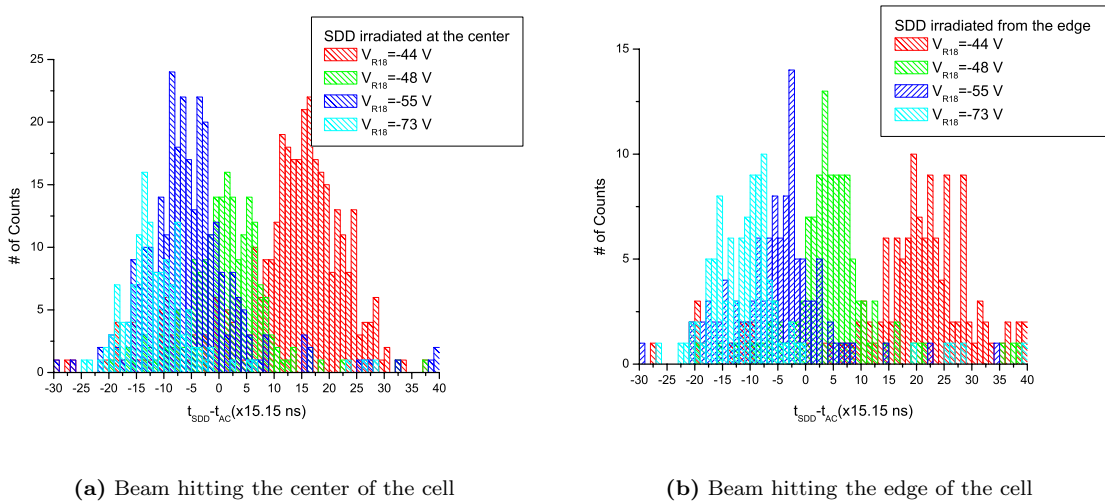


**Fig. 6.17:** The distribution of the difference of the SDD and Anger camera time stamps at different V drift fields in the SDD with the finely collimated beam (a) directed to the center of the cell, (b) directed to the edge of the cell.

difference between the SDD and Anger camera events is concentrated in the region from -300 ns to +75 ns. The negative sign indicates that the SDD signals arrive before Anger camera signals in time. As the drift field becomes weaker there is more delay in the SDD signals and the distribution shifts to the right, as expected. Both plots in Fig. 6.17 show a similar behaviour as a function of the changed drift voltage. The mean time difference between the two detector signals obtained from the Gaussian fit of the histograms shown in Fig. 6.17 is plotted as a function of the drift voltage in Fig. 6.18 for the center and the edge cases. The variation of the time difference for the beam hitting the center of the cell and the edge of the cell ( $(t_{SDD} - t_{AC})_{edge} - (t_{SDD} - t_{AC})_{center}$ ) remains stable around 20-35 ns between the drift voltage of -50 to -72 V. For the field voltages below 50 V, the time difference between the SDD and Anger camera signals with the beam directed to the edge of the SDD increases considerably with respect to the beam hitting the center. At -45 V of R18 voltage the difference ( $(t_{SDD} - t_{AC})_{edge} - (t_{SDD} - t_{AC})_{center}$ ) becomes 90 ns. Therefore, in principle, it should be possible to discriminate the events occurring in the middle of the SDD cell from those occurring at the edge of the cell when the drift field is much lower than

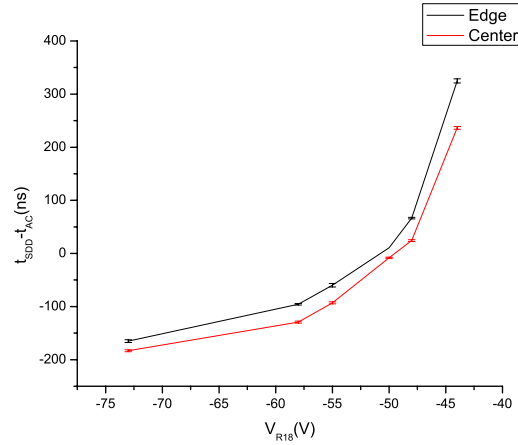


**Fig. 6.18:** The mean time difference between the SDD and the Anger camera signals as a function of the voltage at the Ring 18 which determines the strength of the drift field.

usual at the expense of the energy resolution due to the loss of charge that can reach the anode.

Further coincidence measurements have been performed to gather high statistics of coincidence events for systematical analysis of energy and angular distribution. These measurements are performed at normal operating conditions of the SDD and with a shaper having a peaking time of 100 ns. The position of the SDD was adjusted such that the beam hits the center of the single cell of the detector. The Anger camera is positioned to cover the scattered photons in an angular range of  $10^\circ$  -  $50^\circ$ . At the energy of the  $^{137}\text{Cs}$  source, the distribution of the scattered photons peak around  $30^\circ$ , therefore, this angular range is suitable to collect high statistics of Compton coincidences. With the first version of the data acquisition

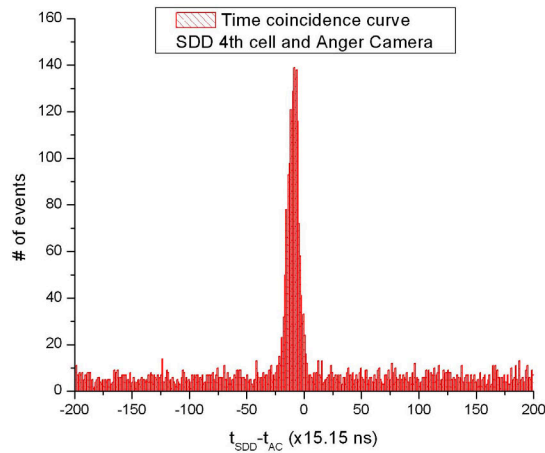


**Fig. 6.19:** Time coincidence curve for the events occurring in the 4th cell of the SDD and the Anger camera.

software, all the events were collected from the scatter and absorption detectors and the coincidence events were filtered by the offline analysis software. As a result of 128 hours of data taking,  $4.50 \cdot 10^8$  Anger camera events and  $4.35 \cdot 10^5$  SDD events in a single channel of the SDD are collected. The data collected consists of the time stamp and peak data of the SDD and time stamp, peak, corrected peak, x

and y coordinate data of the Anger camera. The time coincidence curve obtained using the time stamp information from both detectors is shown in Fig. 6.19 for the time stamp difference restricted to  $\pm 3 \mu\text{s}$ . There are 3840 coincidence events in the time coincidence window of  $\pm 3 \mu\text{s}$  and in the peak region which is between  $-300 \text{ ns}$  to  $+75 \text{ ns}$  there exist 1653 coincidence events. The FWHM value of the time coincidence peak is around  $250 \text{ ns}$  which mainly results from the drift time of the electrons in the SDD. Although a wide region of time coincidences are scanned, most of the events concentrate in the region where  $-300 \text{ ns} < t_{SDD} - t_{AC} < 75 \text{ ns}$ . The events located in this region are selected for further analysis of coincidence events.

The energy spectra of these events in the scatter detector and in the absorption detector are shown in Fig. 6.20. The energy of the scattered photon ranges from  $650 \text{ keV}$  to  $453 \text{ keV}$  for the scattering angular region of  $10^\circ$ - $50^\circ$ . The photopeak region in Fig. 6.20(a) agrees with the theoretical assumption, namely the energy range is around  $450$ - $650 \text{ keV}$ . The events located below this range correspond to Compton scattering events in the absorption detector. The energy spectrum of recoil electrons shown in Fig. 6.20(b) ranges up to about  $200 \text{ keV}$  and at low energies there are more events located due to the higher probability of electron absorption at lower energies.

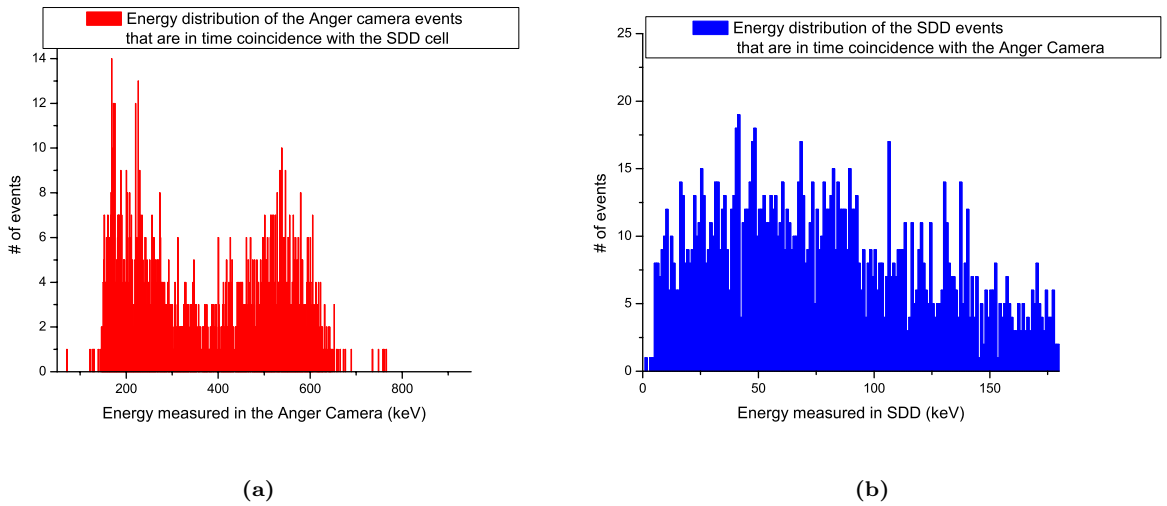


**Fig. 6.20:** Energy spectra of the coincidence events in the scatter and the absorption detectors. The events located in the peak region of the time coincidence curve have been selected for this analysis.

Electron energy distribution as a function of the Compton scattering angle is shown in Fig. 6.21. In Fig. 6.21(a) the Compton scattering angle is calculated from the energy measured in the absorption detector. The theoretical expectation curve is also plotted in the figure and the electron energy distribution does not really show a pattern similar to the theoretical curve. This is due to the fact that the Anger camera's energy resolution imposes a large uncertainty in determining the scattering angle. Besides, the fraction of the Compton events with an escaping scattered photon in the Anger camera is quite high as shown in Fig. 6.22 where the events around the theoretical curve are photoabsorption events, whereas the rest events below this curve are Compton events. This causes an error in the calculation of the scattering angle since it is assumed that the total energy of the scattered photon is measured in the absorption detector, however for Compton scattering events only a part of this energy is absorbed. With the fine collimation of the beam which has an angular spread of only  $0.03^\circ$ , one can assume that the incoming photons are directed perpendicular to the surface of the SDD. In this case, the Compton scattering angle can be measured using the coordinate information of the events occurring in both detectors as shown in Fig. 6.16 where  $\theta$  is assumed to be equal to  $\theta_{Compton}$ . The energy of the recoil electron measured in the SDD as a function of the Compton scattering angle which is calculated using the coordinate measurement in the Anger camera is shown in Fig. 6.21(b). The resulting distribution is located around the expected

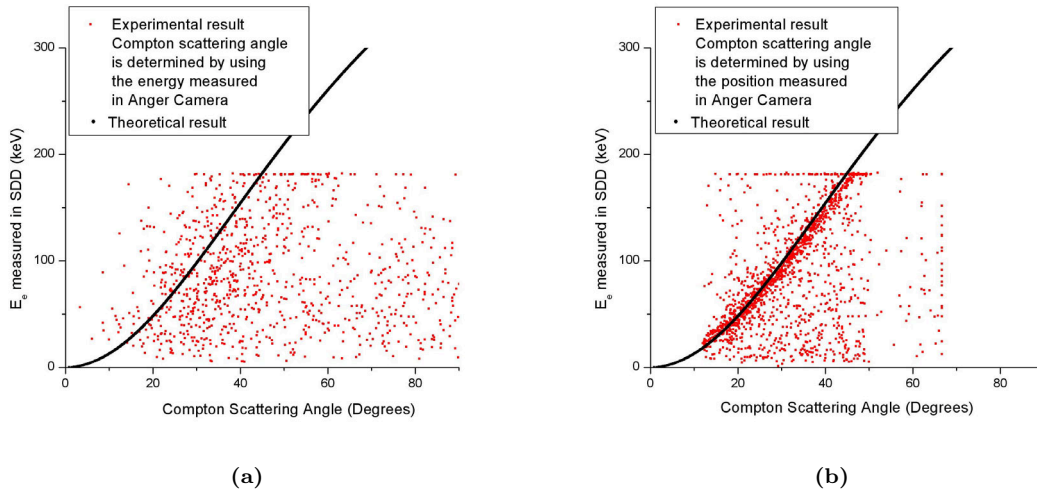


**Fig. 6.21:** Electron energy measured in the scatter detector as a function of the Compton scattering angle which is calculated (a) from the energy measured in the absorption detector, (b) from the coordinate measurements in both detectors.

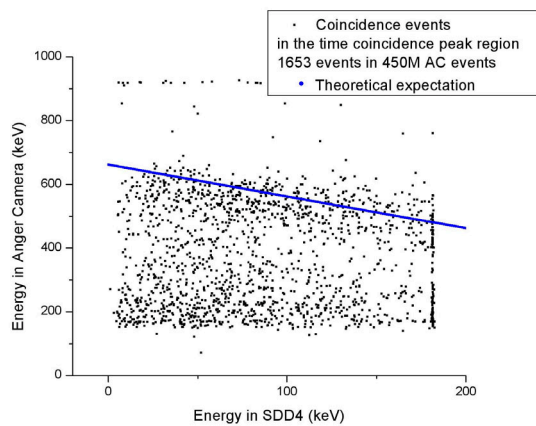


**Fig. 6.22:** Measured photon energy in the absorption detector as a function of the electron energy measured in the scatter detector.

curve with some other events where mostly the recoil electron is not fully captured in the scatter detector. Such partial events are located below the theoretical curve and there are also few events located above this curve which would result in a total energy measured in both detectors that is higher than the incoming photon energy. Some of these events are located very close to the theoretical curve and they are due to the uncertainties in the energy and position measurements. The rest which are well above this curve mainly corresponds to false coincidence events which occur within the narrow time coincidence window but are independent of each other.

Using the energy measured in the scatter detector and the coordinates measured in both detectors, the image of the point-like source is reconstructed. Fig. 6.23(a) shows the simple backprojected image and Fig. 6.23(b) shows the resulting image after applying a reconstruction algorithm. For the image reconstruction a new implemented algorithm [Chi04] which is based on the imaginary time expectation maximization (ITEM) algorithm [Pau02] is used. ITEM is a minimization technique motivated from quantum mechanics. This technique works with a Hamiltonian-like operator acting on the actual image

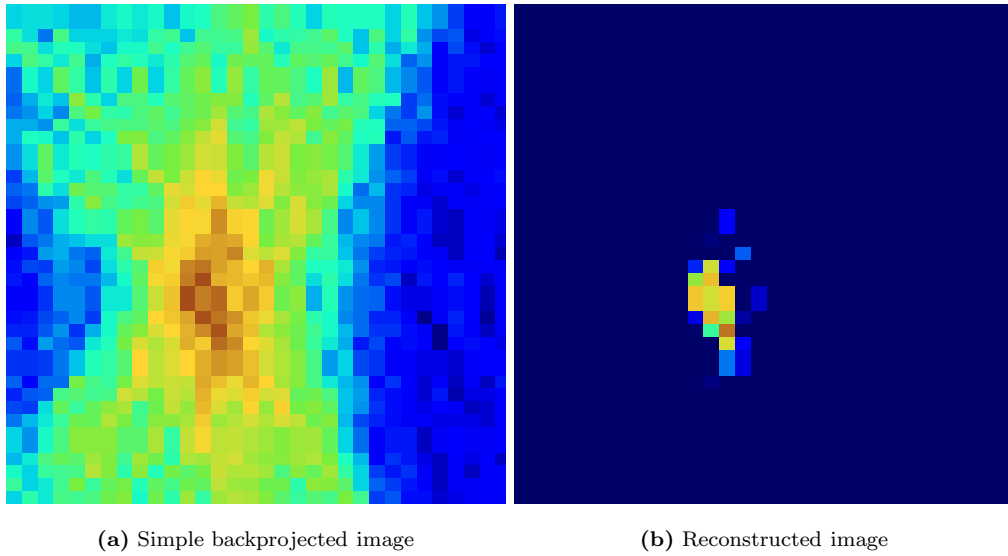


**Fig. 6.23:** Reconstructed image for 1653 coincidence events after applying a (a) simple backprojection, (b) reconstruction algorithm. Each pixel in the reconstructed image is 2 mm.

which is identified with a wavefunction. The reconstruction is performed in two steps:

- preanalysis: a simple backprojection is performed with voxels that are large (instead of 1x1, 4x4 voxels are chosen) and the obtained distribution is used for defining different parameters required for the reconstruction process
- reconstruction: iterative process starts with the distribution obtained in the preanalysis stage. A modified projection method together with a Monte-Carlo technique is used to improve the reconstructed image iteratively. In this way, one obtains the reconstructed three-dimensional distribution of the source at the final iteration.

With the present system, due to the restricted pixel resolution, the 3D reconstruction was not possible, therefore the results presented here corresponds to 2D reconstructed images. The cones in the backprojected image are concentrated on the upper and the lower part of the image due to the restricted angular region covered by the absorption detector.

## 6.5 High-Statistics Coincidence Measurements

The hole collimator is removed in order to obtain higher statistics of coincidence events. Without the hole collimator, the beam spread is around a factor of 10 larger and simultaneously more SDD cells can be covered by the beam. The Anger camera's orientation is adjusted such that an angular range of  $10^\circ$ - $50^\circ$  is covered for the scattered photons leaving the scatter detector. With the FPGA on the master card programmed for online trigger selection, the acquisition of the time coincidence events within a selected time window became possible. In this way, with the new version of the data acquisition software, one can acquire only the useful data from the two detectors which fulfill the time coincidence requirement. The time window for these good events are selected to be between the  $-300 \text{ ns} < t_{SDD} - t_{AC} < 75 \text{ ns}$  where most of the coincidence events are peaked. The coincidence rate between the 13 SDD cells and the Anger camera is around 9 time coincidence events per 10 seconds (0.9 Hz) which makes the collection of  $10^6$  Compton events within 2 weeks possible.

2D histogram plot of the electron energy distribution in the SDD as a function of the scattering angle is shown in Fig. 6.24. The scattering angle is calculated using the energy measured in the absorption

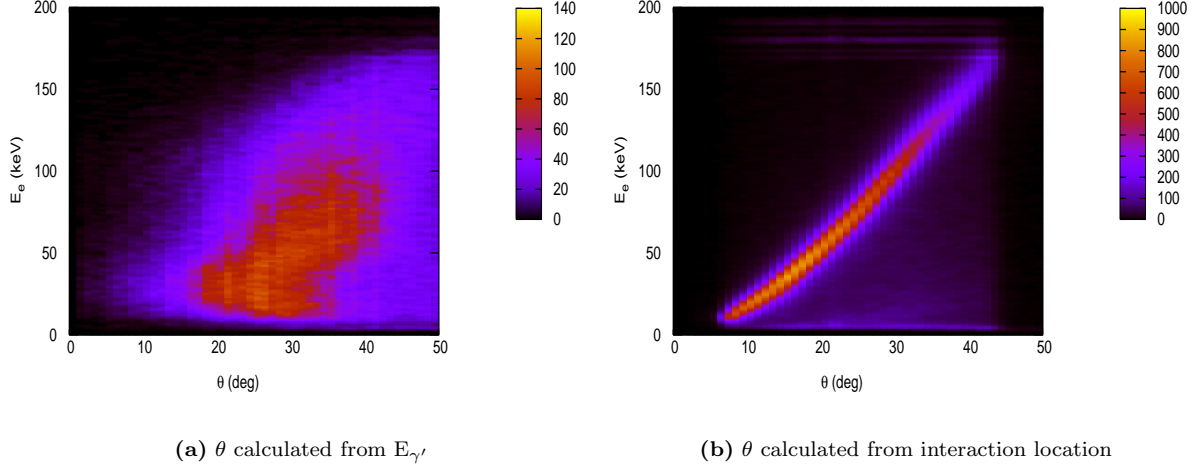


**Fig. 6.24:** Electron energy measured in the scatter detector as a function of the Compton scattering angle which is calculated (a) from the energy measured in the absorption detector, (b) from the coordinate measurements in both detectors.

detector in Fig. 6.24(a), whereas in Fig. 6.24(b), it is calculated using the location of the coincidence events measured in the Anger camera. The beam spread is still quite small ( $0.3^\circ$ ), therefore, while the scattering angle is calculated from the coordinate measurement, it was assumed that the beam hits the scatter detector orthogonal at each cell location.

Fig. 6.24 shows that when the scattering angle is calculated from the energy measured in the Anger camera, the result is not promising due to the large uncertainty in the energy measurement of the scattered photons in the absorption detector and large fraction of Compton scattering in this detector which results in a partial absorption of the  $E_{\gamma'}$ . However, the coordinate measurement in the absorption detector that delivers the information on the location of the events produce much more accurate distribution of the electron energy as a function of the scattering angle.

Electron energy at different scattering angles is obtained using the data of Fig. 6.24(b). The electron energy distribution at various scattering angles is shown in Fig. 6.25. As the scattering angle increases the number of events decreases due to a lower Compton cross section at high scattering angles and also higher energy of the recoil electron which results in a lower probability of the electron capture in the scatter detector. The distribution of the electron energy at  $20^\circ$  of scattering angle is analyzed in detail in Fig. 6.25(b). The tail of the distribution on the left side is due to the partial absorption of the electron energy in the scatter detector. The uncertainty in the distribution includes the contributions from the energy resolution, Doppler broadening and the uncertainty in coordinate measurements. Besides, due to the binning of the histogram the angular range of consideration is  $20^\circ$ - $21^\circ$  which results in an energy fluctuation of 4.5 keV. The contribution from the energy resolution of the silicon drift detector at the mean energy of 50 keV is 485 eV FWHM and the Doppler broadening contributes about 2.75 keV. Therefore, the broadening of the energy distribution is mainly due to the uncertainty in the measurement of the interaction position which is used to calculate the Compton scattering angle.

The energy distribution of the scattered photons measured in the absorption detector as a function of the Compton scattering angle is shown in Fig. 6.26. In Fig. 6.26(a) the scattering angle is calculated from the energy measured in the scatter detector using the following relation:

$$\theta = \arccos \left( \frac{\frac{1}{m_e c^2} (E_\gamma^2 - E_e E_\gamma) - E_e}{\frac{1}{m_e c^2} (E_\gamma^2 - E_e E_\gamma)} \right) \quad (6.1)$$

, whereas in Fig. 6.26(b), it is calculated from the location of the interactions. Unlike in Fig. 6.24, where the scattering angle calculated from the energy measured in the absorption detector is almost unusable,

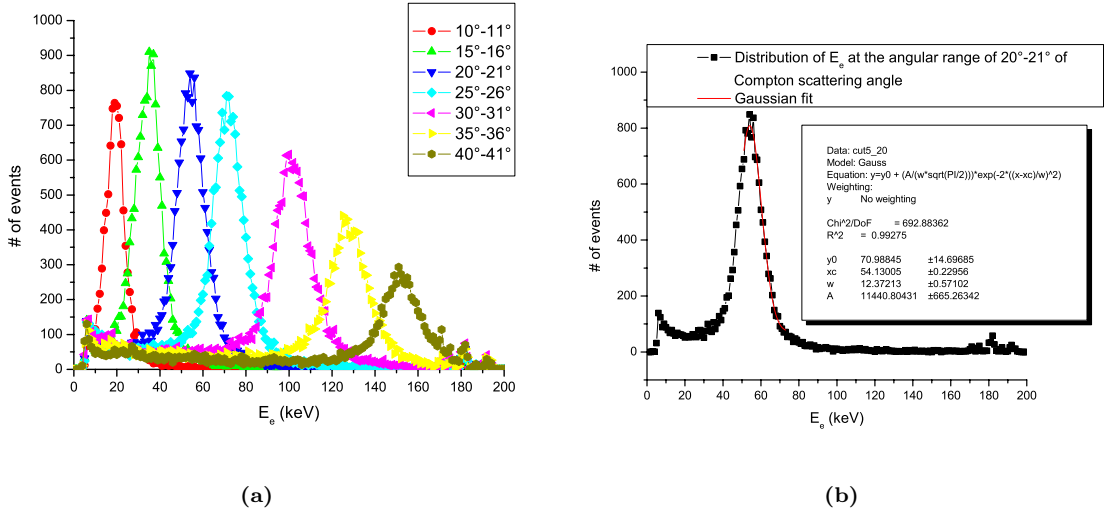


**Fig. 6.25:** Electron energy distribution measured in the scatter detector at various scattering angles where the Compton scattering angle is calculated using the coordinate measurement of the coincidence events.

here the energy measured in the scatter detector provides a similar result like the coordinate measurement. When the figures 6.24(b) and 6.26(b) are compared, it is clear that the energy measurement in the silicon

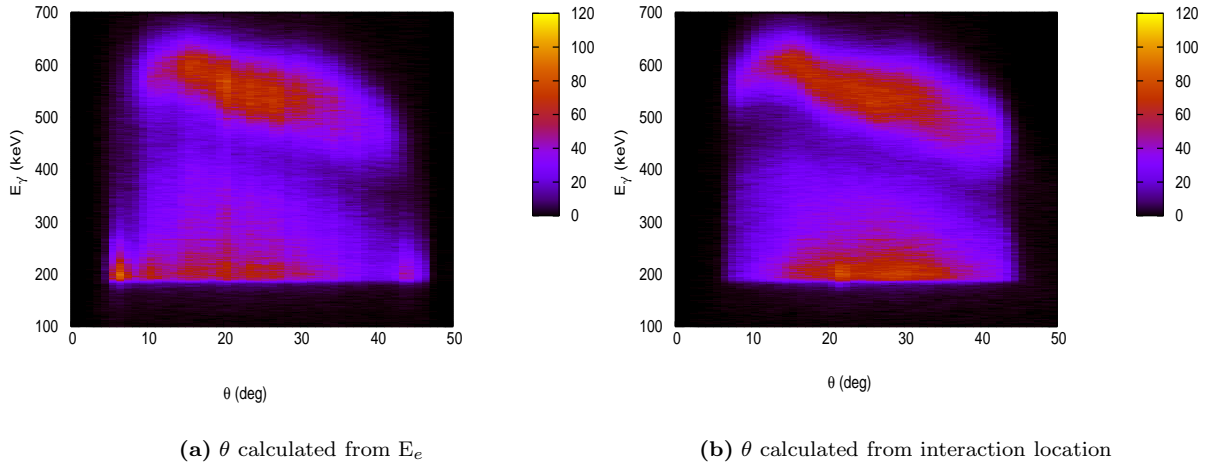


**Fig. 6.26:** Scattered photon energy measured in the absorption detector as a function of the Compton scattering angle which is calculated (a) from the energy measured in the scatter detector, (b) from the coordinate measurements in both detectors.

detector provides much more accurate result than the energy measured in the Anger camera, as expected. The energy distribution of the scattered photon consists of two parts in both plots where the upper curve represents the scattered photons undergoing a photoelectric absorption following the relation between the  $E_{\gamma'}$  and  $\theta$  which is defined as:

$$E_{\gamma'} = E_{\gamma} \frac{m_e c^2}{m_e c^2 + E_{\gamma}(1 - \cos\theta)} \quad (6.2)$$

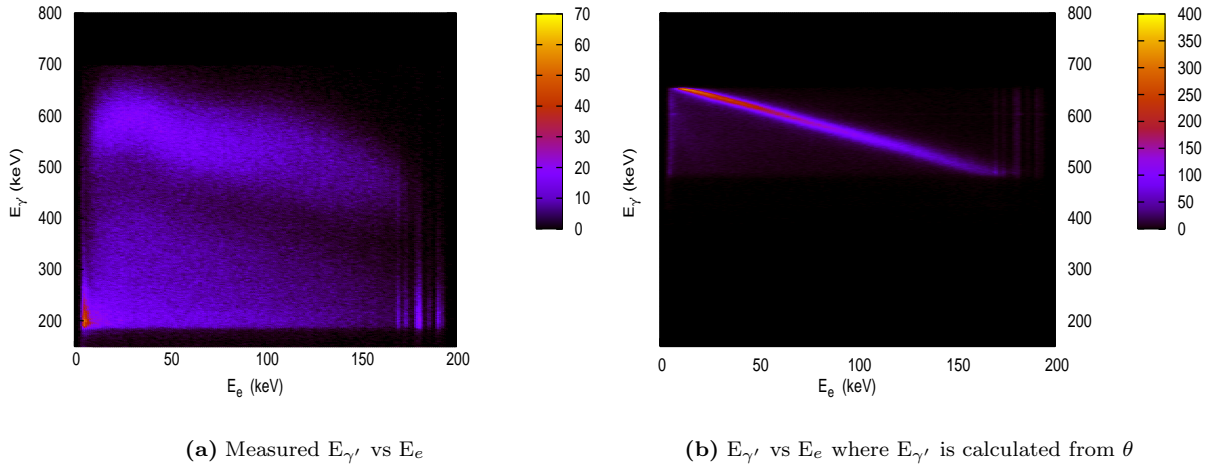


**Fig. 6.27:** Scattered photon energy as a function of the recoil electron energy measured in the scatter detector: (a) both energies measured, (b) energy of the scattered photon is determined from the scattering angle which is calculated from the locations of the interactions.

and the events below this curve contain the Compton scattered photons in the absorption detector which result in the partial absorption of the  $E_{\gamma'}$ . This demonstrates the fact that the fraction of the Compton scatter events in NaI(Tl) is quite high at this energy range. The photoabsorption efficiency of the absorption detector can be improved by choosing a detector material of higher  $Z$  but it is more efficient to get use of the Compton scatter events by tracking the scattered photon in the absorption detector.

Scattered photon energy as a function of the recoil electron energy measured in the scattered detector is shown in Fig. 6.27. In Fig. 6.27(a) the energy of the scattered photon is determined from the energy measurement in the absorption detector. The broad distribution is due to the energy resolution of the Anger camera which is not good enough to resolve the energy of the scattered photons accurately. The plot again consists of two parts where the upper curve contains the scattered photons undergoing a photoelectric absorption in the Anger camera and the events below are Compton scattering events in this detector. Fig. 6.27(b) shows a much better distribution which follows the theoretical expectation closely. In this plot, the energy of the scattered photon is calculated from the scattered angle that is determined using the interaction location measured in the Anger camera, rather than the energy measured in this detector. The difference between these figures is not only due to the energy resolution in the Anger camera but also due to the partial absorption of the energy of the scattered photon in this detector. When the interaction location is used to determine the scattering angle, these events are not taken into account as partial events but rather as complete events, whereas the energy measurement demonstrates such events which broaden the distribution.

The total angular uncertainty estimated for the reference system defined in Section 3.3 is plotted as a function of the scattering angle in Fig. 6.28. The scatter detector is a silicon drift detector with an ENC of 40 electrons rms and the energy of the incoming photon is 661.7 keV. This system corresponds to the present detector system but the source-scatter detector and the inter-detector distances are taken to be 10 cm and 20 cm, respectively. For this configuration, the geometric uncertainty is obviously the dominant factor up to about  $110^\circ$  where the Doppler effect becomes dominant.

The spatial spread in the measurement of the source location can be written as:

$$\Delta x = D_1 \tan(\Delta\theta) \quad (6.3)$$

which is about 4.5 mm in average in the forward scattering region for the system considered in Fig. 6.28. There are several parameters which can be improved to get much better result. The Doppler broadening imposes a lower limit in the achievable resolution. 40 electrons rms energy resolution of the silicon drift detector is a very good performance compared to other available detectors and in fact, detector of

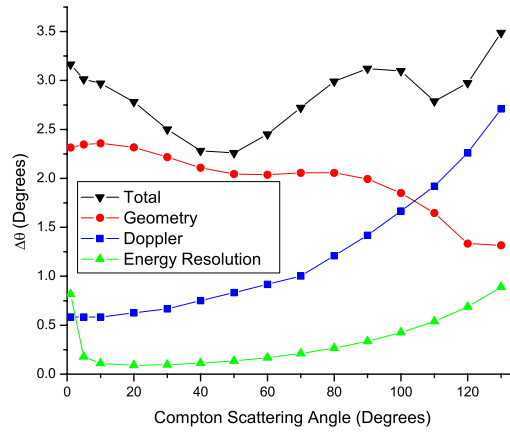
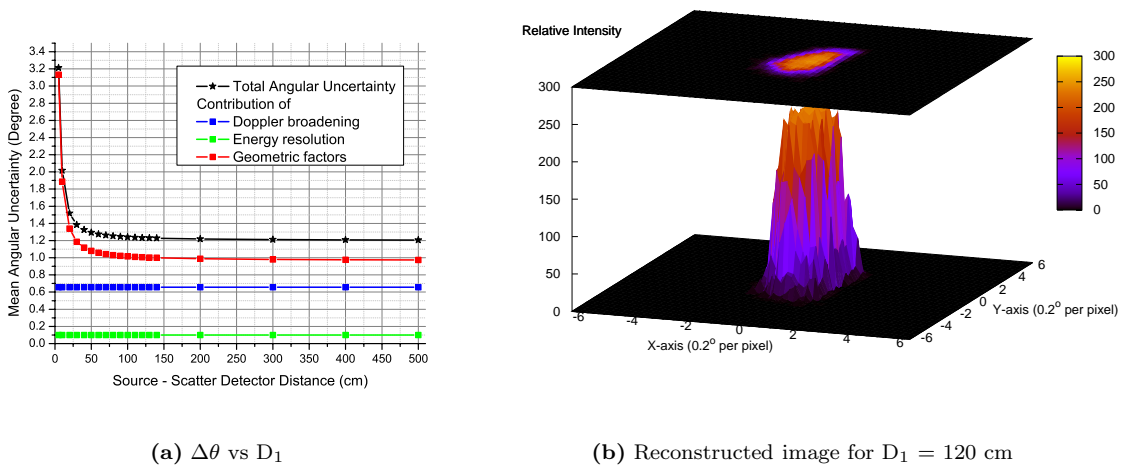


**Fig. 6.28:** Total angular uncertainty estimated for a system with  $300 \mu\text{m}$  thick Si scatter detector having 2.35 mm pixel size and 40 electrons rms ENC placed 10 cm away from the  $^{137}\text{Cs}$  source and 20 cm away from the NaI detector with a thickness of 0.95 cm and a position resolution of 3 mm

this type even with a better energy resolution is available. Therefore, the geometric factors need to be improved in a way that better spatial resolution and depth of interaction resolution in both detectors are achieved. Other parameters such as the distance between the source and the first detector and the inter-detector distance are parameters which can be relatively easily modified.

The total mean angular resolution and individual contributions from the system geometry, energy resolution of the scatter detector and the Doppler broadening calculated theoretically for the current system are shown in Fig. 6.29(a) as a function of the source-scatter detector distance. The energy



(a)  $\Delta\theta$  vs  $D_1$

(b) Reconstructed image for  $D_1 = 120$  cm

**Fig. 6.29:** (a) Mean angular uncertainty calculated theoretically with individual components shown explicitly, (b) the reconstructed image for a point-like source located 120 cm away from the scatter detector. The FWHM angular uncertainty calculated at this distance is within expectation limits.

measured in the scatter detector and the positions of the events measured in both detectors are used for the image reconstruction of the source with the methods mentioned in the previous section. The

reconstructed image is shown in Fig. 6.29(b) where the FWHM angular uncertainty corresponds to  $1.4^\circ$  which is in good agreement with the expected value of the FWHM angular resolution of  $1.3^\circ$  at a source-scatter detector distance of 120 cm.

## 7. Conclusions and Future Work

A detector system to study the performance of Compton cameras for gamma-ray imaging with a focus on nuclear medicine applications has been designed, constructed and tested. The system is the first Compton camera imager using a silicon drift detector with on-chip electronics as the scattering detector. The detector has an excellent energy resolution even at room temperature. With a measured mean ENC of 45 electrons rms at room temperature, it owns the best energy resolution among the silicon detectors that have been used as a scatter detector in Compton camera prototypes. A refurbished Anger camera, with its hole collimator removed, was used as an absorption detector to obtain a large field of view for the scattered photons.

In this chapter, first the achievements reported in this work and conclusions will be summarized and then the future plans for improving the system in terms of efficiency and imaging performance will be discussed.

### 7.1 Conclusions

The influence of the detector parameters on the quality of a Compton camera image has been investigated using Monte Carlo simulations and efficiency calculations. Radionuclides with gamma energies larger than 300 keV should be used to keep the uncertainty due to the Doppler effect in the Compton scattering process sufficiently small. The mean angular uncertainty due to Doppler broadening and energy resolution of the scatter detector together with the Doppler contribution alone are summarized in Tab. 7.1 for various radionuclides. The equivalent noise charge of 26 electrons rms was considered for the scatter detector because this value is easily achievable with the silicon drift detector having the first transistor integrated directly on the chip. The position resolution is also calculated for a source located 15 mm away from the scatter detector. Only the forward scattering region is considered, namely the mean of the angular uncertainty is calculated for a Compton scattering region of  $[0^\circ, 90^\circ]$ .

Radionuclide	$E_\gamma$	$\langle \Delta\theta \rangle_{Doppler}$	$\langle \Delta\theta \rangle_{Doppler+\Delta E}$	$\langle \Delta x \rangle$ for $D_1 = 15$ mm
$^{113m}\text{In}$	391.7 keV	1.26°	1.37°	359 $\mu\text{m}$
$^{58}\text{Co}$	810.8 keV	0.73°	0.76°	199 $\mu\text{m}$
$^{47}\text{Ca}$	1.3 MeV	0.56°	0.58°	152 $\mu\text{m}$
$^{24}\text{Na}$	2.75 MeV	0.42°	0.44°	115 $\mu\text{m}$

**Tab. 7.1:** Angular and position resolutions due to Doppler broadening and energy resolution of the scatter detector

Doppler broadening contributes to the achievable position resolution much more than the energy resolution with this scatter detector. Thus, it is wise to use the SDD as a scatter detector since it offers a good energy resolution which contributed negligible amount of uncertainty compared to other detectors. With an increasing photon energy, the contribution from the Doppler broadening becomes less important and the geometric factors dominate. The thickness of the scatter detector in which the energy of the Compton scattered electron has to be measured plays an important role in terms of efficiency. On the other hand, if the detector is made thicker, it should have a depth of interaction resolution. A scatter detector with a depth of interaction resolution of 50  $\mu\text{m}$  contributes 0.588° to the mean angular uncertainty in the forward scattering region, whereas this contribution would increase to 0.88° for a

detector with a depth of interaction resolution of 1 mm. Therefore, both efficiency and the resolution should be considered for the Compton camera system design. It was shown that the contribution of the geometrical uncertainty to the overall uncertainty is larger than other factors for the Compton camera system presented in this work. The intrinsic resolution of the detectors and the depth resolution which is limited with the thicknesses of the detectors influence the overall resolution considerably.

Fast readout of the SDD signals was achieved within the frame of this work by an additional transistor in emitter follower configuration following the on-chip transistor. In this way, the typical rise time of the preamplified SDD signal has been reduced from 300 ns to 60 ns which made the fast shaping of these signals possible. Shaper with a rise time of 50 ns has been used for fast timing measurements. Tracking of the recoil electron is an important issue which reduces the uncertainty in the event circle to an arc. First attempts to extract a useful information from the pulse shape analysis of the scatter detector have been presented. Single layer of 300  $\mu\text{m}$  thick Si detector without a fast trigger signal from the back electrode is not an ideal scatter detector for tracking the recoil electron but multiple layers of Si detectors with fast trigger signals would be appropriate for this purpose.

Coincidence measurements have been performed with a collimated  $^{137}\text{Cs}$  source emitting 661.7 keV photons. Anger camera's orientation was adjusted to cover the angular range of  $10^\circ$ - $50^\circ$  for the scattered photons. The Compton scattering cross section has a maximum around  $30^\circ$  of scattering angle at this energy, therefore it is useful to obtain high statistics of coincidence events in a short time. The collimated source emits approximately 120000 photons per second and with the readout of 13 SDD channels the time coincidence rate was around 9 events per 10 seconds. This corresponds to a system efficiency of  $7.5 \cdot 10^{-6}$ . The efficiency estimated considering the Compton efficiency in the scatter detector, interaction efficiency in the absorption detector and the solid angle covered by the second detector is approximately of the order of  $3 \cdot 10^{-5}$ . The difference between the estimated and measured efficiency is mainly due to the fact that not all the SDD cells irradiated by the beam are readout.

The energy measured in both detectors have been analyzed as a function of the Compton scattering angle. For the recoil electron energy the scattering angle is calculated using the energy of the scattered photon measured in the absorption detector. It was shown that the energy resolution of the Anger camera is not sufficiently good for the accurate calculation of the Compton scattering angle. However, with a finely collimated beam it could be assumed that the beam is directed orthogonal to the scatter detector which enabled the determination of the scattering angle from the coordinate measurement in the absorption detector. As a result, the distribution of the electron energy measured in the SDD as a function of the scattering angle calculated from the coordinate measurement agrees with the theoretical expectation curve much better than the distribution where the scattering angle is calculated from the measured energy in the Anger camera. On the other hand, the energy measured in the absorption detector as a function of the scattering angle calculated both from the energy measured in the silicon detector and from the coordinate measured in the Anger camera produced similar results due to the good energy resolution of the scatter detector and the broadened distribution of the scattered photon's energy.

At the energy range of scattered photons which is 450-650 keV for these measurements, Compton scattering cross section is larger than a photoabsorption cross section by a factor of 3.5-7.5. This can easily be seen at the energy distribution plots where the energy measured in the absorption detector is shown. The distribution has mainly two parts the photoabsorption events are located on the upper curve and the rest of the distribution corresponds to Compton scattering events. One can benefit from such a large fraction of Compton events by tracking the scattered photons in the absorption detector. Without this method, one should apply an energy window for the total energy measured in two detectors to filter such events which unfortunately reduces the event statistics.

Finally, using the energy measured in the scatter detector and the interaction locations in both detectors, it was attempted to reconstruct the point source which is located 120 cm away from the scatter detector. The reconstructed image has an angular uncertainty of  $1.4^\circ$  FWHM which agrees well with the theoretically expected angular uncertainty of  $1.3^\circ$ . The theoretical result indicates that the main limit of the angular resolution is due to the geometric factors which can be improved by having detectors with better position and depth of interaction resolutions.

## 7.2 Future Work

Compton camera system can only be considered as an alternative to the existing imaging systems in nuclear medicine if its sensitivity and resolution outperform these systems.

The sensitivity of the camera system can be improved by having a stack of detectors, especially for the scatter detector [Wal03]. The recoil electrons can have energies up to few hundred keVs and considering the standard wafer thickness for silicon, it is more likely that they hit consecutive detectors. In this case, tracking the recoil electron by the methods of pattern recognition of track segments not only provide full detection of its energy but also improve the reconstruction process since only a segment of the backprojected cone is considered. A state-of-the-art Controlled Drift Detector (CDD) [Cas04a] is an excellent candidate for the scatter detector due to its excellent energy resolution even at room temperature (ENC  $\approx$  30 electrons rms), good position resolution which is around  $150 \mu\text{m} \times 150 \mu\text{m}$  and its time resolution which can be as short as 5 ns.

It was shown that a large fraction of events in the absorption detector is composed of Compton events even in a heavy scintillator detector. Gamma tracking techniques used in nuclear physics research [Bec02] can be applied in Compton camera applications to improve the sensitivity of the system. With the multiple events also utilized in the absorption detector for the reconstruction, a thick Si detector with much better position and energy resolution than a scintillator detector can also be used as an absorption detector. Si(Li) detector with double sided readout [Pro04] allowing a three dimensional vertex resolution of the interactions in this detector is an appropriate candidate for the purpose of the reconstruction of multiple scattering events in the absorption detector.

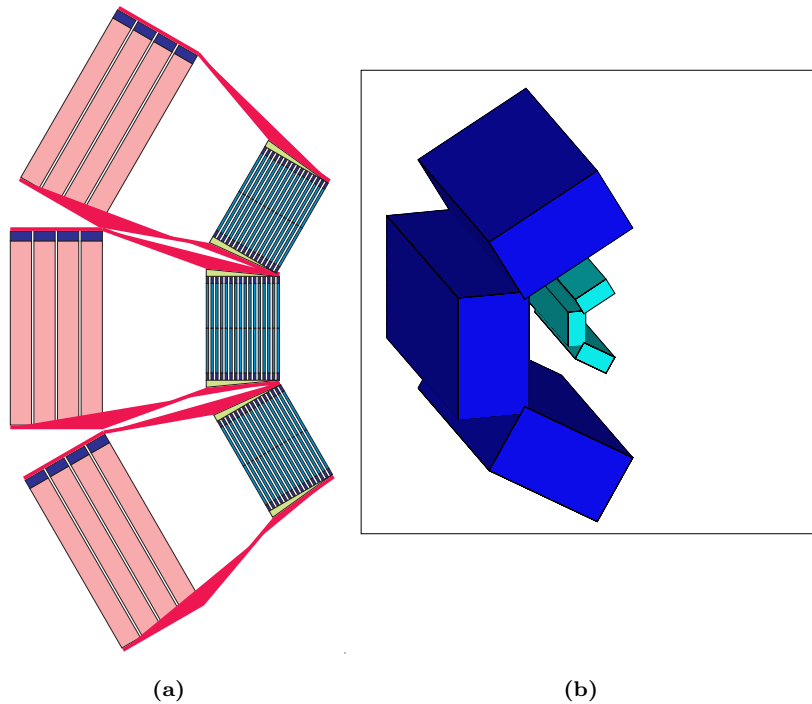


**Fig. 7.1:** Conceptual future detector system consisting of a stack of scatter and absorption detectors and its Geant model.

A Compton camera system consisting of multilayer scatter and absorption detectors shown in Fig. 7.1(a) has been simulated with Geant as shown in Fig. 7.1(b). The dead regions between the detectors is neglected by considering the layers being tightly packed which is technologically possible and a single block of detectors is considered to reduce the simulation time.

Each scatter detector module considered has an area of  $20 \times 40 \text{ mm}^2$  and a thickness of 10 mm which

in principle can be built by 20 layers of 500  $\mu\text{m}$  thick silicon wafers. Each absorption detector module has an area of  $70 \times 140 \text{ mm}^2$  and a thickness of 40 mm. The source is located 20.32 mm away from the scatter detector and the distance between the source and the absorption detector is taken to be 75.62 mm for the simulations. 1 million photons emitted from a  $^{137}\text{Cs}$  source has been simulated. When all the single and multiple events with full energy deposition are considered the efficiency of the system is found to be around 2.27% with the following solid angle acceptances and efficiencies for the two detectors:

$$\begin{aligned} \frac{\Delta\Omega_s}{\Omega_s} &= 43.32 \% \\ \varepsilon_1 &= 15.26 \% \\ \frac{\Delta\Omega_a}{\Omega_a} &= 64.05 \% \\ \varepsilon_2 &= 53.71 \% \end{aligned}$$

37 % of the backscattering events produce signal at both detectors and the fraction of such events among all the interactions occurring in the scatter detector is only about 3. %. Simulations with the same geometry have been performed also for an LSO absorption detector. With all the single and multiple interactions taken into account, the efficiency of the system increased only to 3.85 % with the following geometrical acceptance and efficiency figures:

$$\begin{aligned} \frac{\Delta\Omega_s}{\Omega_s} &= 43.41 \% \\ \varepsilon_1 &= 15. \% \\ \frac{\Delta\Omega_a}{\Omega_a} &= 64.02 \% \\ \varepsilon_2 &= 92.39 \% \end{aligned}$$

As expected, there is no change either in the geometrical acceptances for the two detectors or in the efficiency of the scatter detector. The main improvement obtained by replacing the absorption detector material with LSO is to gain more efficiency in this detector. The fraction of the backscattering events is also reduced by a factor of four. However, the overall efficiency improvement is not very prominent and considering better energy and position resolution that can be obtained with a silicon detector, it is even less attractive to use a scintillator detector for the tracking of the gamma-ray in the absorption detector.

Therefore, with such a detector system, it is not only possible to reach a sensitivity limit which is at least compatible with PET systems but also a sub-mm resolution approaching Fano and Doppler broadening limits.

# Appendix



# A. Appendices for Chapter 2

## A.1 Derivation of the Compton Equation

Let's consider a photon with momentum vector  $\mathbf{p}_\gamma$  being Compton scattered by an electron which is initially at rest with a rest mass  $m_e$  (Fig. A.1).

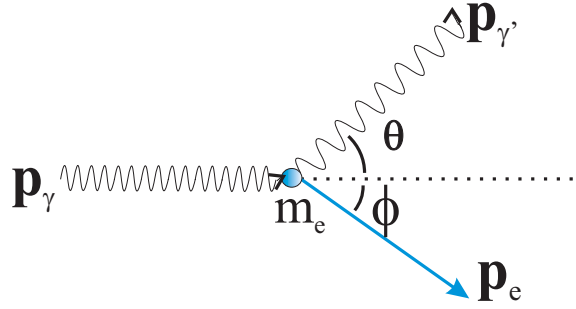


**Fig. A.1:** Compton scattering of an incident photon (momentum  $\mathbf{p}_\gamma$ ) by a quasi-free electron through an angle  $\theta$ . The momentum of the scattered photon is  $\mathbf{p}_{\gamma'}$ , the electron recoils at an angle  $\phi$  with a momentum  $\mathbf{p}_e$

After the interaction, the scattered photon is emitted at an angle  $\theta$  with four momentum  $\mathbf{p}_{\gamma'}$  and the electron recoils with a momentum vector of  $\mathbf{p}_e$  at an angle  $\phi$ . By conservation of momentum, the relation between the initial and final momenta is

$$\mathbf{p}_\gamma = \mathbf{p}_{\gamma'} + \mathbf{p}_e \quad (\text{A.1})$$

The momentum of the electron can then be written as:

$$\mathbf{p}_e = \mathbf{p}_\gamma - \mathbf{p}_{\gamma'} \quad (\text{A.2})$$

Taking the square of both sides in A.2 gives:

$$p_e^2 = p_\gamma^2 + p_{\gamma'}^2 - 2\mathbf{p}_\gamma \cdot \mathbf{p}_{\gamma'} \quad (\text{A.3})$$

The total relativistic energy  $E$  of a particle can be expressed in terms of momentum  $\mathbf{p}$  and its rest mass  $m$  as  $E^2 = \mathbf{p} \cdot \mathbf{p}c^2 + m^2c^4$ . By conservation of energy, the relation between the initial and final energy is

$$p_\gamma c + m_e c^2 = p_{\gamma'} c + \sqrt{p_e^2 c^2 + m_e^2 c^4} \quad (\text{A.4})$$

By rearranging the terms and squaring both sides, one gets another equation for  $p_e^2$ :

$$\begin{aligned} p_e^2 c^2 + m_e^2 c^4 &= (p_\gamma c + m_e c^2 - p_{\gamma'} c)^2 \\ &= p_\gamma^2 c^2 + p_{\gamma'}^2 c^2 - 2p_\gamma p_{\gamma'} c^2 + 2m_e c^3 (p_\gamma - p_{\gamma'}) + m_e^2 c^4 \\ \frac{1}{c^2} p_e^2 c^2 &= \{p_\gamma^2 c^2 + p_{\gamma'}^2 c^2 - 2p_\gamma p_{\gamma'} c^2 + 2m_e c^3 (p_\gamma - p_{\gamma'})\} \frac{1}{c^2} \\ p_e^2 &= p_\gamma^2 + p_{\gamma'}^2 - 2p_\gamma p_{\gamma'} + 2m_e c (p_\gamma - p_{\gamma'}) \end{aligned}$$

Equating right sides of equation A.3 and the last equation yields

$$\begin{aligned} p_\gamma^2 + p_{\gamma'}^2 - 2\mathbf{p}_\gamma \cdot \mathbf{p}_{\gamma'} &= p_\gamma^2 + p_{\gamma'}^2 - 2p_\gamma p_{\gamma'} + 2m_e c (p_\gamma - p_{\gamma'}) \\ m_e c (p_\gamma - p_{\gamma'}) &= p_\gamma p_{\gamma'} - \mathbf{p}_\gamma \cdot \mathbf{p}_{\gamma'} \end{aligned}$$

Then both sides can be divided by  $m_e c p_\gamma p_{\gamma'}$  to obtain the relation between the energies of the incoming and scattered photon and the scattering angle  $\theta$

$$\begin{aligned} \frac{1}{m_e c p_\gamma p_{\gamma'}} m_e c (p_\gamma - p_{\gamma'}) &= \{p_\gamma p_{\gamma'} - \mathbf{p}_\gamma \cdot \mathbf{p}_{\gamma'}\} \frac{1}{m_e c p_\gamma p_{\gamma'}} \\ \frac{1}{c} \left\{ \frac{1}{p_{\gamma'}} - \frac{1}{p_\gamma} \right\} &= \frac{1}{m_e c} (1 - \cos \theta) \frac{1}{c} \end{aligned}$$

from which the final form of the equation can be written as:

$$\frac{1}{E_{\gamma'}} - \frac{1}{E_\gamma} = \frac{1}{m_e c^2} (1 - \cos \theta) \quad (\text{A.5})$$

## A.2 Probability of Single Compton Scattering

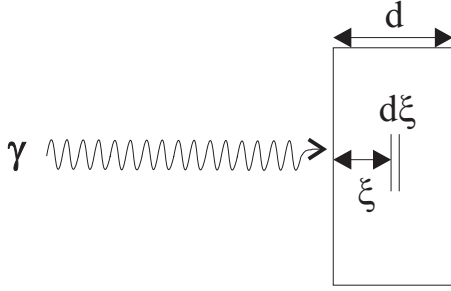
The probability of Compton interaction in  $d\xi$  can be expressed as:

$$dP_C(\xi) = \frac{d\xi}{\chi_C} e^{-\frac{\xi}{\chi_0}} \quad (\text{A.6})$$

where:

$\chi_0$  : mean attenuation length of  $\gamma$

$\chi_C$  : Compton attenuation length of  $\gamma$ .



In order to calculate the single Compton interaction probability, one should consider a single Compton interaction where the scattered photon leaves the detector without interacting further. The probability of the single Compton interaction is therefore the product of the Compton probability for the incoming photon and the no-interaction probability for the scattered photon:

$$dP(\xi) = dP_C(\xi) e^{-\frac{d-\xi}{\chi_0}} \quad (\text{A.7})$$

$$= \frac{d\xi}{\chi_C} e^{-\frac{\xi}{\chi_0}} e^{-\frac{d-\xi}{\chi_0}} \quad (\text{A.8})$$

where  $\chi_0'$  is the mean attenuation length of the scattered photon. Integrating A.8 to get the total probability gives:

$$\begin{aligned} P &= \int_0^d d\xi \left\{ \frac{1}{\chi_C} e^{-\frac{\xi}{\chi_0}} e^{-\frac{d-\xi}{\chi_0'}} \right\} \\ &= \frac{1}{\chi_C} \int_0^d e^{-\frac{\chi_0' \xi + d \chi_0 - \xi \chi_0}{\chi_0 \chi_0'}} d\xi \\ &= \frac{1}{\chi_C} e^{-\frac{d}{\chi_0}} \int_0^d e^{\frac{\chi_0 - \chi_0'}{\chi_0 \chi_0'} \xi} d\xi \\ &= \frac{1}{\chi_C} e^{-\frac{d}{\chi_0}} \frac{\chi_0 \chi_0'}{\chi_0 - \chi_0'} e^{\frac{\chi_0 - \chi_0'}{\chi_0 \chi_0'} \xi} \Big|_0^d \end{aligned}$$

Therefore the probability of a single Compton interaction can be expressed as:

$$P = \frac{1}{\chi_C} e^{-\frac{d}{\chi_0}} \frac{\chi_0 \chi_0'}{\chi_0 - \chi_0'} \left[ e^{\frac{\chi_0 - \chi_0'}{\chi_0 \chi_0'} d} - 1 \right] \quad (\text{A.9})$$

### A.3 Angular and Energy Distribution of Recoil Electrons

The number of photons scattered into a solid angle  $2\pi \sin \theta d\theta$  must be equal to the number of electrons projected at a solid angle  $d\Omega' = 2\pi \sin \phi d\phi$  [Eva82]:

$$\frac{d\sigma}{d\Omega} 2\pi \sin \theta = \frac{d\sigma}{d\Omega'} 2\pi \sin \phi \quad (\text{A.10})$$

where  $d(\sigma)/d\Omega$  is given in equation (2.2a). The number of recoil electrons per unit projection angle  $\phi$  is then equal to:

$$\frac{d\sigma}{d\phi} = \frac{d\sigma}{d\Omega'} 2\pi \sin \phi \quad (\text{A.11})$$

$$= \frac{d(\sigma)}{d\Omega} \frac{\sin \theta}{\sin \phi} \frac{d\theta}{d\phi} 2\pi \sin \phi \quad (\text{A.12})$$

Using equation (2.17) which gives the relation between the scattering angles  $\theta$  and  $\phi$  for scattered photon and recoil electron, respectively:

$$\cot \phi = (1 + \epsilon) \frac{1 - \cos \theta}{\sin \theta} \quad (\text{A.13})$$

and taking the partial derivatives of both sides of the equation with respect to  $\theta$  and  $\phi$ :

$$\begin{aligned} \frac{\partial}{\partial \theta} \frac{\partial}{\partial \phi} (\cot \phi) &= \frac{\partial}{\partial \theta} \frac{\partial}{\partial \phi} \left( (1 + \epsilon) \frac{1 - \cos \theta}{\sin \theta} \right) \\ -\frac{1}{\sin^2 \phi} d\phi &= (1 + \epsilon) \frac{1 - \cos \theta}{\sin^2 \theta} d\theta \\ \frac{d\theta}{d\phi} &= -\frac{\sin^2 \theta}{(1 + \epsilon) \sin^2 \phi (1 - \cos \theta)} \\ \frac{\sin \theta}{\sin \phi} \frac{d\theta}{d\phi} &= -\frac{\sin^3 \theta}{(1 + \epsilon) \sin^3 \phi (1 - \cos \theta)} \end{aligned}$$

Therefore, the equation (A.12) becomes:

$$\frac{d\sigma}{d\phi} = -\frac{d(\sigma)}{d\Omega} \frac{\sin^3 \theta}{(1 + \epsilon) \sin^3 \phi (1 - \cos \theta)} 2\pi \sin \phi \quad (\text{A.14})$$

The number-energy distribution of recoil electrons can be calculated using equation (A.14):

$$\frac{d\sigma}{dE_e} = \frac{d\sigma}{d\phi} \frac{d\phi}{dE_e} \quad (\text{A.15})$$

similarly  $d\phi/dE_e$  can be written as:

$$\frac{d\phi}{dE_e} = \frac{d\phi}{d\theta} \frac{d\theta}{dE_e} \quad (\text{A.16})$$

Using equation (2.5)(also equation (A.5)) the Compton angle can be written in terms of the energy of the recoil electron:

$$\theta = \arccos \left( 1 - \frac{E_e}{\epsilon(E_\gamma - E_e)} \right) \quad (\text{A.17})$$

Taking the derivative of both sides with respect to  $E_e$  gives:

$$\begin{aligned}
\frac{d\theta}{dE_e} &= -\frac{1}{\sqrt{1 - \left(1 - \frac{E_e}{\epsilon(E_\gamma - E_e)}\right)^2}} \left( \frac{-\epsilon(E_\gamma - E_e) - \epsilon E_e}{\epsilon^2(E_\gamma - E_e)^2} \right) \\
&= \frac{\epsilon(E_\gamma - E_e)}{E_e \sqrt{\frac{2\epsilon(E_\gamma - E_e)}{E_e} - 1}} \frac{E_\gamma}{\epsilon(E_\gamma - E_e)^2} \\
&= \frac{E_\gamma}{E_{\gamma'}} \frac{1}{\sqrt{2\epsilon E_e E_{\gamma'} - E_e^2}} \\
&= \frac{E_\gamma}{E_{\gamma'}} \frac{1}{\sqrt{2\epsilon^2 E_{\gamma'}^2 (1 - \cos\theta) - \epsilon^2 E_{\gamma'}^2 (1 - \cos\theta)^2}} \\
&= \frac{E_\gamma}{\epsilon E_{\gamma'}^2} \frac{1}{\sin\theta}
\end{aligned}$$

with  $E_{\gamma'}$  expressed in terms of  $\theta$  the equation takes the following form:

$$\frac{d\theta}{dE_e} = \frac{(1 + \epsilon(1 - \cos\theta))^2}{\epsilon \sin\theta E_\gamma} \quad (\text{A.18})$$

Putting this term in equation (A.15), one gets:

$$\frac{d\sigma}{dE_e} = \frac{d\sigma}{d\Omega} \frac{2\pi \sin\theta}{\sin\phi} \frac{\sin\theta}{\sin\phi} \frac{d\theta}{d\phi} \frac{d\phi}{d\theta} \frac{(1 + \epsilon(1 - \cos\theta))^2}{\epsilon \sin\theta E_\gamma} \quad (\text{A.19})$$

The energy distribution of recoil electrons can therefore be calculated using:

$$\frac{d\sigma}{dE_e} = \frac{d\sigma}{d\Omega} 2\pi \sin\theta \frac{(1 + \epsilon(1 - \cos\theta))^2}{\epsilon \sin\theta E_\gamma} \quad (\text{A.20})$$



Finite spatial and depth resolutions of the scatter detector causes some error in the measurement of the angular uncertainty due to the fact that exact location can by no means be determined. For detectors with no depth of interaction resolution, the thickness of the detector determines the depth resolution. The readout structure is assumed to be at point C, therefore due to the finite resolution of the detector, events occurring at C' and C'' are taken to occur at C which causes an error in determining the scattering angle of the incoming photon. In fact, this error in the measurement of the scattering angle results in detecting the source at wrong locations like O' or O'' instead of O. It is important to note that these calculations reflect the worst case scenario by taking the edge points of the resolution element for the sample event. By using geometric and trigonometric identities, the contribution of the parameters of the scatter detector,  $d$ , to the angular uncertainty,  $\Delta\theta$  can be calculated. The calculation of  $\Delta\theta_1$  is performed by using following relations:

$$\begin{aligned}\tan(\theta_1 - (\alpha - \phi_1)) &= \frac{|AB'|}{|B'C'|} \Rightarrow |AB'| = |B'C'| \tan(\theta_1 - \alpha + \phi_1) \\ \tan(\theta_1 - (\alpha - \Delta\theta_1)) &= \frac{|AB|}{D_2} \Rightarrow |AB| = D_2 \tan(\theta_1 + \Delta\theta_1 - \alpha) \\ |B'C'| &= D_2 - |CT| & |BB'| &= |C'T| \\ \sin(180 - (\xi + \alpha)) &= \frac{|C'T|}{|CC'|} \Rightarrow |C'T| = |CC'| \sin(180 - \xi - \alpha) \\ \cos(180 - (\xi + \alpha)) &= \frac{|CT|}{|CC'|} \Rightarrow |CT| = |CC'| \cos(180 - \xi - \alpha) \\ |CC'| &= \frac{1}{2} \sqrt{d^2 + L^2}\end{aligned}$$

where  $\phi_1 = \frac{d/2}{D_1 - L/2}$  and  $\xi = \arctan(\frac{d}{L})$ . The distance  $|AB|$  can be written as the sum of  $|AB'|$  and  $|BB'|$ :

$$\begin{aligned}D_2 \tan(\theta_1 - \alpha + \Delta\theta_1) &= |B'C'| \tan(\theta_1 - \alpha + \phi_1) + |C'T| \\ D_2 \tan(\theta_1 - \alpha + \Delta\theta_1) &= (D_2 - |CC'| \cos(180 - \xi - \alpha)) \tan(\theta_1 - \alpha + \phi_1) + |CC'| \sin(180 - \xi - \alpha) \\ D_2 \tan(\theta_1 - \alpha + \Delta\theta_1) &= \left( D_2 - \frac{1}{2} \sqrt{d^2 + L^2} \cos(180 - \xi - \alpha) \right) \tan(\theta_1 - \alpha + \phi_1) \\ &+ \frac{1}{2} \sqrt{d^2 + L^2} \sin(180 - \xi - \alpha) \\ \theta_1 - \alpha + \Delta\theta_1 &= \arctan \left\{ \left[ 1 - \frac{1}{2D_2} \sqrt{d^2 + L^2} \cos(180 - \xi - \alpha) \right] \tan(\theta_1 - \alpha + \phi_1) \right. \\ &+ \left. \frac{1}{2D_2} \sqrt{d^2 + L^2} \sin(180 - \xi - \alpha) \right\}\end{aligned}$$

Therefore,  $\Delta\theta_1$  can be written as:

$$\Delta\theta_1 = \alpha - \theta_1 + \arctan \left\{ \left[ 1 - \frac{1}{2D_2} \sqrt{d^2 + L^2} \cos(180 - \xi - \alpha) \right] \tan(\theta_1 - \alpha + \phi_1) + \frac{1}{2D_2} \sqrt{d^2 + L^2} \sin(180 - \xi - \alpha) \right\} \quad (\text{B.1})$$

Similarly,  $\Delta\theta_2$  can be obtained as follows:

$$\begin{aligned}\tan(\theta_2 - (\phi_2 + \alpha)) &= \frac{|AB''|}{|C''B''|} \Rightarrow |AB''| = |C''B''| \tan(\theta_2 - \phi_2 - \alpha) \\ \tan(\theta_2 - (\Delta\theta_2 + \alpha)) &= \frac{|AB|}{D_2} \Rightarrow |AB| = D_2 \tan(\theta_2 - \Delta\theta_2 - \alpha) \\ |C''B''| &= D_2 + |C''T''| = D_2 + |CT| & |BB''| &= |CT''| = |C'T|\end{aligned}$$

where  $\phi_2 = \frac{d/2}{D_1 + L/2}$ . The distance  $|AB''|$  can be written as the sum of  $|AB|$  and  $|BB''|$  which then gives

the following relation:

$$\begin{aligned}
|C''B''| \tan(\theta_2 - \phi_2 - \alpha) &= D_2 \tan(\theta_2 - \Delta\theta_2 - \alpha) + |C'T| \\
(D_2 + |CT|) \tan(\theta_2 - \phi_2 - \alpha) &= D_2 \tan(\theta_2 - \Delta\theta_2 - \alpha) + |CC'| \sin(180 - \xi - \alpha) \\
(D_2 + |CC'| \cos(180 - \xi - \alpha)) \tan(\theta_2 - \phi_2 - \alpha) &= D_2 \tan(\theta_2 - \Delta\theta_2 - \alpha) + |CC'| \sin(180 - \xi - \alpha) \\
(D_2 + \frac{1}{2}\sqrt{d^2 + L^2} \cos(180 - \xi - \alpha)) \tan(\theta_2 - \phi_2 - \alpha) &= D_2 \tan(\theta_2 - \Delta\theta_2 - \alpha) \\
&+ \frac{1}{2}\sqrt{d^2 + L^2} \sin(180 - \xi - \alpha)
\end{aligned}$$

Rearranging the terms to get  $\Delta\theta_2$  gives:

$$\begin{aligned}
\tan(\theta_2 - \Delta\theta_2 - \alpha) &= \left(1 + \frac{1}{2D_2}\sqrt{d^2 + L^2} \cos(180 - \xi - \alpha)\right) \tan(\theta_2 - \phi_2 - \alpha) \\
&- \frac{1}{2D_2}\sqrt{d^2 + L^2} \sin(180 - \xi - \alpha) \\
\theta_2 - \Delta\theta_2 - \alpha &= \arctan\left\{\left[1 + \frac{1}{2D_2}\sqrt{d^2 + L^2} \cos(180 - \xi - \alpha)\right] \tan(\theta_2 - \phi_2 - \alpha)\right. \\
&\left. - \frac{1}{2D_2}\sqrt{d^2 + L^2} \sin(180 - \xi - \alpha)\right\}
\end{aligned}$$

By arranging the terms further,  $\Delta\theta_2$  becomes equal to:

$$\Delta\theta_2 = \theta_2 - \alpha - \arctan\left\{\left[1 + \frac{1}{2D_2}\sqrt{d^2 + L^2} \cos(180 - \xi - \alpha)\right] \tan(\theta_2 - \phi_2 - \alpha) - \frac{1}{2D_2}\sqrt{d^2 + L^2} \sin(180 - \xi - \alpha)\right\} \quad (\text{B.2})$$

To get the total contribution B.1 and B.2 should be combined for  $\theta = \theta_1 = \theta_2$  which gives the following result :

$$\begin{aligned}
\Delta\theta_s &= \arctan\left\{\left[1 - \frac{1}{2D_2}\sqrt{d^2 + L^2} \cos(180 - \xi - \alpha)\right] \tan(\theta - \alpha + \phi_1) + \frac{1}{2D_2}\sqrt{d^2 + L^2} \sin(180 - \xi - \alpha)\right\} \\
&- \arctan\left\{\left[1 + \frac{1}{2D_2}\sqrt{d^2 + L^2} \cos(180 - \xi - \alpha)\right] \tan(\theta - \phi_2 - \alpha) - \frac{1}{2D_2}\sqrt{d^2 + L^2} \sin(180 - \xi - \alpha)\right\} \quad (\text{B.3})
\end{aligned}$$

### B.1.3 The Contribution of the Absorption Detector

The spatial resolution and depth of interaction in the absorption detector also contribute to the angular uncertainty due to the uncertainty in the measurement of the interaction position of the scattered photon. As in the case of the scatter detector, it is also possible to study these factors together, without separating them. In fact, this method of analyzing the effects of these two factors together has also been tried and the results were compared with the results obtained by studying them separately. The difference between the two methods were found to be negligible.

#### B.1.3.1 The Contribution of the Pixel Size of the Absorption Detector

Let's take the pixel size of the absorption detector being equal to  $r$ . For a detector where the signal is detected at the middle of a pixel, any event occurring within a distance  $r/2$  is supposed to occur in the middle. This causes a fluctuation in the determination of the  $\theta$  as shown in Fig. B.2. By using geometric and trigonometric identities,  $\Delta\theta_{\text{apix el width}}$  can be derived:

$$\begin{aligned}
\tan\left(\theta - \alpha - \frac{\Delta\theta}{2}\right) &= \frac{|DO|}{D_2} & \Rightarrow & & |DC| &= D_2 \tan\left(\theta - \alpha - \frac{\Delta\theta}{2}\right) \\
\tan(\theta - \alpha) &= \frac{|BO|}{D_2} & \Rightarrow & & |BO| &= D_2 \tan(\theta - \alpha) \\
|BO| &= |BD| + |DO|
\end{aligned}$$

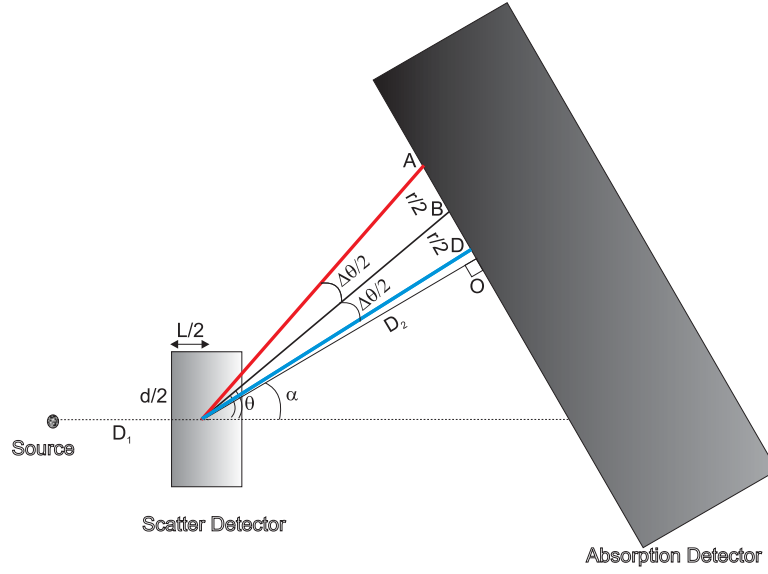


**Fig. B.2:** Influence of the spatial resolution of the second detector to the measurement of Compton scattering angle

where  $|BD|$  is equal to  $r/2$ , then the last equation can be written as:

$$\begin{aligned} D_2 \tan(\theta - \alpha) &= \frac{r}{2} + D_2 \tan\left(\theta - \alpha - \frac{\Delta\theta}{2}\right) \\ \tan\left(\theta - \alpha - \frac{\Delta\theta}{2}\right) &= \tan(\theta - \alpha) - \frac{r}{2D_2} \\ \theta - \alpha - \frac{\Delta\theta}{2} &= \arctan\left(\tan(\theta - \alpha) - \frac{r}{2D_2}\right) \end{aligned}$$

Finally, the angular uncertainty due to the spatial resolution of the absorption detector can be written as follows:

$$\Delta\theta_{\text{apixel width}} = 2(\theta - \alpha) - 2 \arctan\left[\tan(\theta - \alpha) - \frac{r}{2D_2}\right] \quad (\text{B.4})$$

### B.1.3.2 The Contribution of the Depth of Interaction in the Absorption Detector

The scattered photon can have energies of at least few hundred keV and such energetic photons penetrate into the absorption detector deeply. The penetration depth of the scattered photon affects the angular resolution in a considerable amount. Depending on the orientation of the detector, the angular uncertainty becomes minimum at different scattering angles due to the effect of depth of interaction. The model used for the calculation of the effect of the depth of interaction in the absorption detector is shown in Fig. B.3.

Similar to the method used for other resolution elements, the angular uncertainty due to the penetration in the absorption detector can be derived using geometric and trigonometric relations as follow:

$$\begin{aligned} \tan(\theta - \alpha) &= \frac{|AO|}{D_2} \Rightarrow |AO| = D_2 \tan(\theta - \alpha) \\ \tan\left(\theta - \alpha + \frac{\Delta\theta}{2}\right) &= \frac{|A'O|}{D_2} \Rightarrow |A'O| = D_2 \tan\left(\theta - \alpha + \frac{\Delta\theta}{2}\right) \\ \tan(\theta - \alpha) &= \frac{|AA'|}{z} \Rightarrow |AA'| = z \tan(\theta - \alpha) \end{aligned}$$





# C. Appendices for Chapter 4

## C.1 Decay Scheme for $^{137}\text{Cs}$

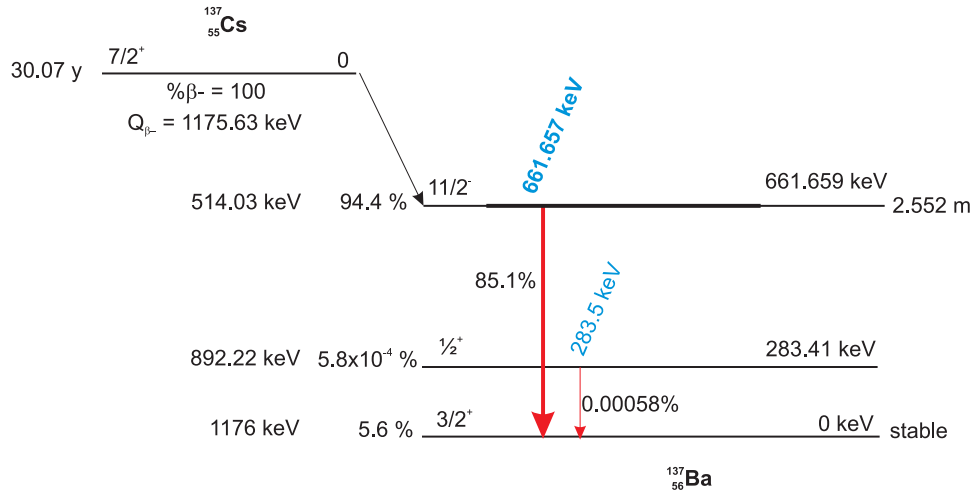
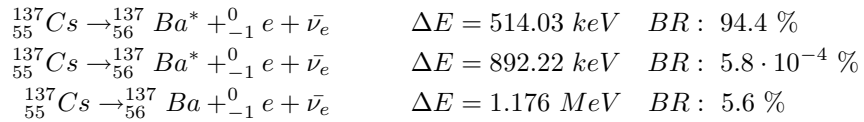
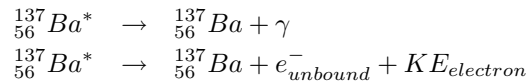


**Fig. C.1:** Decay scheme for  $^{137}\text{Cs}$

$^{137}\text{Cs}$  isotope beta decays (Fig. C.1) into  $^{137}\text{Ba}$  with a half-life of 30.07 years as follows:



Therefore, the maximum beta energy is 514.03 keV for the decay to the excited state and 1.176 MeV for the decay directly to the ground state. The excited state has a half-life of 2.552 minutes and decays 90.15 % of the time via the emission of a 661.657 keV photon and 9.85 % of the time with the emission of an atomic conversion electron as follows:



As a result the probability that all beta decays of this isotope produce a photon of 661.657 keV is 85.1 % ( $0.9015 \cdot 0.944 = 0.851$ ). The list of X-rays,  $\gamma$ 's and  $\beta$ 's emitted by this source are given in Tab. C.1, Tab. C.2 and Tab. C.3, respectively.

E (keV)	I (%)	Assignment
3.954	0.0143	Ba L <sub>l</sub>
4.331	0.0064	Ba L <sub>h</sub>
4.451	0.040	Ba L <sub>a2</sub>
4.466	0.36	Ba L <sub>a1</sub>
4.827	0.226	Ba L <sub>b1</sub>
4.852	0.023	Ba L <sub>b4</sub>
4.927	0.039	Ba L <sub>b3</sub>
4.994	0.0030	Ba L <sub>b6</sub>
5.156	0.074	Ba L <sub>b2</sub>
5.531	0.033	Ba L <sub>g1</sub>
5.797	0.0065	Ba L <sub>g2</sub>
5.809	0.0093	Ba L <sub>g3</sub>
31.452	0.000263	Ba K <sub>a3</sub>
31.817	2.04	Ba K <sub>a2</sub>
32.194	3.76	Ba K <sub>a1</sub>
36.304	0.352	Ba K <sub>b3</sub>
36.378	0.680	Ba K <sub>b1</sub>
36.652	0.0079	Ba K <sub>b5</sub>
37.255	0.215	Ba K <sub>b2</sub>
37.349	0.0481	Ba K <sub>b4</sub>

Tab. C.1: X-rays from  $^{137}\text{Cs}$  [LBL]

$E_\gamma$ (keV)	$I_\gamma$ (%)	Decay Mode
283.53	0.00058	$\beta$ -decay
661.657	85.1	$\beta$ -decay

Tab. C.2: Gammas from  $^{137}\text{Cs}$  [LBL]

$E_b$ endpoint (keV)	$I_b$ (%)	Decay Mode
513.97	94.4	$\beta$ -decay
892.22	0.00058	$\beta$ -decay
1175.63	5.6	$\beta$ -decay

Tab. C.3: Betas from  $^{137}\text{Cs}$  [LBL]

## C.2 Layout of the Single Cell SDD

The layout of the cylindrical single cell SDD is shown in Fig. C.2. This is the front side of the chip where the  $p^+$  field electrodes are implanted. The bonding pads for various voltage supplies and the signal are placed around the middle of the chip. The last ring of the voltage divider of the drift field is followed by guard rings. On the upper right and the lower left region the temperature diodes are located. The test transistor and the guard ring for it can be found on the lower right corner of the chip. The radiation enters from the homogeneous  $p^+$  back side of the device.

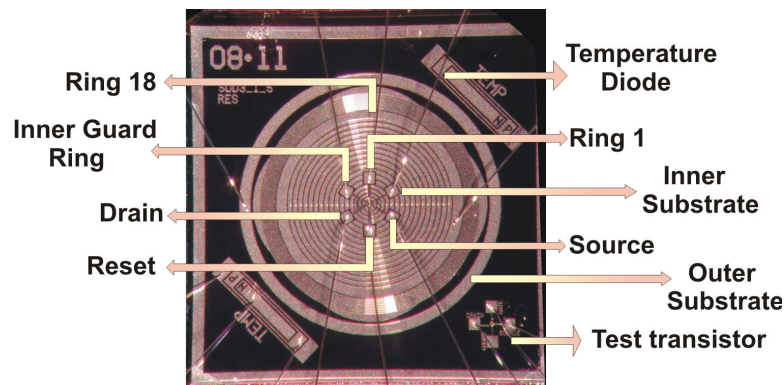


Fig. C.2: Cylindrical single cell SDD delivered by MPI HLL. The bonding pads for various contacts, temperature diode and the test transistor are shown in detail.

The pin layout of the carrier ceramic is shown in Fig. C.3. Due to time constraints, existing ceramic designed for a larger detector was used for mounting the detector at Politecnico di Milano. The main connections necessary for the detector operation are written in *italic*. The extra connections for the test transistor and the temperature diode are also shown in the figure.

R1 and R18 corresponds to the first and the last field electrodes. Voltages to these rings should be supplied externally and the other electrodes are biased through the internal voltage divider in a decreasing fashion from innermost to the outermost ring. Inner guard ring (IGR) is the guard ring splitting the transistor channel from the bulk of the detector. The voltage values used for the detector are as follow:

$$V_{R1} = -14.9 \text{ V} \quad (I_{R1} = 10 \text{ } \mu\text{A})$$

$$V_{R18} = -73.1 \text{ V} \quad (I_{R18} = 10 \text{ } \mu\text{A})$$

$$V_{IGR} = -15.0 \text{ V}$$

$$V_{Back} = -85.2 \text{ V}$$

$$V_{Reset} = -15.03 \text{ V}$$

$$V_{OS} = 0 \text{ V}$$

$$V_{IS} = 0 \text{ V}$$

$$V_{Drain} = +12.07 \text{ V} \quad (I_{Drain} = 400 \text{ } \mu\text{A})$$

$$V_{CSSource} = -9.91 \text{ V} \quad (I_{CSSource} = 400 \text{ } \mu\text{A})$$

$$V_{CSGate} = -4.6 \text{ V}$$

$$V_{TMGR} = -11.92 \text{ V}$$

$$V_{TMP} = +4.52 \text{ V}$$

$$V_{TMN} = 0 \text{ V}$$

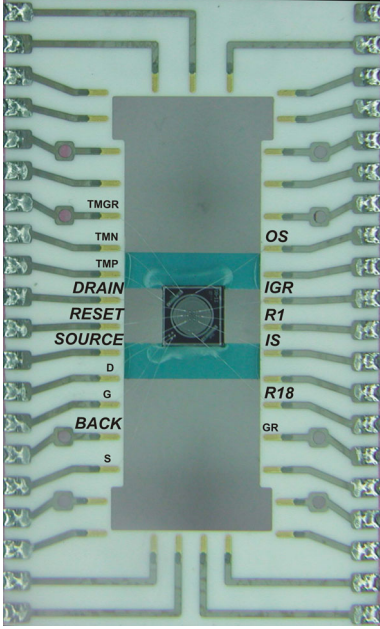


**Fig. C.3:** Carrier ceramic for a single cell SDD

## C.3 19-cell Silicon drift detector

### C.3.1 Bonding Layout of the 19-cell SDD

In order to test the bonding layout of the 19 cell detector, 17.5 mm x17.5 mm x 0.26 mm Si wafers [Sie] with Al metallization layers at the locations of the bonding pads and the rings were used. The carrier

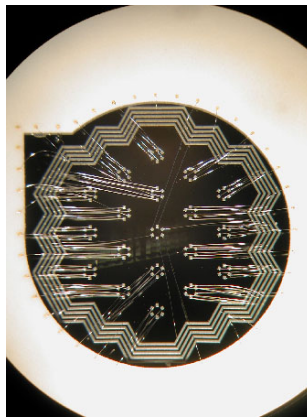


**Fig. C.4:** The dummy silicon chip with bonding pads and rings wire bonded to a carrier ceramic produced for the bonding test

ceramic was produced with thick film technology at the hybrid laboratory of our group. The bonding test was performed at CERN using 15  $\mu\text{m}$  thick Al bond wires. It was reported by a bonding expert [Hon00] that a bonding connection with a height of 500  $\mu\text{m}$  and a length of 4 mm is safe enough with 15  $\mu\text{m}$  wire, therefore, he could easily achieve to bond 122 wires from the chip to the ceramic on the front side of the chip. The bonded sample shown in Fig. C.4 and some extra wafers with ceramics were used by KETEK GmbH to examine the bonding plan and test it further with their bonding machine.

### C.3.2 Aluminum Nitride Carrier Ceramic

AlN was chosen as the ceramic material for the detector mounting. This ceramic has an excellent thermal conductivity which is close to the thermal conductivity of Al itself. The thermal performance of the carrier ceramic is important due to the fact that the cooling of the peltiers is transmitted to the detector chip via this ceramic to which the detector is mounted. The typical property values for the Carborundum Hi-Therm AlN, other typical ceramic materials and Si are shown in Tab. C.4.

Property	Hi-Therm AlN	Al <sub>2</sub> O <sub>3</sub> (99.5%)	SiC	BeO (99.5%)	Si
Density (g/cm <sup>3</sup> )	3.30	3.89	3.2	2.85	2.33
Thermal Conductivity (W/m <sup>2</sup> K)	170-190	36	270	260	150
Thermal Expansion Coefficient (10 <sup>-6</sup> /°K)	4.6	8.2	3.7	8.5	4.05
Specific Resistance (Ohm.cm)	>10 <sup>4</sup>	>10 <sup>4</sup>	10 <sup>13</sup>	>10 <sup>4</sup>	10 <sup>-4</sup> -10 <sup>4</sup>
Dielectric Constant (RT-1 MHz)	8.9	9.8	15-45	6.7	11.8
Young Modulus (GPa)	331	372	380	345	170

**Tab. C.4:** Typical property values for AlN and some other materials

The layout of the carrier ceramic designed and produced by the thick film hybrid technology at our hybrid laboratory is shown in Fig. C.5. The ceramic has an area of 35x50 mm<sup>2</sup> and its thickness is 600  $\mu\text{m}$ . The bonding pads located around the detector opening have dimensions of 0.7 mm x 0.7 mm. The solderable AgPd pads are 0.75 mm wide and 2.5 mm long with a pitch of 1/20 inches. The conducting paths printed on the AlN ceramic using gold paste are 0.5 mm wide.

The signal lines are distributed on the right and the left sides of the ceramic resulting from the bonding plan. The path for the power lines were chosen such that they are as isolated from the signal lines as possible. Originally it was planned to use two sets of two peltier elements located on the upper and the lower part of the ceramic. However, there is a risk of electromagnetic disturbance they may create on the signal or power lines and also water drops which may be created in the peltier region in case of failure in drying the air in the box. For this reason, it was decided to locate the peltiers on the back side of the ceramic and at a region which has no signal or power lines on the corresponding front side. The only available region with these constraints is the lower part of the ceramic and eventually two peltiers electrically connected in series were mounted there. The back and back guard ring connections are bonded on the back side and are carried to the front side of the ceramic via through-contacts. The diameter of the hole in the middle of the ceramic is 16.6 mm. The whole SDD chip is in the shape of a square and the corners of the square were used to glue the chip to the ceramic. It was planned to locate the first stage of the front-end electronics and the power filters on this ceramic but due to the difficulties in bonding with some surface mount devices soldered on the ceramic, this plan could not be realized.

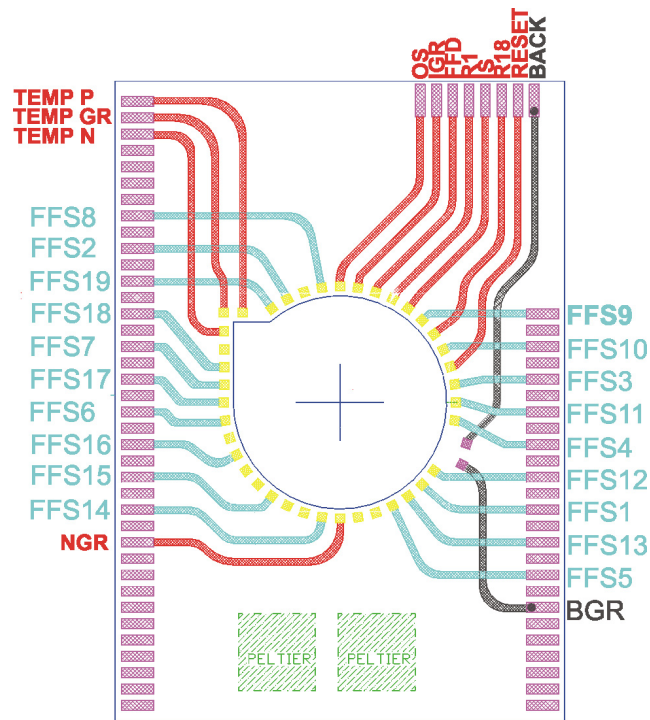


Fig. C.5: The layout of the carrier ceramic for the 19-cell SDD

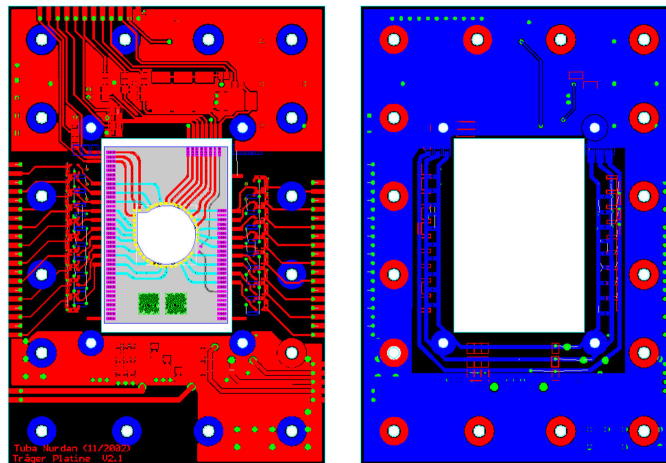
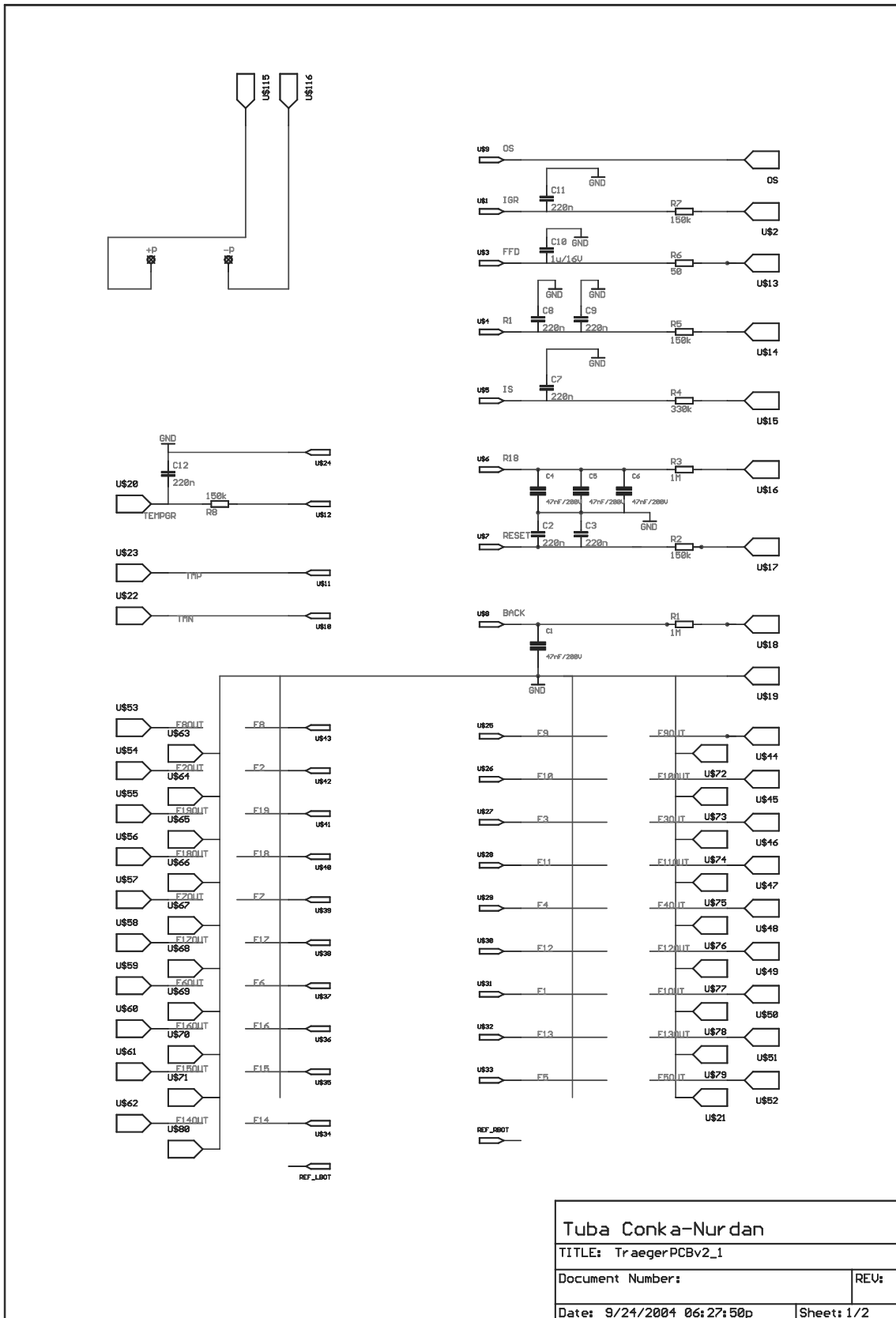


Fig. C.6: The front and the back side of the carrier PCB. The holes around the board are for mounting the detector box and the holes around the ceramic are to compress the interconnecting rubbers which are used to connect the ceramic and the PCB.

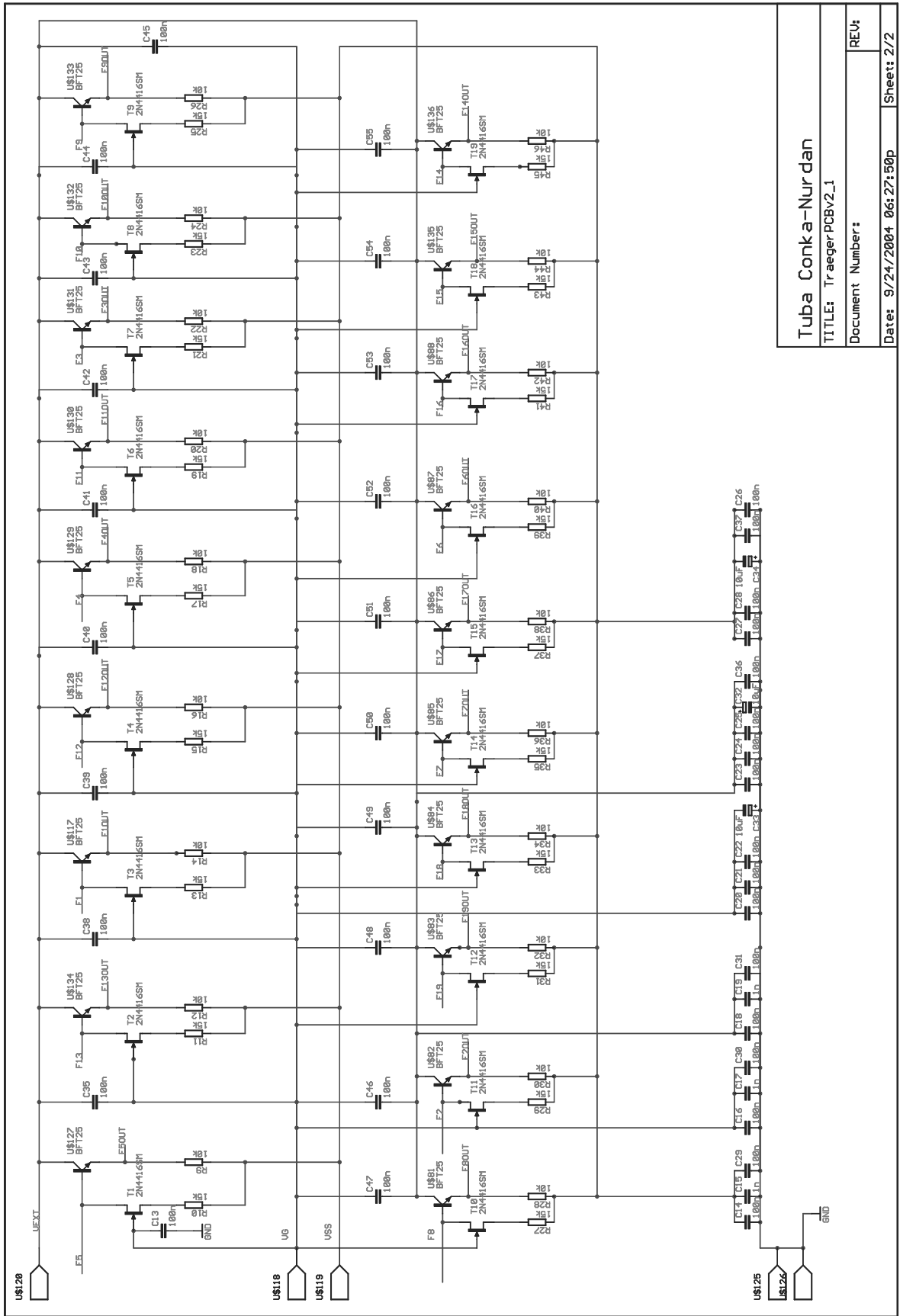
### C.3.3 Bias Board with the First Stage Readout Electronics

The first stage of the readout electronics and the filter circuits for various voltage sources are implemented on a single double-sided PCB (Fig. C.7, Fig. C.8). The board was designed such that there is a hole in the middle where the support ceramic is placed as shown in Fig. C.6.



9/24/2004 06:39:17p f=0.72 C:/projects/hardware/eagle/trägerCeramic\_platinv2.1/TraegerPCBv2\_1.sch (Sheet: 1/2)

Fig. C.7: First part of the schematics of the bias board including power filters



<b>Tube Conka-Nurjan</b> TITLE: TraegerPCBV2_1 Document Number:	
Date: 9/24/2004 06:27:50p	Sheet: 2/2
REV:	

Fig. C.8: Second part of the schematics of the bias board including the first stage readout electronics

### C.3.4 Rubber Inter-connectors

Special compression type inter-connectors are used for the connection between the carrier ceramic and the PCB. It consists of a gold-plated brass filaments lined in the conductive part and of insulating silicone rubber on both sides. They are also named as “leitergummi” which is a German word for the “conducting rubber” and are widely used in LCD displays. The structure of the connector is explained in Fig. C.9.

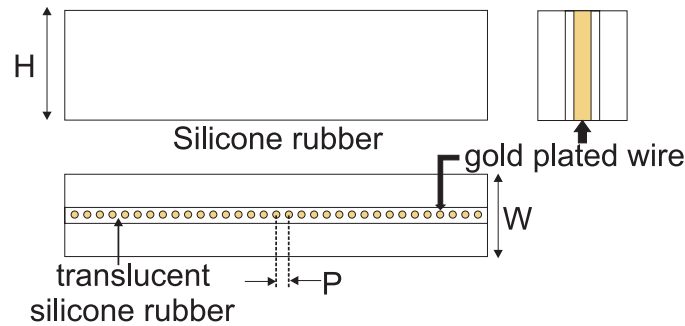


**Fig. C.9:** The structure of the GB type inter-connector produced by ShinEtsu Polymer Co, Ltd.

Dimensional information and basic properties of these inter-connectors are given in Tab. C.5. The connector used for this project is 45 mm long, 2.8 mm high, 3 mm wide and the wire pitch is  $100\ \mu\text{m}$ .

Property	Component	Units	
Pitch (P)		$\mu\text{m}$	50/100
Length (L)		mm	2.0-250.0
Height (H)		mm	1.0-10.0
Width (W)		mm	1.0-4.0
Wire diameter		$\mu\text{m}$	30/40
Current carrying capacity		mA/wire	50
Contact resistance		$\Omega$	$\leq 0.1$
Volume resistivity	Insulator		$10^5\text{M}$
	Conductor	$\Omega\text{cm}$	$\leq 10\mu$
	Edge insulation part		100M

**Tab. C.5:** Basic properties and dimensions for available inter-connectors.

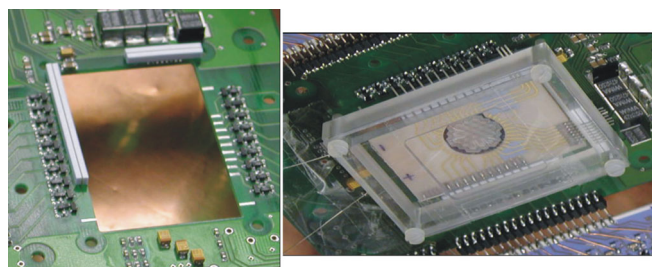


**Fig. C.10:** Rubber inter-connectors placed on the PCB (left) and the final appearance with the compressing frame to provide the secure connection.

The rubbers are first carefully placed on the PCB, then the pins of the support ceramic are placed on the rubber connectors and the plexiglass frame made for compressing the rubber is placed on top as shown in Fig. C.10. The screws passing through the frame and the PCB and the screw nuts at the back are adjusted until a safe connection between the ceramic pins and the PCB is obtained.

### C.3.5 Detector Housing

The housing of the scatter detector (Fig. C.11) is designed to be gas-tight for the continuous flush of dry nitrogen. It is composed of two parts and the bias board with a rubber frame on both sides is sandwiched between these parts. Each Al part has an O-ring in the inner side in order to provide a leak-tight environment. The bottom part of the detector box was produced such that water can flow inside of it. For this purpose some through holes were made inside the metal and only two of the holes were left open for the water inlet and the outlet.

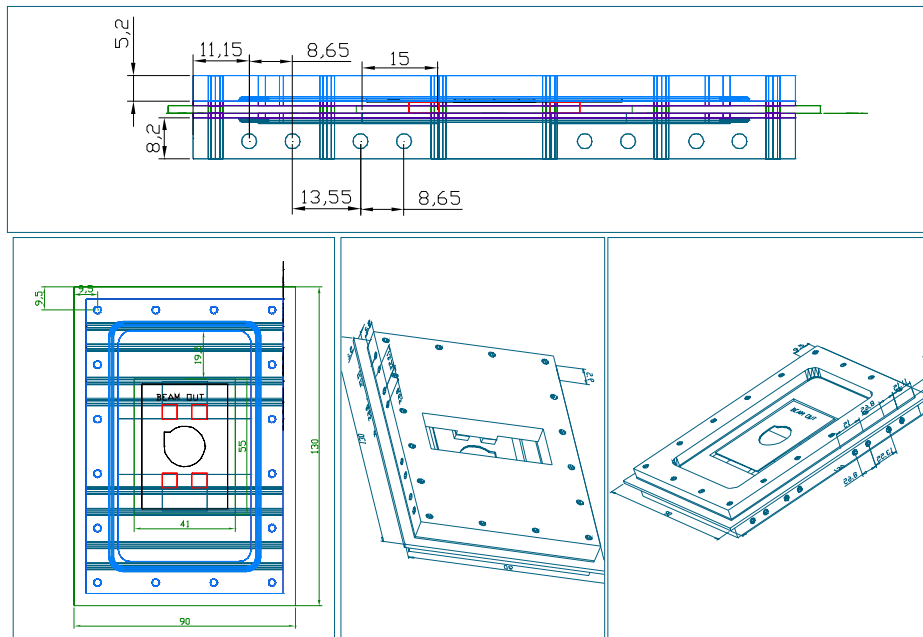


**Fig. C.11:** The AutoCAD design of the detector housing

Water cooling kit produced for CPU overclocking is used for cooling the warm side of the peltiers which is contacted to the housing with a thermal glue. The cooling kit consists of a water pump (AquaFlow 3), radiator with a fan to cool the water, ALU protect liquid to protect Al from corrosion and some other parts like pipes, T-connectors etc. During the operation of the peltiers, water is pumped continuously from a bucket filled with water and some ALU protect liquid to remove the heat from the peltiers.

### C.3.6 Detector Window

The detector window for the SDD should be thin enough to enable the transmission of the low energetic photons and it should be opaque to provide a light tight environment for the operation of the detector. Thin beryllium window is the most commonly used material for silicon detectors. However, considering the large area of the coverage needed for the SDD window (around  $12 \times 9 \text{ cm}^2$ ), this would be very expensive including the mounting of the window to the detector housing.  $8 \mu\text{m}$  thick light-tight Al foil was chosen as a window material and the mounting of the foil has been done by ourselves. X-ray transmission performances [CXR] for Al and Be are shown in Fig. C.12 as a function of the photon

energy.

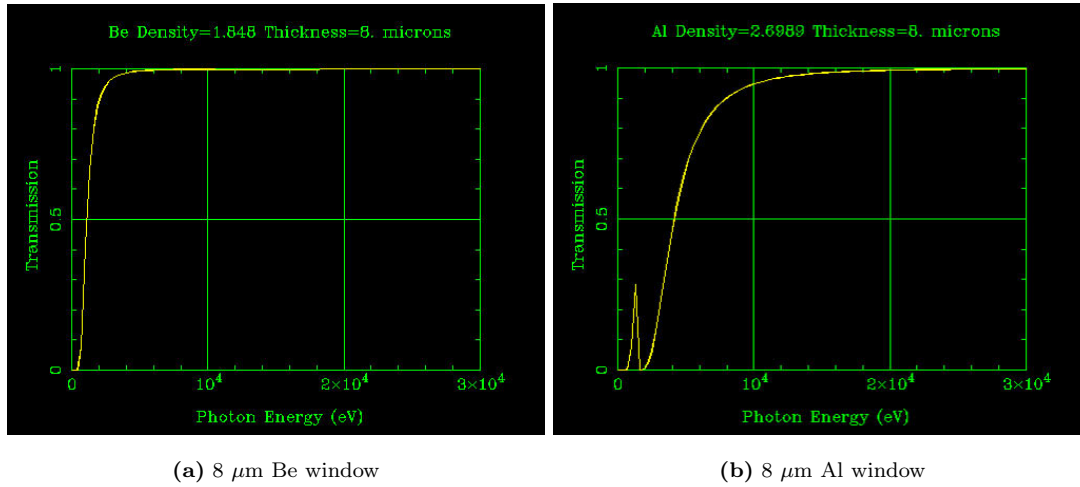


**Fig. C.12:** X-ray transmission fraction in 8  $\mu\text{m}$  thick Be and Al foils (from [CXR])

## C.4 Power Supply for the SDD

Several voltages should be supplied for the operation of the SDD. For practical purposes, instead of using commercial power supply modules, a single power supply has been designed and produced at the



**Fig. C.13:** The power supply of the SDD

electronics workshop of the department. The schematics for different parts of the power supply are shown in Fig.'s C.14, C.15, C.16 and C.17. The design was based on the power supply circuit designed for a single cell SDD at Ketek and it was modified considering the higher current value needed at the constant current source for 19 cells. In addition to this modification, a special sequence [Fio02a] has been implemented in switching the power on and off. The sequence used in switching the power on is as follows:

- R1, IGR, RESET
- CSGate
- Drain

- CSSource
- R18, BACK

The opposite sequence is applied when switching the power off. The schematics for the important parts of the power supply are shown in the following figures. The operating voltages for the 19 cell SDD have been adjusted as follows:

$$\begin{aligned}
 V_{R1} &= -7 \text{ V} & (I_{R1} = 30 \mu\text{A}) \\
 V_{R18} &= -70 \text{ V} & (I_{R18} = 71 \mu\text{A}) \\
 V_{IGR} &= -15 \text{ V} \\
 V_B &= -80 \text{ V} \\
 V_R &= -13.91 \text{ V} & (I_R = 12.49 \mu\text{A}) \\
 V_D &= +10.48 \text{ V} & (I_D = 4.66 \text{ mA}) \\
 V_G &= -5.97 \text{ V} \\
 V_S &= -6.2 \text{ V} \\
 V_C &= +6 \text{ V (emitter follower)}
 \end{aligned}$$

4.66 mA of drain current corresponds to 245  $\mu\text{A}$  of constant current for each SDD cell. Normally the currents at R1 and R18 are almost equal and the reset current is much lower than the value observed with this detector. It seems that some current is flowing from R1 to reset but luckily this does not seem to affect the operation and the performance of the detector.

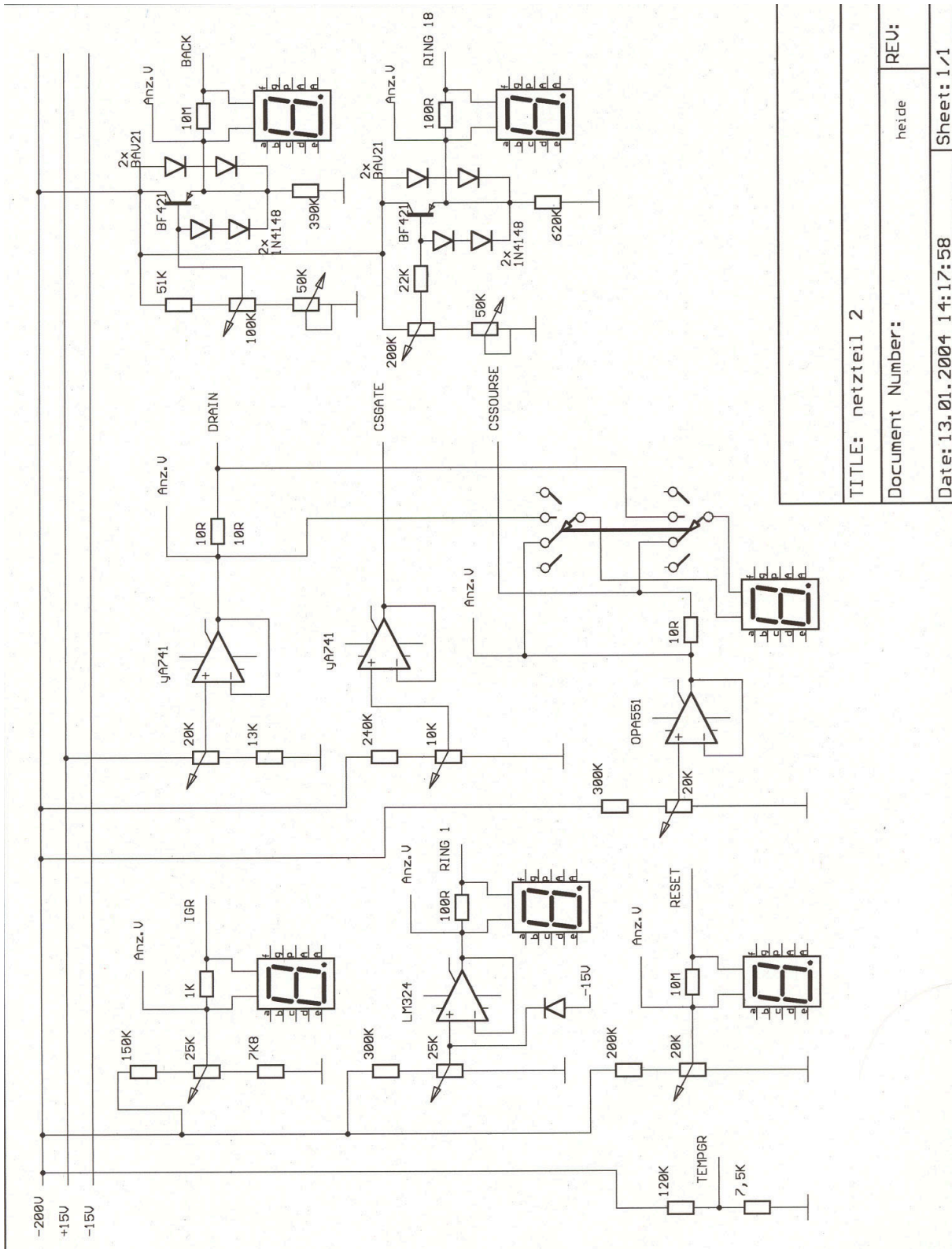
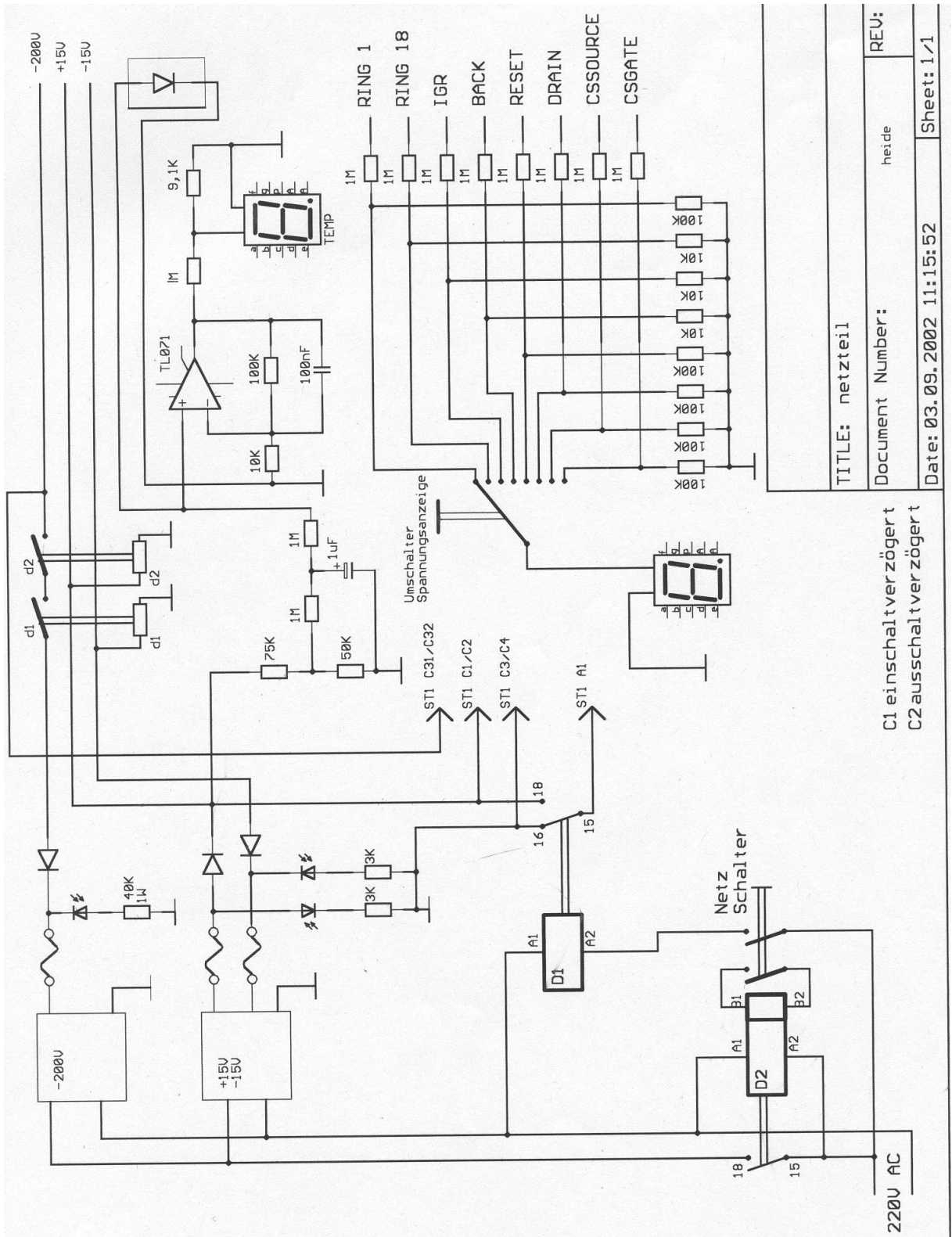


Fig. C.14: Power Supply Schematics: Part 1



TITLE: netzteil	REU:
Document Number: heide	
Date: 03.09.2002 11:15:52	Sheet: 1/1

C1 einschaltverzögert  
C2 ausschaltverzögert

Fig. C.15: Power Supply Schematics: Part 2



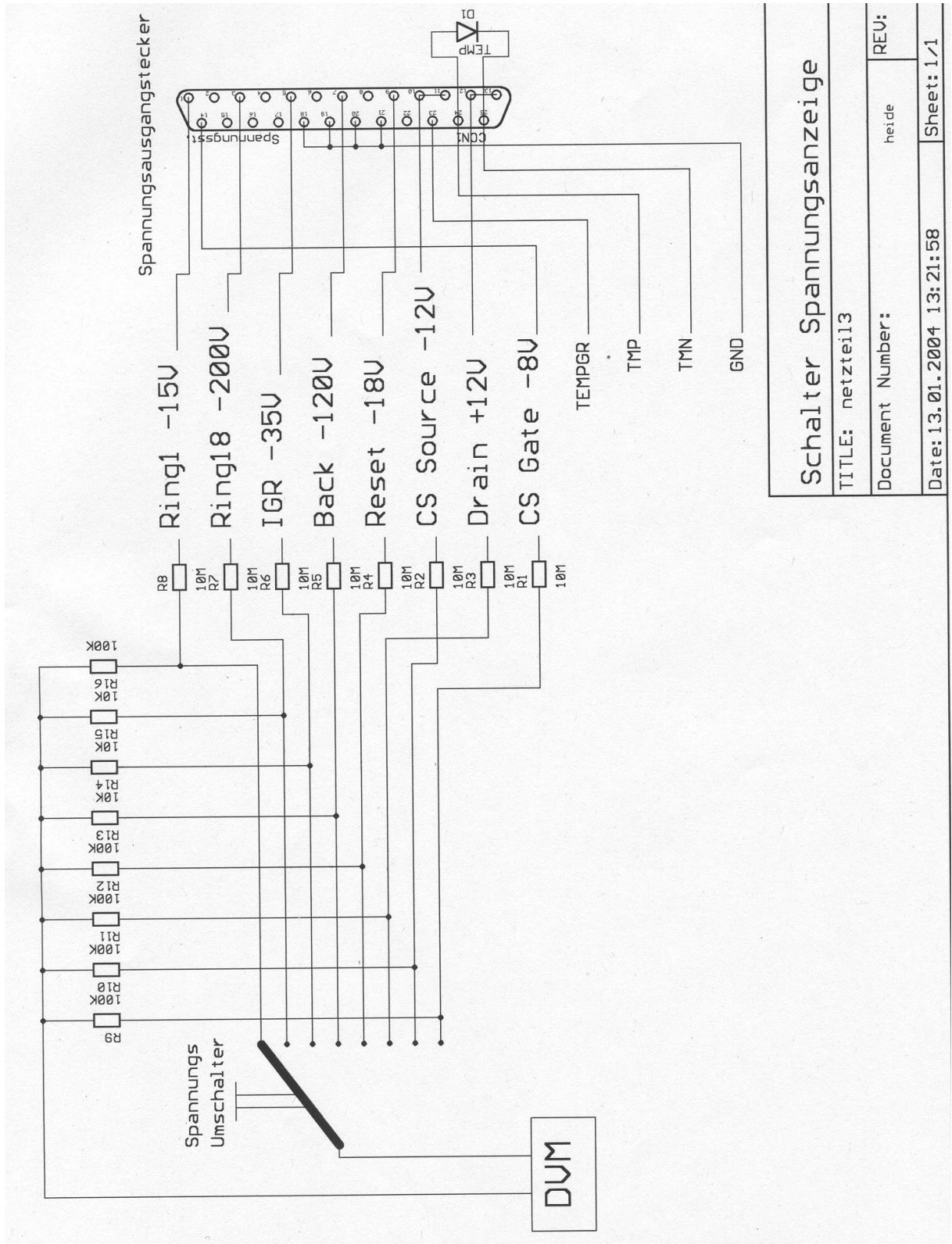


Fig. C.17: Power Supply Schematics: Part 4



## D. Appendices for Chapter 5

### D.1 Choice of the Transistors for the First Stage of the SDD Front-End Electronics

Different combinations of transistors were considered to be used in the circuit of the constant current source connected to the on-chip JFET and of the emitter follower stage proposed for the fast readout of the SDD. Both measured and simulated rise time of the preamplifier output, the measured signal amplitude and the rms-noise for these combinations are presented in Table D.1. The noise contribution

CCS+EF	$\tau_{rise}$ (ns) measurement	$\tau_{rise}$ (ns) PSPICE simulation	$V_{out}$ (mV)	$V_{rms-noise}$ (mV)
2N4416+BFT25	8.5	8	263	4.1
2N4416+no EF	72	20	117	2.2
BFP405+BFP405	3.2	2	265	4.1
BFT25+BFT25	7	4	269	4.6
2N4416+BFP405	NA	7.6	NA	NA
2N4416+BFP520	NA	6.8	NA	NA

**Tab. D.1:** Various transistor combinations tested for the constant current source of the on-chip JFET and the emitter follower circuits.

of the emitter follower circuit can be neglected, in fact the ratio of the  $V_{rms-noise}$  to the  $V_{out}$  is larger without the emitter follower which shows that the signal becomes more noisy due to the increased stray-capacitance and pick-up. This measurement was performed by keeping the experimental setup for both cases fixed in order to eliminate any additional factors. The first stage of the front-end electronics is implemented on a small PCB and the layout of the PCB with the emitter follower is a slightly modified version of the PCB without the emitter follower where only the emitter follower circuit was added, therefore the geometry of the PCB and the conducting lines were kept unchanged. The SiGET (Siemens Grounded-Emitter Transistor) transistors do not outperform BJT or JFETs selected in terms of noise but they are by at least a factor of 2 faster than other combinations. However, the range of their  $V_{CE}$  operating voltages is quite narrow which makes them not very suitable especially for the constant current source since the collector voltage depends on the operating conditions of the on-chip JFET. Considering the high dynamic range, low noise, input capacitance match and speed requirements, 2N4416 for the constant current source and BFT25 for the emitter follower have been selected.

### D.2 Calculation of the Equivalent Noise Charge

Equivalent noise charge (ENC) is the charge which when injected to the preamplifier input make the signal-to-noise ratio unity. ENC relates the root mean squared noise voltage at the output of the shaper directly to the signal strength at the input. For the measurement of the ENC, the peak pulse height at the shaper output for a known input charge should be determined. An impulse of known size is injected as shown in Fig. D.1:

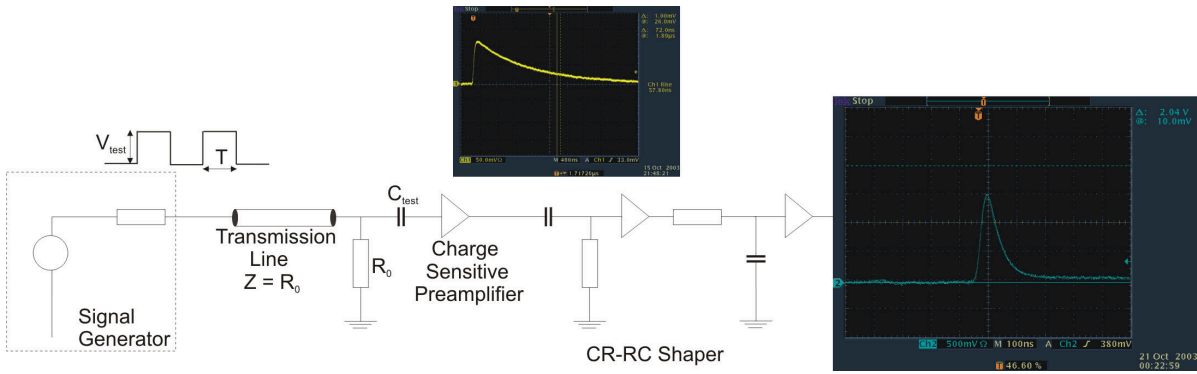
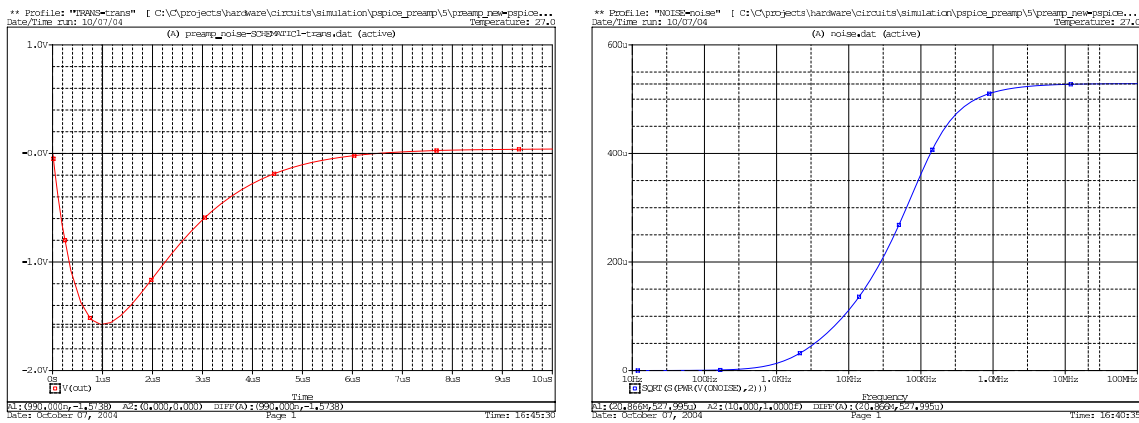


Fig. D.1: Block diagram for the ENC measurement setup

For 1 pF of test capacitor and 2 mV of step voltage the injected charge corresponds to:

$$\begin{aligned}
 Q_{test} &= C_{test} V_{test} \\
 &= 2 \cdot 10^{-15} \text{ C} \\
 &\Rightarrow \frac{2 \cdot 10^{-15}}{1.6 \cdot 10^{-19}} = 12500 \text{ electrons injected}
 \end{aligned}$$

The preamplifier used for the readout of the SDD is a voltage preamplifier and its input capacitance corresponds to the test capacitance in this figure. Using the peak pulse height at the shaper output, one can calculate the corresponding number of electrons per mV of signal. With the pulse signal disconnected from the preamplifier input the rms noise voltage is determined. This measurement can be performed by true rms voltmeter or using digital oscilloscope’s rms calculation facility or with an analog oscilloscope. The peak-to-peak noise voltage measured with the analog oscilloscope corresponds to about 4-5 times the rms noise voltage. Once the rms noise voltage is determined, it can easily be converted into the units of electrons rms by multiplying it with the calibration constant.



(a) The output of the ideal shaper obtained with the transient analysis (b) The total rms voltage noise summed over all the frequencies

Fig. D.2: Noise analysis of the preamplifier whose output is connected to an ideal shaper.

The noise analysis of the preamplifier was also performed in PSPICE simulations [Rud01; Rud96]. For this purpose, an ideal shaper is used in order to analyze the noise performance of the preamplifier.

First of all, the transient analysis is done by applying a voltage step of 2 mV to the input capacitor of the amplifier. The amplitude of the shaper output shown in Fig. D.2(a) is recorded. For the noise analysis, the simulation option should be switched to AC analysis and the noise analysis option should be switched on. This time a current source is applied at the input of the preamplifier in the absence of the input capacitor. The output noise is measured at the output of the shaper with refer to an input current source. A small macro is written that calculates the total noise over all frequencies (Fig. D.2(b)) using the following equation:

$$\sqrt{\sum_{\text{all frequencies}} V_{\text{output-noise}}^2} \quad (\text{D.1})$$

Having the values for the peak pulse height at the shaper output and the output noise, the ENC can be calculated in the same way as described in D.2.

### D.3 SPICE Simulations for the Preamplifier and Shaper

One important requirement for the preamplifier is that it should have a fast response. The simulations performed by applying a step voltage with 1 ns rise time result in a rise time of about 8 ns at the output of the preamplifier as shown in Fig. D.3.

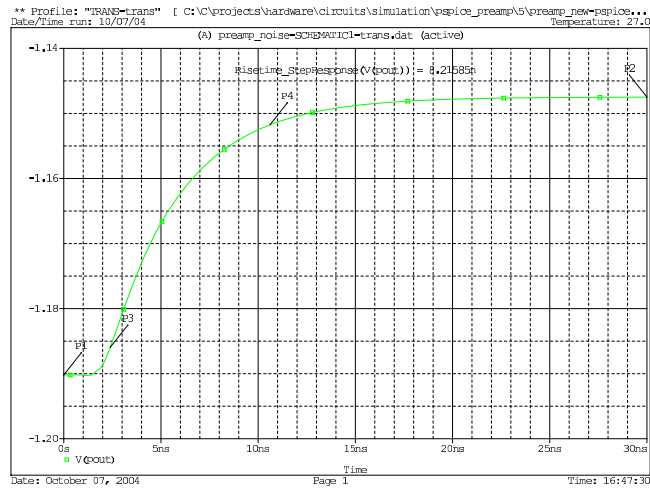


**Fig. D.3:** The response of the preamplifier to a step voltage.

The schematics of the shaper is shown in Fig. D.4. The first potentiometer is used for pole-zero and the second one for gain adjustments. There is another version of this shaper where the shaping time is also controllable. This flexibility is obtained by replacing the 5 k $\Omega$  resistance which is parallel to 2.2 nF with a potentiometer. The output of the preamplifier is connected to this shaper in order to analyze the whole analog readout chain. The shaper output and the total rms voltage noise are shown in Fig. D.5.

### D.4 Preamplifier-Shaper Carrier PCB

The support ceramic for the SDD was designed such that there are 10 SDD signal lines on the right side of the ceramic and the rest 9 on the left side. This requires one 10-channel preamplifier hybrid board on each side of the detector. The preamplifier board and five of 2-channel shaper boards are placed on a carrier PCB to which the hybrid boards are connected via pin-connectors. The signal paths from the preamplifier output to the shaper input are kept as short as possible, considering the unipolar output of the preamplifier. The carrier PCB with the hybrid boards mounted is placed in an Al box to provide

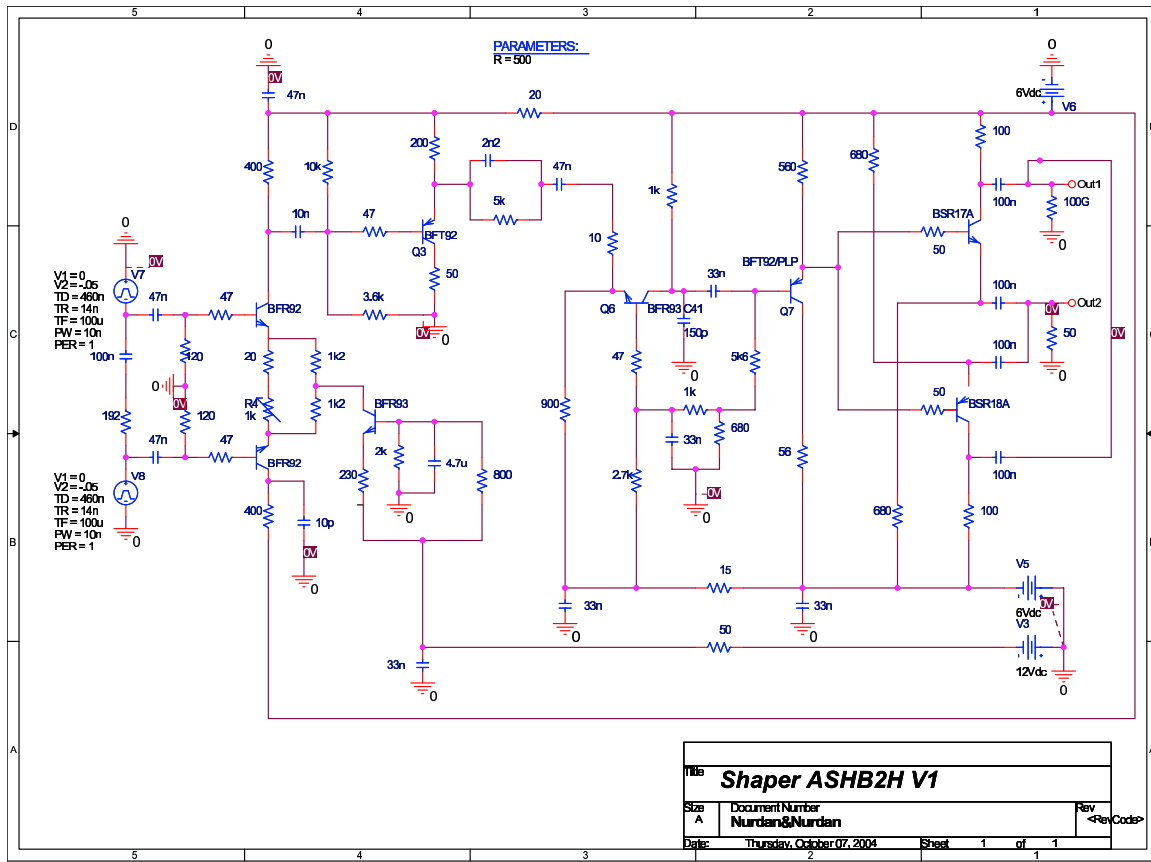
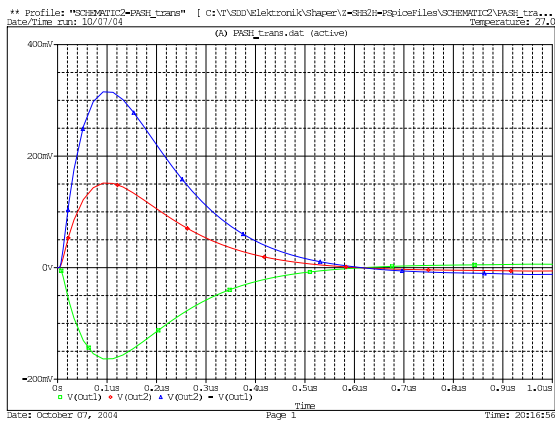
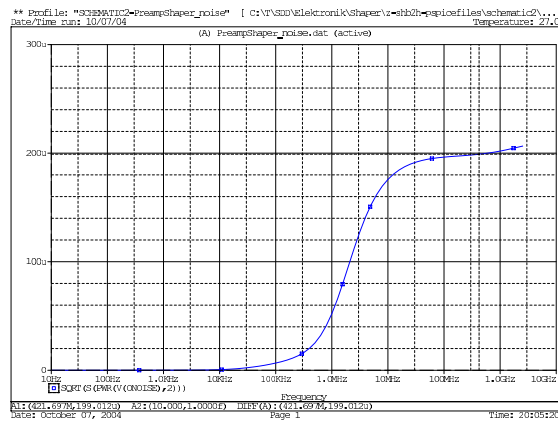


Fig. D.4: Schematics of the semi-Gaussian shaper used in the analog readout of the SDD.



(a) The output of the hybrid shaper for the step voltage applied at the input of the preamplifier



(b) The total rms voltage noise summed over all the frequencies

Fig. D.5: The transient and noise analysis of the preamplifier and shaper chain.

the electromagnetic shielding for the electronics. The schematics and the layout of the board is shown in Figures D.6 and D.7, respectively.

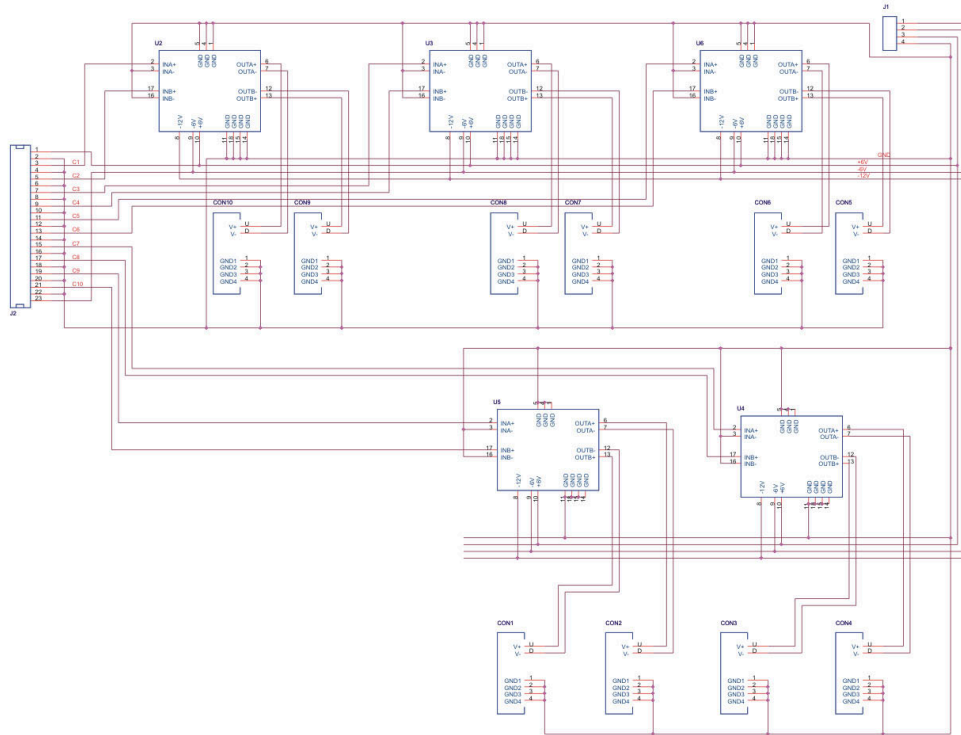
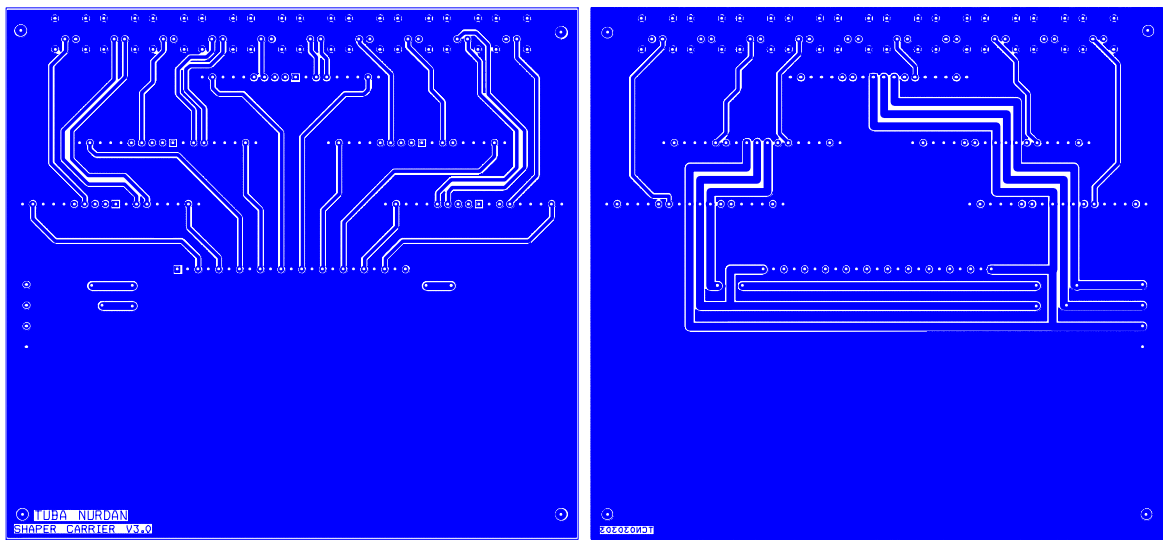


Fig. D.6: Schematics of the preamplifier-shaper carrier board.



(a) The top layer of the PCB

(b) The bottom layer of the PCB

Fig. D.7: The layout of the preamplifier-shaper carrier board.



# Bibliography

- [AMP] Amptek Inc. <http://www.amptek.com/a250.html/>.
- [AMS] AMS Technologies AG (Distributor of Melcor). <http://www.ams.de>.
- [And03] R. Andritschke, A. Zoglauer, G. Kanbach, F. Schrey, P. Bloser, S. Hunter, j. Macri, R. Miller, V. Litvinenko, M. Ahmed, and A. Donchev. The Calibration Setup of the MEGA Prototype at the High Intensity Gamma-Ray Source, 2003. Preprint submitted to New Astronomy.
- [Ang58] H. Anger. Scintillation Camera. *Review of Scientific Instruments*, vol. 29(3):pp. 27–33, 1958.
- [Ant90] P. Antich, M. Atac, R. Chaney, D. Chrisman, D. Cline, E. Fenyves, and J. Park. Development of a High Resolution Scintillating Fiber Gamma Ray Telescope. *Nucl Instr Meth A*, vol. 297:pp. 514–520, 1990.
- [Apr89] E. Aprile and M. Suzuki. Development of Liquid Xenon Detectors for Gamma Ray Astronomy. *IEEE Trans Nucl Sci*, vol. 36:pp. 311–315, Feb 1989.
- [Apr02] E. Aprile, A. Curioni, K. Giboni, M. Kobayashi, U. Oberlack, E. Chupp, P. Dunphy, T. Doke, J. Kikuchi, and S. Ventura. The LXeGRIT Compton Telescope Prototype: Current Status and Future Prospects. In *SPIE Proceedings*. 2002.
- [Ata89] M. Atac, D. Cline, D. Chrisman, J. Kolonko, J. Park, E. Fenyves, and R. Chaney. High Resolution Gamma Ray Telescope Using Scintillating Fibers and Position Sensitive Photomultipliers. *Nuclear Physics B (Proc Suppl)*, vol. 10B:pp. 139–142, 1989.
- [Bec02] F. Beck, I. Piqueras, E. Pachoud, G. Duchêne, O. Dorvaux, P. Medina, and C. Ring. An alternative  $\gamma$ -tracking method using the Compton-scattering probability. In *Nuclear Structure with Large  $\gamma$ -arrays: Status and perspectives, NS 2002, Eur. Phys. J. A 20 (2004) 203*. Legnaro-Padova, Italy, 2002.
- [Bha04] D. Bhattacharya, T. O’Neill, A. Akyüz, J. Samimi, and A. Zych. Prototype TIGRE Compton Gamma-Ray Balloon-Borne Telescope. In *Proceedings of Astronomy with Radioactivities IV and Filling the Sensitivity Gap in MeV Astronomy*, vol. 48, pp. 287–292. New Astronomy Reviews, Kloster Seeon Conference Center, Germany, May 26-30, 2003, 2004.
- [Big75] F. Biggs, L. Mendelsohn, and J. Mann. *Atomic Data and Nuclear Data Tables*, vol. 16:p. 201, 1975.
- [Blo04] P. Bloser, S. Hunter, J. Ryan, M. McConnell, R. Miller, T. Jackson, and B. B. S. Jung. Applications of Gas Imaging Micro-well Detectors to an Advanced Compton Telescope. In *Proceedings of Astronomy with Radioactivities IV and Filling the Sensitivity Gap in MeV Astronomy*, vol. 48, pp. 299–303. New Astronomy Reviews, Kloster Seeon Conference Center, Germany, May 26-30, 2003, 2004.
- [Bog04] S. Boggs, W. Coburn, D. Smith, J. Bowen, P. Jean, J. Kregenow, R. Lin, and P. von Ballmoos. Overview of the Nuclear Compton Telescope. In *Proceedings of Astronomy with Radioactivities IV and Filling the Sensitivity Gap in MeV Astronomy*, vol. 48, pp. 251–255. New Astronomy Reviews, Kloster Seeon Conference Center, Germany, May 26-30, 2003, 2004.

- [Bol97] A. Bolozdynya, V. Egorov, A. Koutchenkov, G. Safronov, G. Smirnov, S. Medved, and V. Morgunov. A High Pressure Xenon Self-Triggered Scintillation Drift Chamber with 3D Sensitivity in the Range of 20-140 keV Deposited Energy. *Nucl Instr Meth A*, vol. 385:pp. 225–238, 1997.
- [Bol98] A. Bolozdynya and V. Morgunov. Multilayer Electroluminescence Camera: Concept and Monte Carlo Study. *IEEE Trans Nucl Sci*, vol. 45:pp. 1646–1655, 1998.
- [Bri04] A. Brill. Compton Camera Collaboration Meeting, Rome, March 2004.
- [BSR] bsr braun & storie representatives mbh (Distributor of Saint-Gobain Industrial Ceramics). <http://www.bsr-europe.com/>.
- [Cas04a] A. Castoldi, A. Galimberti, C. Guazzoni, L. Strüder, and A. Walenta. New Silicon Drift Detector Design for High Resolution Compton Cameras for Radiopharmaceuticals Mapping. In *IEEE Nuclear Science Symposium and Medical Imaging Conference NSS-MIC 2004, N45-7*. Rome, Italy, 2004.
- [Cas04b] A. Castoldi, E. Gatti, and C. Guazzoni. Fast Triggering in Silicon Drift Detectors by means of Holes' Induction. *Nucl Instr Meth A*, vol. 518:pp. 429–432, 2004.
- [Ch.96] Ch. Gauthier and J. Goulon and E. Moguiline and A. Rogalev and P. Lechner and L. Strüder and C. Fiorini and A. Longoni and M. Sampietro and H. Besch and R. Pfitzner and H. Schenk and U. Tafelmeier and A. Walenta and K. Misiakos and S. Kavadias and D. Loukas. A High Resolution, 6 Channels, Silicon Drift Detector Array with Integrated JFET's Designed for XAFS Spectroscopy: First X-ray Fluorescence Excitation Spectra Recorded at the ESRF. *Nucl Instr Meth A*, vol. 382:pp. 524–532, 1996.
- [Chi04] I. Chiosa. *New Implementation of a Compton Camera Image Reconstruction Algorithm for Biomedical Applications*. Master's thesis, University of Siegen, 2004.
- [CLH] CLHEP - A Class Library for High Energy Physics. <http://wwwasd.web.cern.ch/wwwasd/lhc++/clhep/>.
- [ÇN01] T. Çonka-Nurdan, K. Nurdan, F. Constantinescu, B. Freisleben, H. Kamberaj, N. Pavel, I. Rauhut, K. Reichmann, and A. Walenta. Influence of the Detector Parameters on a Compton Camera. In *IEEE Nuclear Science Symposium and Medical Imaging Conference NSS-MIC 2000, MIC-50*. Lyon, France, 2001.
- [ÇN02] T. Çonka-Nurdan, K. Nurdan, F. Constantinescu, B. Freisleben, N. Pavel, and A. Walenta. Impact of the Detector Parameters on a Compton Camera. *IEEE Trans Nucl Sci*, vol. 49(3):pp. 817–821, Jun 2002.
- [ÇN03] T. Çonka-Nurdan, K. Nurdan, K. Laihem, A. Walenta, C. Fiorini, N. Hörnel, L. Strüder, and C. Venanzi. Compton Electrons in Silicon Drift Detector: First Results. In *IEEE Nuclear Science Symposium and Medical Imaging Conference NSS-MIC 2003, M6-41*. Portland, USA, 2003.
- [ÇN04a] T. Çonka-Nurdan, K. Nurdan, K. Laihem, A. Walenta, C. Fiorini, B. Freisleben, N. Hörnel, N. Pavel, and L. Strüder. Preliminary Results on Compton Electrons in Silicon Drift Detector. *IEEE Trans Nucl Sci*, vol. 51(5):pp. 2526–2532, 2004.
- [ÇN04b] T. Çonka-Nurdan, K. Nurdan, A. Walenta, H. Besch, C. Fiorini, B. Freisleben, and N. Pavel. Silicon Drift Detector Readout Electronics for a Compton Camera. *Nucl Instr Meth A*, vol. 523:pp. 435–440, 2004.
- [ÇN04c] T. Çonka-Nurdan, K. Nurdan, A. Walenta, I. Chiosa, B. Freisleben, N. Pavel, and L. Strüder. Compton Camera Coincidences in the Silicon Drift Detector. In *IEEE Nuclear Science Symposium and Medical Imaging Conference NSS-MIC 2004, M10-60*. Rome, Italy, 2004.

- [Com23] A. H. Compton. A Quantum Theory of the Scattering of X-rays by Light Elements. *The Physical Review*, vol. 21(5):pp. 483–502, 1923.
- [Con01] F. Constantinescu. *Klinische Anwendungen von  $^{113m}\text{In}$  mit einer Compton Kamera*. Ph.D. thesis, Medizinische Fakultät der Universität Bonn, 2001.
- [CXR] Center for X-Ray Optics at Lawrence Berkeley Laboratory. [http://www-cxro.lbl.gov/optical\\_constants/filter2.html](http://www-cxro.lbl.gov/optical_constants/filter2.html).
- [Dog90] N. Dogan, D. Wehe, and G. Knoll. Multiple Compton-scattering Gamma-ray Imaging Camera. *Nucl Instr Meth A*, vol. 299:pp. 501–506, 1990.
- [Dog94] N. Dogan and D. Wehe. Efficiency and Angular Resolution Calculations for a Prototype Multiple Compton Scatter Camera. *Nucl Instr Meth A*, vol. 345:pp. 296–302, 1994.
- [Du01] Y. Du, Z. He, G. Knoll, D. Wehe, and W. Li. Evaluation of Compton Scattering Camera Using 3-D Position Sensitive CdZnTe Detectors. *Nucl Instr Meth A*, vol. 457:pp. 203–211, 2001.
- [DuM29] J. DuMond. Compton Modified Line Structure and Its Relation to the Electron Theory of Solid Bodies. *Phys Rev*, vol. 33(5):pp. 643–658, May 1929.
- [Eis72] P. Eisenberger and W. Reed. Gamma-Ray Compton Scattering: Experimental Compton Profiles for He, N<sub>2</sub>, Ar, and Kr. *Phys Rev A*, vol. 5(5):pp. 2085–2093, May 1972.
- [ESL] Agmet Ltd - Electro-Science Laboratories, Inc. Europe. <http://www.ElectroScience.com/>.
- [Eva82] R. D. Evans. *The Atomic Nucleus*. Robert E. Krieger Publishing Company, Malabar, Florida, Reprint edition of 1972 14th edn., 1982.
- [Fan47] U. Fano. Ionization Yield of Radiations. II. The Fluctuations of the Number of Ions. *Phys Rev*, vol. 72(1):pp. 26–29, Jul 1947.
- [Far83] W. Farr and G. Smith. Emitter followers and source followers as low noise pre-amplifiers for gas proportional detectors. *Nucl Instr Meth*, vol. 382:pp. 159–167, 1983.
- [Fio97] C. Fiorini, A. Longoni, F. Perotti, C. Labanti, P. Lechner, and L. Strüder. Gamma Ray Spectroscopy with CsI(Tl) Scintillator Coupled to Silicon Drift Chamber. *IEEE Trans Nucl Sci*, vol. 44(6):pp. 2553–2560, 1997.
- [Fio98] C. Fiorini. *High-resolution X-ray Spectroscopy with Silicon Drift Detectors*. Ph.D. thesis, Politecnico di Milano, 1998.
- [Fio99a] C. Fiorini and A. Longoni. In-Situ, Non-Destructive Identification of Chemical Elements by Means of Portable EDXRF Spectrometer. *IEEE Trans Nucl Sci*, vol. 46(6):pp. 2011–2016, Dec 1999.
- [Fio99b] C. Fiorini, F. Perotti, C. Labanti, A. Longoni, and E. Rossi. Position and Energy Resolution of a new Gamma-ray Detector Based on a Single CsI(Tl) Scintillator Coupled to a Silicon Drift Chamber Array. *IEEE Trans Nucl Sci*, vol. 46(4):pp. 858–863, Aug 1999.
- [Fio02a] C. Fiorini. Politecnico di Milano, personal communication, Jul 2002.
- [Fio02b] C. Fiorini, A. Longoni, F. Perotti, C. Labanti, E. Rossi, P. Lechner, H. Soltau, and L. Strüder. A Monolithic Array of Silicon Drift Detectors for High-resolution Gamma-ray Imaging. *IEEE Trans Nucl Sci*, vol. 49(3):pp. 995–1000, Jun 2002.
- [Gat84a] E. Gatti and P. Rehak. Semiconductor Drift Chambers - An Application of a Novel Charge Transport Scheme. *Nucl Inst Meth in Phys Res*, vol. 225:pp. 608–614, 1984.
- [Gat84b] E. Gatti, P. Rehak, and J. Walton. Silicon Drift Chambers - First Results and Optimum Processing of Signals. *Nucl Inst Meth A*, vol. 226:pp. 129–141, 1984.

- [GEA94] GEANT: Detector Description and Simulation Tool, Version 3.21, 1994. [http://wwwasdoc.web.cern.ch/wwwasdoc/geant\\_html13/geantall.html](http://wwwasdoc.web.cern.ch/wwwasdoc/geant_html13/geantall.html).
- [Geb90] M. Gebser. *Messung der Ejektionsrichtung von Compton-Elektronen fuer die Bildrekonstruktion mit einer Compton-Kamera nach dem TEC-Prinzip*. Ph.D. thesis, University of Siegen, 1990.
- [Goo] Good Fellow GmbH. <http://www.goodfellow.com>.
- [Gru96] C. Grupen. *Particle Detectors*. Cambridge University Press, Cambridge, Great Britain, 1996.
- [Han00] K. Hansen and L. Tröger. A Novel Multicell Silicon Drift Detector Module for X-Ray Spectroscopy and Imaging Applications. *IEEE Trans Nucl Sci*, vol. 47(6):pp. 2748–2757, Dec 2000.
- [Her75] D. Herzo, R. Koga, W. Millard, S. Moon, J. Ryan, R. Wilson, A. Zych, and R. White. A Large Double Scatter Telescope for Gamma Rays and Neutrons. *Nuclear Instruments and Methods*, vol. 123:pp. 583–597, 1975.
- [HLL] Max-Planck-Institute Semiconductor Laboratory. <http://www.hll.mpg.de>.
- [Hof50] R. Hofstadter and J. McIntyre. Measurement of Gamma-Ray Energies with Two Crystals in Coincidence. *Physical Review*, vol. 78:pp. 619–620, 1950.
- [Hol00] M. Holder. University of Siegen, personal communication, 2000.
- [Hon00] A. Honma. CERN, personal communication, Oct 2000.
- [Int] Inter Medical Medizintechnik GmbH. <http://www.intmed.de>.
- [Joh95] W. Johnson, C. Dermer, R. Kroeger, J. Kurfess, N. Gehrels, J. Grindlay, M. Leising, T. Prince, W. Purcell, J. Ryan, and T. Tümer. Advanced Telescope for High Energy Nuclear Astrophysics (ATHENA). *SPIE Proceedings*, vol. 2518:pp. 74–84, 1995.
- [Kam87] T. Kamae, R. Enomoto, and N. Hanada. A New Method to Measure Energy, Direction, and Polarization of Gamma-rays. *Nucl Instr Meth A*, vol. 260:pp. 254–257, 1987.
- [Kan72] K. Kanaya and S. Okayama. Penetration and Energy-loss Theory of Electrons in Solid Targets. *Journal of Physics D: Applied Physics*, vol. 5:pp. 43–58, 1972.
- [Kan04] G. Kanbach, R. Andritschke, F. Shopper, V. Schönfelder, A. Zoglauer, P. Blosler, S. Hunter, J. Ryan, M. McConnell, V. Reglero, G. DiCocco, and J. Knödlseher. The MEGA Project. In *Proceedings of Astronomy with Radioactivities IV and Filling the Sensitivity Gap in MeV Astronomy*, vol. 48, pp. 275–280. New Astronomy Reviews, Kloster Seon Conference Center, Germany, May 26-30, 2003, 2004.
- [Kem80] J. Kemmer. Fabrication of Low Noise Silicon Radiation Detectors by the Planar Process. *Nucl Inst Meth*, vol. 169:pp. 499–502, 1980.
- [Kem87] J. Kemmer, G. Lutz, E. Belau, U. Prechtel, and W. Welser. Low Capacity Drift Diode. *Nucl Inst Meth A*, vol. 253:pp. 378–381, 1987.
- [KET] KETEK GmbH Halbleiter- und Reinraumtechnik. <http://www.ketek.net>.
- [Kin94] S. King, G. Phillips, P. Haskins, J. McKisson, R. Piercey, and R. Mania. A Solid-State Compton Camera for Three-Dimensional Imaging. *Nucl Instr Meth A*, vol. 353:pp. 320–323, 1994.
- [Kip02] R. M. Kippen. GLECS: GEANT Low-Energy Compton Scattering, Version 3.33, 2002. [http://nis-www.lanl.gov/~mkippen/actsim/glecs/glecs\\_readme.txt](http://nis-www.lanl.gov/~mkippen/actsim/glecs/glecs_readme.txt).
- [Kle29] O. Klein and Y. Nishina. Über die Streuung von Strahlung durch freie Elektronen nach der neuen relativistischen Quantendynamik von Dirac. *Zeitschrift für Physik*, vol. 52:pp. 853–868, 1929.

- [Kno99] G. F. Knoll. *Radiation Detection and Measurement*. John Wiley & Sons, Inc., New York, USA, third edn., 1999.
- [Kro00] R. Kroeger, W. Johnson, J. Kurfess, B. Philips, P. Luke, M. Momayezi, and W. Warburton. Position Sensitive Germanium Detectors for the Advanced Compton Telescope. *AIP Conference Proceedings*, vol. 510:pp. 794–798, 2000.
- [Kur00] J. Kurfess, W. Johnson, R. Kroeger, and B. Philips. Considerations for the Next Compton Telescope Mission. *AIP Conference Proceedings*, vol. 510:pp. 789–793, 2000.
- [Kur02] J. Kurfess and B. Philips. Coincident Compton Nuclear Medical Imager. In *2001 IEEE Nuclear Science Symposium and Medical Imaging Conference*. San Diego, California, USA, 2002.
- [Lai04] K. Laihem. *Effect of Temperature on the Performance of Si-Drift Detector, Analysis and Technical Implementation*. Master’s thesis, University of Siegen, 2004.
- [LBL] LBNL Isotopes Project - LUNDS Universitet, WWW Table of Radioactive Isotopes. <http://ie.lbl.gov/toi/>.
- [LeB98] J. LeBlanc, N. Clinthorne, C.-H. Hua, E. Nygård, W. Rogers, D. Wehe, P. Weilhammer, and S. Wilderman. C-SPRINT: A Prototype Compton Camera System for Low Energy Gamma Ray Imaging. *IEEE Trans Nucl Sci*, vol. 45:pp. 943–949, Jun 1998.
- [LeB99a] J. LeBlanc. *A Compton Camera for Low Energy Gamma-Ray Imaging in Nuclear Medicine Applications*. Ph.D. thesis, University of Michigan, 1999.
- [LeB99b] J. LeBlanc, X. Bai, N. Clinthorne, C. Hua, D. Meier, W. Rogers, D. Wehe, P. Weilhammer, and S. Wilderman.  $^{99m}\text{Tc}$  Imaging Performance of the C-SPRINT Compton Camera. In *IEEE Nuclear Science Symposium and Medical Imaging Conference, N16-3*. 1999.
- [LeB99c] J. LeBlanc, N. Clinthorne, C.-H. Hua, W. Rogers, D. Wehe, and S. Wilderman. A Compton Camera for Nuclear Medicine Applications Using  $^{113m}\text{In}$ . *Nucl Instr Meth A*, vol. 422:pp. 735–739, 1999.
- [Lec93] P. Lechner, L. Andricek, N. Findeis, D. Hauff, P. Holl, J. Kemmer, P. Klein, G. Lutz, N. Meidinger, E. Pinotti, R. Richter, L. Strüder, and C. Zanthier. New DEPMOS Applications. *Nucl Inst Meth A*, vol. 326:pp. 284–289, 1993.
- [Lec96] P. Lechner, S. Eckbauer, R. Hartmann, S. Krisch, D. Hauff, R. Richter, H. Soltau, L. Strüder, C. Fiorini, E. Gatti, A. Longoni, and M. Sampietro. Silicon Drift Detectors for High Resolution Room Temperature X-ray Spectroscopy. *Nucl Inst Meth A*, vol. 377:pp. 346–351, 1996.
- [Leo94] W. R. Leo. *Techniques for Nuclear and Particle Physics Experiments*. Springer-Verlag, Berlin Heidelberg, second edn., 1994.
- [Loc81] J. Lockwood, W. Webber, L. Friling, J. Macri, and L. Hsieh. Observations of Gamma Radiation Between 0.4 MeV and 7 MeV at Balloon Altitudes Using a Compton Telescope. *The Astrophysical Journal*, vol. 248:pp. 1194–1201, Sep 1981.
- [Lu05] J. Lu. *Coordinate Calibration of the Anger Camera for Compton Camera Measurements*. Master’s thesis, University of Siegen, 2005.
- [Lut99] G. Lutz. *Semiconductor Radiation Detectors*. Springer-Verlag, Berlin Heidelberg, 1999.
- [Mar69] P. Marmier and E. Sheldon. *Physics of Nuclei and Particles*. Academic Press, New York, USA, 1969.
- [Mar93] J. Martin, G. Knoll, D. Wehe, N. Dogan, V. Jordanov, and N. Petrick. A Ring Compton Scatter Camera for Imaging Medium Energy Gamma Rays. *IEEE Trans Nucl Sci*, vol. 40:pp. 972–978, Aug 1993.

- [Mar94] J. Martin, N. Dogan, J. Gormley, G. Knoll, M. O'Donnell, and D. Wehe. Imaging Multi-Energy Gamma-Ray Fields with a Compton Scatter Camera. *IEEE Trans Nucl Sci*, vol. 41:pp. 1019–1025, Aug 1994.
- [Mar04] M. Marisaldi, C. Labanti, A. Bulgarelli, E. Celesti, G. D. Cocco, F. Gianotti, A. Mauri, E. Rossi, A. Traci, and M. Trifoglio. Calorimeter Prototype Based on Silicon Drift Detectors Coupled to Scintillators for Compton Telescope Application. In *Proceedings of Astronomy with Radioactivities IV and Filling the Sensitivity Gap in MeV Astronomy*, vol. 48, pp. 305–308. New Astronomy Reviews, Kloster Seeon Conference Center, Germany, May 26-30, 2003, 2004.
- [Mes] Messer Griesheim GmbH (Air Liquide Deutschland GmbH). [http://www.spezialgase.de/spezialgasekatalog/gase/stickstoff/6\\_0/index.%html](http://www.spezialgase.de/spezialgasekatalog/gase/stickstoff/6_0/index.%html).
- [MHW] MH&W Elektronik-Vertrieb GmbH (Distributor of ShinEtsu Polymer Co., Ltd.). <http://www.speurope.nl/>.
- [Mus95] G. Musiol, J. Ranft, R. Reif, and D. Seeliger. *Kern- und Elementarteilchenphysik*. Verlag Harri Deutsch, Frankfurt am Main, second edn., 1995.
- [NMR] Nuclear Medicine Research Council Website. <http://www.cbvcp.com/nmrc/mia.html>.
- [Nur03a] K. Nurdan, H. Besch, T. Çonka-Nurdan, B. Freisleben, N. Pavel, and A. Walenta. Development of a Compton Camera Data Acquisition System Using FPGAs. In *Proceedings of ISPC (International Signal Processing Conference)*. Dallas, USA, 2003.
- [Nur03b] K. Nurdan, T. Çonka-Nurdan, H. Besch, B. Freisleben, N. Pavel, and A. Walenta. FPGA Based Data Acquisition System for a Compton Camera. In *Proceedings of SAMBA II (Symposium on Applications of Particle Detectors in Medicine, Biology and Astrophysics)*, vol. 510, pp. 122–125. Nucl. Instr. Meth. A, Trieste, Italy, May 27-29, 2002, 2003.
- [Nur05] K. Nurdan. *Data Acquisition, Event Building and Signal Reconstruction for Compton Camera Imaging*. Ph.D. thesis, University of Siegen, 2005.
- [O'N92] T. O'Neill, F. Ait-Ouamer, I. Schwartz, O. Tümer, R. White, and A. Zych. Compton Recoil Electron Tracking with Silicon Strip Detectors. *IEEE Trans Nucl Sci*, vol. 39:pp. 629–634, 1992.
- [O'N03] T. O'Neill, D. Bhattacharya, M. Polsen, A. Zych, J. Samimi, and A. Akyüz. Development of the TIGRE Compton Telescope for Intermediate-Energy Gamma-Ray Astronomy. *IEEE Trans Nucl Sci*, vol. 50:pp. 251–257, Apr 2003.
- [Pau02] J. Pauli, E. Pauli, and G. Anton. ITEM - QM Solutions for EM Problems in Image Reconstruction Exemplary for the Compton Camera. *Nucl Instr Meth A*, vol. 488:pp. 323–331, 2002.
- [Pet61] L. Peterson and R. Howard. *IRE Trans Nucl Sci*, vol. NS-8(4):pp. 21–29, 1961.
- [Pie89] R. Piercey, A. Weisenberger, J. McKisson, and C. Girit. Preliminary Characteristics of a Germanium-Based, Compton-Scatter Telescope. *IEEE Trans Nucl Sci*, vol. 36:pp. 887–890, Feb 1989.
- [Pro03] D. Protić, T. Krings, and R. Schleichert. Development of DOuble-sided Microstructured Si(Li)-Detectors. In *IEEE Nuclear Science Symposium and Medical Imaging Conference NSS-MIC 2001, R16-2*. San Diego, California, USA, 2003.
- [Pro04] D. Protić, E. Hull, T. Krings, and K. Vetter. Large-Volume Si(Li) Orthogonal-Strip Detectors for Compton Effect Based Instruments. In *IEEE Nuclear Science Symposium and Medical Imaging Conference NSS-MIC 2004, N16-197*. Rome, Italy, 2004.
- [PSP03] PSPICE: Professional Simulation Package with Integrated Circuit Emphasis Release 10.0, 2003. <http://www.orcad.com/products/pspice/>.

- [Ree72] W. Reed and P. Eisenberger. Gamma-Ray Compton Profiles of Diamond, Silicon, and Germanium. *Phys Rev B*, vol. 6(12):pp. 4596–4604, Dec 1972.
- [Rib75] R. Ribberfors. Relationship of the Relativistic Compton Cross Section to the Momentum Distribution of Bound Electron States. *Phys Rev B*, vol. 12(6):pp. 2067–2074, Sep 1975.
- [Rib82] R. Ribberfors and K. Berggren. Incoherent-x-ray-scattering Functions and Cross Sections  $(d\sigma/d\Omega')_{incoh}$  by means of a pocket calculator. *Phys Rev A*, vol. 26(6):pp. 3325–3333, Dec 1982.
- [Roy04] G. Royle, R. Speller, P. Sellin, J. Gabathuse, and W. Ghoggali. Development of a Pixellated Germanium Compton Camera for Nuclear Medicine. In *2003 IEEE Nuclear Science Symposium and Medical Imaging Conference, CC1-5*. Portland, USA, 2004.
- [Rud96] A. Rudge. Noise Simulation Using PSpice. *CERN IT-CE Newsletter: Computing for Engineers*, vol. 21, Nov 1996.
- [Rud01] A. Rudge. CERN, personal communication, Dec 2001.
- [San88] H.-J. Sanden. *Die physikalischen Grundlagen der Energieauflösung einer Time Expansion Chamber (TEC)*. Ph.D. thesis, University of Siegen, 1988.
- [Sca00] M. Scannavini, R. Speller, G. Royle, I. Cullum, M. Raymond, G. Hall, and G. Iles. Design of a Small Laboratory Compton Camera for the Imaging of Positron Emitters. *IEEE Trans Nucl Sci*, vol. 47:pp. 1155–1162, June 2000.
- [Sch73] V. Schönfelder, A. Hirner, and K. Schneider. A Telescope for Soft Gamma Ray Astronomy. *Nuclear Instruments and Methods*, vol. 107:pp. 385–394, 1973.
- [Sch84] V. Schönfelder, R. Diehl, G. Lichti, H. Steinle, B. Swanenburg, A. Deerenberg, H. Aarts, J. Lockwood, W. Webber, J. Macri, J. Ryan, G. Simpson, B. Taylor, K. Bennett, and M. Snelling. The Imaging Compton Telescope COMPTEL on the Gamma Ray Observatory. *IEEE Transactions on Nuclear Science*, vol. NS-31:pp. 766–770, Feb 1984.
- [Sch95] V. Schönfelder. A Survey of COMPTEL Results. *Advanced Space Research*, vol. 15(5):pp. (5)1–(5)12, 1995.
- [Sch01] G. Schmid, D. Beckedahl, J. Kammeraad, J. Blair, K. Vetter, and A. Kuhn. Gamma-Ray Compton Camera Imaging with a Segmented HPGe. *Nucl Instr Meth A*, vol. 459:pp. 565–576, 2001.
- [Sch03] V. Schönfelder. Lessons Learnt from COMPTEL for Future Telescopes. In *Proceedings of Astronomy with Radioactivities IV and Filling the Sensitivity Gap in MeV Astronomy*. Kloster Seon Conference Center, Germany, May 26-30, 2003.
- [Sho00] F. Shopper, R. Andritschke, H. Shaw, C. Nefzger, A. Zoglauer, V. Schönfelder, and G. Kanbach. CsI Calorimeter with 3-D Position Resolution. *Nucl Instr Meth A*, vol. 442:pp. 394–399, 2000.
- [Sie] Siegert TFT GmbH - Thinfilm Technology. <http://www.siegert-tft.de/>.
- [Sin83] M. Singh. An Electronically Collimated Gamma Camera for Single Photon Emission Computed Tomography. Part I: Theoretical Considerations and Design Criteria. *Medical Physics*, vol. 10(4):pp. 421–427, Jul/Aug 1983.
- [Sin84] M. Singh and D. Doria. Germanium-Scintillation Camera Coincidence Detection Studies for Imaging Single Photon Emitters. *IEEE Trans Nucl Sci*, vol. NS-31:pp. 594–598, Feb 1984.
- [Sin86] M. Singh, R. Brechner, and C. Horne. Single Photon Imaging at High Energies with Electronic Collimation. *Proc SPIE - Int Soc Opt Eng(USA)*, vol. 671:pp. 184–188, 1986.

- [Sin95] M. Singh, F. Doty, S. Friesenhahn, and J. Butler. Feasibility of Using Cadmium-Zinc-Telluride Detectors in Electronically Collimated SPECT. *IEEE Trans Nucl Sci*, vol. 42(4):pp. 1139–1146, Aug 1995.
- [Sol88] C. Solomon and R. Ott. Gamma Ray Imaging with Silicon Detectors - A Compton Camera for Radionuclide Imaging in Medicine. *Nucl Instr Meth A*, vol. 273:pp. 787–792, 1988.
- [Str98] L. Strüder, C. Fiorini, E. Gatti, R. Hartmann, P. Holl, N. Krause, P. Lechner, A. Longoni, J. Kemmer, N. Meidinger, M. Popp, H. Soltau, U. Weber, and C. von Zanthier. High-Resolution High-Count-Rate X-ray Spectroscopy with State-of-the-Art Silicon Detectors. *Journal of Synchrotron Radiation*, vol. 5:pp. 268–274, 1998.
- [Stu03] A. Studen, V. Cindro, and N. C. et al. Development of Silicon Pad Detectors and Readout Electronics for a Compton Camera. *Nucl Instr Meth A*, vol. 501:pp. 273–279, 2003.
- [Tin03] C. Tindall, I. Hau, and P. Luke. Evaluation of Si(Li) Detectors for Use in Compton Telescopes. *Nucl Instr Meth A*, vol. 505:pp. 130–135, 2003.
- [Tod74] R. Todd, J. Nightingale, and D. Everett. A Proposed  $\gamma$  Camera. *Nature*, vol. 251:pp. 132–134, Sep 1974.
- [Vet] High-Sensitivity, Gamma-Ray Detection and Imaging Spectrometers Project web site at LLNL. [http://rdc.llnl.gov/rdp/high\\_sensitivity.html](http://rdc.llnl.gov/rdp/high_sensitivity.html).
- [Wal81] A. Walenta and A. Brill. Project presentation to DOE at Rockville Program Review Meeting, 1981.
- [Wal03] A. Walenta, A. Brill, A. Castoldi, T. Ç. Nurdan, C. Guazzoni, K. Hartmann, A. Longoni, K. Nurdan, and L. Strüder. Vertex Detection in a Stack of Si-drift Detectors for High Resolution Gamma-ray Imaging. In *IEEE Nuclear Science Symposium and Medical Imaging Conference NSS-MIC 2003, M3-40, submitted to IEEE Trans. Nucl Sci*. Portland, USA, 2003.
- [Web88] S. Webb. *The Physics of Medical Imaging*. Institute of Physics Publishing, Bristol and Philadelphia, 1988.
- [Wil31] E. J. Williams. The Rate of Loss of Energy by  $\beta$ -Particles in Passing Through Matter. *Proceedings of the Royal Society of London*, vol. A130:pp. 310–327, 1931.
- [Win92] C. Winkler, K. Bennett, H. Bloemen, W. Collmar, A. Connors, R. Diehl, A. van Dordrecht, J. den Herder, W. Hermsen, M. Kippen, L. Kuiper, H. Lichti, J. Lockwood, M. McConnell, D. Morris, J. Ryan, V. Schönfelder, G. Stacy, H. Steinle, A. Strong, B. Swanenburg, B. Taylor, M. Varendorff, and C. de Vries. The Gamma-ray Burst of 3 May 1991 Observed by COMPTEL on Board GRO. *Astronomy and Astrophysics*, vol. 225:pp. L9–L12, 1992.
- [Wul02] E. Wulf, J. Ampe, W. Johnson, R. Kroeger, J. Kurfess, and B. Philips. Depth Measurement in a Germanium Strip Detector. *IEEE Trans Nucl Sci*, vol. 49:pp. 1876–1880, Aug 2002.
- [XCO] XCOM: Photon Cross Sections Database. <http://physics.nist.gov/PhysRefData/Xcom/Text/XCOM.html>.
- [Zha04] L. Zhang, W. Rogers, and N. Clinthorne. Potential of a Compton Camera for High Performance Scintimammography. *Physics in Medicine and Biology*, vol. 49:pp. 617–638, 2004.
- [Zog03] A. Zoglauer and G. Kanbach. Doppler Broadening as a Lower Limit to the Angular Resolution of Next Generation Compton Telescopes. In *SPIE Proceedings*, vol. 4581, pp. 1302–1309. 2003.

# Acknowledgments

I have been looking forward to reach these last pages of my thesis in order to get the unique occasion to express my gratefulness to numerous local and global “peers” who have directly or indirectly contributed to my PhD.

First and foremost, I would like to express my gratitude to my “doktorvater” Prof. Albert Heinrich Walenta. When I was offered a PhD position to work in his group, almost everybody that I respect both personally and scientifically strongly advised me to take this offer. I am very glad that I made this decision and did not miss this great opportunity of my carrier. I can not imagine having a better advisor and mentor for my PhD, and without his common-sense, immense knowledge, perceptiveness and very bright field of experience, this work could not have been completed. I feel very lucky to have the chance to gain enormous experience by working with him and it is a privilege to be his student...

I am indebted to Prof. Nikolaj Pavel who supervised me during the first two years of my PhD, while Prof. Walenta was still the rector of our university, and continued to be my co-advisor afterwards. I would like to thank him for being a great supervisor, whose office is almost 24 hours open to his students who visit him with all kinds of problems. His support and encouragement made it possible for me to adapt myself to the completely new working and living environment very quickly. He was always optimistic, patient, enthusiastic and found practical solutions even for the most complicated problems. I am much grateful that he continued to be my second supervisor after starting his new position in Berlin and many thanks for reading my thesis carefully despite his numerous duties.

I would like to express my gratitude to the third member of my PhD committee, Prof. Hans Dieter Dahmen, for his readiness to be present at my PhD defense. He always gave me the motivation to finish my thesis as soon as possible and I am glad to get to know such a person like him who is not only a great physicist but also is a great person with immense knowledge in various aspects of life.

Without the financial support of CAESAR (Center of Advance European Studies and Research), this work would not have been possible. I would like to express my gratitude to Prof. Karl-Heinz Hoffmann and Dr. Hartwig Bechte for providing the financial support for the project and a position for me during the first three years.

My PhD project was not quite a trivial one and it would had been even more tough without my colleague Dipl.Ing. Kıvanç Nurdan. It was a very fruitful experience for us to combine his engineering talent with my physics knowledge. We had quite stressful days while mounting and operating the detectors for the first time and I am much grateful to him for being always calm in tackling the hardware problems which I managed to learn from him to a certain extend. The data acquisition system designed and built by him is one of the most important part of our system which made the collection of many coincidence events without any interruption during weeks-long operation possible.

We were not always a group of two PhD students during our project but we had some colleagues who completed their master theses in this project and contributed to this work. It was nice to work with Dipl.Phys. Karim Laihem who built the temperature controller system and worked in the mechanical setup of the whole system with us. I would like to thank him and his family for the friendly atmosphere we had both at work and at home with them. Thanks to Dipl.Phys. Iurie Chiosa for his reconstruction algorithm which produced the images presented in this work. It was also very nice to work with Jiwu Lu and I hope he will successfully complete his master thesis soon.

I would like to thank Dr. Hans-Jürgen Besch for many fruitful discussions and his intense support on the production of the power supply of the SDD. I am indebted to Prof. Martin Holder for his help in implementing the Doppler broadening in my simulation code which is vital for the theoretical estimation of the detector performance. I would like to express my gratitude to Prof. Randy Brill for his guidance on the Compton camera medical applications and on the suitable radionuclides. I am very grateful to Prof. Lothar Strüder for several instructive discussions and for the SDDs he provided. I would like to express my gratitude to Dr. Carlo Fiorini for sharing his low-noise preamplifier design and his invaluable experience on the SDD with us. Without his support, it would have been even more stressful to operate the SDD, his presence during the first operation of the 19 SDD meant a lot to me. Many ICFA instrumentation schools I participated as an instructor have been a great experience for me and the most important benefit I gained during these schools was to get to know great scientists, one of which is Dr. Alan Rudge. I am much grateful to him for sharing his immense knowledge in low noise readout electronics, for being

with us during our first experience with the single cell SDD and his continuous support and belief in our work. Special thanks for introducing us to Dr. Alan Honma who successfully bonded the dummy 19 SDD. I would like to mention three other scientists I met at ICFA schools who helped me on my work: Many thanks to Dr. Ralf Hendrik Menk for letting me play with his SDD so that I could gain some experience and for his invaluable suggestions, to Dr. Helmuth Spieler for very fruitful discussions on the front-end electronics and to Prof. Antonio Longoni for helping me to get the single cell SDD bonded. Particular thanks to Dr. Peter Lechner from MPI-HLL, Dr. Peter Goldstrass and Ralf Stötter from KETEK, Herr Osiek and Herr Kliche from InterMedical for answering my countless technical questions. I would like to thank Prof. Claus Grupen for his continuous support and especially for introducing me to my “doktorvater”. I would like to express my appreciation to Dr. Karl Reichmann for his guidance on the Anger camera. Thanks to Dr. Hendrik Wagner, Prof. Grupen and Dipl.Phys.Ing. Dieter Gebauer for helping me with the German version of the abstract...

The production of the preamplifier hybrids and the detector ceramic would not be possible without the excellent work of the members of our hybrid laboratory: Dipl.Phys.Ing. Dieter Gebauer, Dieter Junge and Alfred Peper. I would like to express my special thanks to Dieter Gebauer for his careful design of the hybrid boards and his special support in this project. I am thankful to Helmut Kolz and Ralf Ringelmann from CAESAR and Dieter Junge for their help in ordering the equipment for our project. Many thanks to Bernd Dostal for soldering the SMD components of the preamplifier and preparing the cables for the readout. I would like to thank Albert Heide from the electronic workshop of the department who did a great work in the production of the power supply for the SDD. I am very grateful to the members of our mechanical workshop, especially to Guido Schmidt, Rainer Neumann, Joachim Behner, who did an excellent job in various parts of our detector system. I would like to thank them especially for being patient with the last-minute tasks I delivered for them.

I would like to thank all the members of the detector physics and electronics group, the physics department and the colleagues from CAESAR for the nice working atmosphere. I would like to express my gratefulness to Ulrike Wermescher from CAESAR, Frau Merte and Andrea Brombach for their guidance on administrative issues. My special thanks go to Andrea for being an excellent colleague and friend for me who make me feel at home. Thanks to Dipl.Phys. Cristian Venanzi, Linjuan Yu, both Dieters, Alfred and many other colleagues for their friendship and the warm atmosphere they provide in the group. I would also like to express my gratefulness to a couple of ex-group members: Dipl.Phys. Wolf Meissner and Dipl.Ing. Martin Adamek and their families for being our friends.

The road to my graduate degree has been long and winding, so I would also like to thank some people from the early days. First of all, I would like to acknowledge my physics teacher at the high school Mehmet Tartar for making me love physics. Without the great physics education I got at Boğaziçi University, I could not have reached that point. I would like to express my gratefulness to my professors there, especially thanks to Prof. Engin Arık and Dr. Arif Mailov for introducing me the field of experimental physics. Many thanks to Dr. Mailov for his continuous support in my carrier... Thanks are due also to his family who were the emotional and moral support for us.

Before coming to the family part, I would like to thank my “Deutsche/Französische Mutter” Madame Walenta. I am much grateful to her for her continuous support since my first day in Germany. She is a great teacher who taught me German in a very short time which made my life here much easier. Merci pour tout Madame Walenta...

I would like to thank my mother, my parents in-law, my grandmothers, my nephew, my sisters in-law, my brothers and the rest of the family for their understanding and patience during all these years we had to spend away from them and for their continuous support and belief in me.

I am indebted to my husband and colleague Kivanç Nurdan for his patience, support and encouragement.

Lastly, and most importantly, I wish to thank my parents Türel and İsmail Çonka. They bore me, raised me, supported me, taught me, and loved me. I am very sad that my father could not live long enough to see my graduation but I hope he somehow watches over me even today. This thesis is dedicated to my dear parents and my husband...

# Publications List

- T. Çonka-Nurdan, K. Nurdan, F. Constantinescu, B. Freisleben, H. Kamberaj, N.A. Pavel, I. Rauhut, K. Reichmann, A.H. Walenta. Influence of the Detector Parameters on a Compton Camera. *2000 IEEE Nuclear Science Symposium and Medical Imaging Conference: Conference Proceedings*. (2001) M50 P. 22–26, ISBN 0-7803-6506-2.
- T. Çonka-Nurdan, K. Nurdan, F. Constantinescu, B. Freisleben, N.A. Pavel, and A.H. Walenta. Impact of the Detector Parameters on a Compton Camera. *IEEE Transactions on Nuclear Science*. **49(3)** (June 2002) 817-821.
- K. Nurdan, T. Çonka-Nurdan, H.J. Besch, B. Freisleben, N.A. Pavel, A.H. Walenta. FPGA Based Data Acquisition System for a Compton Camera. *Nuclear Instruments and Methods in and Methods in Physics Research Section A* **510** (2003) 122-125.
- K. Nurdan, H.J. Besch, T. Çonka-Nurdan, B. Freisleben, N.A. Pavel, A.H. Walenta. Development of a Compton Camera Data Acquisition System Using FPGAs. *2003 International Signal Processing Conference: Conference Proceedings* (2003) Paper 406, ISBN 1009129.
- A.H. Walenta, A.B. Brill, A. Castoldi, T. Çonka-Nurdan, C. Guazzoni, K. Hartmann, A. Longoni, K. Nurdan, L. Strüder. Vertex Detection in a Stack of Si-drift Detectors for High Resolution Gamma-ray Imaging. *2003 IEEE Nuclear Science Symposium and Medical Imaging Conference: Conference Proceedings*. (2004) M3-40, ISBN 0-7803-8258-7.
- T. Çonka-Nurdan, K. Nurdan, K. Laihem, A.H. Walenta, C. Fiorini, N. Hoörncl, L. Strüder, C. Venanzi. Compton Electrons in Silicon Drift Detector: First Results. *2003 IEEE Nuclear Science Symposium and Medical Imaging Conference: Conference Proceedings*. (2004) M6-41, ISBN 0-7803-8258-7.
- C. Venanzi, T. Çonka-Nurdan, K. Nurdan, A.H. Walenta, R. Longo. A New Front-End Electronics Design for Silicon Drift Detector. *2003 IEEE Nuclear Science Symposium and Medical Imaging Conference: Conference Proceedings*. (2004) N36-63, ISBN 0-7803-8258-7.
- T. Çonka-Nurdan, K. Nurdan, A.H. Walenta, H.J. Besch, C. Fiorini, B. Freisleben, N.A. Pavel. Silicon Drift Detector Readout Electronics for a Compton Camera. *Nuclear Instruments and Methods in Physics Research Section A* **523** (2004) 435-440.
- T. Çonka-Nurdan, K. Nurdan, K. Laihem, A.H. Walenta, C. Fiorini, B. Freisleben, N. Hoörncl, N.A. Pavel, and L. Strüder. Preliminary Results on Compton Electrons in Silicon Drift Detector. *IEEE Transactions on Nuclear Science*. **51(5)** (October 2004) 2526-2532.
- T. Çonka-Nurdan, K. Nurdan, A.H. Walenta, I. Chiosa, B. Freisleben, N.A. Pavel, L. Strüder. Compton Camera Coincidences in the Silicon Drift Detector. *2004 IEEE Nuclear Science Symposium and Medical Imaging Conference: Conference Proceedings*. (2004) M10-60.
- T. Çonka-Nurdan, K. Nurdan, A.H. Walenta, I. Chiosa, B. Freisleben, N.A. Pavel, L. Strüder. First Results on Compton Camera Coincidences with the Silicon Drift Detector. *submitted to IEEE Transactions on Nuclear Science for publication*. (Nov. 2004)

